The Contemporary Stress Field of Australia's North West Shelf and Collision-Related Tectonism

by

Scott D. Mildren

Department of Geology and Geophysics

University of Adelaide

Submitted as fulfilment of the higher degree

Doctor of Philosophy

June 1997

Table of Contents

List of Figures

CHAPTER 1

CHAPTER 2

CHAPTER 3

CHAPTER 4

CHAPTER 5

CHAPTER 6

CHAPTER 7

List of Tables

CHAPTER 3

CHAPTER 4

CHAPTER 5

CHAPTER 6

List of Equations

CHAPTER 3

CHAPTER 4

CHAPTER 5

CHAPTER 6

CHAPTER 7

Abstract

A major new analysis of borehole breakouts in the Carnarvon and Bonaparte Basins of the Australian North West Shelf has revealed contemporary maximum horizontal stress (σ_{Hmax}) directions to be 090°N-100°N and 055°N-060° respectively. The first-order σ_{Hmax} direction rotates 40° between the western and eastern ends of the North West Shelf.

Stress magnitude analyses reveal that in both the Carnarvon and Bonaparte Basins the stress regime is broadly on the boundary between strike-slip and extension. In the Carnarvon Basin stress regime changes from strike-slip near the shoreline to extensional with increasing distance northwest towards the Indian Ocean Basin. In the Bonaparte Basin the stress regime changes from extension in the southwest to strike-slip northeast towards the plate margin.

In the context of the plate boundary forces controlling regional stress orientations, the observed stress rotation can be explained solely by the focusing of the forces balancing ridge push along collisional segments of the northeastern boundary of the Indo-Australian Plate.

Stress indicators in the Carnarvon Basin exhibit consistent orientations that differ between the basin's depocentres and its flanks. σ_{Hmax} is consistently oriented E-W within the relatively structureless depocentres of the Barrow-Dampier Sub-basins, and oriented NE-SW in the more structurally complex basin margins. Stress orientations in the faulted basin margins may differ from the regional mean due to: contrasting elastic

properties between rocks forming the basin margins and those comprising the depositional centre (i.e a lower Young's modulus on the basin margins), and/ or; active faults locally perturbing stress magnitude and orientation.

The contemporary σ_{Hmax} directions determined have important consequences for the style and orientation of fault reactivation within the North West Shelf. On the margins of the Barrow-Dampier Sub-basins, faults oriented NE are most susceptible to normal reactivation, the E-W faults to sinistral strike-slip reactivation and the N-S faults to dextral strike-slip reactivation and the NW oriented faults are not likely to be reactivated. In the Bonaparte Basin, the dominant NE/E-NE structural trend is susceptible to extensional reactivation, the E-W trend is most susceptible to sinistral strike-slip reactivation and the Palaeozoic NW structural is unlikely to be reactivated.

Statement

This thesis contains no material which has been accepted for the award of any other degree or diploma in any university or other tertiary institution and, to the best of my knowledge and belief, contains no material previously published or written by another person, except where due reference has been made in the text.

I give consent to this copy of my thesis, when deposited in the University Library, being available for loan and photocopying.

15/6/'17

Scott D. Mildren Date

Acknowledgments

This project would not have been possible without a postgraduate research scholarship funded by the Australian Geological Survey Organisation (AGSO) or the data and support from the following oil companies: Ampol, Apache, BHP, BP, MIM, Norcen, Phillips, Santos, TCPL, and WMC and also from the Australian Bureau of Resource Sciences.

To Richard Hillis, thankyou for four years of enthusiastic and dedicated supervision. I hope it was as good for you as it was for me! Thankyou to Chris Pigram for your remote guidance, pep talks and reality checks and also to David Castillo for contributing important discussions during the final critical stages of write up.

Thanks to David Coblentz, Murray and Sam for help with various and numerous computer problems. Thanks to all the staff in the front office Gerald, Soph, Kim, Mary and to Sherry for drafting. Thankyou to all fellow geology students who I have had the privilege of meeting since I started in the department. In particular I would like to thank Rob 'the blob', Bruce, John, Eike, Mandy, Betina, Paul, Gary, Jack, Miles (take care of The Beast), Big Nick (an honorary geologist), Bunge (the early years) and the Geology II class of 1989. You all made my candidature a memorable experience.

I would like to thank my family for their support and encouragement since I started at University. Last but by no means least I would like to thank Lisa for her friendship, understanding, reference typing and unyielding belief that I would finally finish.

Chapter 1

Introduction

1.1 Project Rationale

Recently, knowledge of the contemporary stress field of the earth's crust has expanded dramatically as a result of the World Stress Map Project (Zoback, 1992). The World Stress Map Project compiled maximum horizontal stress orientations throughout the world based on a variety of stress indicators. Knowledge of stress orientation has been used to analyse tectonic and engineering problems ranging from elucidating the forces that drive plate motions (Cloetingh & Wortel, 1986; Coblentz et al., 1995) to planning most stable horizontal drilling directions (Bradley, 1979; Hillis & Williams, 1993b).

In comparison with areas such as North and South America, and Western Europe, regional maximum horizontal stress (σ_{Hmax}) orientations in the Australian continent are unclear (Zoback et al., 1989; Denham & Windsor, 1991; Zoback, 1992). Fewer data are available for Australia than for continental areas with well-defined stress orientations. Furthermore, such data as are available for Australia suggest that horizontal stress orientations are variable, in contrast to midplate North America, for example (Zoback et al., 1989).

The aim of this thesis is to improve the understanding of the contemporary stress field of the Australian Continent, and more specifically that of the Australian North West Shelf (Figure 1.1). The thesis focuses on the Australian North West Shelf region for two principal reasons.

(i) The Australian North West Shelf is an area of significant Mio-Pliocene - Recent tectonism associated with collision between the Australian Continent and the Banda Island Arc. Data on the contemporary stress field of the North West Shelf has the potential to elucidate the nature of this tectonism which has been extensively debated (Woods, 1988; Nelson, 1989). Such data can also help constrain the forces acting at plate boundaries adjacent to the North West Shelf, and thus analyse the forces driving plate motion. The application of data on the contemporary stress field to such tectonic problems was the motivation for the Australian Geological Survey Organisation to fund this project.

(ii) The North West Shelf has been a focus of hydrocarbon exploration over the last forty years. Hydrocarbon production from the North West Shelf recently overtook that from what was previously Australia's most important hydrocarbon province, the Bass Strait (Baillie, 1995). Data obtained whilst drilling and logging hydrocarbon exploration wells can be used to constrain the contemporary stress field. Furthermore, not only do hydrocarbon exploration provinces provide the data to analyse the contemporary stress field, but, as discussed below, an understanding of the contemporary stress field is particularly important to the exploration for, and production of hydrocarbon reserves.

Figure 1.1 Location of the North West Shelf of Australia (Purcell & Purcell, 1988).

1.2 Determining the Contemporary Stress Field

This thesis was inspired by the World Stress Map Project, and the realisation that the World Stress Map was lacking results for Australia. Zoback's (1992) World Stress Map compilation incorporated approximately 75 stress indicators for Australia compared to, for example, 2611 in North America and 1827 in Europe. Stress orientation indicators can be obtained using four different types of measurement methods: earthquake focal mechanisms, borehole breakouts, in-situ stress measurements (hydraulic fracture and overcoring) and young geologic data including fault slip and volcanic alignments (Zoback, 1992). As discussed in Chapter 4, borehole breakouts provide the only significant new source of stress orientation data available for the North West Shelf region, and have been used extensively in this project. Furthermore, leak-off tests, which are routinely undertaken to determine the maximum mud-weight that can be used whilst drilling, provide an indication of the magnitude of the minimum principal stress (Ervine & Bell, 1987; Bell, 1990b; Gaarenstroom et al., 1993). Given that prior to this thesis very little data was available on the stress field of

the North West Shelf, the project philosophy was to utilise the large amount of data already available from hydrocarbon exploration for analysing the stress field. For this reason the focus of this thesis is on the determination of stress orientation from breakout data and stress magnitude analysis has been limited to that possible from leak-off tests.

1.3 Applications for Contemporary Stress Field Data

The motivation for determining the contemporary stress field stems from the wide range of applications to which such data can be put. As discussed above, the nature of the contemporary stress field can help elucidate plate-driving forces and the nature of recent tectonism. Knowledge of the contemporary stress field can also be applied to a range of geological and engineering problems related to hydrocarbon exploration and production, namely:

- planning most stable deviated drilling directions (e.g. Bradley, 1979; Addis et al., 1993; Hillis et al., 1995);
- prediction of open, natural and induced fracture orientation in hydrocarbon reservoirs (e.g. Bell & Babcock, 1986; Bell, 1990a; Hillis & Williams, 1993b), and;
- assessing the hydraulic integrity of hydrocarbon traps (e.g.. Caillet, 1993; Gaarenstroom et al., 1993; Mildren et al., 1994).

Each of these applications are pertinent to hydrocarbon exploration and development on the North West Shelf of Australia.

1.4 Structure of Thesis

After outlining the geology and tectonic evolution of the North West Shelf in Chapter 2, this thesis outlines how stress magnitudes and orientations were determined from

exploration drilling data obtained in the region (Chapters 3 and 4 respectively). The results of the analyses are presented in Chapter 5, and discussed in the context of both contemporary tectonics (Chapter 6) and of applications to petroleum exploration and production (Chapter 7). This thesis concludes with a summary of the project findings (Chapter 8).

Chapter 2

Geological Framework of Australia's North West Shelf

2.1 Introduction

When interpreting a contemporary stress field, it is important to provide a geological context in which to place the results. Properties such as tectonic history, structural setting, and stratigraphy all relate to the geomechanical setting of an area. Each must be addressed in order to ensure sensible interpretation of the stress data. It is the interaction of all of these factors with far field stresses, which defines the in-situ stress distribution at all scales (Bell, 1990b; Cloetingh et al., 1990; Teufel, 1991; Aleksandrowski, et al., 1992; Yassir and Bell, 1994, Coblentz et al., 1995).

This chapter reviews the tectonics of the Indo-Australian plate, the structural framework and evolution of the North West Shelf, and the geological setting of the Carnarvon and Bonaparte basins, from which the stress data was obtained. These and other factors are combined to elucidate the geomechanical setting of the North West Shelf. A general description of the North West Shelf's location, physiography and exploration history is also given.

2.2 Location and Physiography of the Australian North West Shelf

The North West Shelf of Australia extends approximately 2400 km between Exmouth Gulf in the south and Melville Island in the north (Figure 2.1). Although it lies predominantly within offshore Western Australia, its most northern reaches are in the offshore Northern Territory. It is comprised not only of the continental shelf itself but

also the outer shelf and marginal plateaus. The average width of the region is approximately 300 km and its area is over 720,000 km^2 (Purcell & Purcell, 1988). The area is remote from large population centres, the southern most extent lying approximately 1000 km from the closest large city, Perth. There are smaller population centers and port facilities along the shelf's length at Onslow, Dampier, Port Hedland, Broome, Derby and Darwin, which provide supply bases for both petroleum and mineral exploration activities. These towns are connected to Perth by the North West Coastal Highway and the Great Northern Highway. They are all serviced daily by flights from Perth or Darwin and those on the coast are on regular domestic shipping routes for petroleum and mineral exports.

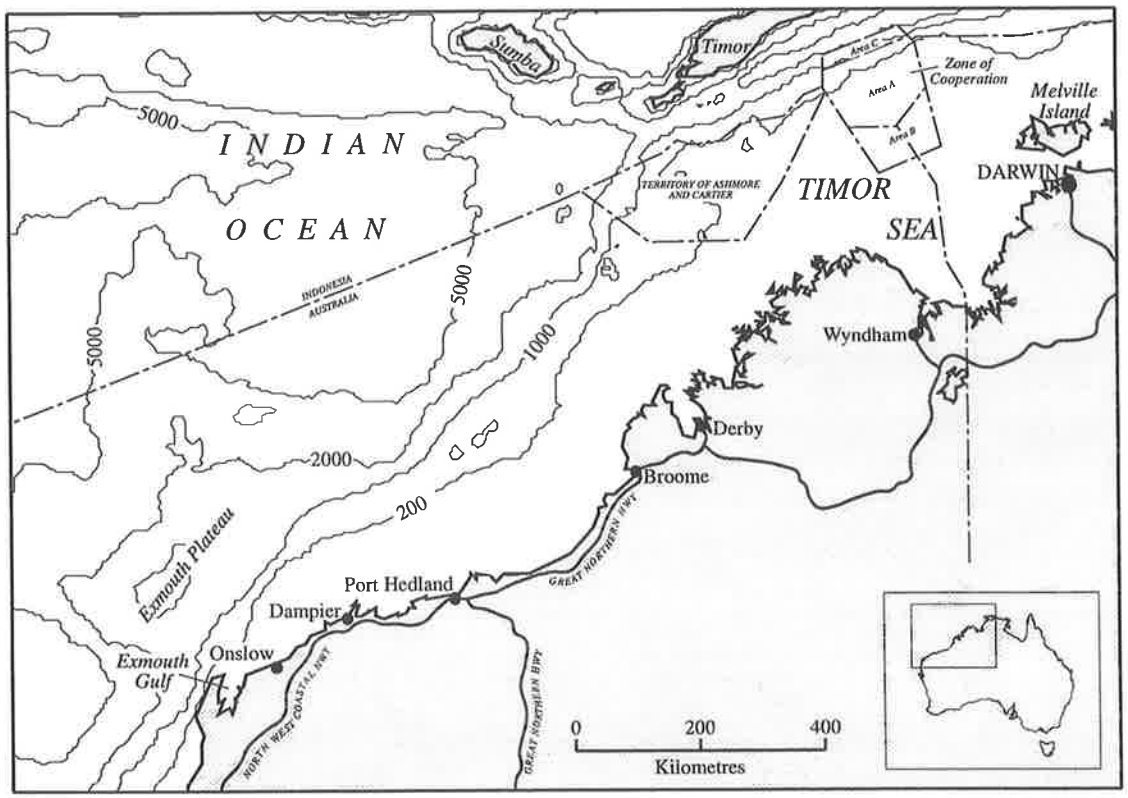

Figure 2.1 Geography of the North West Shelf of Australia.

The climate along the North West Shelf varies from tropical in the north to semi-arid in the south. Mean daily maximum temperatures range between 36.7°C to 26.6°C in Port

Hedland and 33.2°C to 30.4°C in Darwin. The effect of the monsoon season increases to the north providing mean yearly rainfalls of 309 mm and 1668 mm in these two centres respectively[1]. The region is susceptible to extensive thunderstorms and occasional cyclones due to the monsoon and southerly migrating highs causing hot dry easterly winds from the interior. The cyclones are the major threat to petroleum operations along the North West Shelf (Purcell & Purcell, 1994).

2.3 Exploration History

The North West Shelf region is of economic importance for Australia, based primarily on its hydrocarbon content. Ever since the discovery of non-commercial oil in the Rough Range-1 well during 1953, the region has been the focus of hydrocarbon exploration.

During 1963, the first economic oil discovery was made in the Carnarvon Basin at the Barrow-1 well. The resulting Barrow Island Field has been in production since 1967 and remains the largest in Western Australia. The search for hydrocarbons following the Barrow Island find spread north to the Bonaparte Basin and led to the discovery of the non-commercial Petrel Gas Field at Petrel-1 in 1969. A wave of exploration drilling followed, delivering mixed results. Several new fields were discovered in the Carnarvon Basin during the early seventies (North Rankin giant gas and condensate field in the Dampier, the Angel Field and the Goodwyn Field), although no commercial developments resulted from 32 wildcat wells drilled in the Bonaparte Basin during the same period.

[1] Mean temperature and rainfall statistics are taken from the Australian Bureau of Meteorology's world wide web page (1996). URL - http://www.bom.gov.au/climate/averages/index.shtml

A second wave of exploration drilling was initiated in the early eighties by the dramatic increase in oil price and led to a string of discoveries. These included Gorgon, Dixon, Harriet, South Pepper, Talisman, Saladin and Rosette in the Carnarvon Basin and Jabiru, Challis/Cassini and Skua in the Bonaparte Basin. Further successes were made in the Carnarvon region during the late eighties and the early nineties, such as the Wanaea/Cossack, Wandoo, Leatherback and Maitland fields. Although two thirds of Australia's offshore exploration occurred in the Bonaparte Basin during this time, success there remained elusive and exploration activity declined.

The signing of the Timor Gap Zone of Cooperation Treaty and the award of production sharing contract areas in 1992 encouraged further exploration in the Bonaparte region. Renewed exploration has been rewarded with several important discoveries in the area during 1994-1995: Elang, Elang West, Kakatua, Laminaria, Corallina and Undan/Bayu. Similarly, discoveries continue to be made in the Carnarvon Basin with fields such as Alkimos, Crest, Chrysaor and Saffron (Taylor, 1995).

The current exploration climate of the North West Shelf, has also stimulated academic interest. Projects ranging from structural and sedimentary interpretations to reservoir analyses and defining hydrocarbon charge histories have since been implemented. These studies, like this project on the contemporary stress field, will be used by the hydrocarbon exploration community to make informed decisions regarding production methods and future exploration targets.

2.4 The Indo-Australian Plate

The Indo-Australian plate is bounded by a mid-ocean ridge to its south-west and a complex convergent margin to its north-east (Figure 2.2). The convergent boundary comprises continental collision in the Himalayas, New Guinea and New Zealand, the Banda Island Arc, subduction at the Sumatra, Java, Solomon and New Hebrides Trenches, and subduction of the Pacific plate beneath the Indo-Australian plate at the Tonga-Karmadec Trench (Figure 2.2).

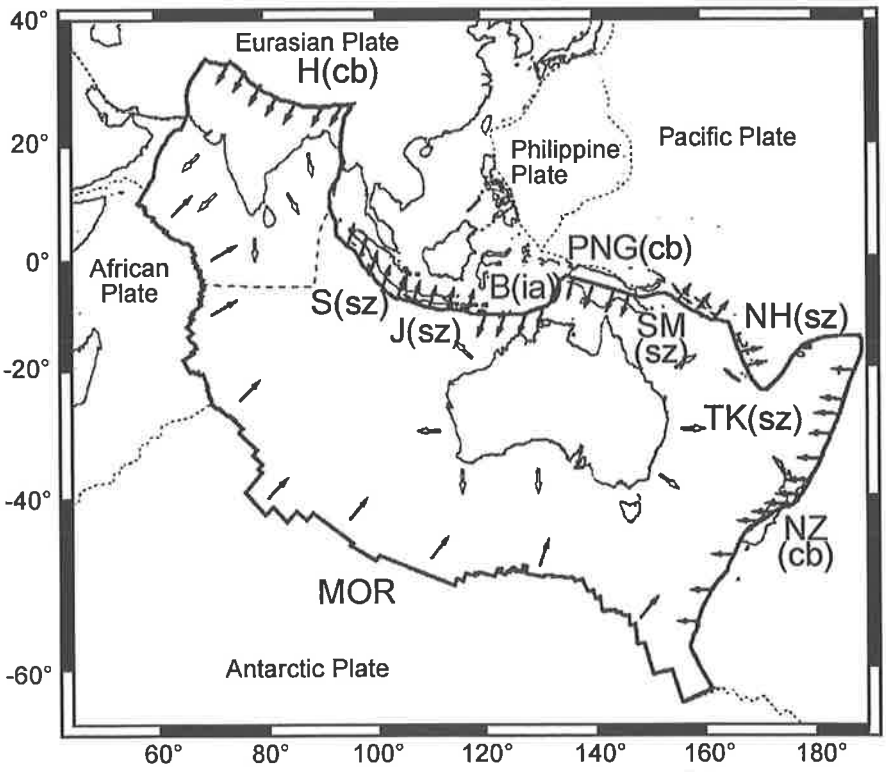

Figure 2.2 Indo-Australian Plate with boundaries as defined by Minster and Jordan (1978). Solid filled arrows represent the boundary forces acting on the plate. Open arrows represent the topographic forces associated with the continental margins. Force arrows are not drawn to scale. The plate boundaries are characterized as cb = collisional boundary; sz = subduction zone; and ia = island arc. H = Himalayas; S = Sumatra Trench; J = Java Trench; B = Banda Arc; PNG = Papua New Guinea; SM = Solomon Trench; NH = New Hebrides Trench; TK = Tonga-Kermadec Trench; NZ = New Zealand; and MOR = Mid Ocean Ridge. From Coblentz et al. (1995).

The Australian North West Shelf is located south of the convergent northeastern boundary of the Indo-Australian Plate. The western end of the North West Shelf lies

approximately 800 km directly south of the Java subduction zone while the eastern end is immediately south of the zone of collision between the Australian continent and the Banda Arc. Since the breakup of Gondwana in the Middle Jurassic the shelf has been a passive margin although its most northern extent is becoming active, with Australia/Banda Arc collision.

2.5 The Sedimentary Basins of the North West Shelf

The North West Shelf is underlain by four Phanerozoic continental margin rift basins, the Carnarvon, Roebuck/Canning, Browse and Bonaparte Basins (Figure 2.3). Each basin, with the exception of the Browse Basin, contains two structurally and stratigraphically different components, namely a Palaeozoic, northwest oriented element, and an overlying northeast trending, mostly Mesozoic element (Teichert, 1958; Playford et al., 1975; Bradshaw et al., 1988). The Browse Basin is a Mesozoic feature dominated by a northeast structural grain. With respect to hydrocarbon exploration, the majority of interest has been focused on the Mesozoic basin components, all of which comprise the Westralian Superbasin. Yeates et al. (1987) defined the Westralian Superbasin as 'the Permian to Cretaceous fill, generally around 10 km thick, preserved along the western margin of Australia'. Inshore, the superbasin abuts or merges with the cross-trending Palaeozoic basins or it simply laps onto Precambrian cratonic elements that separate the Palaeozoic basins (Figure 2.3).

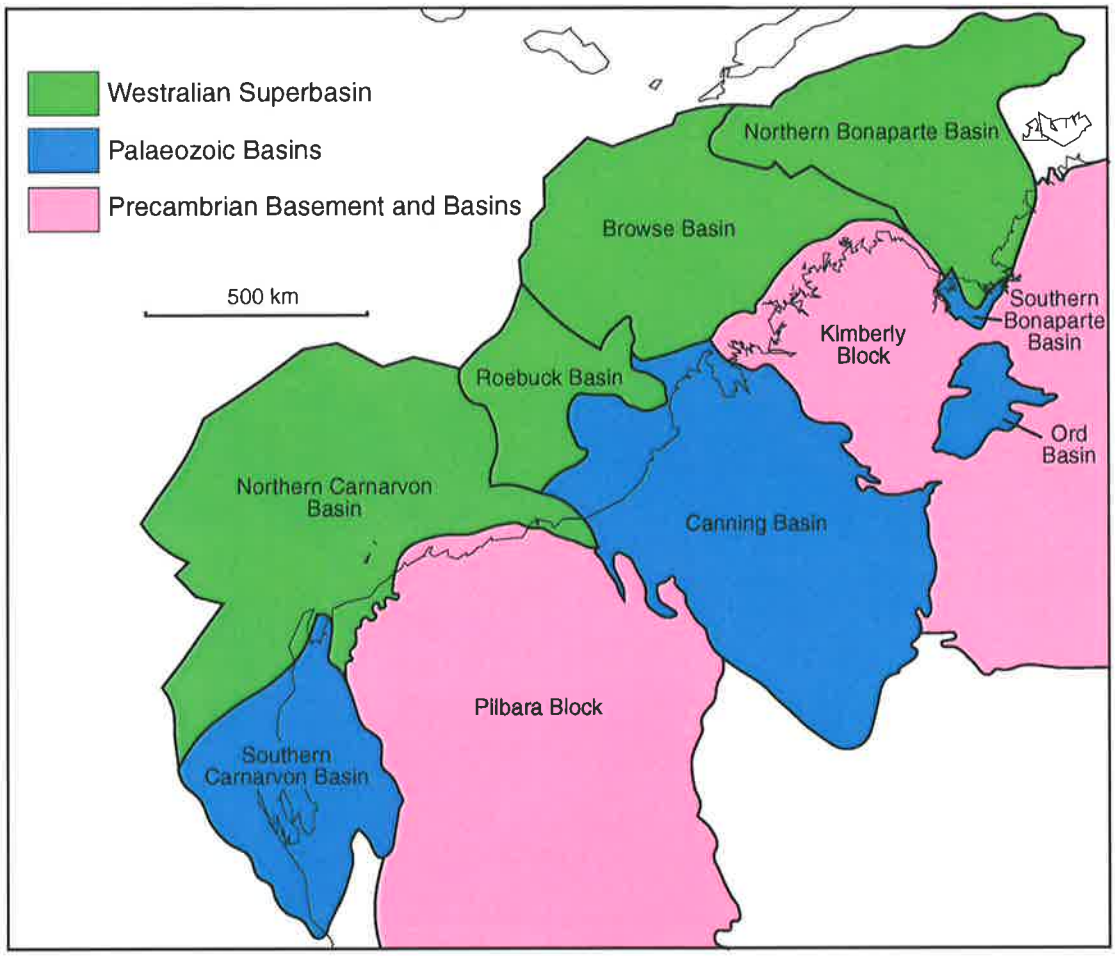

Figure 2.3 Phanerozoic and Precambrian basins and cratons in the northwest of Australia (after Hocking et al., 1994).

The nomenclature of Westralian Superbasin elements has been defined by Bradshaw et al. (1988), and later by Hocking et al. (1994), to recognise the substantial differences in structure and stratigraphy between them and their Palaeozoic counterparts. The offshore and onshore components of the Carnarvon and Bonaparte Basins become the Northern and Southern Carnarvon Basin and the Northern and Southern Bonaparte Basins respectively. In both cases the southern components contain the northwest trending Palaeozoic sediments and the northern components contain the overlying Permian and Mesozoic sequences. Bradshaw et al. (1988) referred to the offshore Canning Basin as an 'unnamed basinal element' leaving its definition to be decided by future reviewers. Hocking et al. (1994), following the suggestion of Horstman and

Purcell (1988), named the offshore Canning Basin the Roebuck Basin. In summary, the Northern Carnarvon, Roebuck, Browse and Northern Bonaparte Basin are the elements comprising the Westralian Superbasin and the Southern Carnarvon, Canning and Southern Bonaparte Basin are the older Phanerozoic elements. Reference to the Carnarvon and Bonaparte Basins in the following chapters refer to the Northern Carnarvon and Northern Bonaparte Basins respectively.

2.6 Subdivisions of Basins of the North West Shelf

The basins of the North West Shelf are themselves divided into elements. The subdivisions of each basin are referred to throughout this thesis and therefore require definition (Figure 2.4). The divisions presented here are those of Hocking et al. (1994).

The Northern Carnarvon Basin is comprised of marginal shelves (Peedamullah and Lambert Shelves), two complex grabens (Barrow and Dampier Sub-basins), a mid-basin ridge (Rankin Platform), and an outer series of faulted troughs (Exmouth, Investigator and Dixon Sub-basins, Kangaroo Trough). The boundaries are generally well defined, with the exception of the boundary between the Barrow and Dampier Sub-basins. The Beagle Sub-basin is transitional into the Roebuck Basin although it is included in the Northern Carnarvon Basin because of its apparent continuity of structural trends from the adjoining Dampier Sub-basin and Rankin Platform (Hocking et al., 1994).

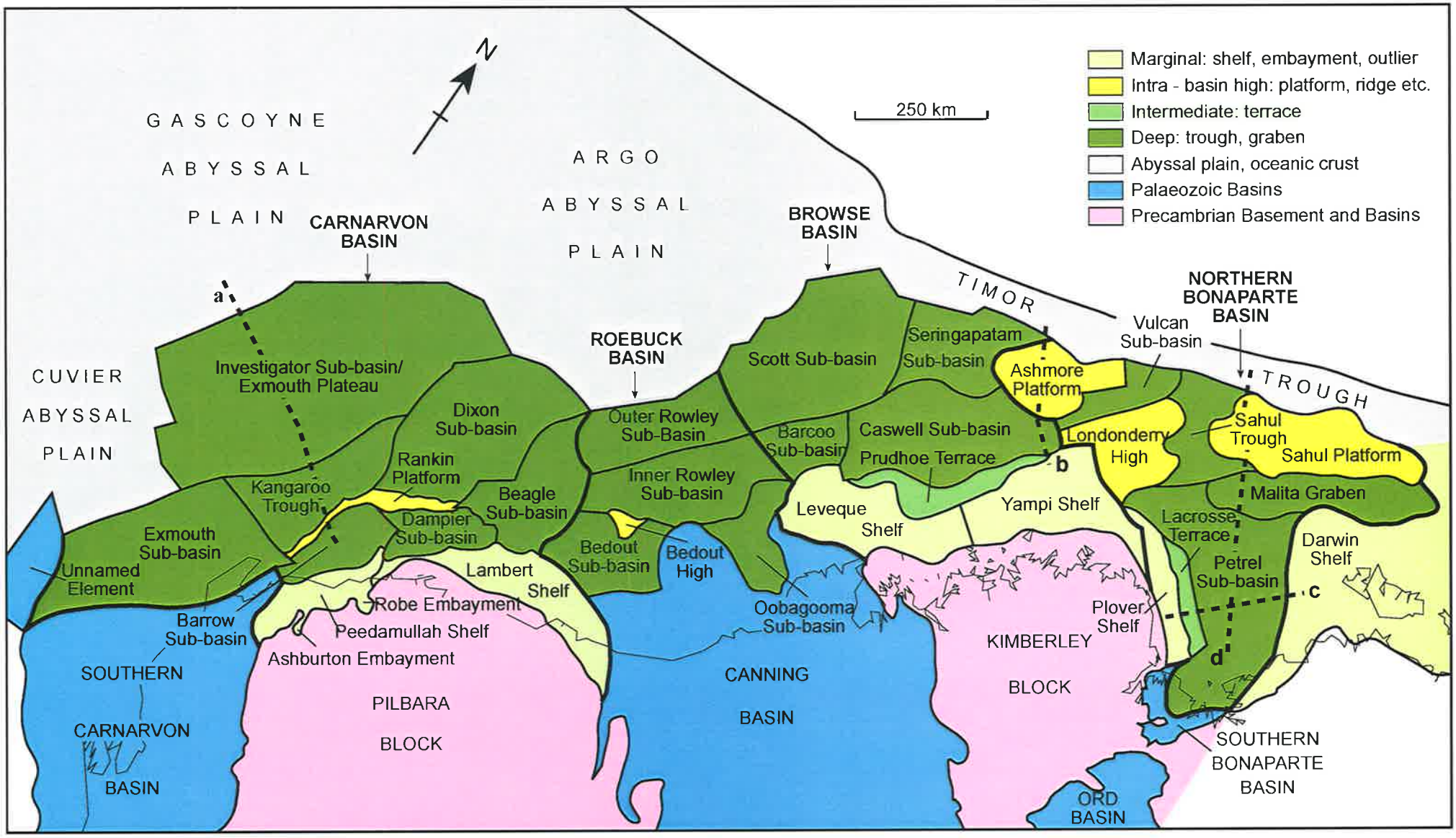

Figure 2.4 Subdivisions of basins comprising the North West Shelf of Australia (after Hocking et al., 1994). Dashed lines denoted by a, b, c, and d correspond to the line drawings of AGSO deep-seismic profiles illustrated in Figure 2.11.

The Roebuck Basin is comprised of the Bedout and Rowley Sub-basins. They are separated by an elongate high along the seaward margin of the Bedout Sub-basin culminating in the Bedout High. The basin also contains the Oobagooma Sub-basin which is the offshore extension of the Fitzroy Trough (Hocking et al., 1994).

The Browse Basin is comprised of marginal shelves on the landward side (Leveque and Yampi Shelves), which are separated from the central trough (Barcoo and Caswell Sub-basins) by an intermediate-depth terrace (Prudhoe Terrace). The Caswell Sub-basin contains several broad anticlinal trends (Brewster, Caswell, Scott Reef and Buffon trends) and grades to the southwest and northeast into the Barcoo and Vulcan Sub-basins respectively. To the northwest it grades into the Scott and Seringapatarn Sub-basins via a faulted hingeline (Hocking et al., 1994).

The largest feature of the Northern Bonaparte Basin is the Petrel Sub-basin which is dominated by the Palaeozoic northwest-southeast trend. The Petrel Sub-basin is separated from the Kimberly Block to the southwest by the Lacrosse Terrace and the Plover Shelf, and bounded to the northeast by the Darwin Shelf. The main depocentres lie to the north and east of the Petrel Sub-basin in the Malita Graben and Vulcan Sub-basin, respectively. These sub-basins are in turn separated from the Timor Trough by the Sahul and Ashmore Platforms. The Londonderry High is most likely an extension of the Sahul Platform, separated by the Sahul Trough, a broad, northwest-oriented syncline.

2.7 Tectonic and Stratigraphic History

The evolution of both the Palaeozoic and Mesozoic basins of the North West Shelf are addressed in the following sections. The basin evolution presented below is based on the work of Hocking (1988), Mory (1988), Stagg & Colwell (1994), Colwell & Stagg (1994), and Baillie et al. (1994) unless otherwise stated. There is no formally defined stratigraphic nomenclature for the Browse Basin (Maung et al., 1994). Most authors have referred to sedimentary units in the basin by age, tectonics or by association with those in adjacent basins. In this study, sedimentary units in the Browse Basin are referred to by association with those in the Bonaparte Basin. Figures 2.5, 2.6, and 2.7 illustrate composite stratigraphic columns for Carnarvon, Roebuck and Bonaparte Basins.

2.7.1 Palaeozoic Onshore Basins

Latest Precambrian to Ordovician

The Australian continent, comprising part of East Gondwanaland, underwent a significant phase of dextral shear from the Marinoan (600 Ma) until the end of the Precambrian (540 Ma). The shearing uplifted central parts of the continent, creating a northwest structural grain and culminated in continental breakup along its eastern and northern margins in the Latest Precambrian. This was associated with a vast outpouring of continental basalt, the Antrim Plateau Volcanics, which formed the floor to the Southern Bonaparte Basin. The volcanics were succeeded unconformably by widespread carbonate deposition during the Early Cambrian (Tarrara Formation), followed by deposition of predominantly shallow to marginal-marine siliclastics of the Carlton Group which continued until the Early Ordovician. This broad transgression across central and northern Australia reflected a global rise in sea level associated with

the renewed sea floor spreading activity of continental breakup. By Early Ordovician, the final assembly of East and West Gondwanaland was complete and Australia's eastern margin had become a zone of convergence.

Following the assembly of Gondwanaland there began a renewed phase of extension along Australia's eastern margin. Deposition of marine clastics passing up into carbonates and shales was initiated in the Canning Basin (Nambeet, Willara, Goldwyer and Nita Formations), while fluvial to shallow-marine sandstones were deposited in the Southern Carnarvon Basin (Baillie et al., 1994). Although the geological history of this period is relatively unknown, these deposits have been interpreted by some authors to be initial fill of failed rift arms extending from triple junctions along the ancestral northwest margin (Burke & Dewey, 1973; Veevers, 1976, Veevers, 1988).

Silurian to Mid-Carboniferous

Glaciation in North Africa around the Latest Ordovician to Early Silurian (Caputo & Crowell, 1985) led to a global drop in sea level, causing the development of shallow hypersaline conditions. Evaporite deposits were laid down in the Southern Carnarvon Basin (Yaringa Evaporite of the Kalbarri Group), the Canning Basin (Carribuddy Formation) and the Southern Bonaparte Basin. These arid conditions persisted through the Early Devonian with deposition only occurring in the Canning Basin. The northern parts of the basin received marginal marine carbonates and clastic sediments (Poulton Formation) while aeolian and playa sediments (Tandalgoo Red Beds) were deposited in the south. Brown et al. (1984) interpret these deposits as a result of a pre-rift thermal upwarp phase prior to rifting in the Mid to Late Devonian.

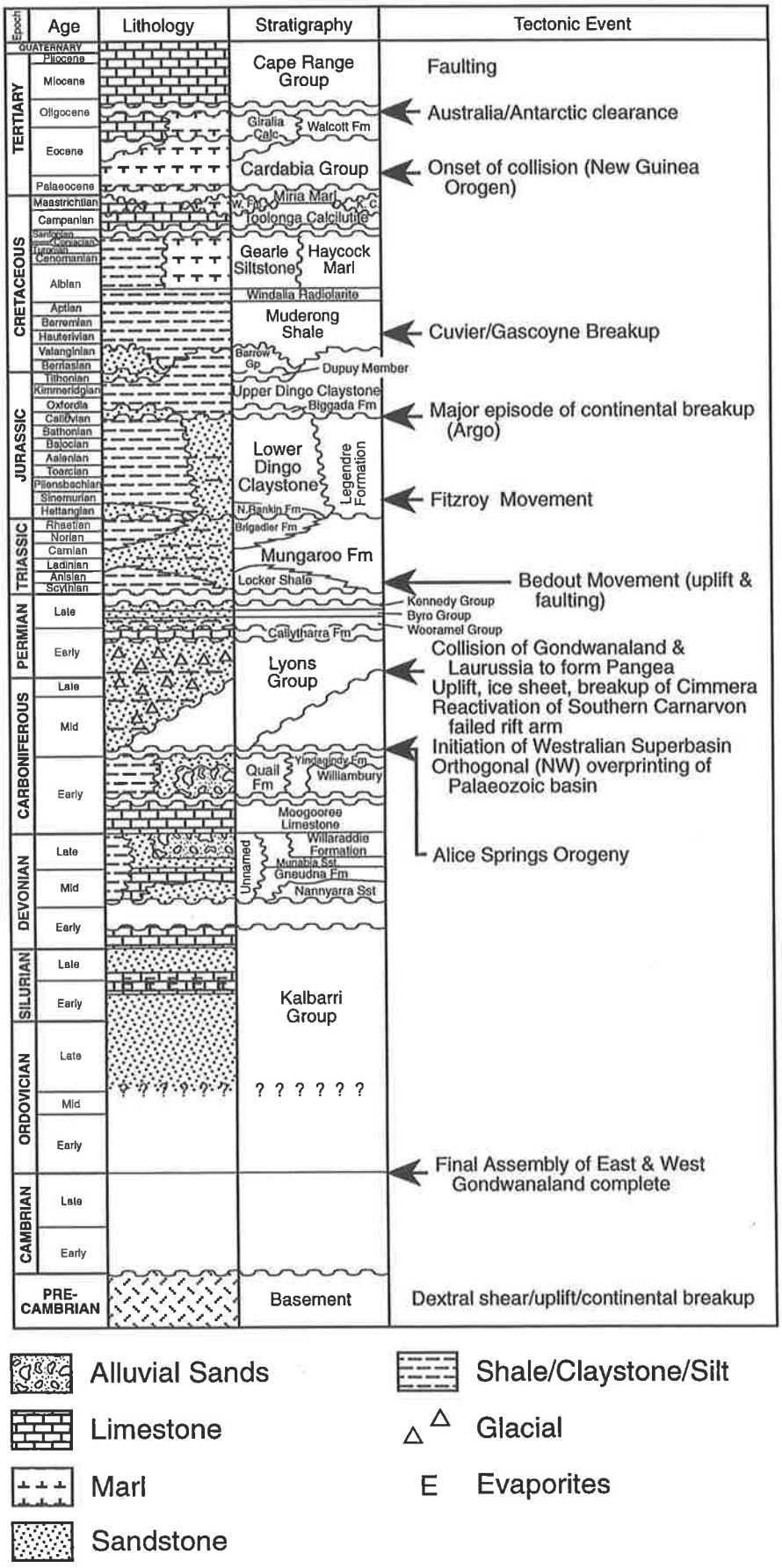

Figure 2.5 Summary stratigraphy for the Carnarvon Basin (after Hocking, 1988; Woodside, 1988; Stagg & Colwell, 1994).

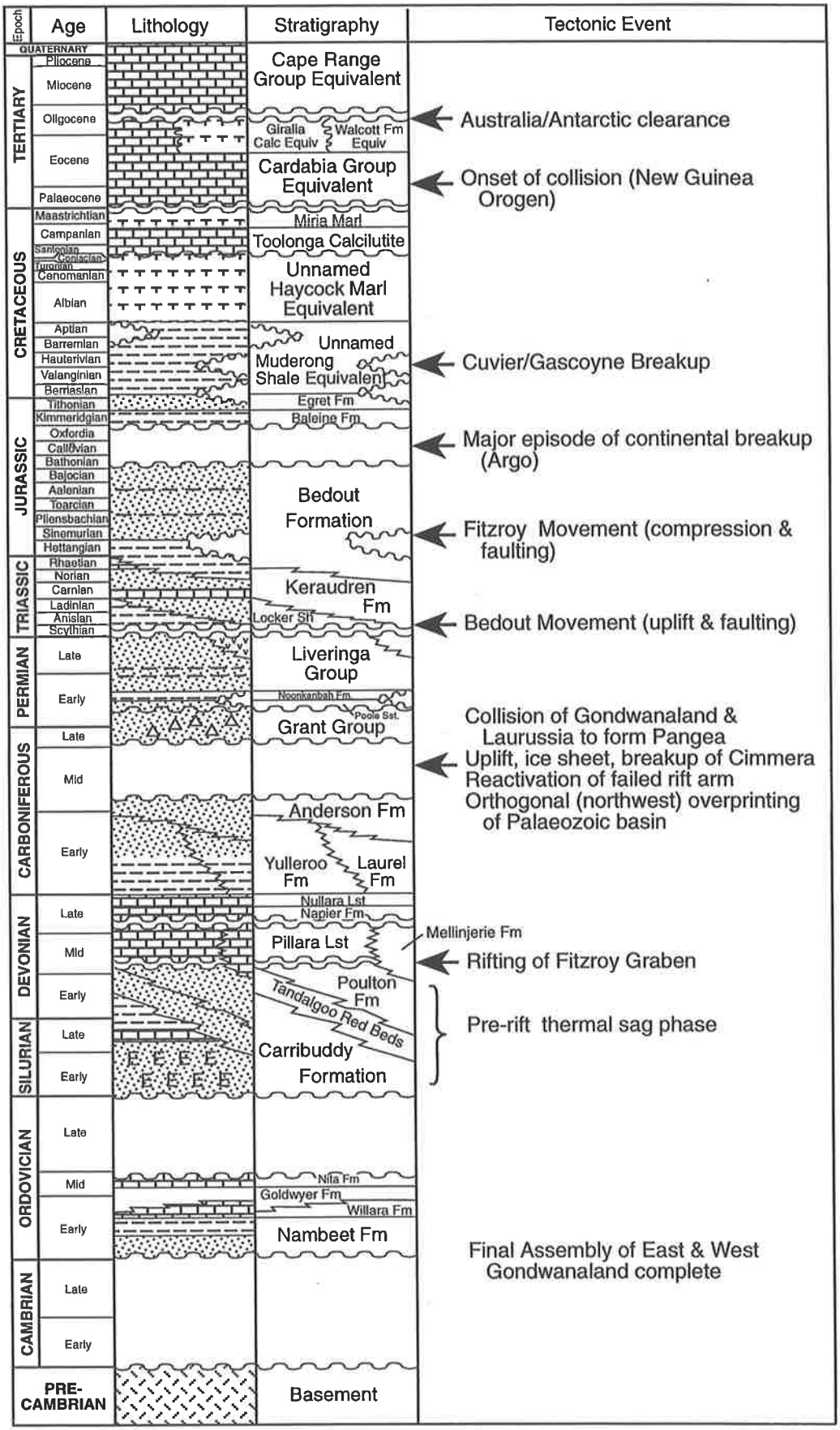

Figure 2.6 Summarised stratigraphy for the Canning and Roebuck Basins (after Kennard et al., 1994; Stagg & Colwell, 1994). See Figure 2.5 for lithological legend.

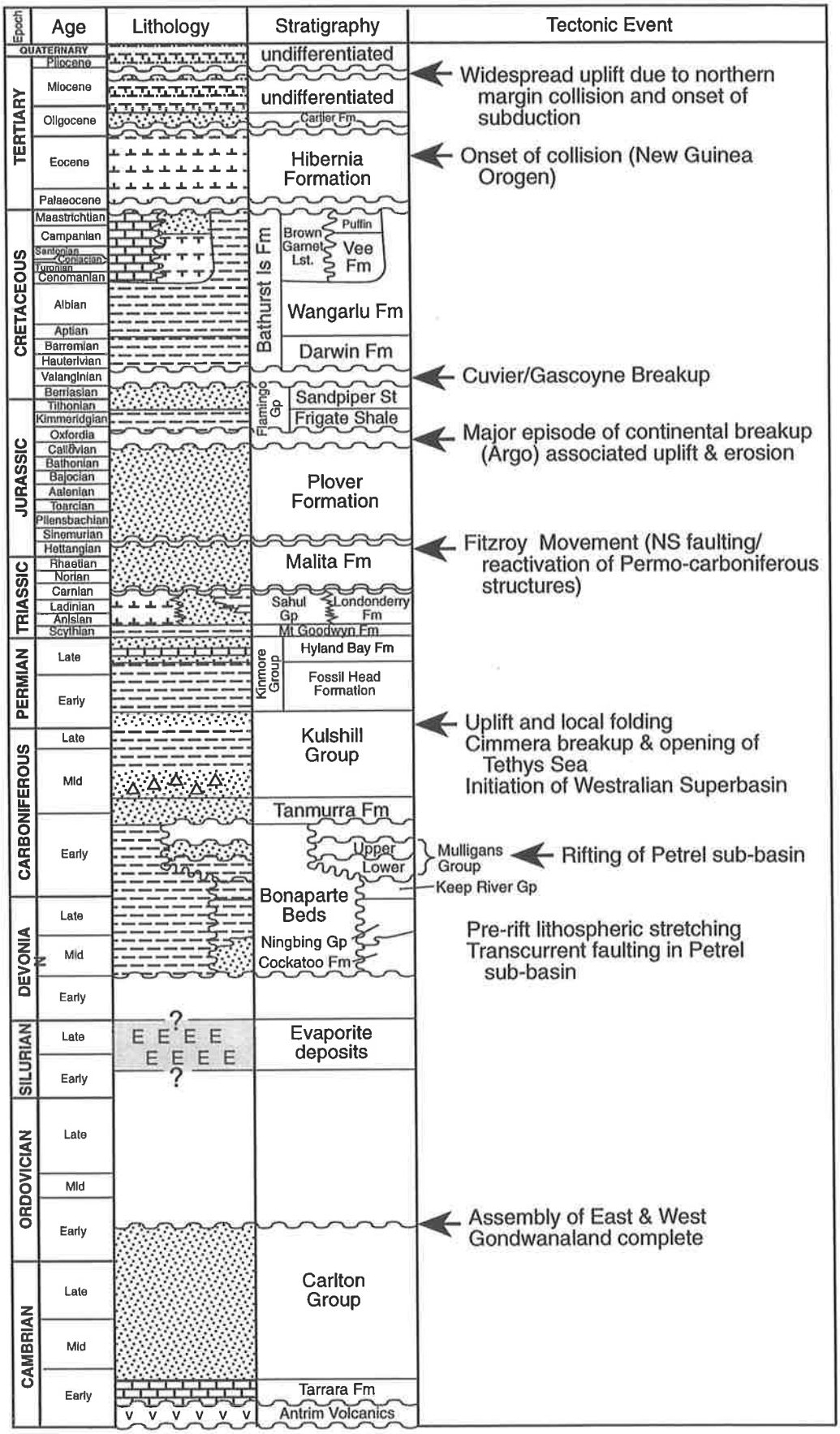

Figure 2.7 Summarised stratigraphy for the Bonaparte Basin (after Lavering &Ozimic, 1988; Lee & Gunn, 1988). See Figure 2.5 for lithological legend.

Widespread deposition recommenced in the Middle Devonian in conjuction with a global sea level rise. Shallow seas spread across the Canning Basin and entered the Bonaparte Basin. Rejuvenation of the Canning and Bonaparte Basin failed arms also occurred causing rifting of the northwest trending Fitzroy Graben, and pre-rift lithospheric stretching and transcurrent faulting in the Petrel Sub-basin (Gunn, 1988; Veevers, 1988). In the Canning Basin, basinal rift phase sediments (not penetrated) are predicted to have accumulated in the rapidly subsiding Fitzroy Graben while reef complexes (Pillara Limestone) were deposited on the margins (Brown et al., 1984). South of the graben, conformable shallow marine to sabkha environment deposits (Mellinjerie Formation) accumulated in the gentle downwarp of the Kidson Sub-basin. Subsequent to a sea level fall or a decline in subsidence (Playford, 1980), erosion of the exposed fault blocks provided a source of mixed carbonate and clastic breccia to the trough (Napier Formation). A second reef complex (Nullara Limestone) followed, in some areas, possibly as a continuation of the Pillara Limestone (Brown et al., 1984). By the end of the Early Carboniferous a period of subsidence and rapid infilling provided the deposition of the Yulleroo, Laurel and Anderson Formations, representing a northwest prograding delta sequence.

In the Petrel Sub-basin, pre-rift phase shales and siltstones comprise the basinal Bonaparte Beds while coarse to medium grained clastics, evaporites and carbonates make up equivalent shelf deposits (Cockatoo Formation, Ningbing Limestone and Keep River Group). Tilted blocks of pre-rift accumulations are overlain by syn-rift, fine grained marine shale, siltstone and sandstone of the Mulligans Formation. A major unconformity within this formation separates a lower graben fill sequence from an overlying prograding clastic sequence. Marking the termination of the Devonian-

Carboniferous rifting cycle and crustal spreading, is a widespread deposition of sands and thin carbonates on shelf areas (Tanmurra Formation), associated with relatively thick shale sequences in the deeper parts of the basin (Lee & Gunn, 1988).

The Southern Carnarvon Basin underwent an interior-sag phase receiving dominantly regressive marine-shelf deposits during the Mid Devonian to Early Carboniferous. This phase was initiated with the transgressive near shore marine Nannyarra Formation and the shallow marine sands to intermixed silts and carbonates of the Gneudna Formation. Local fault movement near the basin margin created tidal and then braided-fluvial environments for deposition of the Munabia Sandstone culminating in alluvial fans of the Willaraddie Formation in the Late Devonian marking the end of the regressive sequence. After fault activity ceased, deposition of the Moogooree Limestone occurred on what was a broad shallow-marine ramp (Hocking, 1988). Renewed tectonic activity lead to the development of alluvial fans along the basin margin (Williambury Formation). A return to transgressive conditions led to mixed siliclastic/carbonate deposition near the basin margin (Yindagindy Formation) while deposition of shales and siltstones of the Quail Formation continued on the marine shelf.

2.7.2 Westralian Superbasin (Offshore Basins)

Mid Carboniferous to Late Permian

The Middle Carboniferous of the North West Shelf is distinguished by a period of non-deposition within most onshore sedimentry basins (Baillie et al., 1994). It also marks the time when Australia moved from a relatively low to high latitude, and collision occurred between Gondwanaland and Laurussia to form the Supercontinent Pangea

(Chen et al., 1993, 1994). Powell & Veevers, (1987) and Veevers & Powell, (1987) believe deformation and uplift along the Pacific border extended through central Australia (Lachlan and Alice Springs Orogenies) and triggered a major continental ice sheet over southern Gondwanaland. In effect, the ice sheet covered most of the Australian continent preventing the accumulation of sediments in any of the onshore basins. Sengor (1987) proposed that the Late Carboniferous uplift, erosion and local folding in the Southern Bonaparte Basin could have been related to the breakup from the northern margin of Gondwanaland of a group of continental blocks known as Cimmeria. The inception of the Westralian Superbasin was contemperaneous with this event, and was characterised by a major episode of crustal thinning giving rise to the opening of the Tethyan Sea and a dominantly marine sag-phase rim basin (Veevers, 1988). Orthogonal overprinting of the northwest trending Palaeozoic basins occurred in the Bonaparte and Canning Basins (i.e. northwest oriented Petrel Sub-basin overprinted by northeast trending Vulcan Sub-basin in the Northern Bonaparte Basin and the Canning Basin overprinted by elements of the Roebuck Basin) as well as the reactivation of the Southern Carnarvon Basin failed rift arm. It also marked the genesis of the Browse Basin in Late Carboniferous to Early Permian times, as an intracratonic downwarp between the Kimberly Block and the Scott Plateau to the west (Allen et al., 1978). Although this period marks the beginning of the Westralian Superbasin, deposition still continued in the Palaeozoic basinal components. Where appropriate, offshore sedimentation has been referred to separately.

Glacially influenced siliclastic sediments associated with the Gondwanan ice sheet were deposited widely following shallow marine sands and silts. The Southern Carnarvon Basin consists of a series of the Carboniferous to late Early Permian Lyons Group

containing fluvio-glacial sands and silts interbedded with thin marine sands and shales. Unconformably overlying the Lyons Group are the dark grey to black fossiliferous and carbonate sediments of the Callytharra Formation. Disconformably overlying the Callytharra, is a thick, entirely marine section consisting of the Wooramel, Byro and Kennedy Groups aged from late Early Permian to Late Permian times. The basal Wooramel Group is largely sandstone and is overlain by interbedded siltstones and sandstones with occasional interbedded limestones of the Byro Group. The Kennedy Group also contains laminated fine-grained sandstones and siltstones, a deltaic to marine shelf environment.

Fluvio-marine and glaciogenic clastics were deposited in the Canning Basin in Late Carboniferous to Early Permian times, comprising the lower and upper units of the Grant Group. Following minor tectonism, the Grant Group is overlain by a transgressive, shallow marine sand (Poole Sandstone) which marks the termination of glacial conditions across the basin (Kennard et al., 1994). Overlying the Poole Sandstone are the richly fossiliferous marine shales and siltstones of the Noonkanbah Formation followed by the regressive shallow shelf to fluvial siltstones and sandstones of the Liveringa Group. Offshore, in the Bedout and Rowley Sub-basins (Roebuck Basin) the Liveringa Group overlies the Grant Group unconformably due to a period of uplift and erosion in the late Early Permian.

The Pre-Permian development of sedimentary units in the Browse Basin are poorly documented in the literature. Although they have not yet been penetrated by exploration drilling, sediments prior to Late Carboniferous are likely to represent the earliest deposits in the basin (Baldasso, 1993). Passmore (1980) described Late

Carboniferous to Early Permian sediments as a sequence of paralic clastics and carbonates succeeded by non-marine sand and silt along the eastern side of the basin. A Late Permian regressive cycle resulted in the deposition of non-marine sandstones along the southeast margin, where as in the north, recrystallised limestones rich in marine fauna were deposited. These spatial variations in lithology and fauna suggest that the epicontinental sea was in communication with Tethys which regressed towards the center of the basin exposing the eastern margin. In the structurally higher areas to the north along the margin, this unit can be likened to the Hyland Bay Formation of the Bonaparte Basin (Baldasso, 1993).

Deposition of massive fine to medium grained clastics of the Kulshill Group within the Bonaparte Basin was thickest in the onshore Petrel Sub-basin (Southern Bonaparte Basin) although the sequence also drapes over pre-existing highs (Lee and Gunn, 1988). The sequence varies from fluviatile and glaciogenic clastic units at its base to post marine shale and marginal marine sand and shale units at its top. Overlying these units are those of the Kinmore Group which consist of the Fossil Head and Hyland Bay Formations. The Fossil Head Formation is comprised of interbedded dark massive marine to estuarine sandstones and shales with minor coal beds and limestones. The Hyland Bay Formation consists of interbedded sands and shales at its base, an intermediate limestone layer, and is capped by sandstone, all believed to be of deltaic origin.

Late Permian to Late Triassic

In Late Permian times a major episode of uplift faulting and volcanism (Bedout Movement) affected most of the North West Shelf from the Carnarvon Basin to the

Browse Basin (AGSO North West Shelf Study Group, 1994). The event appears to be a plate wide compression (Elliott, 1993) although at present there is no widely accepted explanation for it. This regional structuring episode caused significant unconformities to develop in the Southern Carnarvon Basin, Roebuck Basin and the eastern edge of the Browse Basin, and in the case of the Bedout Sub-basin, volcanism occured on the Bedout High. A major phase of offshore subsidence and deposition followed the Bedout Movement in a rift valley environment across the margin (Allen et al., 1978). This sequence of sedimentation represents a complete cycle from marine transgression in Early Triassic times, through regression in Middle Triassic times, to a period of coastal onlap in Late Triassic times (Bradshaw et al., 1988).

Triassic sedimentation across the North West Shelf was concentrated in a series of northeast trending troughs initiated by the present-day sag-phase (Bradshaw et al., 1988; Hocking, 1988; Stagg & Colwell; 1994). The uplifted Palaeozoic sequences of the Southern Carnarvon Basin in the Early Triassic provided much of the terrigenous input into the newly developed depocentres of the Northern Carnarvon Basin. The Locker Shale is a marine sediment which overlies the Upper Permian Kennedy Group conformably in many areas. Although in those parts of the basin affected by Late Permian structuring, the contact is an angular unconformity (Forrest & Horstman, 1986). This unit grades upwards diachronously into the regressive fluvial to deltaic Mungaroo Formation, the contact becoming younger to the northwest. Deposition of the sands, silts and claystone of the Mungaroo Formation began in late Early Triassic and continued through Triassic times. By Late Triassic time a marine transgression had begun, reworking the previously deposited deltaic sands and depositing a thinly interbedded sequence of calcareous sands, siltstones and limestones in some areas.

This unit (Brigadier Formation) did not completely transgress the Mungaroo Formation until Early Jurassic time.

Deposition of the transgressive Locker Shale was not only constrained to the Southern Carnarvon Basin but also occurred across the Roebuck Basin with equivalents in the Browse and Bonaparte Basins (i.e. Mount Goodwyn Formation) (Lipski, 1994). In the case of the Roebuck Basin, the Locker Shale grades up into a fluvio-deltaic, Mungaroo Formation equivalent, the Kerauden Formation. Similarly, in the northeast, the Mount Goodwyn Formation within the Browse Basin, is overlain conformably by the lithologically variable, clastic-carbonate Sahul Group which also contains reddish-brown shales, and minor coal, evaporites and volcanics. This group consists of the Osprey, Pollard, Challis and Nome Formations. To the east, in the Northern Bonaparte Basin, the Cape Londonderry Formation overlies the Mount Goodwyn Formation. This formation can be distinguished from the coeval Sahul Group in the west by its lack of carbonates. The transgressive Brigadier Formation, overlying the Mungaroo in the Northern Carnarvon Basin, can also be correlated with the Bedout Formation in the Roebuck Basin and the Malita Formation in the Browse and Northern Bonaparte Basins. The Bedout Formation is described as a redbed sequence with micaceous claystones and siltstones with thin sandstone lenses. Similarly the Malita Formation is comprised of interbedded sands and vari-coloured shales, with the latter forming the higher proportion of the sequence.

Early to Middle Jurassic

A major episode of structuring, reactivation and erosion with compression, transpression and extension occurred on the North West Shelf in Late Triassic to Early

Jurassic times (Fitzroy movement) as part of an Australia-wide event (Stagg & Colwell, 1994). The resulting unconformity is evident in each of the four main basins of the shelf although the structural style varies in each case. Through the Jurassic, depositional environments along the shelf progressively became more marine, compared to the non-marine, paralic, and shallow marine systems at its onset.

The Fitzroy Movement played an important part in the deposition of Jurassic sediments. Uplift of the Exmouth Plateau and the southern margin of the Southern Carnarvon Basin as a result of this episode are most likely to have provided the renewed sources for marine sand deposition in this area (North Rankin Formation). Similarly, activation of basin bounding faults occurred in the Roebuck Basin, transpressional reactivation caused further block rotation and possible uplift of basin margins in the Browse Basin, and north-south faulting with oblique reactivation of Permo-Carboniferous structures in the Bonaparte Basin was associated with low amplitude crustal scale buckling and transpressional reactivation of lower plate margins of the Petrel Sub-basin (AGSO North West Shelf Study Group, 1994).

Within the Southern Carnarvon Basin, the North Rankin Formation was succeeded by the Dingo Claystone, a dark coloured slightly calcareous inner shelf claystone. A new phase of regional regression, although not affecting the southern parts of the basin, caused the marine claystones to pass upwards into a sandy deltaic facies termed the Legendre Formation (Woodside, 1988). Further to the northeast in the Roebuck Basin, the Bedout Formation is a thick sequence of non-marine sandstones with thin interbedded claystones and coals, representing essentially fluvio-deltaic sedimentation with occasional marine influences. Continuing the trend, predominantly fluvio-deltaic

sediments were accumulating in the Browse and Bonaparte Basins (Plover Formation). By the end of Middle Jurassic times, the regression reached its maximum extent contemporaneous with a major tectonic episode of continental breakup.

Middle Jurassic to Early Cretaceous

The Middle Jurassic marks the time at which disintegration of the super-continents (Gondwanaland and Laurasia) began, and the present day tectonic plates, continents and oceans were born. The first major tectonic event associated with this breakup was the split of a continental fragment of unknown width from the north-western side of the Westralian depression and continental extension between Australia, India and Antarctica (Veevers et al., 1991). Unconformities were created over most of the North West Shelf with significant uplift and erosion occurring on the major platforms between troughs. Faulting was particularly severe in the Roebuck and Browse Basins. Depocentres along the depression that were active troughs throughout the Jurassic, underwent a period of rapid deepening in Late Jurassic times creating a passive margin rim basin along the northwestern margin of Australia (Veevers, 1988). These accelerated fault movements along basin margins were caused by the start of sea floor spreading in the Argo Abyssal Plain during the Callovian. Coinciding with this event was the extrusion of basalt (Ashmore Volcanics) within parts of the Browse Basin and the Ashmore Platform.

Directly overlying the breakup unconformity in the Northern Carnarvon Basin is a sandy turbidite facies of the transgressive Upper Dingo Claystone (Biggada Formation). The newly uplifted basin margins initially provided an excellent source for sediments at the resumption of deposition. A similar turbidite facies is evident at the

top of the Upper Dingo Claystone during the Tithonian (Dupuy Formation). The deposition of this clastic unit coincided with a regional structuring event across the North West Shelf, corresponding to the initiation of rifting off southern Australia and a decrease in the spreading rate of the Argo Abyssal Plain (AGSO North West Shelf Group, 1994).

In the Roebuck Basin, Upper Dingo Claystone equivalents were deposited, consisting of interbedded marine sands, shales and silts (Egret and Baleine Formations). This post-rift transgressive marine sequence was thin in the eastern part of the basin, thickening to the west. Equivalent sediments were also deposited in the Browse Basin, although the environment was a more restricted setting due to the uplifted structural components surrounding it (Prudhoe Terrace, Leveque Platform and Scott Plateau). Early paralic sandstones gave way to thick marine claystones, transgressing the Scott Plateau in Early Cretaceous times. Fully marine circulation was achieved in this area within the Late Cretaceous. The environment in the Northern Bonaparte Basin was not so restricted, permitting the deposition of a marine shale unit (Frigate Shale) of the Flamingo Formation throughout the Late Jurassic.

The Dingo Claystone was succeeded disconformably by the regressive, clastic, Barrow Group in Early Cretaceous times. The Barrow Group is a major deltaic complex which developed in the southern (shore-ward) parts of the Northern Carnarvon Basin. Subsidence along the developing margin led to the deposition of widespread marine shales that covered the earliest Cretaceous deltaic sands of the Barrow Group (Muderong Shale). Further northwest, glauconitic claystones and siltstones of the Muderong Shale overlay the Upper Dingo Claystone sediments unconformably. A

further rise in sea level led to the deposition of the Windalia Radiolarite conformably above the Muderong Shale. This regressive/transgressive sequence is associated with continental breakup in Valanginian times and is recognisable across the entire North West Shelf by margin-wide unconformities of variable significance. This unconformity at the top of the Barrow Group in the Northern Carnarvon Basin marks the breakup of the Gascoyne, Cuvier, and Perth Abyssal Plains following heating and deep thinning in the far west.

An unnamed marine transgressive sequence consisting mainly of claystones with common interbeds of delta fan and turbiditic sandstones is equivalent to the Muderong Shale in the Roebuck Basin (Lipski, 1994). Similarly, marine sandstones, silts and shales were deposited in the Browse Basin (Cockbain, 1989). The regressive clastic unit forming the upper part of the Flamingo Group (Sandpiper Sandstone) in the Northern Bonaparte Basin was unconformably overlain by sediments of the transgressive marine Bathurst Island Group. The Darwin Formation comprises the bottom-most part of the Bathurst Island Group and consists of a thin basal glauconitic and radiolarian sequence overlain by thick shales and mudstones.

Early Cretaceous to Tertiary

The opening of the Indian Ocean at the end of Early Cretaceous times marked a significant environmental change on the North West Shelf. Rifting in the region had ceased and sedimentation was related to a subsiding continental passive margin. Marine clastic deposition was replaced by carbonates, which accumulated as veneers and prograding wedges along the entire region by Santonian times (Yeates et al.,

1987). The change to carbonate deposition on such a grand scale occurred in conjunction with the main breakup phase on the southern margin of Australia.

In the Barrow area, the Late Cretaceous transgressive cycle deposited a dark greenish, grey and black claystone and siltstone (Gearle Siltstone). Concurrently in the Dampier area, a lateral, more calcareous equivalent of the Gearle Siltstone was deposited, the Haycock Marl. This sequence consists of two argillaceous calcilutite and marl units separated by a thin claystone interval. Equivalent fine grained carbonates containing calcilutite and marl with localised calcarenite and limestone were deposited in both the Roebuck and Browse Basins.

Sedimentation continued in the Petrel Sub-basin and the Malita Graben as part of the Bathurst Island Group. The Darwin Formation was overlain by the predominantly micaceous mudstones of the Wangarlu Formation which was in turn succeeded conformably during the Cenomanian, by the Vee Formation, an interbedded marl, argillaceous limestone and calcareous claystone of the Bathurst Island Group. This formation grades westward into the Brown Gannet Limestone on the Ashmore Platform and is time equivalent with the Toolonga Calcilutite which uncormformably overlays the Gearle Siltstone and Haycock Marl in the Northern Carnarvon Basin.

Deposition in the latest Cretaceous (Campanian-Maastrichtian) occurred over the entire North West Shelf. The fine grained carbonates of the Toolonga Calcilutite in the Northern Carnarvon region are conformably overlain by dark to calcareous claystones of the Withnell Formation which are in turn succeeded disconformably by the Miria

Marl. The Withnell Formation is coeval with the Korojon Calcarenite in some areas. In the Roebuck Basin, the Miria Marl conformably overlies the Toolonga Calcilutite.

Further north in the Bonaparte Basin, the Campanian-Maastrichtian aged Puffin Formation conformably overlays the Vee Formation. It consists of sandstones interbedded with lesser amounts of shale and marl and occurs in the northwestern parts of the Bonaparte Basin (Vulcan Sub-basin, eastern Ashmore Platform and southwestern Londonderry High). Elsewhere in the Bonaparte region sedimentation of the Wangarlu Formation continued. The Puffin Formation also occurs in the Browse Basin. A regional unconformity is recognised at the top of the Mesozoic sequence in the Northern Carnarvon and Roebuck Basins.

Tertiary to Present

Since the beginning of the Tertiary, the expanding Indo-Australian Plate has steadily drifted northwards into increasingly lower (warmer) palaeolatitides and hence altered global oceanic circulation patterns (Baillie et al., 1994). This change is reflected in the sediments of the North West Shelf which have become increasingly calcareous. This period of sedimentation is best described as the outbuilding and upbuilding of the continental shelf during various transgressive/regressive pulses. Tertiary calcareous sediments comprise nearly all of the modern shelf edges.

Deposition throughout Palaeocene and Eocene times was characterised by prograding marine mudstones and marls within shelf and slope environments. Within the Northern Carnarvon Basin these sediments are formally referred to as the Cardabia Group. Two equivalent sequences, the Giralia Calcarenite and the Walcott Formation are separated

from the underlying Cardabia Group by a brief hiatus. The Walcott Formation consists of sandy limestones that were deposited in the deeper water basins, while the calcarenites and calcisiltites of the Giralia Calcarenite were deposited closer to shore. Equivalent units were deposited in the Roebuck, Browse and Northern Bonaparte Basins, although only those in the Bonaparte have a formal nomenclature. The entire Palaeocene to Eocene sequence of shelf carbonates in the Bonaparte are referred to as the Hibernia Formation. Deposition of the Hibernia Formation did not occur in the northwest trending Palaeozoic Petrel Sub-basin at this time.

A shelf-wide unconformity in the stratigraphic record encompasses Early to Mid Oligocene times. Deposition was restricted to the outer parts of the Ashmore and Sahul Platforms in the Bonaparte Basin (Cartier Formation). This lapse in sedimentation coincides with a globally recognised marine regression (Vail, 1977) and the separation between Australia and Antarctica now having become a widening strip of oceanic lithosphere. Pigram & Symonds (1991) have also interpreted the Mid Oligocene to be the onset of the New Guinea Orogen and foreland basin formation associated with collision along the northern margin of the Australian Plate. The collision is believed to have caused widespread uplift during the Early Miocene in the Bonaparte Basin and Miocene to Recent faulting in the Carnarvon Basin (Bradshaw et al., 1988).

Sedimentation of fine grained shelf and slope carbonates recommenced across the North West Shelf in the Mid Oligocene. In the Carnarvon region, post Oligocene sediments are referred to as the Cape Range Group. This sequence consists of the prograding shelf carbonates and deeper water pelagic marls at its base, conformably

overlain in the Mid Miocene by the coarse grained, bioclastics and dolomities. Equivalent calcarenites and dolomites were also deposited in the Roebuck Basin, while reefs built up on the seaward edges of the continental margin in the Browse and Bonaparte Basins (Scott, Ashmore and Troubadour Reefs).

A second regional unconformity during the Cainozoic (Mid to Late Miocene) has been attributed to a major sea level fall (Haq et al., 1987) and possibly also to continued plate collision to the north. Subduction of oceanic lithosphere between the Australian Plate and the Indonesian Arc of the Eurasian Plate was underway and has continued until Recent times. In the Papua New Guinea region, oceanic subduction was overridden during the Miocene by the docking of the East Papuan, Western Irian Jaya and northern Island Arc terraines which are now preserved in the New Guinea Highlands (Pigram & Symonds, 1991; Veevers et al., 1991). The newly created collisional boundary put the northward-moving Australian Plate into contact with the westward-moving Pacific Plate and according to Baillie et al. (1994) resulted in two tectonic effects. The first being lithospheric flexure of the Australian plate, causing down-buckled zones and complementary uplifted zones. Secondly, an anti-clockwise torsion was induced to the Australian continental lithosphere, which is embedded in the predominantly oceanic Indo-Australian Plate. As a result, dextral transcurrent movements along pre-existing fractures were initiated in the continent ocean boundary around Australia.

Continental crust is now continuous between the Australian Continent and the Banda Island Arc (Chamalaun et al., 1976; Jacobson et al., 1978; Whitford and Jezek, 1982). Convergence motion has slowed between the two since mid Pliocene times (Johnston

& Brown, 1981), and volcanism ceased in the Alor/Wetar area of the Banda Arc at 3 Ma (Abbott & Chamalaun, 1981). In conjunction with the relative aseismicity of the Timor Trough (Cardwell & Isacks, 1978), these data all suggest that the arrival of buoyant Australian continental crust has 'choked' the Banda Arc subduction system (Audley-Charles, 1986). North of the Carnarvon Basin, convergence without collision still continues in the Java Trench. The contemporary stress field is believed to have remained constant since the initiation of the Miocene/Pliocene-Recent collision (Hillis & Williams, 1992).

Deposition of shallow shelf and lagoonal calcarenites and dolomite has persisted until the present day, building the continental shelves upwards and outwards to their present shape. The North West Shelf region is currently accumulating sediment at a very slow rate, except in the Timor Trough. Sediments range from fine grained terrigenous deposits close to shore to fine grained carbonates and foraminiferal sands further out on the shelf edges and upper slope regions (Jones, 1973; Bradshaw et al., 1988). The only formally recognised units within the shelf following the Late Miocene unconformity are the Pliocene calcilutites and calcisiltites of the Delambre Formation deposited in the Northern Carnarvon Basin.

2.8 Geomechanical Setting

Anomalous stress orientations can be caused by geomechanical discontinuities in rock masses (Bell et al., 1992a). To understand the present day stress configuration, the geomechanical setting must be addressed (Bell, 1993). If stress patterns are to be interpreted at the crustal scale, it is necessary to demonstrate that the population of stress indicators within a basin, reflects the stress configuration in the upper crust and

not that of a mechanically detached sediment packet. The direction of tilt of a detachment surface can determine horizontal stress orientations in detached sedimentary sequences and basins (Yassir & Bell, 1994; Figure 2.8). The upper sequence may be extended or stretched downslope, aligning the maximum horizontal stress parallel to the strike of the detachment zone (Figure 2.8).

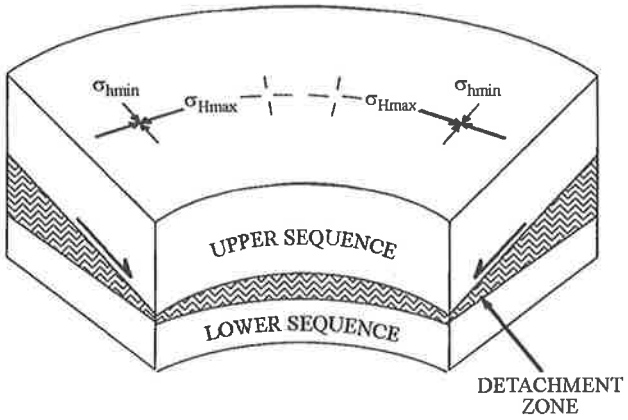

Figure 2.8 Schematic diagram illustrating how the direction of tilt of a potential surface detachment can affect horizontal stress orientations in the rock units contained in detached sedimentary sequences and basins (Yassir & Bell, 1994). The upper sequence is 'stretched' downslope, aligning σ_{hmin} perpendicular to the strike of the top of the detachment zone.

Detachments in the subsurface can be associated with intervals of substantially overpressured shales, significant evaporitic layers (Yassir & Bell, 1994) or extensive listric faulting. The likelihood of these types of detachments in either of the Northern Carnarvon Basin or the Northern Bonaparte Basin are discussed briefly in the following sections. Discussion of how the geomechanical setting affects the interpretation of in situ stress measurements for this project is made in Chapter 6.

2.8.1 Overpressure

Overpressure is defined as any formation pressure which exceeds the hydrostatic pressure exerted by a column of water (9.4 MPa/km or 0.448 psi/ft). Pressures higher

than hydrostatic are commonly found in sandstone-shale successions and as an integral part of hydrocarbon generation within basins (North, 1985). Under circumstances where fluid expulsion from clays is retarded (e.g. rapid sedimentation), excess fluid pressure props open interparticle porosity preventing compaction and pressure equilibrium. Sedimentary rocks over substantially overpressured shales may become detached from those below and subject to their own distribution of stress.

Horstman (1988) stated that nearly all of the oil and gas fields of the North West Shelf, are located within or immediately adjacent to overpressured shales, created by the generation of hydrocarbons. However, in comparison to overpressured regions around the world, the average pressure gradient across the North West Shelf is relatively low i.e. 13 MPa/km (0.62 psi/ft) across the North West Shelf compared to 27 MPa/km (1.3 psi/ft) in Pakistan (Bigelow, 1994; Figure 2.9). Overpressure in the North West Shelf is restricted to the centre of major depositional basins at depths between 1300 and 2500 metres, where de-watering of thick shale sequences has been precluded, and at deeper levels where overpressures have been caused by hydrocarbon generation (Horstman, 1988).

The potential for detachment surfaces caused by overpressured shales at depth does exist across the North West Shelf. However, the magnitude of local pressure gradients may not be significantly great enough to affect stress magnitudes and orientations. The possibility of a detachment surface at depth, and the magnitudes of available formation pressures, are considered when interpreting stress indicators in this study.

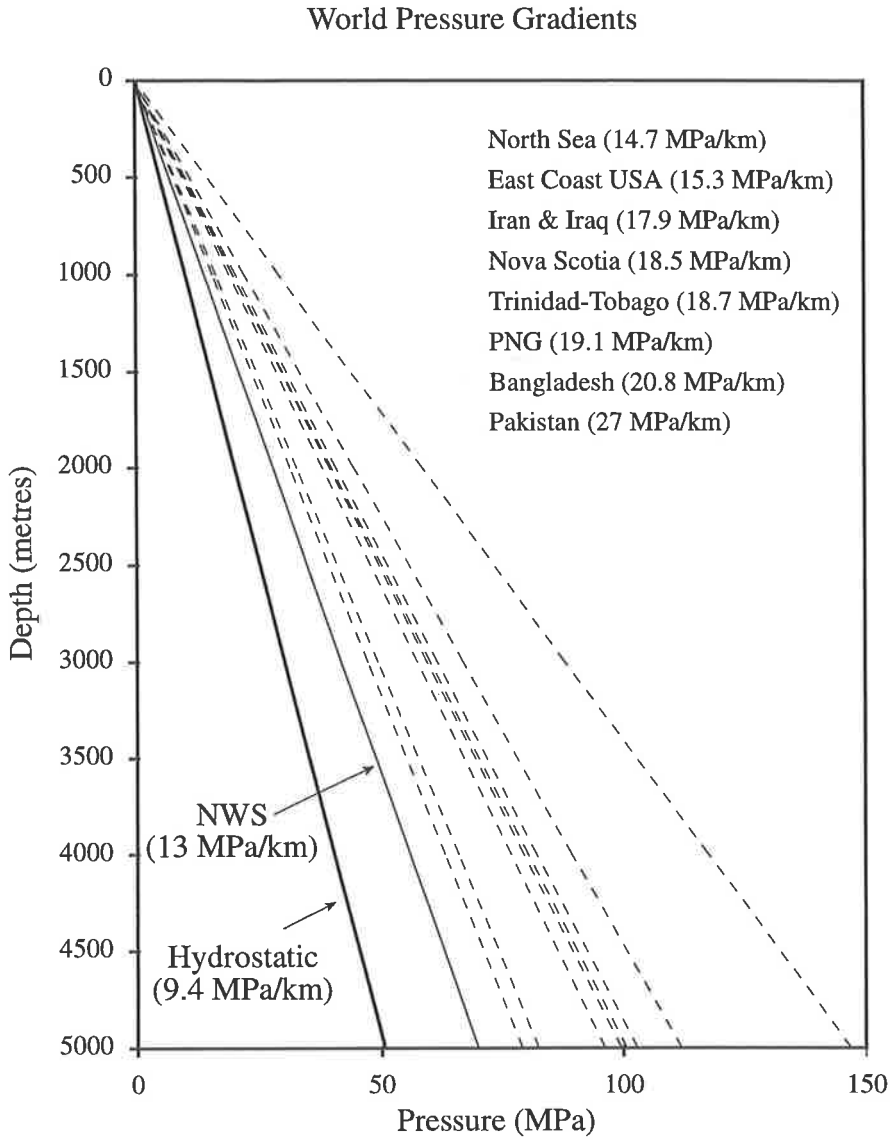

Figure 2.9 Comparison of pressure gradients from around the world to the average pressure gradient of the North West Shelf (NWS) taken from Bigelow (1994). Dashed lines from left to right represent increasing pressure gradients in the order listed above. The hydrostatic pressure gradient is also included.

2.8.2 Evaporite Distribution

Evaporite deposits on the North West Shelf are predominantly limited to the northwest trending Palaeozoic basin components, deposited during Silurian to Devonian times (Section 2.7; Figure 2.10). The Yaringa Evaporite within the Southern Carnarvon Basin is concentrated in the present day onshore areas, although the Tamala-1 well, near Shark Bay, records an intersection of evaporite, covering a depth interval of nearly 150m. Evaporite accumulations have also been intersected in offshore wells

further northwest from this well, although to the north, their absence indicates that evaporites do not extend below the Mesozoic sediments of the Northern Carnarvon Basin (Gorter et al., 1994). Hence, the likelihood of an evaporitic detachment horizon affecting stress measurements in this basin is remote.

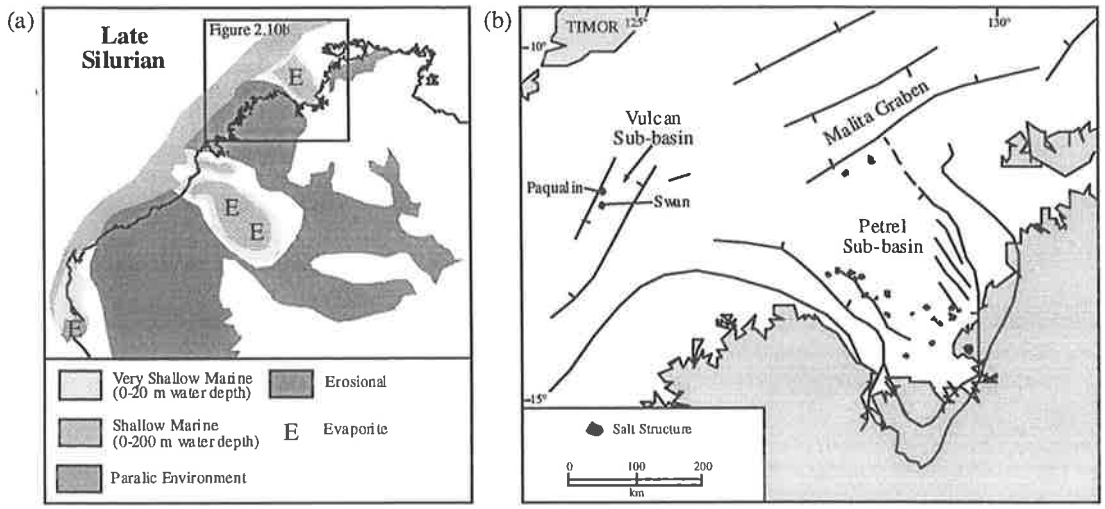

Figure 2.10 (a) The distribution of evaporite sedimentation during the Late Silurian (Bradshaw et al., 1994). (b) The distribution of known salt structures in the Northern Bonaparte Basin (Lee & Gunn, 1988; Smith & Sutherland, 1991).

The presence of extensive evaporites and the occurrence of numerous diapirs in the Bonaparte Basin has previously been documented by several authors (Edgerley & Crist, 1974; Lee & Gunn, 1988; Smith & Sutherland, 1991). The majority of salt structures are located within the Palaeozoic northwest trending Petrel Sub-basin although their occurrence in the orthogonal Mesozoic Vulcan Sub-basin has also been reported in the vicinities of the Paqualin-1 and Swan-1 wells (Smith and Sutherland, 1991; Figure 2.10). Smith and Sutherland (1991) believe that the Vulcan salt structures were sourced from evaporites deposited in an extension of the underlying Palaeozoic Petrel Sub-basin and are coeval with similar structures to the southeast. Woods (1994) proposed a salt related detachment model for the development of the Vulcan Sub-basin based on sandbox models. The limited knowledge of salt

distribution in the northern Bonaparte Basin can neither confirm nor preclude the possibility of salt detachment at depth. Interpretation of stress measurements in the Northern Bonaparte Basin should consider the possible effects of a salt horizon.

2.8.3 Structural Style

Since 1991 the Australian Geological Survey Organisation (AGSO) has been conducting a deep seismic acquisition program producing seismic profiles across the North West Shelf. The resulting seismic profiles are of high quality and typically show interpretable reflection events down to 12 seconds two way time (TWT) (AGSO North West Shelf Study Group, 1994). This section gives a brief description of seismic profiles across the Northern Carnarvon and Bonaparte Basins, acquired and interpreted by AGSO's North West Shelf Study Group (1994) which are shown in Figure 2.11.

Northern Carnarvon Basin

Interpretations of deep seismic lines 101/07 and 110/15 by the AGSO North West Shelf Study Group (1994) are shown in Figure 2.11a. Deposition is characterised by a layer cake geometry that has undergone a gentle arching beneath the Exmouth Plateau region. With the exception of predominantly high angle faulting, the only major disruption to the flat-lying sediments is the North Rankin Fault System. The Rankin Fault System cuts the section from the Triassic through to the Lower Crust and is most likely to have controlled the deposition in the synclinal depocentre to the southeast during the Jurassic-Cretaceous (Stagg & Colwell, 1994). The presence of high angle strike-slip or wrenching faulting indicates minimal evidence of upper crustal extension

and suggests that sediments are firmly attached to the basement across the Northern Carnarvon Basin.

Bonaparte Basin

Figure 2.11 also illustrates (b) Line 98/07 across the Ashmore Platform and Vulcan Sub-basin, (c) Line 100/02 across the Petrel Sub-basin and (d) Lines 1005/05 and 116/04 across the Sahul Platform, Malita Graben and Petrel Sub-basin. In each case the interpretation has been made by AGSO's North West Shelf Study Group (1994).

Two distinct structural styles can be seen in the interpretation of Line 98/07 (Figure 2.11b). The northwest flank is dominated by extensional listric faulting, with extension estimated at approximately 20%, in Triassic sediments directly above the interpreted basement. Faults within the Triassic section sole out either at the basement interface or within the upper basement section (AGSO, 1994). In comparison the southeast is characterised by strike-slip/wrench faulting and the presence of the Vulcan Sub-basin, a major depocentre viewed by AGSO (1994) to be a large scale flower structure itself.

The second section across the Bonaparte Basin (Figure 2.11c) illustrates the basin forming features of the Palaeozoic Petrel Sub-basin. The overall characteristics of the profile are of an upper plate/lower plate pair overlying a basin forming detachment, generated within a transtensional environment (AGSO, 1994). O'Brien et al. (1993) discusses the reversal of upper and lower plate polarity along the sub-basin axis. On this profile the upper plate underlies the northeast flank.

The final Bonaparte Basin section, Lines 100/05 and 116/04 (Figure 2.11d), follow the northwest trending axis of the Petrel Sub-basin. This profile shows the deepening of the basement in the northwest below the Palaeozoic basin, as well as several distinctive flower structures emanating from the basement surface under the Petrel/Malita depocentre. The overall structure is similar to the interpretation of Line 98/07 (Figure 2.11b), with the exception of the listric faulting in the Sahul Platform region.

Structural detachment between the basement and overlying sediments may occur in the Petrel Sub-basin and may also extend beneath the Malita Graben towards the northwest. Sediments in the vicinity of the Vulcan Sub-basin, can generally be assumed to be attached to the basement although the presence of some listric detachments at the basement interface indicates that the Ashmore Platform may be the exception. These structural features should be taken into consideration when interpreting stress measurements from the Bonaparte Basin.

(a) Northern Carnarvon Basin: Lines 101/07 & 110/15

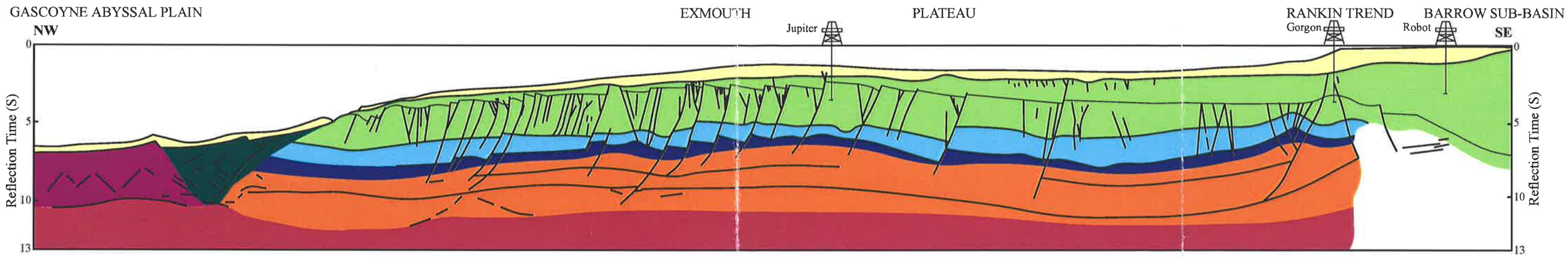

(b) Vulcan Sub-basin: Line 98/07

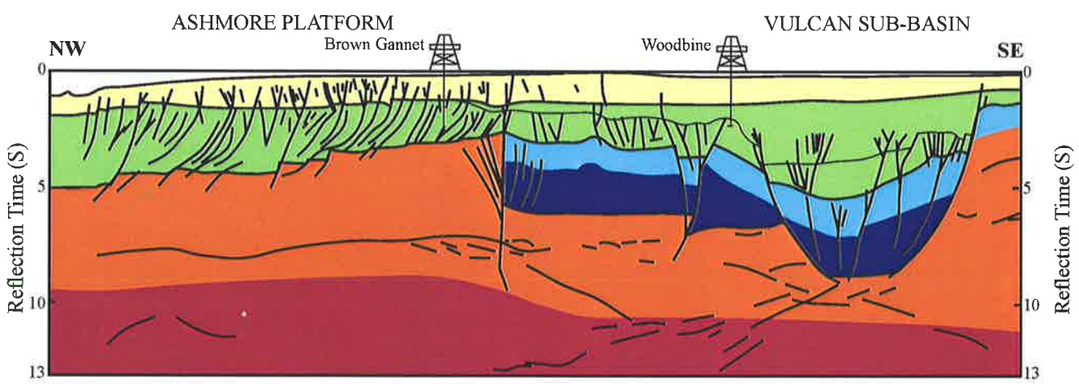

(c) Petrel Sub-basin: Line 100/02

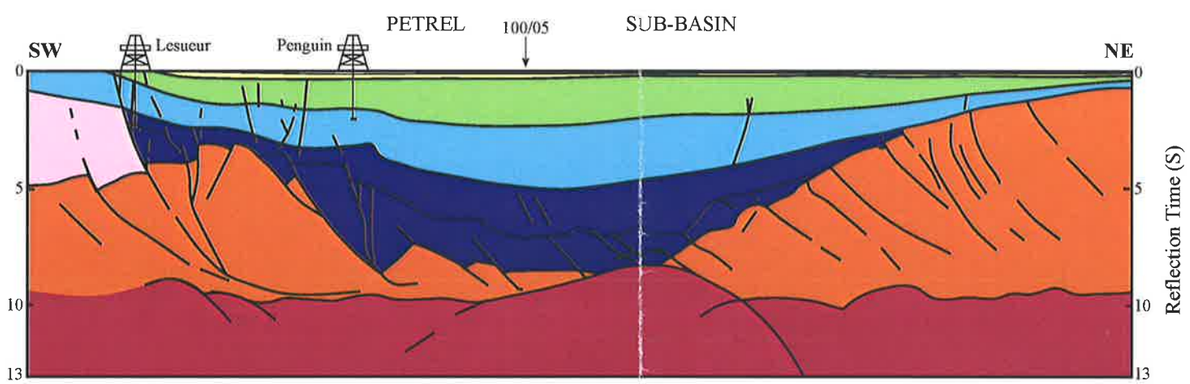

(d) Bonaparte Basin: Lines 100/05 & 116/04

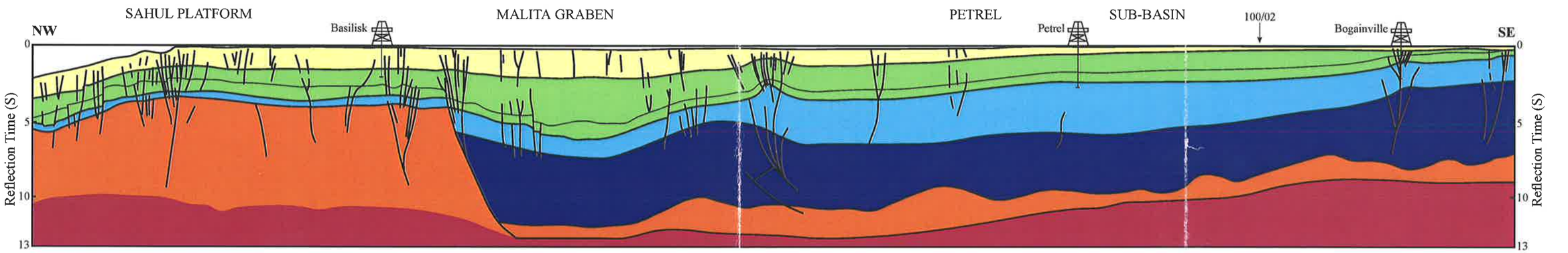

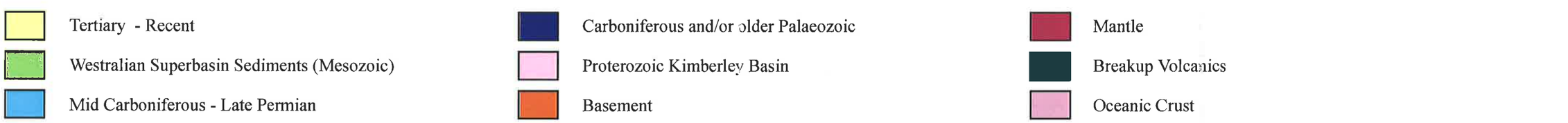

Figure 2.11 Line drawings of AGSO deep-seismic profiles from the North West Shelf showing Westralian Superbasin and underlying Palaeozoic sediments (AGSO North West Shelf Study Group, 1994). Location of lines shown in Figure 2.4

Chapter 3

Stress Fields and Stress Magnitudes

3.1 Principal Stresses and Fault Condition

The stress acting at any point in the crust can be resolved into three mutually orthogonal planes on which the shear stresses are zero. These three planes are known as the principal planes of stress and their normals are known as the principal stress axes. The stresses normal to the principal planes (parallel to the principal stress axes) are denoted as σ_1, σ_2 and σ_3, given that:

$$\sigma_1 > \sigma_2 > \sigma_3 \tag{3.1}$$

(Hobbs et al., 1976). These are the maximum, intermediate and minimum principal stresses respectively. A positive value indicates compression and a negative value indicates tension. The state of stress at a point can be characterised by constraining the orientation of the three principal axes and the magnitudes of the three principal stresses.

Since there is no shear stress acting at the surface of the earth (unless adjacent to areas of significant topography), it can be assumed that the vertical stress (σ_v) is a principal stress (McGarr & Gay, 1978). The other two principal stresses are therefore constrained to the horizontal plane and denoted σ_{hmin} (minimum horizontal compressive stress) and σ_{Hmax} (maximum horizontal compressive stress). The orientation and magnitude of the principal stresses determines the fault condition in the crust.

Anderson (1951) combined the orientation of the principal stresses with the geometrical relationship between fracture planes and stress directions to propose a

threefold dynamic classification of faults based on the relative stress magnitudes of the principal stresses (Figure 3.1):

extensional regime (normal fault condition)

$$\sigma_{h\,\min} < \sigma_{H\,\max} < \sigma_v \tag{3.2}$$

strike-slip regime (strike-slip fault condition)

$$\sigma_{h\,\min} < \sigma_v < \sigma_{H\,\max} \tag{3.3}$$

compressional regime (reverse fault condition)

$$\sigma_v < \sigma_{h\,\min} < \sigma_{H\,\max} \tag{3.4}$$

The methods used to determine the magnitudes of the vertical and horizontal stresses are presented in this chapter. The method used to determine the orientation of the principal horizontal stresses is described in Chapter 4.

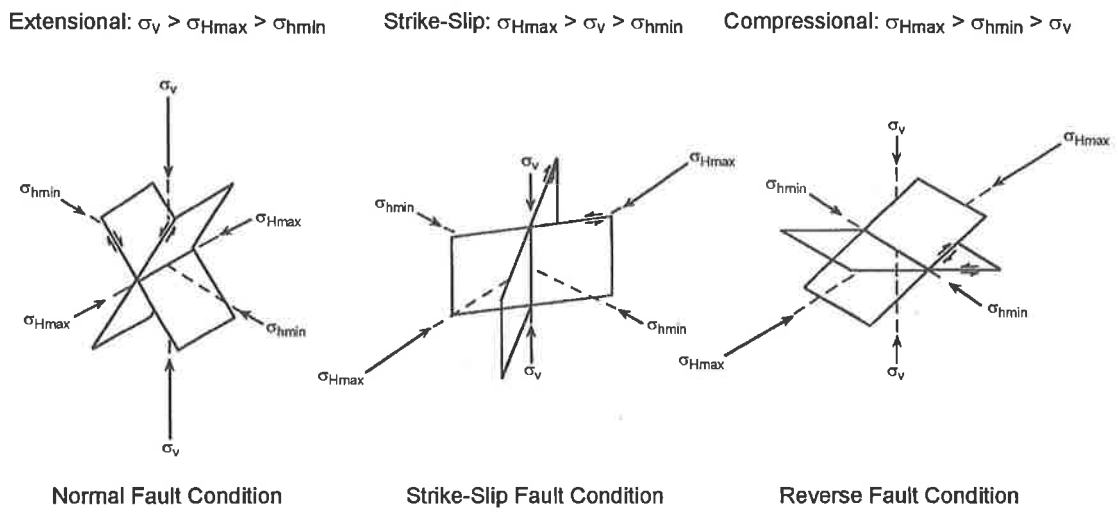

Figure 3.1 Classification of stress regimes and associated dynamic classification of fault condition (Anderson, 1951).

3.2 Vertical Stress Magnitude Measurement

3.2.1 Determining Vertical Stress Magnitude

Calculation of the vertical stress magnitude is based on the assumption that the weight of the overburden equals the vertical stress magnitude (McGarr & Gay, 1978). This relationship can be expressed as:

$$\sigma_v = \int_z^0 \rho(z) g \, dz \tag{3.5}$$

where ρ is the density of the overlying rock column at depth z, and g is the acceleration due to gravity. This calculation is made using data from density logs that are widely run in hydrocarbon exploration wells.

Density logs are not normally run from the surface, therefore vertical stress cannot be determined by simply integrating the density log data from the surface to the depth of interest. However, sonic velocity and density are strongly related. Check shot velocity survey data were used to determine average sonic velocity from the surface to the top of the density log data, and the average velocities were then converted to average densities. See Serra (1984) for details of operation of sonic and density logs and Balch & Lee (1984) for operation of check shot surveys.

Ludwig et al. (1970) plotted experimental data for compressional and shear wave velocities against observed densities for unconsolidated marine sediments, consolidated sediments, metamorphic and igneous rocks (Figure 3.2). They observed that the main trend could provide estimates of density from velocity. Figure 3.3 illustrates density vs. sonic velocity cross-plots from wells on the North West Shelf based on logging intervals over which both sonic and density logs were run. These data show a reasonable correlation with the Nafe-Drake transform, hence average density values

from sea level to the top of the density log, were calculated from average check shot velocities using the Nafe-Drake transform.

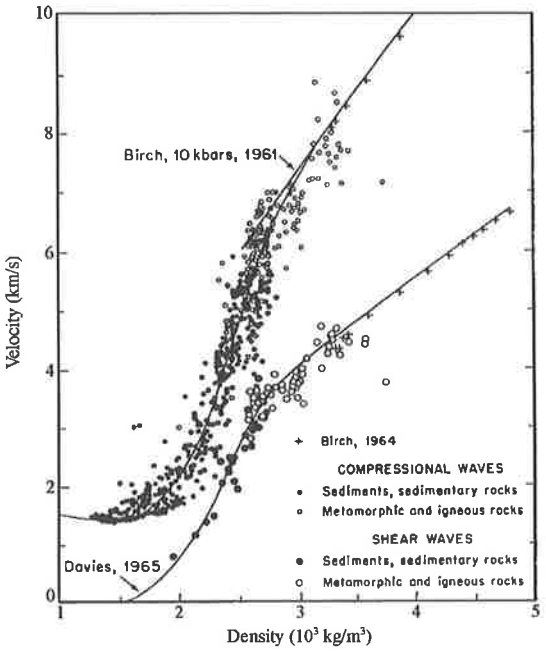

Figure 3.2 Nafe-Drake density vs. velocity curve (after Ludwig et al., 1970).

Check shot velocity surveys were not available for every well in which a density log was run. The wells for which check shot velocity surveys were available are listed in Table 3.1. All the available surveys were plotted (Figure 3.4a), revealing different velocity depth trends for different areas. Hence, the North West Shelf velocity/depth data were divided into three groups: Carnarvon, Browse and Bonaparte (Figures 3.4, 3.5 and Table 3.1). A logarithmic regression line was fitted to the check shot velocity dataset from each area (Figure 3.4):

Carnarvon $\quad Velocity = 456.57 \ln(Depth) - 761$

$$R^2 = 0.7539 \qquad (3.6)$$

Browse $$Velocity = 421.5\ln(Depth) - 707.37$$

$$R^2 = 0.6813 \quad (3.7)$$

Bonaparte $$Velocity = 450.91\ln(Depth) - 520.93$$

$$R^2 = 0.8698 \quad (3.8)$$

where velocity is in ms^{-1}, depth is in m (below sea level) and R^2 is the regression coefficient; $R^2 = 0$ implies no correlation and $R^2 = 1$ implies perfect correlation.

The average sonic velocity from the surface to the top of the density log was calculated using the appropriate regional velocity-depth relationship (Equations 3.6, 3.7 and 3.8). This value was then converted to an average density using the Nafe-Drake velocity-density transform. These results are summarised in Table 3.2.

Carnarvon Group	Browse Group	Bonaparte Group
Angel 1	Barcoo 1	Anderdon 1
Bambra 1	Brecknock 1	Asterias 1
Emma 1	Brewster 1A	Avocet 1A
Flores 1	Caswell 1	Brown Gannet 1
Griffin 3	Gryphaea 1	Challis 1
Griffin 4	Lombardina 1	Crane 1
Harriet 1	Londonderry 1	Cygnet 1
Judy 1	Prudhoe 1	Drake 1
Lambert 1		Eclipse 1
Macedon 1		Ibis 1
Scindian 2		Jabiru 1A
Tanami 2		North Hibernia 1
Wanaea 2		Osprey 1
Wanaea 3		Pollard 1
		Rainbow 1
		Sahul Shoals 1
		Skua 2
		Swift 1
		Tamar 1
		Vulcan 1B

Table 3.1 Wells for which velocity survey data were available. Wells are grouped according to areas exhibiting similar acoustic properties.

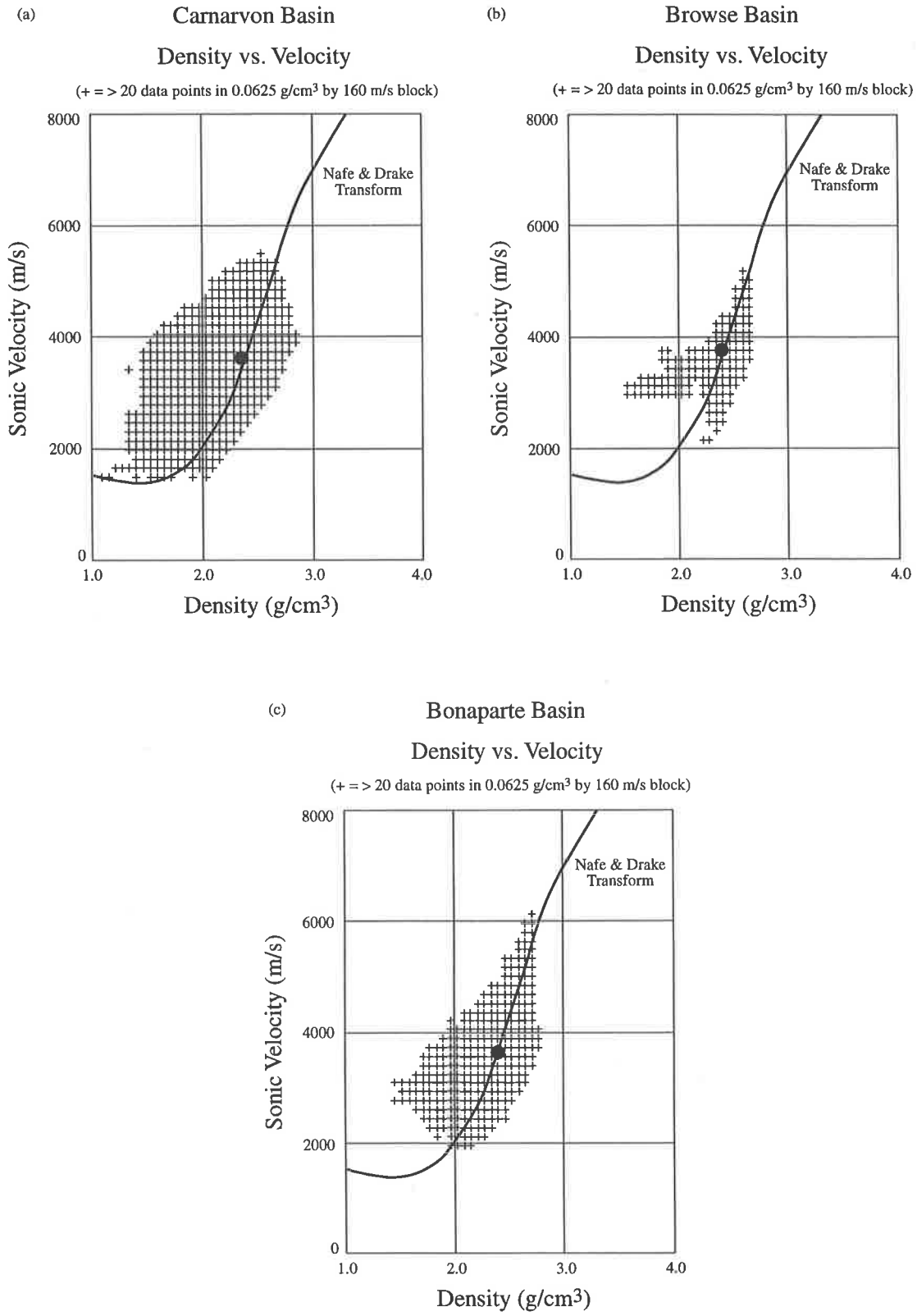

Figure 3.3 Density vs. sonic velocity from log data available in (a) the Carnarvon Basin, (b) the Browse Basin and (c) the Bonaparte Basin. Also shown is the Nafe-Drake curve as shown in Figure 3.2 and the mean density/mean velocity point of the relative data sets.

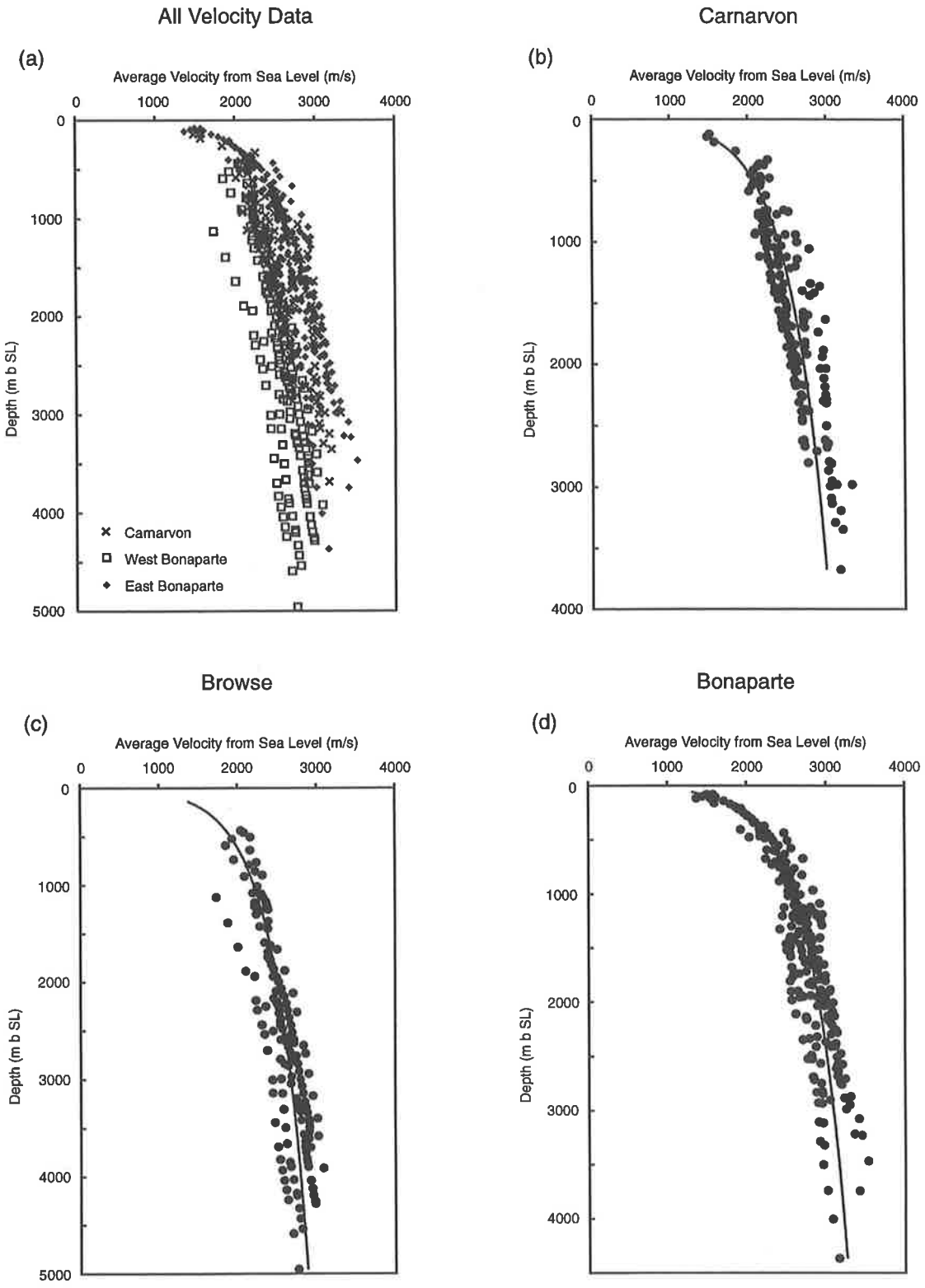

Figure 3.4 Average velocity vs. depth curves from well velocity surveys (a) in all areas, (b) in the Carnarvon, (c) in the Browse and (d) in the Bonaparte. Velocity/depth regression relationships are included for each of the three divisions, corresponding to Equations 3.6, 3.7 and 3.8 respectively.

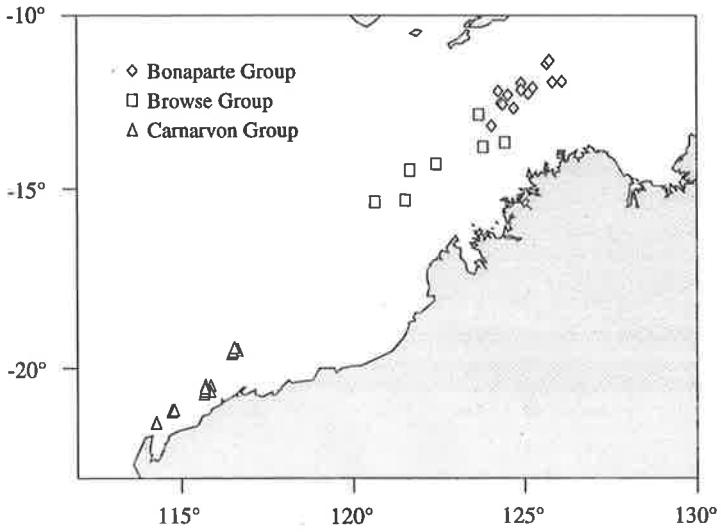

Figure 3.5 Locations of wells listed in Table 3.1.

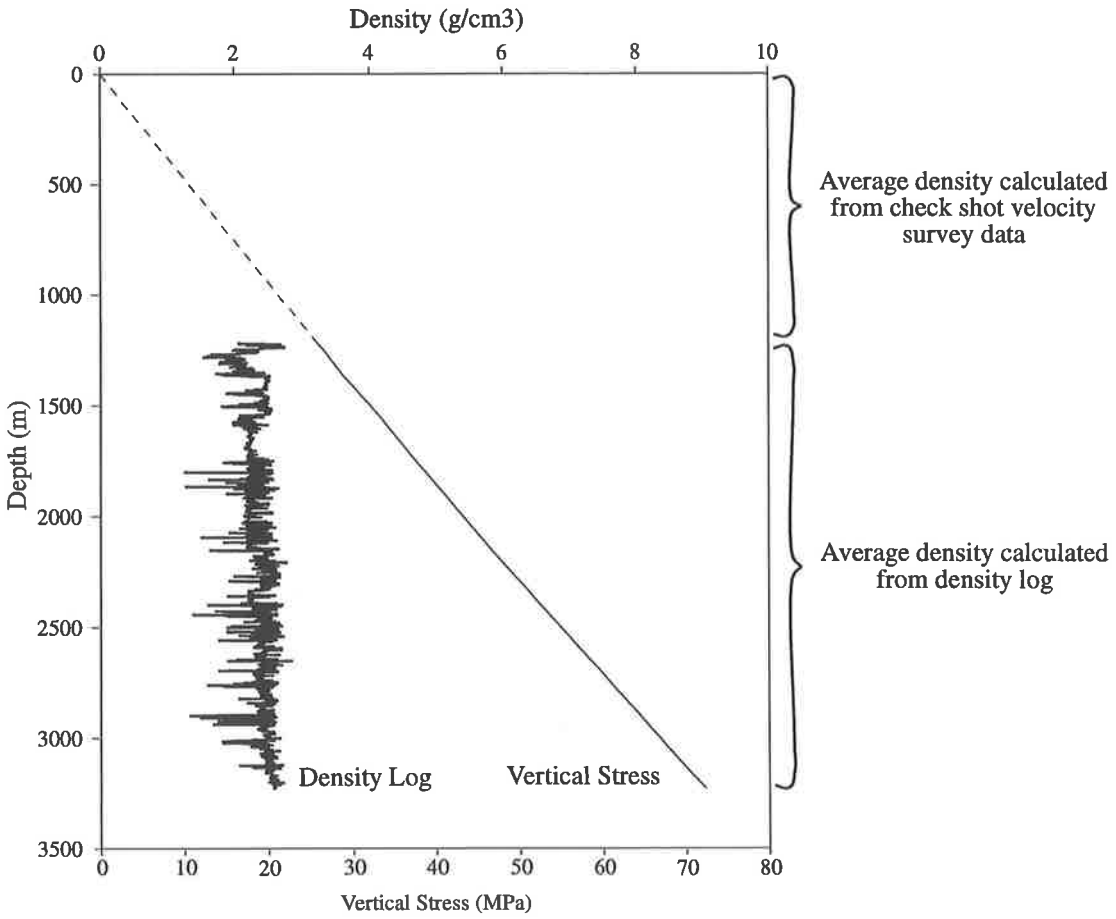

Figure 3.6 Original density log data for within the Jabiru-1A well, and the vertical stress profile calculated as described in the text.

Well Name	Lat	Long	Density Log Interval (m) Top	Bottom	Average Sonic Velocity (m/s)	Average Density (g/cm3)
Carnarvon Group						
Alpha North 1	19°28'	116°58'	1539.09	2194.87	2590	2.15
Angel 1	19°31'	116°35'	1509.37	3024.38	2581	2.14
Angel 2	19°28'	116°40'	2588.98	4388.21	2827	2.18
Bambra 2	20°32'	115°36'	1792.99	3077.57	2659	2.16
Chinook 1	21°10'	114°41'	1707.99	3077.72	2637	2.15
Cossack 1	19°34'	116°30'	401.12	3029.71	1976	1.92
Emma 1	20°32'	115°47'	551.54	2355.19	2121	1.99
Flores 1	20°46'	115°35'	1169.98	2118.97	2465	2.12
Goodwyn 1	19°41'	115°53'	1283.82	3540.71	2507	2.13
Goodwyn 5	19°40'	115°53'	2400.15	3659.89	2793	2.18
Goodwyn 6	19°43'	115°51'	476.10	4662.98	2054	1.95
Griffin 1	21°14'	114°37'	2512.47	3378.71	2814	2.18
Harriet 1a	20°36'	115°37'	898.55	2005.89	2344	2.05
Harriet 3	20°36'	115°37'	2485.03	2648.56	2808	2.18
Orion 1	19°52'	116°32'	365.91	2496.31	1934	1.9
Pepper 1	21°03'	115°18'	459.33	2610.16	2038	1.95
Samson 1	19°43'	116°38'	1973.89	3752.24	2703	2.17
Santo 1	21°33'	114°19'	877.21	1871.93	2333	2.08
Scindian 1a	21°11'	114°42'	2310.54	3134.87	2775	2.18
Walcott 1	19°37'	116°22'	407.06	4375.40	1983	1.93
Browse Group						
Caswell 1	14°14'	122°28'	2500.73	3681.22	2591	2.15
Gryphaea 1	12°49'	123°44'	2631.65	3868.53	2612	2.15
Kalyptea 1	13°02'	123°52'	3288.79	4575.05	2706	2.17
Bonaparte Group						
Anderdon 1	12°38'	124°47'	2002.08	2907.80	2907	2.2
Avocet 1a	11°22'	125°46'	1191.16	2200.00	2673	2.16
Barita 1	11°26'	125°43'	1281.68	2488.54	2706	2.17
Beluga 1	11°00'	129°33'	2428.34	3083.97	2994	2.22
Bilyara 1st	12°41'	124°30'	2600.25	2838.91	3025	2.22
Brown Gannet 1	12°06'	123°51'	259.84	2733.45	1986	1.91
Challis 1	12°07'	125°00'	1194.06	1954.08	2674	2.16
Eclipse 1	12°16'	124°37'	1411.23	2987.66	2749	2.17
Fagin 1	11°34'	125°08'	2883.41	3261.36	3071	2.23
Iris 1	11°17'	126°33'	3403.09	3906.77	3146	2.24
Jabiru 1a	11°56'	125°00'	1219.05	3228.90	2683	2.16
Jabiru 2	11°56'	124°59'	1198.02	2344.98	2675	2.16
Osprey 1	12°13'	125°13'	264.57	3182.58	1994	1.92
Skua 4	12°29'	124°26'	2196.69	2652.98	2949	2.21
Swan 2	12°07'	124°18'	1555.09	3222.50	2793	2.18
Swift 1	12°32'	124°27'	1451.31	2798.22	2762	2.18
Vulcan 1b	12°09'	124°20'	1387.00	2870.61	2741	2.17

Table 3.2 List of wells for which vertical stress profiles were calculated where lat and long are the latitude and longitude of the well, top and bottom are the top and bottom depths of the density log run, average sonic velocity is the average check shot velocity calculated from either Equation 3.6, 3.7 or 3.8 depending on the well location (see Table 3.1 and Figure 3.5), and average density is the Nafe-Drake transform from average check shot velocity to average density for the interval between the surface and the top of the density log.

A Pascal program ('Vstress', Appendix A) was written to evaluate Equation 3.5 from the density log data. This program calculates the average density over the entire log depth and uses it to calculate the overburden weight. The overburden weight to the top of the density log is calculated from the check shot velocity data as described above, and is added to the value determined from the density log data. Figure 3.6 illustrates a vertical stress profile calculated for the Jabiru-1A well.

3.2.2 Depth Corrections

The wells from which vertical stress profiles were calculated, all have drilling trajectories that deviate at least very slightly, from the vertical. This implies that the logging depth, (reference depth for each density log), does not equal the true vertical depth (TVD), causing a degree of error in estimating vertical stress profiles in deviated wells.

Vertical stress profiles were calculated for 41 wells in this study. The majority of wells have a maximum deviation less than 5°, with only three wells exceeding a maximum deviation of 10°. In the case of the well with the greatest deviation, Swan-2, the maximum possible error can be estimated by assuming the maximum deviation (13°) for the entire well. The logging depth at the base of the well is 3222 m. Assuming that the well is consistently deviated from the vertical by 13°, the equivalent TVD is 3140 m. This corresponds to an error of less than 2MPa for the vertical stress magnitude at the base of the well.

The assumption that the well is deviated over its entire length at the maximum deviation angle is inaccurate. When an inclined well is drilled, the deviation angle is

gradually built up as the depth of penetration increases. Therefore, the error in vertical stress magnitude calculation at the base of the Swan-2 well is substantially less than 2MPa. On this basis the small errors in vertical stress magnitudes caused by well deviations have been ignored.

3.3 Horizontal Stress Magnitude Measurement

There are several methods by which the magnitude of horizontal stresses can be evaluated. Possible techniques include: in situ methods, including the flatjack method (Froidevaux et al., 1980) and overcoring techniques such as doorstopper and triaxial strain gauge methods (Baumann, 1981; Baumann & Becker, 1986)]; methods based on wellbore failure, which most commonly utilise breakout shape (Haimson & Herrick, 1986; Zoback et al., 1986; Peska & Zoback, 1995), and; strain relaxation methods (summary by Engelder, 1993). In situ techniques cannot generally be applied in the offshore North West Shelf. The relationship between breakout shape and stress magnitude is still rather poorly defined (Engelder, 1993), and it was considered that an approach utilising such techniques, while it holds great promise for the North West Shelf, would require a dedicated project in its own right. The application of strain relaxation techniques to the North West Shelf would require thorough integration with drilling and operational procedures in the North West Shelf that was again considered beyond the scope of this project.

The most reliable and widely used techniques for determining horizontal stress magnitude are those based on the hydraulic fracture methodology. Although full hydraulic fracture tests have not been undertaken on the North West Shelf, Leak-off tests, which resemble the first stage of a hydraulic fracture test have been widely

undertaken. This thesis follows several workers who have used leak-off test data to investigate horizontal stress magnitudes (Breckels & van Eeckelen, 1982; Ervine & Bell, 1987; Gaarenstroom et al., 1993). All hydraulic fracture-type techniques require an understanding of the disturbance to a homogenous stress field caused by a wellbore. The following sections describe the theory regarding the stress distribution around a borehole, and explain how that distribution is related to hydraulic fracture.

3.3.1 Stress Field Around a Borehole

The stress field acting on a vertical borehole can be described by considering the classic two dimensional (plane-strain) solution for a small circular hole within an isotropic elastic plate subjected to uniaxial compressive stress. Provided that the plate is infinitely large compared with the hole, the radial (σ_r), tangential or circumferential (σ_θ) and shear ($\tau_{r\theta}$) stresses near the hole associated with a uniaxial compression can be expressed in polar coordinates at a point (θ, r) given by the Kirsch equations (Kirsch, 1898; Jaeger and Cook, 1969; Engelder, 1993):

$$\sigma_r = \frac{\sigma_h}{2}\left(1-\frac{R^2}{r^2}\right)+\frac{\sigma_h}{2}\left(1+3\frac{R^4}{r^4}-4\frac{R^4}{r^4}\right)\cos 2\theta \qquad (3.9)$$

$$\sigma_\theta = \frac{\sigma_h}{2}\left(1+\frac{R^2}{r^2}\right)-\frac{\sigma_h}{2}\left(1+3\frac{R^4}{r^4}\right)\cos 2\theta \qquad (3.10)$$

$$\tau_{r\theta} = -\frac{\sigma_h}{2}\left(1-3\frac{R^4}{r^4}+2\frac{R^2}{r^2}\right)\sin 2\theta \qquad (3.11)$$

where R is the radius of the borehole, r is the distance from the centre of the borehole and θ is measured clockwise from the direction of compressive stress, σ_h. At the hole wall where r = R, σ_r and $\tau_{r\theta}$ become zero and:

$$\sigma_\theta = \sigma_h - 2\sigma_h \cos 2\theta. \qquad (3.12)$$

The circumferential stress acts tangentially to the borehole perimeter and is maximised on the borehole wall when $\theta = 90°$ ($\cos 2\theta = -1$) such that $\sigma_\theta = 3\sigma_h$. At $\theta = 0°$ ($\cos 2\theta = 1$), the circumferential stress is tensional ($\sigma_\theta = -\sigma_h$). Hence the presence of a vertical borehole in a uniaxial stress field realigns horizontal stress trajectories, concentrating circumferential compressional stress at right angles to the direction of the far field uniaxial stress (Figure 3.7).

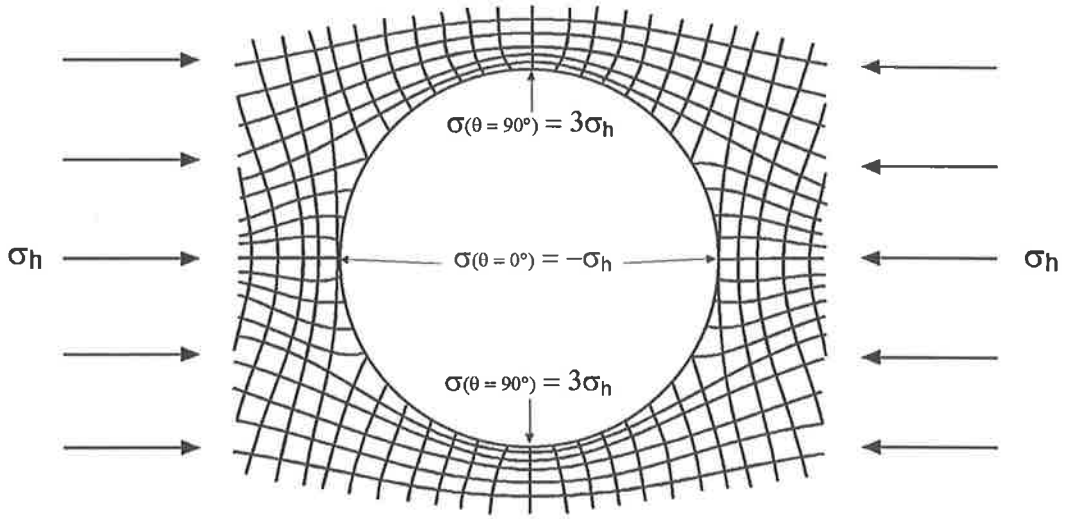

Figure 3.7 Stress trajectories about a vertical borehole within a uniaxial horizontal stress field (σ_h). Note that there is a stress concentration at $\theta = 90°$ and a stress reduction at $\theta = 0°$ (after Jaeger & Cook, 1969).

In reality, a vertical borehole is subject to a biaxial horizontal stress field, superimposing a second non-zero horizontal stress at right angles to the original stress component. The magnitudes of the two horizontal stresses are commonly unequal. The effects of σ_{hmin} and σ_{Hmax} are superimposed on each other such that in the biaxial case:

$$\sigma_\theta = \left(\sigma_{Hmax} + \sigma_{hmin}\right) - 2\left(\sigma_{Hmax} - \sigma_{hmin}\right)\cos 2\theta . \qquad (3.13)$$

Figure 3.8 illustrates the circumferential stresses around a wellbore at $\theta = 0°$ and 90° due to the far field σ_{hmin}, and those due to the far field σ_{Hmax}, and also shows the resultant superimposed stress distribution.

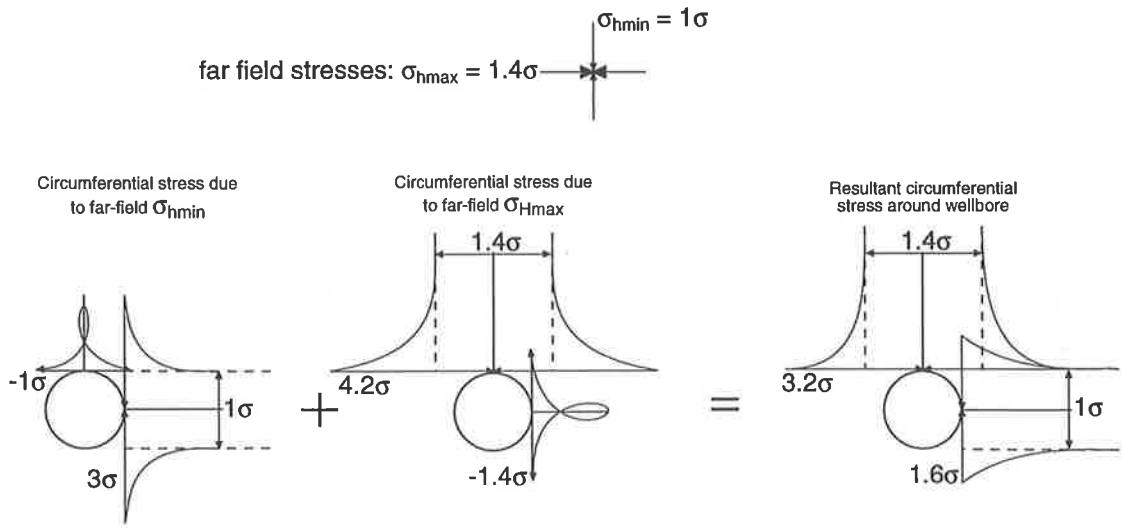

Figure 3.8 The superpostion of maximum and minimum horizontal stresses acting on a vertical borehole illustrating the circumferential stress at $\theta = 0°$ and $\theta = 90°$. Negative values indicate tensile stress (Hubbert & Willis, 1957).

The maximum and minimum circumferential stresses acting on a borehole within a biaxial stress environment are given by:

$$\sigma_{\theta=90°} = 3\sigma_{Hmax} - \sigma_{hmin} \tag{3.14}$$

$$\sigma_{\theta=0°} = 3\sigma_{hmin} - \sigma_{Hmax} . \tag{3.15}$$

Note that since $\sigma_{Hmax} \geq \sigma_{hmin}$, then $\sigma_{\theta = 90°} \geq \sigma_{\theta = 0°}$. It is at these orientations that the borehole wall is most susceptible to stress induced failure. Compressional shear failure (borehole breakout) tends to occur in the minimum horizontal stress direction (at $\theta = 90°$) and tensional failure (hydraulic fractures) tends to occur in the maximum horizontal stress direction (at $\theta = 0°$). Hydraulic fracture is discussed in the following section and borehole breakout is discussed in Chapter 4.

3.3.2 Hydraulic Fracture and the Effects of Mud-weight

Hydraulic fracturing is widely performed in the petroleum industry to maximise recovery from low permeability reservoirs. Hydraulic fractures may also occur inadvertently in petroleum exploration wells under conditions where the weight of the fluid column (mud-weight) within the wellbore causes tensile fracture of the borehole wall, resulting in a loss of drilling fluid into the formation.

Hydraulic fractures open against the least principal stress, and propagate in a plane parallel to the maximum principal stress direction (Hubbert and Willis, 1957; Cornet and Valette, 1984; Hickman et. al, 1985). A hydraulic fracture will form at a wellbore wall when the minimum circumferential and the tensile strength of the rock (T_0), are exceeded by the fluid pressure within the wellbore (P_f):

$$P_f \geq \sigma_\theta + T_0 . \tag{3.16}$$

The pressure at which fracture occurs is known as the breakdown pressure (P_b). Haimson & Fairhurst (1967) used Hubbert & Willis' (1957) analysis to derive P_b, which is based on this stress distribution around a wellbore:

$$P_b = 3\sigma_{\text{hmin}} - \sigma_{\text{Hmax}} - P_p + T_0 . \tag{3.17}$$

Vertical tensile failure of the borehole wall occurs along an axis parallel to the maximum horizontal stress, provided vertical stress is not the least principal stress. Under a compressional (reverse) stress regime, the vertical stress is the minimum principal stress (Equation 3.4), therefore once the fluid pressure in the wellbore exceeds the vertical stress and tensile strength of the rock, a hydraulic fracture will propagate in the horizontal plane.

Figure 3.9 illustrates the superposition of fluid pressure within a borehole on circumferential stresses associated with σ_{hmin} and σ_{Hmax} (described previously in Figure 3.8). The fluid pressure within the wellbore exerts a negative circumferential stress of magnitude equal to the fluid pressure, reducing the possibility of borehole breakout (at $\theta = 90°$), but increasing the possibility of tensile failure (at $\theta = 0°$). The circumferential stress acting at a borehole wall with a mud column within the well is given by:

$$\sigma_\theta = (\sigma_{Hmax} + \sigma_{hmin}) - 2(\sigma_{Hmax} - \sigma_{hmin})\cos 2\theta - P_f, \qquad (3.18)$$

where P_f is the fluid pressure (pressure exerted by the drilling mud). The weight of the mud column must exceed formation pore pressure so as to prevent kicks (i.e. entry of formation fluids into the wellbore), and must exert enough pressure on the borehole to prevent compressive shear failure (breakouts). However, it should not be so high as to induce tensional failure (hydraulic fracture). The mud-weights between these limits is often referred to as the safe mud-weight envelope.

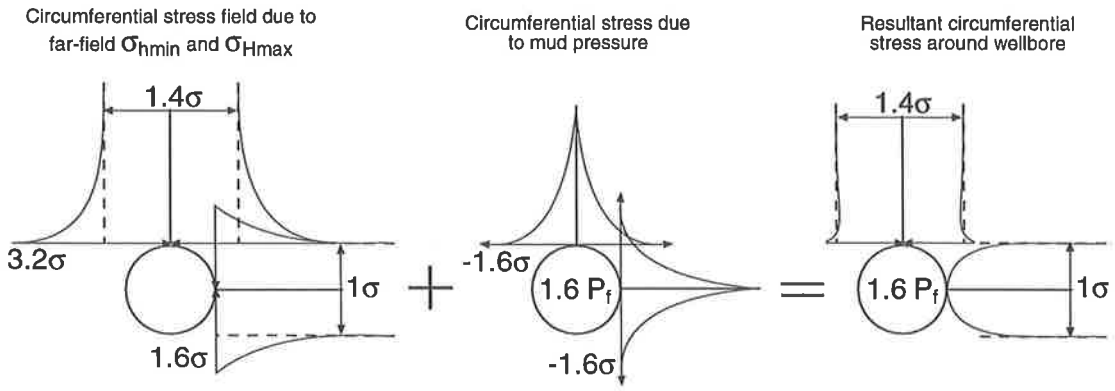

Figure 3.9 Schematic representation of circumferential stresses about a vertical borehole within a biaxial stress field (Figure 3.8), and the superimposed effect of fluid pressure acting on the borehole walls (after Hubbert & Willis, 1957). Negative values indicate tensile stress.

3.3.3 Hydraulic Fracturing Procedure

Hydraulic fracturing involves isolating an interval of wellbore with inflatable packers so that fluid, pumped into that interval under pressure, is prevented from flowing up or down the wellbore (Engelder, 1993). The pressure between the packers (injection interval) is increased until it induces a fracture in the surrounding rocks i.e. the fluid pressure reaches the breakdown pressure (P_b) at which the fluid pressure is greater than the circumferential stress and the tensile strength of the rock (Equation 3.16). The pressure is then reduced (bled off) to allow the fracture to close and the cycle is repeated. The pressure at which major flow from the fracture into the wellbore ceases is known as the instantaneous shut-in pressure (P_i) or ISIP. At this point, especially in small volume tests, the walls of the fracture are considered to come into contact and the fluid pressure at this point is taken to equal σ_{hmin} in extensional and strike-slip stress regimes. The ISIP can be recognised as an inflection point on the pressure decay slope of the pressure-time record (Engelder, 1993; Figure 3.10). Several re-opening cycles may be undertaken to propagate the fracture into the far-field and to obtain repeatable ISIP's.

Fracture initiation, or breakdown pressure during the first cycle of the hydraulic fracture test is described by Equation 3.16. In subsequent cycles of the test, only the effective circumferential stress, and not the tensile strength of the rock, needs to be overcome to open the existing rupture. Therefore Equation 3.16 can be modified as follows:

$$P_r = 3\sigma_{h\min} - \sigma_{H\max} - P_p, \qquad (3.19)$$

where (P_r) is the fracture opening pressure; the pressure at which the pre-existing fracture will open (Bredehoeft et al., 1976). Given fracture re-opening pressure, σ_{hmin}

(ISIP), and the pore pressure, an estimate of σ_{Hmax} can be made from Equation 3.19. For a more complete discussion of the hydraulic fracture procedure in an Australian context see Enever (1988) and Enever et al. (1996).

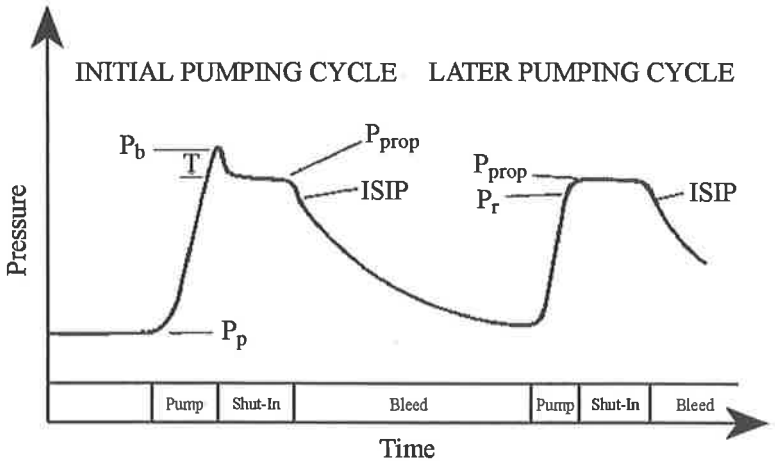

P_p	- Pore pressure	P_{prop}	- Propogation Pressure
T	- Tensile Strength	ISIP	- Instantaneous Shut-in Pressure
P_b	- Breakdown Pressure	P_r	- Fracture Opening Pressure

Figure 3.10 Schematic pressure-time record of a hydraulic fracture test (Bell, 1990a).

3.3.4 Determining Horizontal Stress Magnitude from Leak-Off Tests

Unfortunately, hydraulic fracturing tests of the type described are not routinely performed in hydrocarbon exploration wells. However, a related procedure, called a leak-off test, is standard procedure. The leak-off test is basically the first part of a hydraulic fracture test. They are used in hydrocarbon exploration drilling for three reasons: to test the resistance of the formation at the casing shoe depth; to verify the casing cement, and; to establish the maximum mud column pressure that the wellbore can withstand without hydraulically fracturing the formation.

After casing has been placed in a section of the wellbore, cement is injected between the casing pipe and the borehole wall. Once the cement has hardened, it is drilled out at the bottom and the hole is deepened several metres beneath the base of the casing (Bell, 1990a). At this point the leak-off test is performed. Mud is pumped into the well, increasing fluid pressure on the borehole wall. The drilling mud begins to 'leak-off' when a fracture is initiated in the borehole wall below the casing. Pumping stops and the fluid pressure decays back to normal mud-weight levels. The leak-off pressure is calculated by summing the (surface) pump pressure at leak-off with the weight of the column of mud in the well (Bell, 1990a). An example of a leak-off test from the North West Shelf is illustrated in Figure 3.11.

The disadvantage in using leak-off test data instead of data from a hydraulic fracture test is that only fracture initiation (leak-off) pressures are recorded. Pressure decline is not usually monitored, although it is in Figure 3.11, where surface pump ISIP appears to be approximately 900 psi. The leak-off pressure is considered to be approximately equal to the ISIP, and is used to estimate the minimum horizontal stress magnitude. Fracture initiation during the initial pumping cycle involves overcoming the tensile strength of the rock and the stress concentration around the wellbore, therefore the leak-off pressure tends to overestimate ISIP and σ_{hmin} (as it does in Figure 3.11).

Breckels & Van Eekelen (1981) compared leak-off and ISIP values obtained during the same test for 14 wells in Brunei. On average leak-off values exceeded ISIP's by 11% (with a standard deviation of 9%). Breckels & Van Eekelen (1981) also note that Pilkington's (1978) average leak-off trend-line for the Gulf Coast falls between 11 and 15% above a curve based on ISIP's in the same depth range.

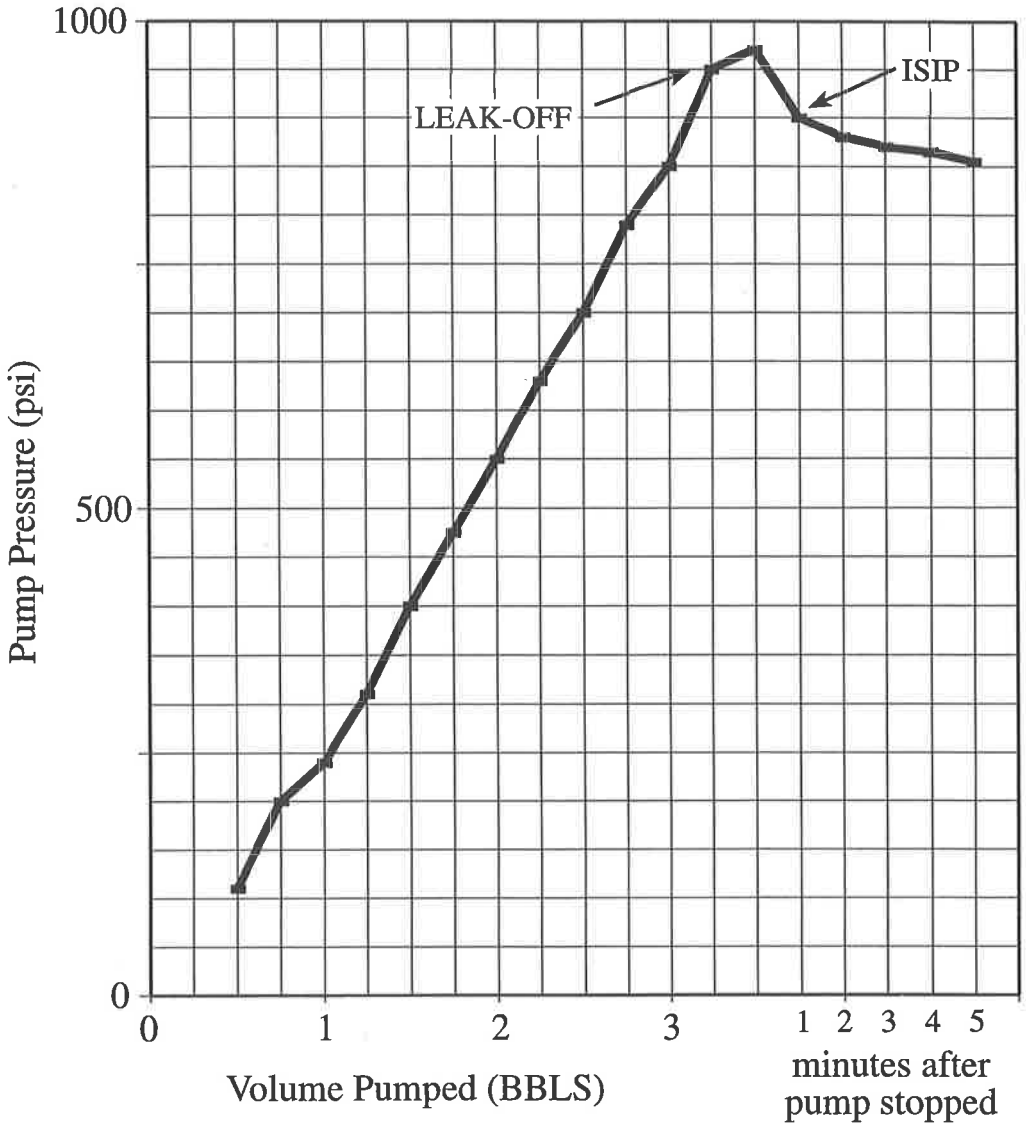

Figure 3.11 Volume-pressure record of mud injected during a leak-off test in the Maple-1 well. The pressure (in barrels) linearly increases with volume pumped until a fracture is initiated at which point it begins to 'leak-off'. The leak-off pressure is determined by adding the pressure at leak-off to the weight of the mud column.

In general the lower bound to leak-off values seems to provide a good estimate of σ_{hmin} (Breckels & Van Eekelen, 1981; Gaarenstroom et al., 1993; Enever et al, 1996). In summary:

$$\text{Lower bound leak-off pressure} \approx P_r \approx \text{ISIP} \approx \sigma_{hmin}. \qquad (3.20)$$

This relationship enables Equation 3.19 to be simplified to:

$$\sigma_{H\,max} = 2\sigma_{h\,min} - P_p, \qquad (3.21)$$

where σ_{hmin} has been estimated by lower bound leak-off pressures and P_p is the pore pressure of the formation (Ervine & Bell, 1987). Formation pore pressures can be inferred from drilling mud-weight records and are measured directly during formation testing (Bell, 1990a). For wells in this project where pore pressure data were unavailable, estimates were made using a standard pressure gradient for a hydrostatic salt water column (9.4 MPa/km or 0.448 psi/ft).

Chapter 4

Determination of Contemporary Stress Orientation

4.1 Indicators of Horizontal Stress Orientation

Horizontal stress orientation can be determined from four different categories of stress measurement: earthquake focal mechanisms; in situ stress measurements (hydraulic fracture, overcoring, flatjack and doorstopper methods); young geologic data (fault slip and volcanic vent alignments), and; borehole breakouts (Zoback et al., 1989; Becker et al., 1990; Zoback and Zoback, 1991; Zoback, 1992). In order for a particular method to be useful, it must first and foremost be a reliable indicator of the contemporary stress field orientation. It should also be easily implemented and provide a good geographic coverage over the region of interest. Although each method has its respective advantages and disadvantages, and the methods are conducted at different depths, the results from different methods often correspond with each other well (Zoback, 1991). Ideally all the different methods would be used to define the orientation of the contemporary stress field in a given area. However, the North West Shelf is an area of low seismicity, therefore earthquake focal mechanism analysis cannot be undertaken. Given that the area is offshore, the in situ techniques cannot be easily implemented, and young geologic data are not available. On the other hand, the large number of hydrocarbon exploration wells on the North West Shelf provide an abundance of easily obtainable stress indicators through borehole breakout analyses. This chapter presents the theory of the origin of borehole breakouts, and a detailed description of the borehole breakout analyses undertaken on the North West Shelf.

4.1.1 Borehole Breakouts

Borehole breakouts occur in vertical wellbores where the circumferential stress exceeds the shear strength of the rock (S_o) at the borehole wall. The circumferential stress is maximised where $\theta = 90°$ according to Equation 3.14. Conjugate compressional shear failure surfaces intersect and pieces of the wellbore wall break off, or spall, forming broad, flat depressions at the azimuth of σ_{hmin} (Gough & Bell, 1982; Zoback et al., 1985; Figures 4.1 and 4.2).

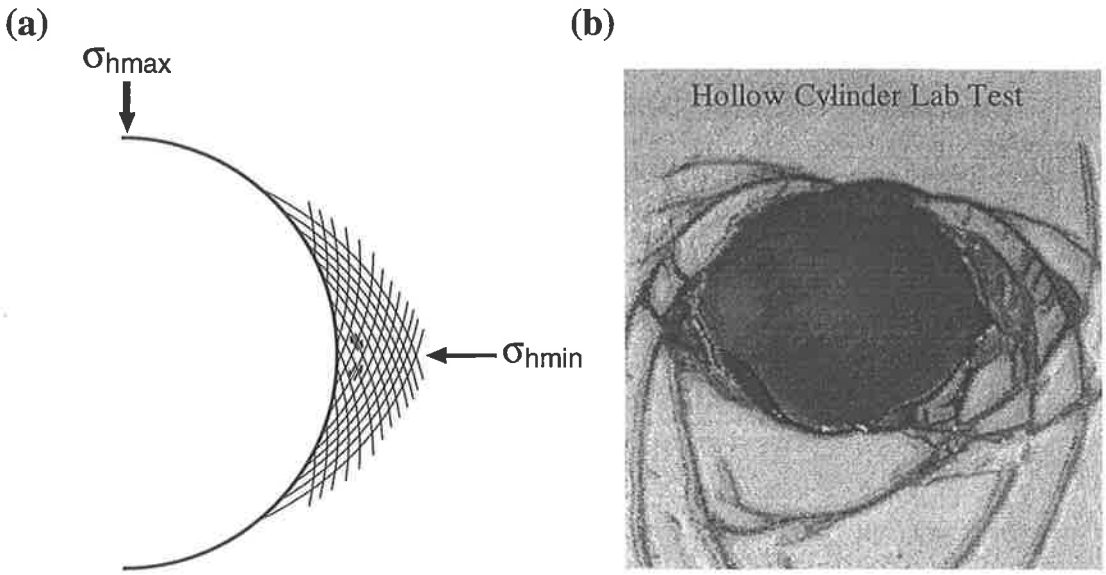

Figure 4.1 (a) Potential shear failure surfaces adjacent to a borehole drilled through biaxialy stressed rock (Bell, 1990a). (b) Results of a hollow cylinder lab test performed by the CSIRO Division of Geomechanics illustrating shear failure in the σ_{hmin} direction.

Using digital borehole televiewer images, Plumb (1989) revealed that the specific mechanism of shear failure of the borehole wall may vary with rock strength, depth or state of stress. He recognised three distinct types of breakout failure which are consistent with the three modes of failure postulated by Guenot and Santarelli (1988). Type 1 breakouts are characterised by diffuse margins with no internal structure, Type 2 breakouts have segmented margin features and Type 3 breakouts consist of larger fracture planes which strike parallel to σ_{hmax} (Figure 4.3). He concluded that each

type of breakout reflects one of three different reference states of stress around the borehole:

$$\sigma_r < \sigma_v < \sigma_\theta : \text{Type 1} \quad (4.1a)$$

$$\sigma_\theta < \sigma_r < \sigma_v : \text{Type 2} \quad (4.1b)$$

$$\sigma_r < \sigma_\theta < \sigma_v : \text{Type 3} \quad (4.1c)$$

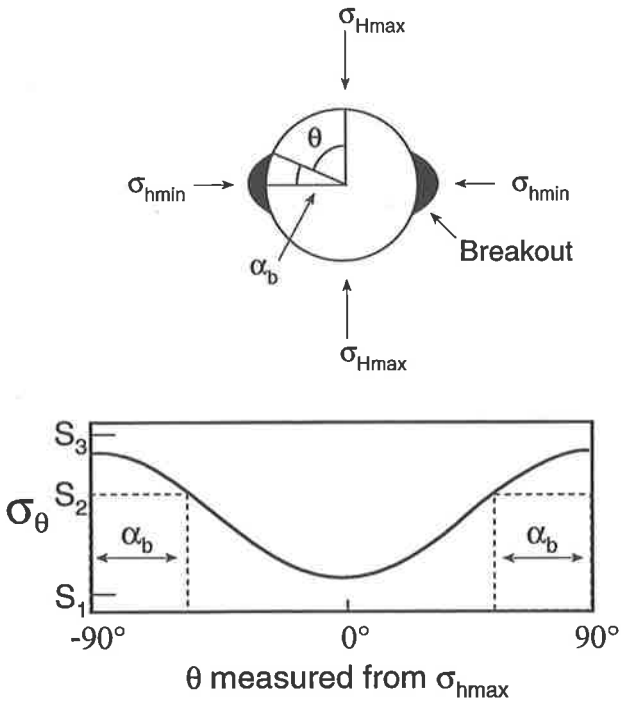

Figure 4.2 (a) Schematic representation of a borehole breakout showing the angle of breakout extent, α_b. (b) The variation of circumferential stress, σ_θ as a function of θ measured from σ_{hmax}. Also illustrated is the relationship between angle of breakout extent and compressive shear strength of the rock (S_0), i.e. α_b defines $S_0 = S_2$. After Castillo and O'Neill (1992).

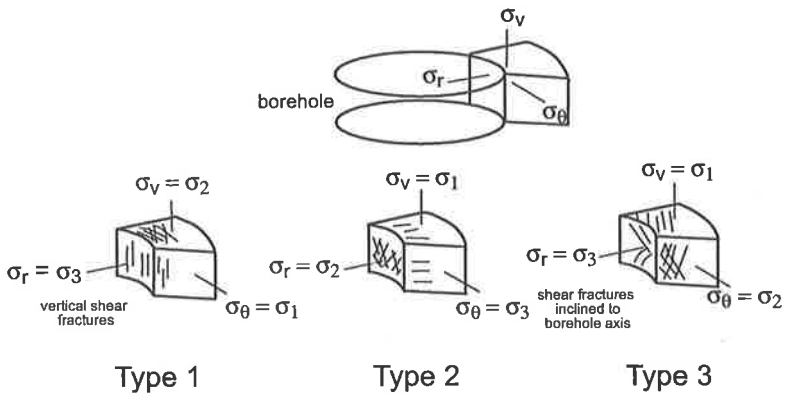

Figure 4.3 The 3 modes of failure associated with borehole breakouts (Plumb, 1989).

4.2 Borehole Breakout Recognition

The orientation of the contemporary stress field throughout the North West Shelf can be determined using borehole breakouts because breakouts can be recognised on log data routinely acquired in hydrocarbon exploration wells, namely the dipmeter or borehole resistivity imaging logs. This section describes the HDT/SHDT dipmeter tools and the FMS[1] imaging tool and explains how data from these tools are used to recognise borehole breakouts.

4.2.1 Dipmeter and Borehole Resistivity Imaging Tools

The FMS has evolved from the older HDT and SHDT four-arm dipmeter tools. It consists of four orthogonal arms which are hydraulically pressed against the wellbore wall (Figure 4.4). Resistivity sensors are mounted at the end of each arm and the tool gives oriented measurements of resistivity and borehole width (two orthogonal readings). The one (HDT) or two (SHDT) microresistivity sensors on each arm have been replaced by 16 sensors on each of the four orthogonal arms of the FMS, producing four 2.5 inch (6.35 cm) swaths of microresistivity readings.

The reference pad (pad 1) is magnetically oriented and two pairs of calipers measure the borehole diameter between pads 1 and 3, and between 2 and 4. As the tool is pulled up the hole, it tends to rotate clockwise due to cable torque induced by the lay of the cable. If the borehole is non-circular in cross-section, (e.g. breakout is present), one pair of caliper arms gets stuck in the long axis of the borehole and rotation ceases. Cessation of tool rotation in conjunction with elongation of one

[1] HDT is the High-Resolution Dipmeter Tool, SHDT is the Stratigraphic High-Resolution Dipmeter Tool and FMS is the Formation Microscanner. HDT, SHDT and FMS are all Schlumberger tool names. Schlumberger tools were run in all the wells analysed in this study.

caliper pair (while the other caliper pair remains at bit size), are indicative of borehole breakout.

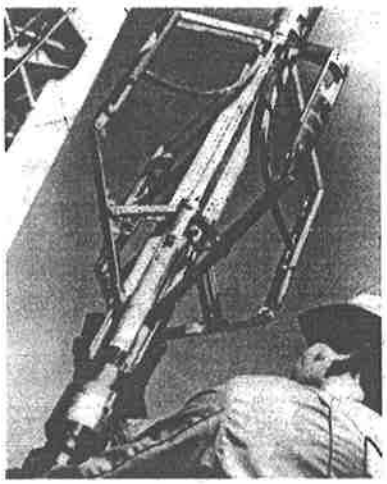

Figure 4.4 High-resolution dipmeter tool. Photo from Plumb and Hickman (1985).

Figure 4.5 illustrates an example of borehole breakout identification using information extracted from an SHDT dipmeter log over a 115m interval from the Wanaea-2 well in the Carnarvon Basin. The right-hand track of the log records the azimuth of the reference pad (pad 1), the centre track records the C1 (pad 1-3 diameter) and orthogonal C2 (pad 2-4 diameter) widths, and the left-hand track records the difference between the C1 and C2 widths, with the zero centreline (i.e. both diameters of equal width) marked. Deviation to the left of this centreline indicates that the C2 width is greater than the C1 width, and deviation to the right indicates that the C1 width is greater than the C2 width.

From the base of the interval illustrated in Figure 4.5, the tool rotated more than 180° before ceasing to rotate at 2987 m with C1 oriented at approximately 180°N. At this depth C1-C2 is positive, therefore the borehole breakout is parallel with the reference pad in a north-south direction. The tool continued to rotate from 2982 m until 2970 m, over which interval the borehole was approximately circular. Rotation ceased at

2970 m with C1 oriented approximately 090°N. At this depth an elongation was recorded on C2, indicating a second borehole breakout oriented NS (C2 is orthogonal to C1). Following approximately 360° of rotation over 15 m, rotation ceased again at 2950 m with C2 again showing a greater diameter than C1 in association with another north-south oriented borehole elongation. The tool then rotated another 100°, then 10° backwards (anti-clockwise direction), before locking into a fourth breakout elongation on C1 at 180° at 2935 m. The tool then rotated another 90° and ceased rotating at approximately 2930 m with C1 oriented 270°. However at this depth there is no borehole elongation. After a further 90° rotation another elongation is observed on C1 at approximately 2920 m. Again the elongation is oriented NS. Over the last 40 m of the interval illustrated, there are two breaks in rotation from 2912 to 2908 m and from 2895 to 2885 m where C1 is oriented approximately 090°. Both of these intervals show elongation on C2, confirming the NS breakout azimuth. Each of the seven breakout zones described above have azimuths aligned NS indicating a NS σ_{hmin} direction and hence an east-west σ_{hmax} direction.

The advantage of FMS data over dipmeter data is that, not only can the caliper data be analysed for breakouts, but the electrical image provided from the resistivity sensors on each pad clearly reveals borehole breakouts, hydraulic fractures, natural fractures and bedding planes. Hydraulic fractures appear as narrow, low resistivity features while breakouts, on the other hand, generally appear as relatively wide blobby zones of low resistivity where the wellbore has been subject to compressive shear failure (spalling).

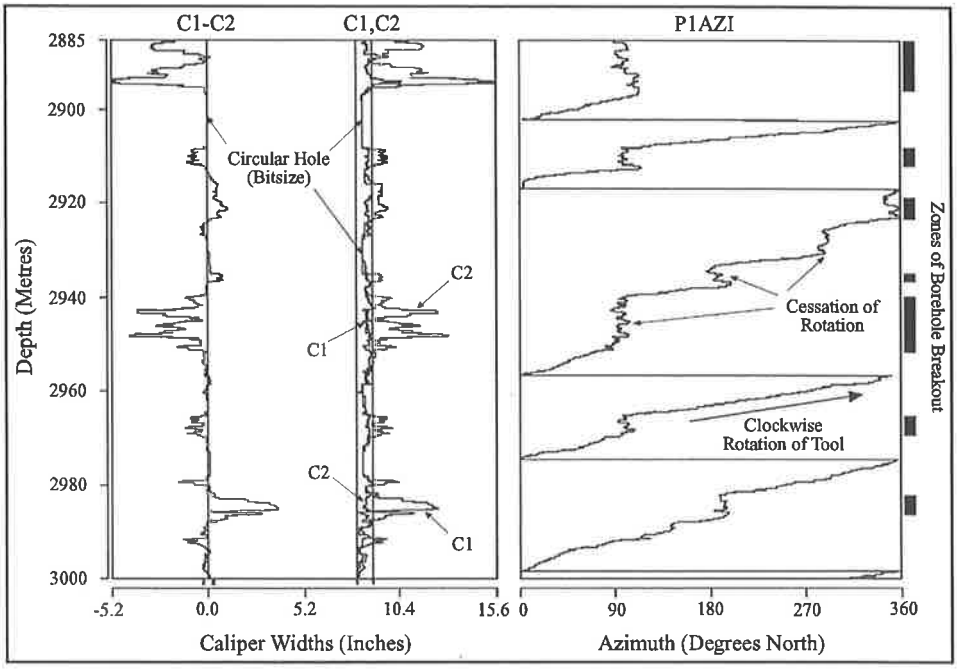

Figure 4.5 Dipmeter log data for Wanaea-2 illustrating borehole breakout identification. See text for discussion.

Figure 4.6 shows a two metre interval of FMS image from the Beluga-1 well in the Bonaparte Basin. Lower resistivity zones appear darker and high resistivity areas appear lighter. Two distinct low resistivity zones are apparent on the second and fourth calipers (180° apart) between 2678.4 and 2677.6 m, oriented approximately 120°N. These zones are interpreted as a borehole breakout. Note the tool rotation at the base of the breakout as two of the pads lock into the elongation. Rotation ceases when the tool is locked into the long axis (2678.1 - 2677.6 m). A narrow, vertical low resistivity feature is also apparent on the first and third caliper images between 2678.8 m and 2677.6 m. This is interpreted as an hydraulic fracture. It is narrower than the breakout, and orthogonal to it. It is clear from the FMS images that hydraulic fractures are not generally associated with elongation of the wellbore cross-section of the typewitnessed by the (S)HDT logs. Hence (S)HDT log interpretation does define breakout and not elongation associated with hydraulic fracturing which would be oriented in the σ_{Hmax} direction (Figure 4.7).

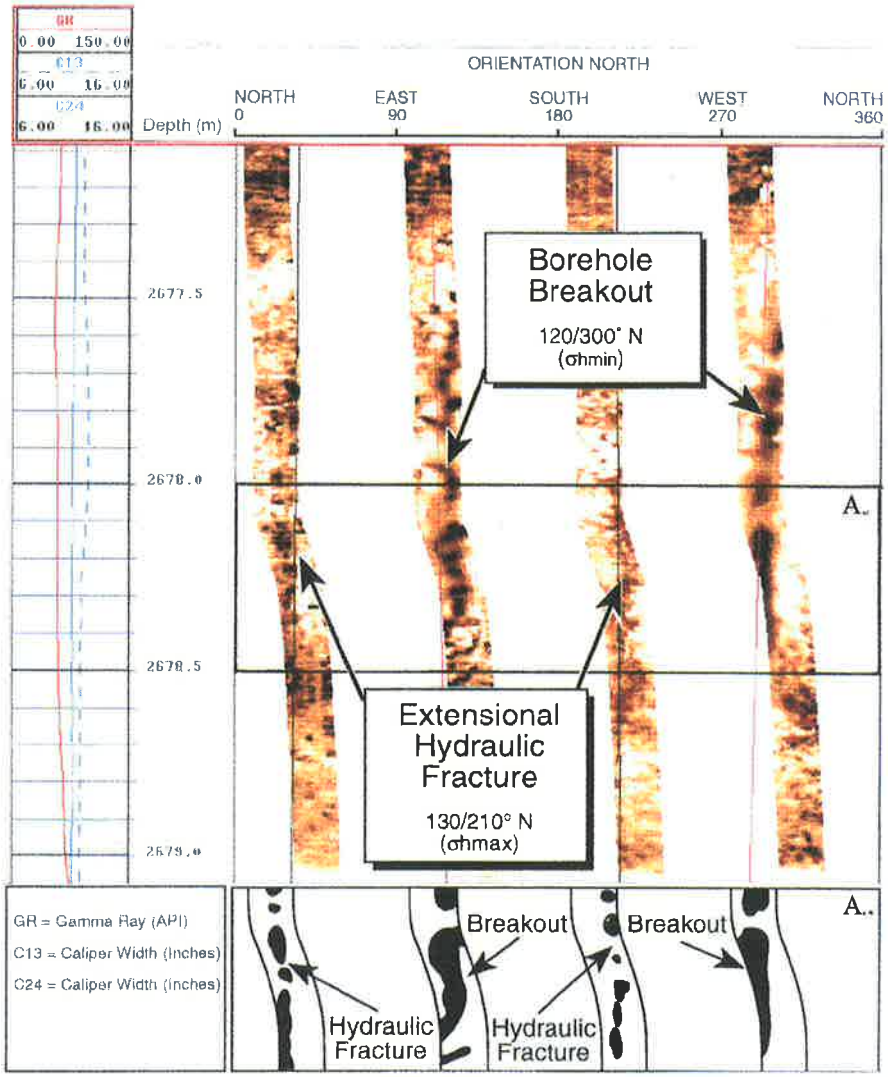

Figure 4.6 Sample interval of FMS electrical wellbore image taken from the Beluga-1 well illustrating both borehole breakouts and hydraulically induced fractures.

Although some FMS resistivity images were analysed in this project, the majority of breakout interpretations were made using four-arm caliper width and orientation data from the HDT, SHDT and FMS logs. The selection criteria for breakout recognition using these data are discussed in the following section.

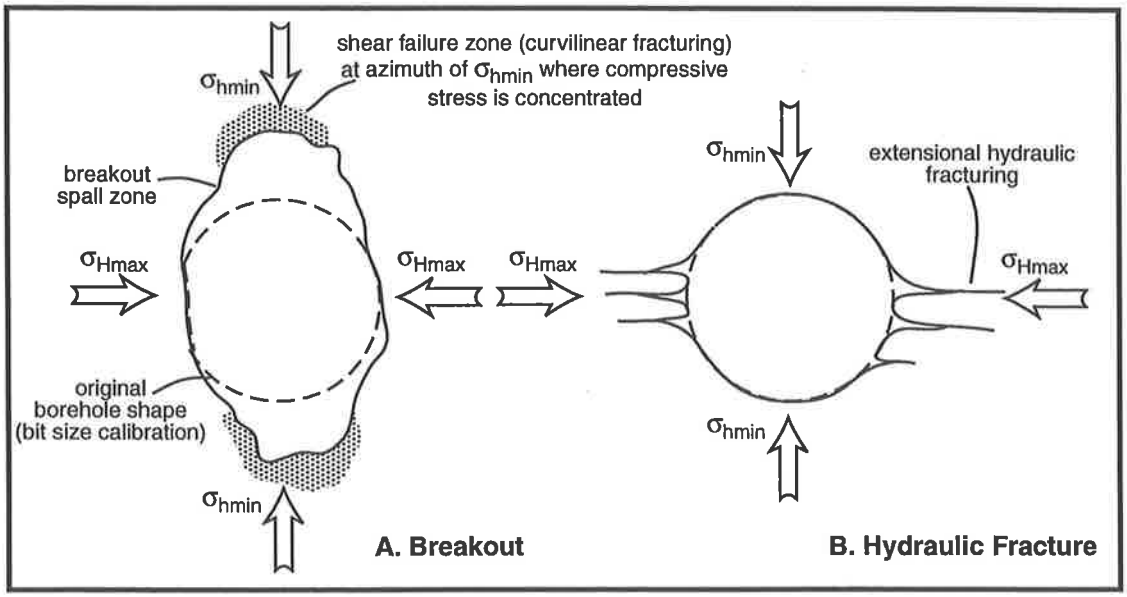

Figure 4.7 Stress induced elongations of the wellbore (after Dart and Zoback, 1989). A comparison of borehole breakout and hydraulic fracture.

4.2.2 Criteria for Identifying Borehole Breakouts

Successful recognition of borehole breakouts using four-arm caliper records requires the distinction between stress-induced elongation of the borehole cross-section (breakouts) and elongations induced by the effects of drilling itself such as mudcakes, washouts and key seats (Plumb and Hickman, 1985; Bell, 1990a; Figure 4.8). The selection criteria applied to ensure drilling induced elongations of the wellbore cross-section are not misidentified as breakouts, are listed in Table 4.1 below and are based on those of Plumb and Hickman (1985) and on the behaviour of the dipmeter/FMS tools as outlined in the previous section.

The majority of data for this study were provided in digital format, allowing numerical application of breakout selection criteria using the program 'Breakout' which was developed in conjunction with the CSIRO Division of Petroleum Resources. The criteria of cessation of tool rotation and prior tool rotation are difficult to apply

manually with absolute consistency. Digital analysis is unbiased, accurate, quick, and facilitates subsequent statistical analysis of breakout orientations.

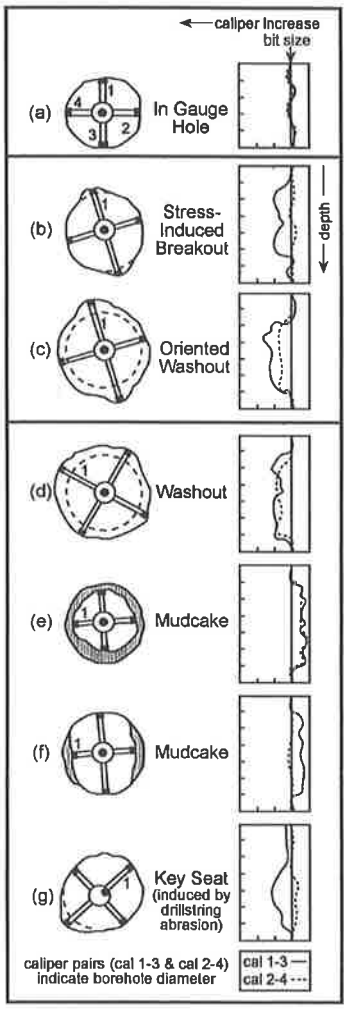

Figure 4.8 Cross-sectional schematics of possible wellbore conditions and their appearance on the four-arm caliper log. The dashed circle on schematics represents bit size, the solid line represents the hole shape, and shading, mudcake. Solid dot indicates centre of the in-gauge hole (after Plumb and Hickman, 1985).

The numerical values of the cessation of rotation and prior rotation rules that were applied (Table 4.1), were selected after extensive trial-and-error, on the basis that they gave results closest to that which manual interpretation yielded (while removing the possibility of bias). However, it was not possible to define a set of numerical rules which replicated manual interpretation exactly (at least using the criteria in Table 4.1). For this reason, in some cases the digitally identified breakouts were subsequently edited manually.

1. The tool rotation stops ±15° in the zone of elongation.
2. The tool must rotate at least 30° in the 30 m immediately beneath the breakout.
3. The smaller caliper width is within 5% of bit size.
4. The difference between the caliper widths is greater than 6 mm.
5. The length of the elongation zone is greater than 1.5 m.
6. The direction of elongation should not coincide ±5° with the high side of the tool if deviation is > 5°.

Table 4.1 Criteria used in the recognition of stress-induced borehole breakout on digital four-arm caliper data using the computer program 'Breakout'.

Digitally identified breakouts tend to be short, with zones that would normally be interpreted as a single breakout zone often picked as several discrete zones. Digital analysis will pick discrete breakouts within a single breakout zone when the larger caliper width just drops below the 6 mm minimum difference between caliper widths (rule 4), or the minimum caliper width just exceeds the 5% tolerance of bit size (rule 3). Such zones were manually edited to form a single breakout. For example, in the Rainier-1 well, a digitally identified breakout at 1600 m has been extended, and several breakouts between approximately 1300-1400 m, have been manually extended and linked (Figure 4.9).

The digital criteria do not permit reverse (anticlockwise) tool rotation prior to a breakout. However, some intervals that satisfied the remaining criteria but were preceded by strong reverse rotation were manually selected as breakouts (eg. prior to the breakout at 2912 m in Figure 4.5).

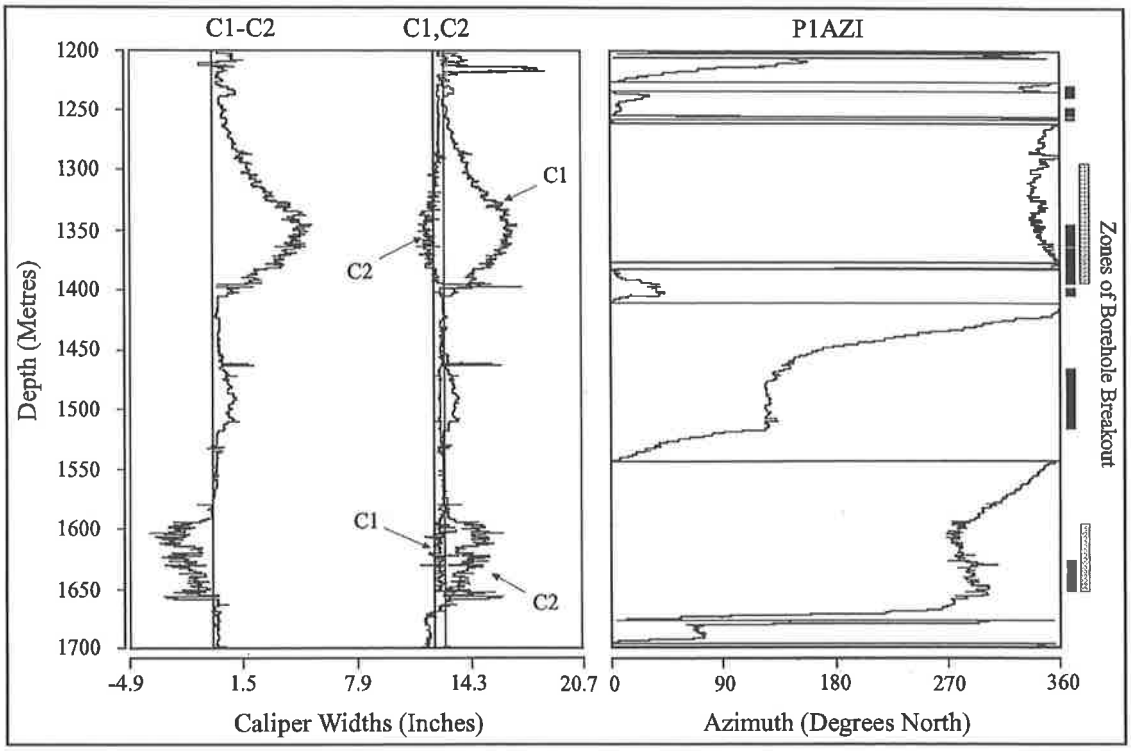

Figure 4.9 A 500 m interval of the Rainier-1 well illustrating the joining (1300 - 1400 m) and extending (1600 - 1650 m) of digitally selected breakouts by manual editing. The manual additions (shown in grey) replace the adjacent original digital breakouts with which they overlap.

If the two orthogonal wellbore diameters are larger than bit size, intervals are generally considered to be washouts and not interpreted as breakouts. However, Bell (1990a) described intervals which exhibited all the characteristics of breakout, but in which minimum caliper size is significantly larger than bit size. These intervals are termed 'oriented washouts' (Figure 4.8). As proposed by Woodland (1988), they are considered to represent an extreme form of breakout. Where oriented washouts showed strongly developed eccentricity (several times more than the normally required 6 mm difference), and satisfied all the rules of breakout identification, except smaller caliper width tolerance with respect to bit size, they were manually selected as true breakouts (Figure 4.10).

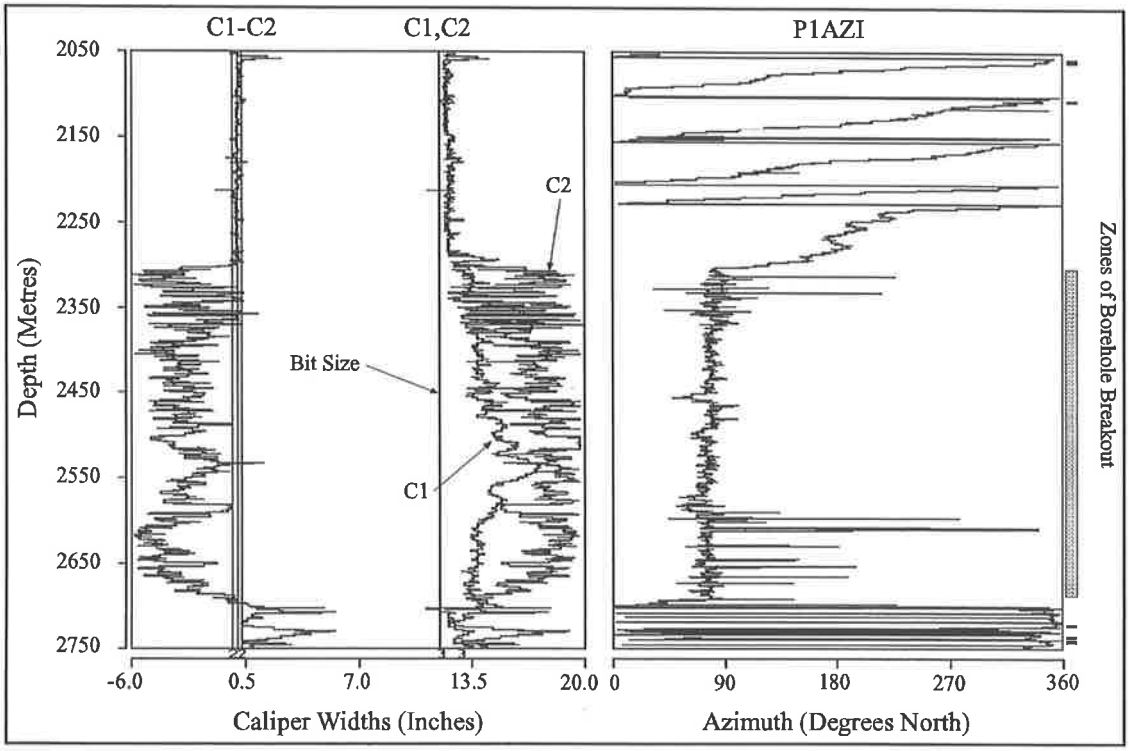

Figure 4.10 A 700 m interval of dipmeter log from the Bambra-1 well illustrating a manually selected oriented washout (shaded grey) to be included with digitally selected breakouts (black). Note that both C1 and C2 caliper diameters are significantly greater than bit size although C2 is greater than C1. The oriented washout is oriented at the same azimuth as the digitally selected breakouts.

4.3 Compilation of Breakout Analyses

Once breakout interpretation has been carried out, the results must be analysed so that an assesment of stress orientation and the accuracy of that orientation can be made. This section describes the magnetic declination correction and statistical analysis applied to the breakout results. Some examples of how the final results are displayed and the criteria by which the resultant stress orientations were quality ranked are presented.

4.3.1 Correction for Magnetic Declination

All breakouts azimuths interpreted in this study have been corrected for magnetic declination. The degree of correction is based on the location of the well in which it

was recognised. Figure 4.11. illustrates the distribution of magnetic declination correction values applied.

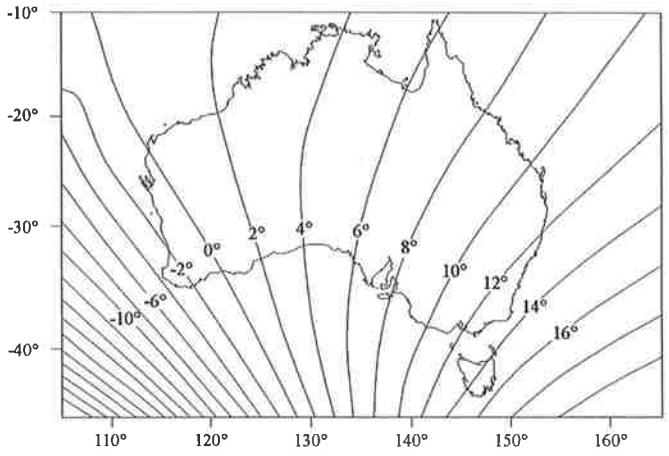

Figure 4.11 AGRF95 magnetic declination with a contour interval of 2° (http://www.agso.gov.au, 1996).

4.3.2 Directional Statistical Analysis

Azimuthal data can be statistically analysed to provide a mean orientation and the variation about that mean. Angular observations such as borehole breakout orientations should not be analysed using linear statistics due to the circular nature of their distribution. For example, the mean of two borehole elongations, one at 020° and one at 160°, would be 090° according to linear statistics, however, by geometrical intuition, the mean ought to be 0° (Figure 4.12). Directional statistical analysis, for the case where the azimuthal range is $(0,\pi)$, as described by Mardia (1972), has been undertaken on the breakout orientations from each well and is summarised below.

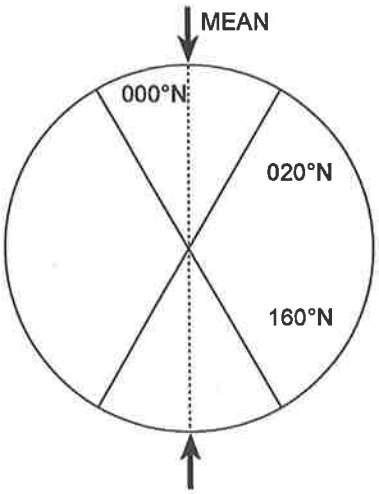

Figure 4.12 An example of directional statistics. The mean of 020° and 160° is 000° not 090° as determined by linear statistics.

The mean azimuth ($\bar{x}$) is given by:

$$\bar{x} = \frac{\bar{x}'}{2} \tag{4.2a}$$

where

$$\bar{x}' = \begin{cases} \bar{x}'' & if \quad S > 0, \quad C > 0, \\ \bar{x}'' + \pi & if \quad C < 0, \\ \bar{x}'' + 2\pi & if \quad S < 0, \quad C > 0 \end{cases} \tag{4.2b}$$

$$\bar{x}'' = \arctan\left(\frac{S}{C}\right), \qquad -\frac{\pi}{2} < \bar{x}' < \frac{\pi}{2} \tag{4.2c}$$

$$C = \frac{1}{n}\sum f_i \cos\theta_i', \tag{4.2d}$$

and

$$S = \frac{1}{n}\sum f_i \sin\theta_i', \tag{4.2e}$$

$\theta' = 2\theta$ (i.e. twice the azimuth of the observation), f is the frequency (weighting) of a given azimuth and n is the total number of observations in the population.

The standard deviation (*sd*), in radians, is given by:

$$sd = \frac{\left(-2\ln R\right)^{1/2}}{2} \tag{4.3a}$$

where

$$R = \left(C^2 + S^2\right)^{1/2}. \tag{4.3b}$$

The application of this statistical method to breakout data allows weighting of individual azimuths according to physical characteristics of breakout zones that impart a greater confidence in their mean orientation. In addition to calculating an un-weighted mean and standard deviation for each well (f = 1 for all azimuths, n = number of breakouts), breakouts were weighted according to length (f = individual breakout length, n = total length of breakouts) as well as borehole eccentricity (f = maximum eccentricity of individual breakout, n = total eccentricity). All statistical calculations were automated within the breakout interpretation software.

4.3.3 Rose Diagrams

Rose diagrams are an excellent tool for graphically viewing statistical trends within directional data. They consist of sectors or petals constructed with their apex at the origin, radius proportional to the class frequency and arc subtending the class interval (Mardia, 1972). The breakout interpretation software used in this project produces separate rose diagrams for the unweighted, length-weighted and eccentricity-weighted breakout azimuths (Figure 4.13). All angles are measured in a clockwise direction from north (0°) at the top of the page. The (0, π) range of breakout data results in symmetrical rose plots.

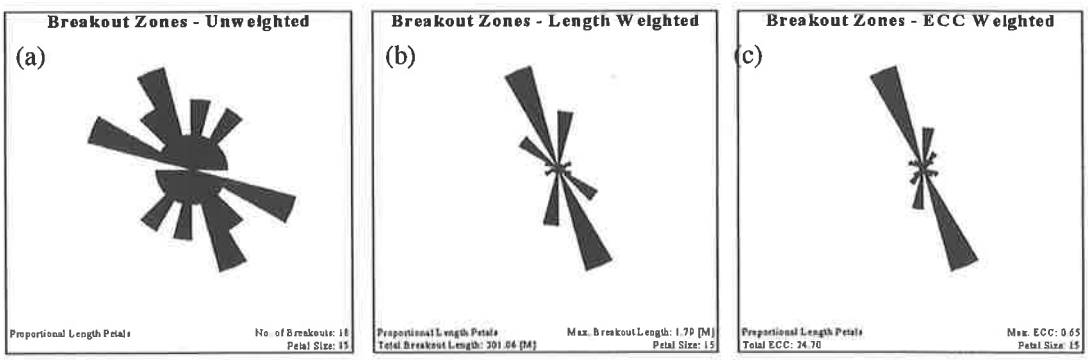

Figure 4.13 Rose diagrams generated by the program 'Breakout' for the Rainier-1 well. ECC is eccentricity.

4.3.4 Stacked Well Plots

In addition to the selection of bona fide breakouts using the criteria of Table 4.1, the program 'Breakout' allows a complementary 'unfiltered' approach to borehole shape analysis. Plotting all the caliper readings at their azimuth for an individual well produces a pseudo cross-section of the well over the entire interval through which the dipmeter was run (Figure 4.14).

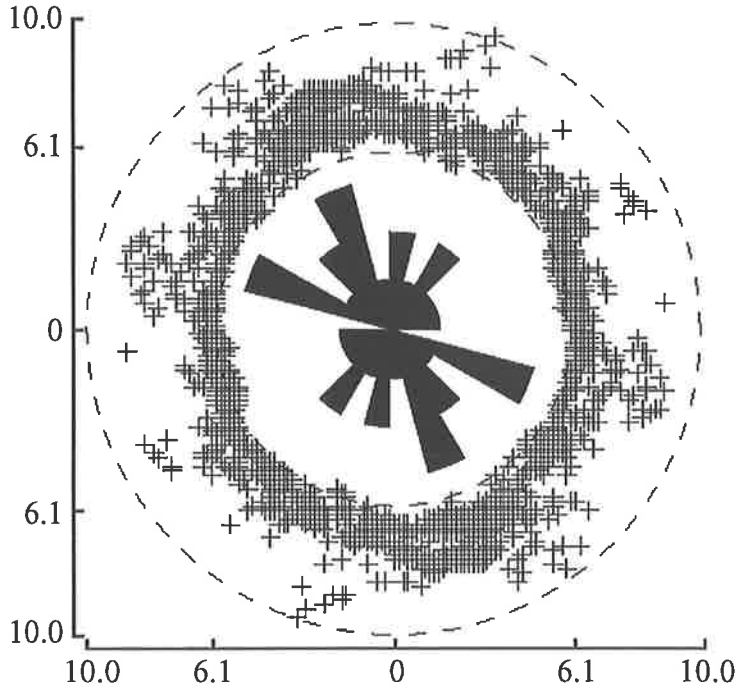

Figure 4.14 Stacked well plot of the Rainier-1 well. Markers (+) denote ratio between caliper widths greater than 0.5 eccentricity. A rose diagram of the unweighted breakout orientations from the same well has also been included, showing that the unfiltered directions of wellbore elongation coincide with breakout directions recognised applying the criteria of Table 4.1.

4.3.5 Quality Ranking

Breakout orientations can vary considerably within individual wells. Where breakout orientation is very variable, little confidence can be placed in the mean azimuth as an indication of σ_{hmin}. Standard deviation of breakout azimuth, total breakout length and the number of breakouts are used to quantify the relative reliability of the mean breakout azimuth for an individual well, and hence the quality of the inferred

contemporary stress direction. The quality ranking scheme used in this project is that of the World Stress Map project (Zoback, 1992). It is summarised in Table 4.2.

QUALITY RATING				
A	B	C	D	E
$sd \leq 12°$	$sd \leq 20°$	$sd < 25°$	$sd \geq 25°$	$sd > 40°$
and either	and either	and either	or	Well in which no reliable breakouts detected.
$N \geq 10$ or $L > 300$ m.	$N \geq 6$ or $L > 100$ m.	$N \geq 4$ or $L > 30$ m.	$N \geq 25°$ or $L < 30$ m.	Extreme scatter of orientations, no significant mean determined.

Table 4.2 Quality ranking system for stress orientations determined from borehole breakout analysis (Zoback, 1992). *sd* is standard deviation, N is the total number of breakouts within the well and L is the total length of breakouts within the well.

Chapter 5

The Contemporary Stress Field of the North West Shelf

5.1 Introduction

The results of the analyses undertaken to determine the orientation and magnitude of the contemporary stress field of the North West Shelf of Australia are presented in this chapter. Although important observations and trends in the data are mentioned here, their implications are discussed in Chapters 6 and 7.

5.2 Contemporary Stress Orientations in the North West Shelf of Australia

5.2.1 The Regional Orientation of the Contemporary Stress Field

The North West Shelf stress orientation map is shown in Figure 5.1. Tables 5.1 and 5.2 summarise mean stress orientations for each well in the Carnarvon and Bonaparte Basins respectively and Appendices B and C give complete listings of breakouts identified in each well and summary rose diagrams. In the Carnarvon Basin, 625 breakouts in 42 wells covering a total depth of 7.7 km indicate a mean σ_{Hmax} direction of 090°N-100°N. In the Bonaparte Basin, 616 breakouts in 46 wells covering a total depth of 6.8 km indicate a mean σ_{Hmax} direction of 055°N-060°N. These mean orientations reflect first-order, regional stress patterns as defined by Zoback (1992). It is clear from Figures 5.1 and 5.2 that the 40° rotation of mean σ_{Hmax} direction between the Carnarvon and Bonaparte Basins is significant.

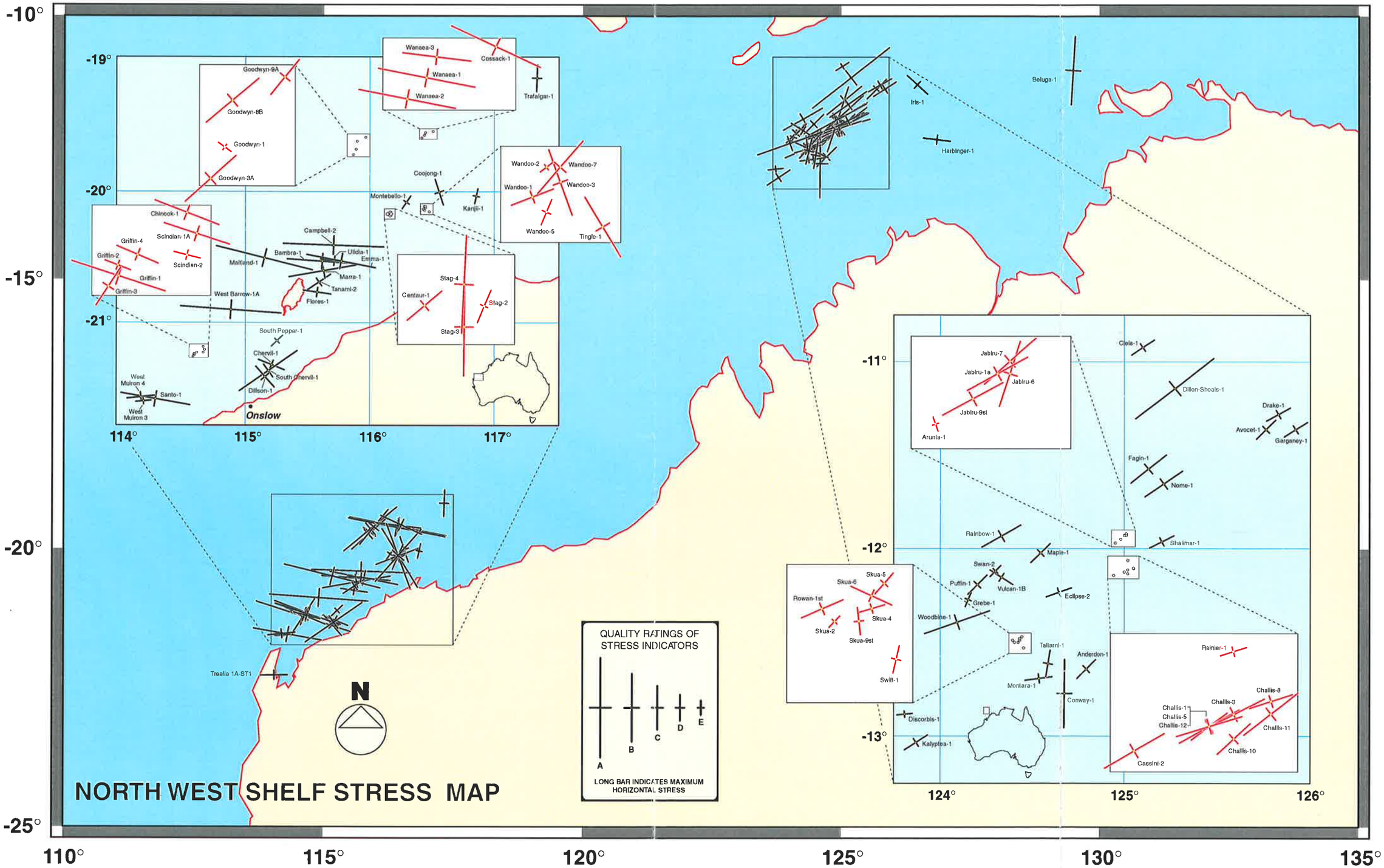

Figure 5.1 Maximum horizontal stress orientations (σ_{Hmax}) inferred from borehole breakouts in the Australian North West Continental Shelf. The long axes of crosses indicate the best quality ranked (A>B>C>D>E) unweighted, length weighted or eccentricity weighted, mean σ_{Hmax} direction in an individual well following Zoback's (1992) classification (Tables 5.1 and 5.2; Section 4.3.5).

Well	Location		Depth Interval (m)		N	Un-weighted			Length-weighted				Ecc-weighted		
	Lat	Long	Top	Bottom		Azimuth	SD	Q	ΣL(m)	Azimuth	SD	Q	Azimuth	SD	Q
Bambra 1	20°32'	115°38'	777	3673	39	163	28	D	1518.36	004	19	B	164	27	D
Campbell 2	20°25'	115°43'	1137	2796	10	164	19	B	1075.33	002	9	A	174	16	B
Chervil 1	21°18'	115°14'	861	1754	6	029	36	D	33.73	015	31	D	022	29	D
Chinook 1	21°10'	114°41'	1723	3403	43	022	25	D	255.38	020	19	B	021	14	B
Coojong 1	20°01'	116°33'	497	805	25	076	36	D	75.74	072	33	D	078	33	D
Cossack 1	19°34'	116°30'	2819	3035	5	022	8	A	47.70	026	6	A	025	5	A
Dillson 1	21°23'	115°11'	1601	2454	2	048	2	D	9.10	049	1	D	048	2	D
Emma 1	20°32'	115°47'	1558	2351	9	049	46	E	642.33	011	14	B	011	21	C
Flores 1	20°46'	115°35'	857	2126	20	003	40	D	240.65	003	32	D	008	30	D
Goodwyn 1	19°41'	115°53'	1119	3535	30	023	55	E	126.80	018	44	E	035	42	E
Goodwyn 3A	19°44'	115°52'	410	993	5	147	29	D	19.39	138	20	B	155	26	D
Goodwyn 8B	19°38'	115°54'	2596	3198	6	132	24	C	54.82	140	14	B	137	21	C
Goodwyn 9A	19°36'	115°58'	2630	3401	4	129	2	C	17.83	129	2	C	129	2	C
Griffin 1	21°14'	114°37'	2508	3378	29	017	22	C	208.50	017	13	B	018	11	A
Griffin 2	21°13'	114°37'	2000	2849	22	018	43	E	137.25	024	39	D	021	27	D
Griffin 3	21°14'	114°37'	2425	2837	5	121	19	C	48.88	123	14	C	123	19	C
Griffin 4	21°13'	114°38'	1779	2310	2	021	8	C	80.00	023	7	C	021	7	C
Kanji 1	20°02'	116°50'	342	1294	33	102	53	E	120.40	017	57	E	023	62	E
Maitland 1	20°30'	115°10'	672	1503	11	018	17	B	51.63	015	10	A	014	9	A
Marra 1	20°36'	115°38'	1302	2090	28	166	21	C	162.77	170	17	B	172	17	B
Montebello 1	20°05'	116°17'	1675	2820	36	087	48	E	158.74	124	47	E	090	48	E
Santo 1	21°33'	114°19'	875	1877	6	011	3	B	119.48	010	2	B	011	3	B
Scindian 1A	21°11'	114°42'	2324	3140	46	017	40	D	302.88	020	25	D	018	19	B
Scindian 2	21°13'	114°41'	1562	2770	8	024	38	D	91.00	020	29	D	014	27	D
South Chervil 1	21°20'	115°12'	792	2292	7	166	34	D	243.52	145	19	B	157	27	D
South Pepper 1	21°07'	115°16'	1842	2552	1	136	0	E	8.94	136	0	E	136	0	E
Tanami 2	20°41'	115°36'	1222	2453	29	145	29	D	314.70	146	29	D	146	28	D
Tingle 1	20°10'	116°28'	322	1056	14	056	30	D	116.74	059	20	B	054	24	C
Trafalgar 1	19°10'	117°19'	2147	2750	2	112	33	D	33.81	092	25	D	095	27	D
Trealla 1A	22°17'	114°04'	1308	1494	9	136	45	E	23.94	147	40	D	179	34	D
Ulidia 1	20°31'	115°43'	1086	2272	9	001	47	E	228.30	012	28	D	007	26	D
Wanaea 1	19°35'	116°26'	2805	3269	21	010	16	B	294.90	004	8	A	011	7	A
Wanaea 2	19°37'	116°25'	2885	3003	11	010	8	A	36.88	009	8	A	011	7	A
Wanaea 3	19°34'	116°26'	2812	2971	5	007	2	B	18.90	009	2	B	008	3	B
Wandoo 1	20°08'	116°25'	314	1582	14	142	35	D	185.47	145	33	D	159	23	C
Wandoo 2	20°07'	116°26'	515	1113	1	143	0	E	7.77	143	0	E	143	0	E
Wandoo 3	20°08'	116°26'	390	797	8	044	22	C	85.04	070	20	B	049	25	D
Wandoo 5	20°09'	116°26'	318	801	15	116	35	D	40.54	115	37	D	113	29	D
Wandoo 7	20°07'	116°26'	378	1001	13	121	25	D	170.23	131	16	B	121	18	B
West Barrow 1A	20°53'	114°55'	2497	3238	32	001	16	B	313.01	004	9	A	003	10	A
West Muiron 3	21°34'	114°13'	829	1086	1	175	0	E	2.00	175	0	E	175	0	E
West Muiron 4	21°32'	114°12'	798	1551	3	045	39	D	14.00	174	33	D	000	39	D
Carnarvon Basin Region					625	003	46		7737.36	003	29		008	32	

Table 5.1 Summary of borehole breakout results for the Carnarvon Basin. Lat and Long are the latitude and longitude of the well locations respectively, and depth interval is the range of depths for which four-arm dipmeter log data were analysed. N is the total number and ΣL the total length of breakouts in the well. Mean and SD are the mean azimuth (000°-360°) of breakouts in the well, and their standard deviation in degrees, as determined by directional statistical analysis. Q is the quality rating of the mean azimuth (Section 4.3.5), length is the depth interval over which the breakout occurs and eccentricity is the difference between two caliper width readings.

5.2.2 Comparison with the World Stress Map

The orientation of σ_{Hmax} on the North West Shelf of Australia taken from the limited available data for the area from the World Stress Map (Zoback, 1992; Figure 5.3), correlates reasonably well with the data presented within this thesis. Both datasets reveal a NE-SW σ_{Hmax} direction in the Bonaparte Basin, however, the limited results from the Carnarvon Basin on the World Stress Map do not agree with the regional

trend revealed by this study. Four of the five stress indicators from the World Stress Map in the Carnarvon Basin show NW-SE σ_{Hmax} directions, inconsistent with the regional E-W trend presented here.

Well	Location		Depth Interval (m)		N	Un-weighted			Length-weighted				Ecc-weighted		
	Lat	Long	Top	Bottom		Azimuth	SD	Q	ΣL(m)	Azimuth	SD	Q	Azimuth	SD	Q
Anderdon 1*	12°38'	124°47'	2456	2906	7	142	36	D	63.00	136	30	D	130	30	D
Arunta 1	11°58'	124°57'	1757	2496	11	092	57	E	66.36	070	46	E	100	56	E
Avocet 2	11°22'	125°46'	1095	1999	25	131	38	D	75.02	135	36	D	135	30	D
Beluga 1	11°00'	129°33'	2430	3105	6	092	24	C	30.86	099	16	B	093	12	B
Cassini 2	12°08'	124°56'	1197	2183	6	146	23	C	164.00	149	10	B	147	12	B
Challis 1	12°07'	125°00'	1189	1950	8	167	30	D	45.00	169	30	D	143	21	C
Challis 3	12°07'	125°01'	1199	1684	6	155	43	E	36.00	155	31	D	153	17	B
Challis 5	12°07'	125°00'	1135	1588	12	161	27	D	64.00	163	19	B	159	19	B
Challis 8	12°07'	125°00'	1102	1686	5	157	10	C	96.00	162	8	C	156	10	C
Challis 10	12°08'	125°01'	1600	1950	2	137	1	C	34.42	137	1	C	137	1	C
Challis 11	12°07'	125°03'	1094	1740	8	150	30	D	180.00	142	11	B	155	24	C
Challis 12	12°07'	125°00'	1124	1731	11	153	22	C	92.00	152	20	B	151	13	B
Cleia 1	10°55'	125°06'	2845	3799	40	152	44	E	331.39	138	45	E	146	40	D
Conway 1	12°46'	124°40'	1995	2315	7	105	19	B	101.23	090	17	B	109	19	B
Dillon Shoals 1*	11°08'	125°16'	1089	3958	12	141	23	C	155.40	142	12	A	143	20	B
Discorbis 1	12°53'	123°49'	3350	3600	44	177	56	E	113.02	172	54	E	175	48	E
Drake 1	11°17'	125°50'	1398	2382	11	139	31	D	218.07	151	25	D	146	29	D
Eclipse 2*	12°14'	124°38'	1957	2922	15	175	45	E	368.60	175	37	D	160	29	D
Fagin 1	11°34'	125°08'	2196	2887	19	147	29	D	189.34	141	23	C	140	23	C
Garganey 1st1	11°22'	125°55'	1170	2483	42	111	49	E	321.54	148	30	D	129	48	E
Grebe 1*	12°16'	124°09'	1219	2969	1	113	0	E	60.40	113	0	E	113	0	E
Harbinger 1	12°19'	126°55'	1943	2186	13	171	41	E	44.46	007	37	D	009	39	D
Iris 1	11°17'	126°33'	3431	3904	6	046	48	E	10.86	043	40	D	045	47	E
Jabiru 1A	11°56'	125°00'	1219	3222	23	145	35	D	271.00	151	19	B	149	23	C
Jabiru 6	11°56'	125°01'	1417	1818	1	108	0	E	184.00	108	0	E	108	0	E
Jabiru 7	11°55'	125°01'	1351	1794	7	138	17	B	44.00	136	20	B	127	25	D
Jabiru 9st	11°57'	124°59'	1343	1826	5	150	15	B	103.00	151	8	B	148	10	B
Kalyptea 1	13°02'	123°52'	1976	3464	68	133	42	E	387.66	150	36	D	146	34	D
Maple 1	12°01'	124°32'	2800	3800	25	129	43	E	217.10	136	38	D	138	40	D
Montara 1	12°41'	124°32'	2409	3299	18	001	48	E	130.17	004	56	E	173	39	D
Nome 1*	11°39'	125°13'	1230	1846	8	146	27	D	50.20	120	54	E	145	22	C
Puffin 1*	12°11'	124°12'	1091	2950	5	134	29	D	37.10	135	34	D	134	31	D
Rainbow 1*	11°56'	124°20'	1674	2701	18	142	31	D	306.30	151	22	C	150	22	C
Rainier 1	12°04'	125°01'	1198	2395	18	164	54	E	301.06	163	32	D	172	32	D
Rowan 1st	12°29'	124°23'	2497	3345	30	161	24	C	188.12	157	23	C	159	28	D
Shalimar 1	11°58'	125°12'	2098	2763	12	034	46	E	82.60	153	39	D	177	49	E
Skua 2*	12°30'	124°24'	1929	2600	10	134	49	E	151.10	105	56	E	112	65	E
Skua 4	12°29'	124°26'	2296	2411	2	139	29	D	6.00	151	26	D	163	13	D
Skua 5	12°28'	124°26'	2324	2402	2	143	17	D	21.00	134	14	D	132	13	D
Skua 6	12°29'	124°26'	1391	2835	4	141	33	D	65.00	025	21	C	170	46	E
Skua 9st	12°30'	124°25'	1957	2551	3	093	18	D	30.00	083	11	D	091	17	D
Swan 2*	12°07'	124°18'	3200	4060	9	135	43	E	315.70	169	46	E	143	46	E
Swift 1*	12°32'	124°27'	1450	2792	2	113	36	D	5.10	110	36	D	104	35	D
Taltarni 1	12°37'	124°35'	2481	3366	15	074	54	E	96.24	104	46	E	099	39	D
Vulcan 1B*	12°09'	124°20'	1388	3315	9	050	42	E	671.10	032	40	D	040	51	E
Woodbine 1*	12°23'	124°05'	1823	3294	5	171	40	D	264.60	160	13	B	164	24	C
Bonaparte Basin Region					616	145	44		6789.15	150	39		148	37	

Table 5.2 Summary of borehole breakout results for the Bonaparte Basin. Lat and Long are the latitude and longitude of the well locations respectively, and depth interval is the range of depths for which four-arm dipmeter log data were analysed. N is the total number and ΣL the total length of breakouts in the well. Mean and SD are the mean azimuth (000'-360') of breakouts in the well, and their standard deviation in degrees, as determined by directional statistical analysis. Q is the quality rating of the mean azimuth (Section 4.3.5), length is the depth interval over which the breakout occurs and eccentricity is the difference between two caliper width readings. * No digital data available, records analysed only manually.

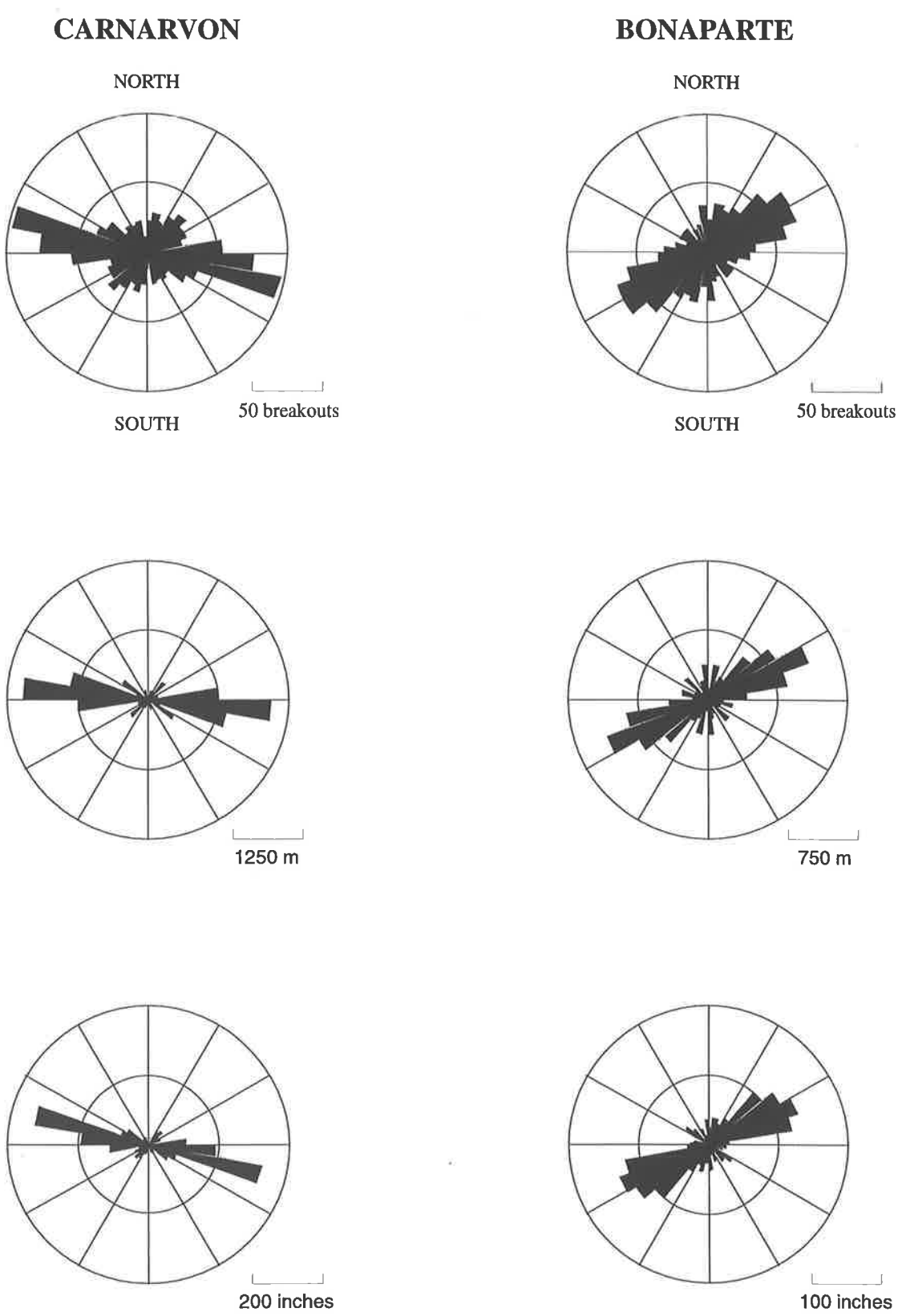

Figure 5.2 Rose diagrams summarizing maximum horizontal stress (σ_{Hmax}) directions inferred from borehole breakouts in the Carnarvon and Bonaparte Basins. The top pair of rose diagrams illustrates the unweighted frequency of breakout azimuths in the two areas, and the lower two pairs of rose diagrams, illustrate length- and eccentricity-weighted frequencies of breakout azimuths respectively.

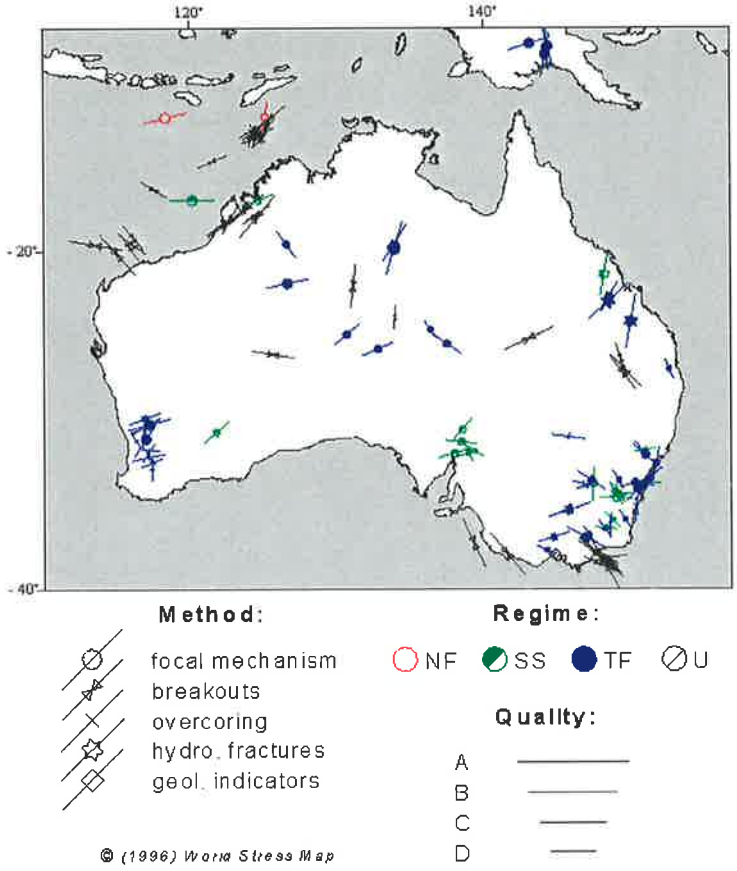

Figure 5.3 Stress indicators taken from the World Stress Map (Zoback, 1992). Long axes indicate σ_{Hmax} direction, NF is normal faulting, SS is strike-slip, TF is thrust faulting and U is unknown. The quality ranking scheme is the same as used in this thesis (Section 4.3.5).

Combining the results of this study with those of the World Stress Map between the Canning Basin and Papua New Guinea region, provides a coherent picture of the regional, first-order stress orientation along the northern Australian margin (Figure 5.4). Breakout data from six wells in the onshore Canning Basin show a consistent 050° σ_{Hmax} direction, sub-parallel to that in the Bonaparte Basin. In New Guinea, σ_{Hmax} directions inferred from earthquake focal mechanisms indicate that the mean σ_{Hmax} direction is approximately 050°N. Hence, regional σ_{Hmax} direction is consistently 050°-060°N from the onshore Canning Basin to New Guinea, over 2000 km of the northern Australian margin. Westward from the onshore Canning Basin, σ_{Hmax} rotates approximately 40° to 090°-100° N in the Carnarvon Basin, over 700 km.

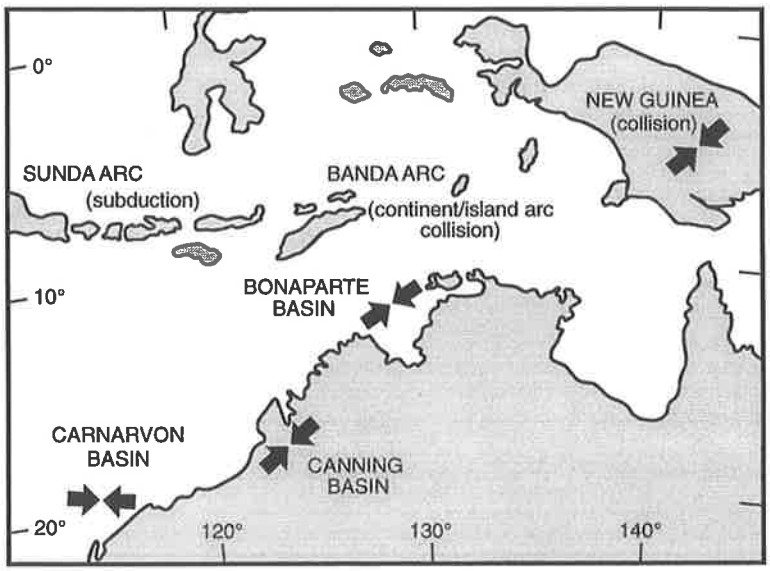

Figure 5.4 Summary of mean σ_{Hmax} orientations across the northern Australian margin using the results of this study and extant data from the World Stress Map (Zoback, 1992).

5.2.3 Variation of Stress Orientations within the Carnarvon and Bonaparte Basins

Stress indicators within the Bonaparte Basin are consistently oriented parallel with the mean σ_{Hmax} for the basin. Stress indicators within the Carnarvon Basin show consistent σ_{Hmax} orientations that deviate from the basin mean (Figure 5.1; Figure 5.2). Locations such as Goodwyn, South Chervil and Wandoo exhibit a secondary trend striking approximately 030°N-060°N as opposed to the regional 090°N-100°N mean for the Carnarvon Basin (Figure 5.1).

The variation of stress orientation across the Carnarvon Basin was characterised by calculating the mean σ_{Hmax} for groupings of adjacent wells (Table 5.3). The group means have been superimposed on a simplified structural elements map of the Carnarvon Basin (Figure 5.5)

Well	Location		Depth Interval (m)		N	Un-weighted			Length-weighted				Ecc-weighted		
	Lat	Long	Top	Bottom		Azimuth	SD	Q	ΣL(m)	Azimuth	SD	Q	Azimuth	SD	Q
Bambra 1	20°32'	115°38'	777	3673	39	073	28	D	1518.36	094	19	B	074	27	D
Campbell 2	20°25'	115°43'	1137	2796	10	074	19	B	1075.33	092	9	A	084	16	B
Emma 1	20°32'	115°47'	1558	2351	9	139	46	E	642.33	101	14	B	101	21	C
Flores 1	20°46'	115°35'	857	2126	20	093	40	D	240.65	093	32	D	098	30	D
Marra 1	20°36'	115°38'	1302	2090	28	076	21	C	162.77	080	17	B	082	17	B
Tanami 2	20°41'	115°36'	1222	2453	29	055	29	D	314.70	056	29	D	056	28	D
Ulidia 1	20°31'	115°43'	1086	2272	9	091	47	E	228.30	102	28	D	097	26	D
Bambra Group					144	075	33	D	4182.44	093	20	B	078	29	D
Chervil 1	21°18'	115°14'	861	1754	6	119	36	D	33.73	105	31	D	112	29	D
Dillson 1	21°23'	115°11'	1601	2454	2	138	2	D	9.10	139	1	D	138	2	D
South Chervil 1	21°20'	115°12'	792	2292	7	076	34	D	243.52	055	19	B	067	27	D
South Pepper 1	21°07'	115°16'	1842	2552	1	046	0	E	8.94	046	0	E	046	0	E
Chervil Group					16	101	45	E	295.30	058	26	D	080	37	D
Chinook 1	21°10'	114°41'	1723	3403	43	112	25	D	255.38	110	19	B	111	14	B
Griffin 1	21°14'	114°37'	2508	3378	29	107	22	C	208.50	107	13	B	108	11	A
Griffin 2	21°13'	114°37'	2000	2849	22	108	43	E	137.25	114	39	D	111	27	D
Griffin 3	21°14'	114°37'	2425	2837	5	031	19	C	48.88	033	14	C	033	19	C
Griffin 4	21°13'	114°38'	1779	2310	2	111	8	C	80.00	113	7	C	111	7	C
Scindian 1A	21°11'	114°42'	2324	3140	46	107	40	D	302.88	110	25	D	108	19	B
Scindian 2	21°13'	114°41'	1562	2770	8	114	38	D	91.00	110	29	D	104	27	D
Griffin Group					155	110	34	D	1123.88	110	26	D	110	19	B
Goodwyn 1	19°41'	115°53'	1119	3535	30	113	55	E	126.80	108	44	E	125	42	E
Goodwyn 3A	19°44'	115°52'	410	993	5	057	29	D	19.39	048	20	B	065	26	D
Goodwyn 8B	19°38'	115°54'	2596	3198	6	042	24	C	54.82	050	14	B	047	21	C
Goodwyn 9A	19°36'	115°58'	2630	3401	4	039	2	C	17.83	039	2	C	039	2	C
Goodwyn Group					45	057	53	E	218.83	062	43	E	082	55	E
Cossack 1	19°34'	116°30'	2819	3035	5	112	8	A	47.70	116	6	A	115	5	A
Wanaea 1	19°35'	116°26'	2805	3269	21	100	16	B	294.90	094	8	A	101	7	A
Wanaea 2	19°37'	116°25'	2885	3003	11	100	8	A	36.88	099	8	A	101	7	A
Wanaea 3	19°34'	116°26'	2812	2971	5	097	2	B	18.90	099	2	B	098	3	B
Wanaea Group					42	101	13	B	398.37	097	10	A	102	8	A
Tingle 1	20°10'	116°28'	322	1056	14	146	30	D	116.74	149	20	B	144	24	C
Wandoo 1	20°08'	116°25'	314	1582	14	052	35	D	185.47	055	33	D	069	23	C
Wandoo 2	20°07'	116°26'	515	1113	1	053	0	E	7.77	053	0	E	053	0	E
Wandoo 3	20°08'	116°26'	390	797	8	134	22	C	85.04	160	20	B	139	25	D
Wandoo 5	20°09'	116°26'	318	801	15	026	35	D	40.54	025	37	D	023	29	D
Wandoo 7	20°07'	116°26'	378	1001	13	031	25	D	170.23	041	16	B	031	18	B
Wandoo Group					65	019	52	E	605.79	028	47	E	024	50	E
Santo 1	21°33'	114°19'	875	1877	6	101	3	B	119.48	100	2	B	101	3	B
West Muiron 3	21°34'	114°13'	829	1086	1	085	0	E	2.00	085	0	E	085	0	E
West Muiron 4	21°32'	114°12'	798	1551	3	135	39	D	14.00	084	33	D	090	39	D
West Muiron Group					10	103	23	C	135.48	099	10	A	100	11	A

Table 5.3 Mean σ_{Hmax} orientations for groupings of adjacent wells in the Carnarvon Basin (Figures 5.1 & 5.3). Lat and Long are the latitude and longitude of the well locations respectively, and depth interval is the range of depths for which four-arm dipmeter log data were analysed. N is the total number and ΣL the total length of breakouts in the well. Mean and SD are the mean azimuth (000°-360°) of calculated from breakouts in the well, and their standard deviation in degrees, as determined by directional statistical analysis. Q is the quality rating of the mean azimuth (Section 4.3.5), length is the depth interval over which the breakout occurs and eccentricity is the difference between two caliper width readings.

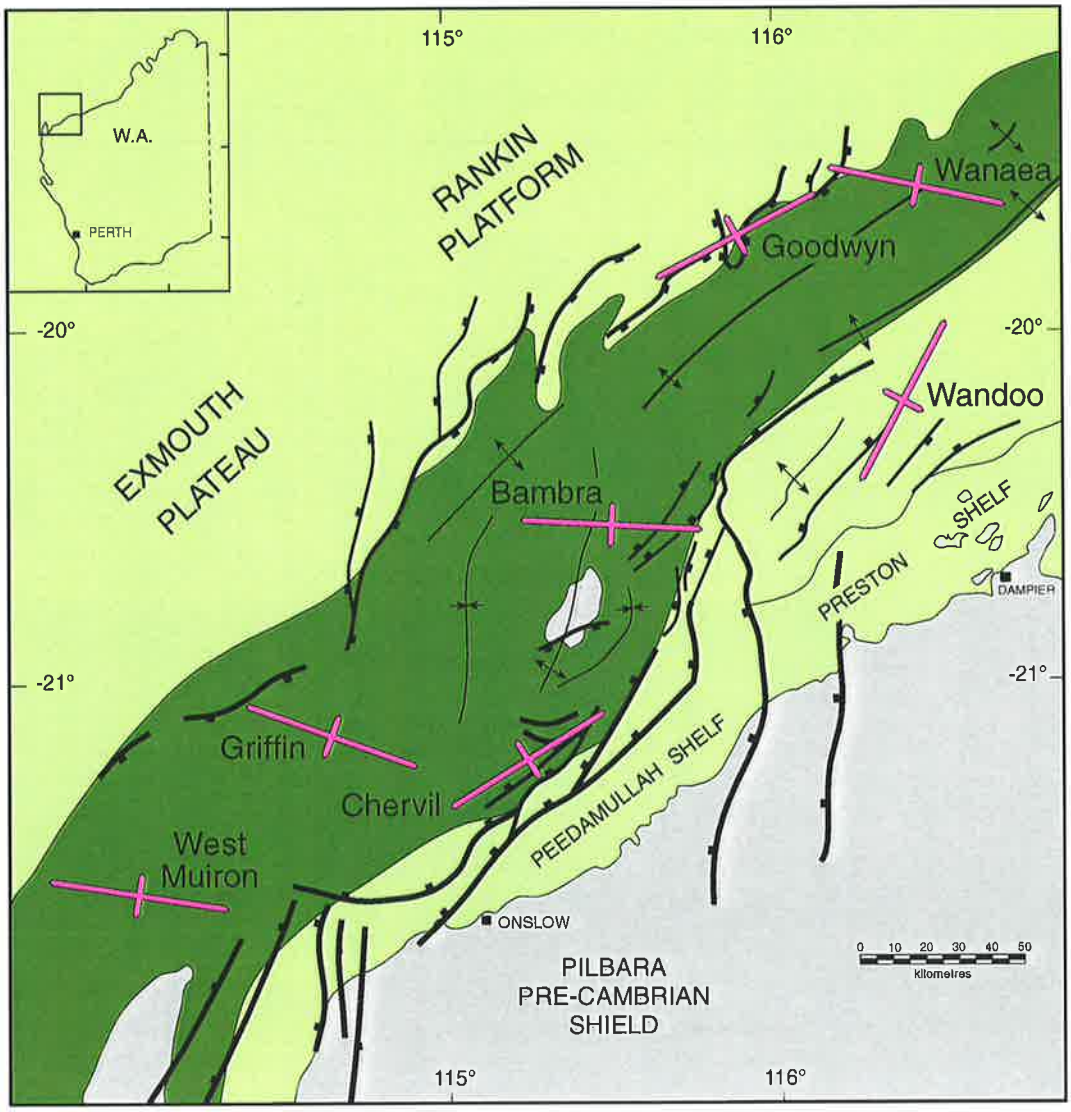

Figure 5.5 Group mean σ_{Hmax} orientations and structural elements of the Carnarvon Basin (after Howell, 1988; Barber, 1994). Long axes of crosses indicate best quality ranked statistical mean σ_{Hmax} direction (Table 5.3). Yellow and green areas represent regional highs and basin depocentres respectively.

The most striking observation from Figure 5.5 is that σ_{Hmax} is a consistently oriented E-W within the relatively structureless depocentre of the Barrow and Dampier Sub-basins, and oriented NE-SW in the more structurally complex basin margins. Statistical analyses of breakout orientations from the seven wells indicate that wells with the higher quality ratings (A and B) are more likely to occur in the centre of the Barrow Dampier Sub-basin than on the sub-basin margins. Nearly half of the wells ranked C, D and E are located on the basin margins given they are comprised of over a third of all wells analysed. This trend is also reflected in the best quality ranked σ_{Hmax}

orientations (unweighted, length-weighted or eccentricity-weighted) or the seven well groupings in the basin (Table 5.3; Figure 5.5). They show considerably higher ratings for the groups within the basin centre (B, B, A and A) compared to those on the basin flanks (E, E, and D). Note that the best quality ranked σ_{Hmax} values are used below unless mentioned otherwise. The distribution of breakout azimuths within each group are described below and illustrated in Figure 5.6.

The Bambra Group consists of 144 breakouts interpreted from seven wells that together have an approximately E-W mean σ_{Hmax} direction. Breakout azimuths within this group are scattered to a certain degree, however the majority are aligned N-S. A number of breakouts are not aligned with the well mean and the different weighted means and their quality ratings reflect this. The unweighted and eccentricity-weighted mean σ_{Hmax} directions are D quality and oriented 075°N and 093°N respectively, and the length-weighted σ_{Hmax} orientation is B quality and oriented 078°N.

The Chervil Group consists of 16 breakouts interpreted from four wells, comprising a mean σ_{Hmax} direction oriented approximately NE. Although this group does not display any obvious trends, there are clusters of breakouts at three separate azimuths, 000-020°N, 140-160°N and 040-060°N. This is reflected by low quality, mean σ_{Hmax} orientations for the group.

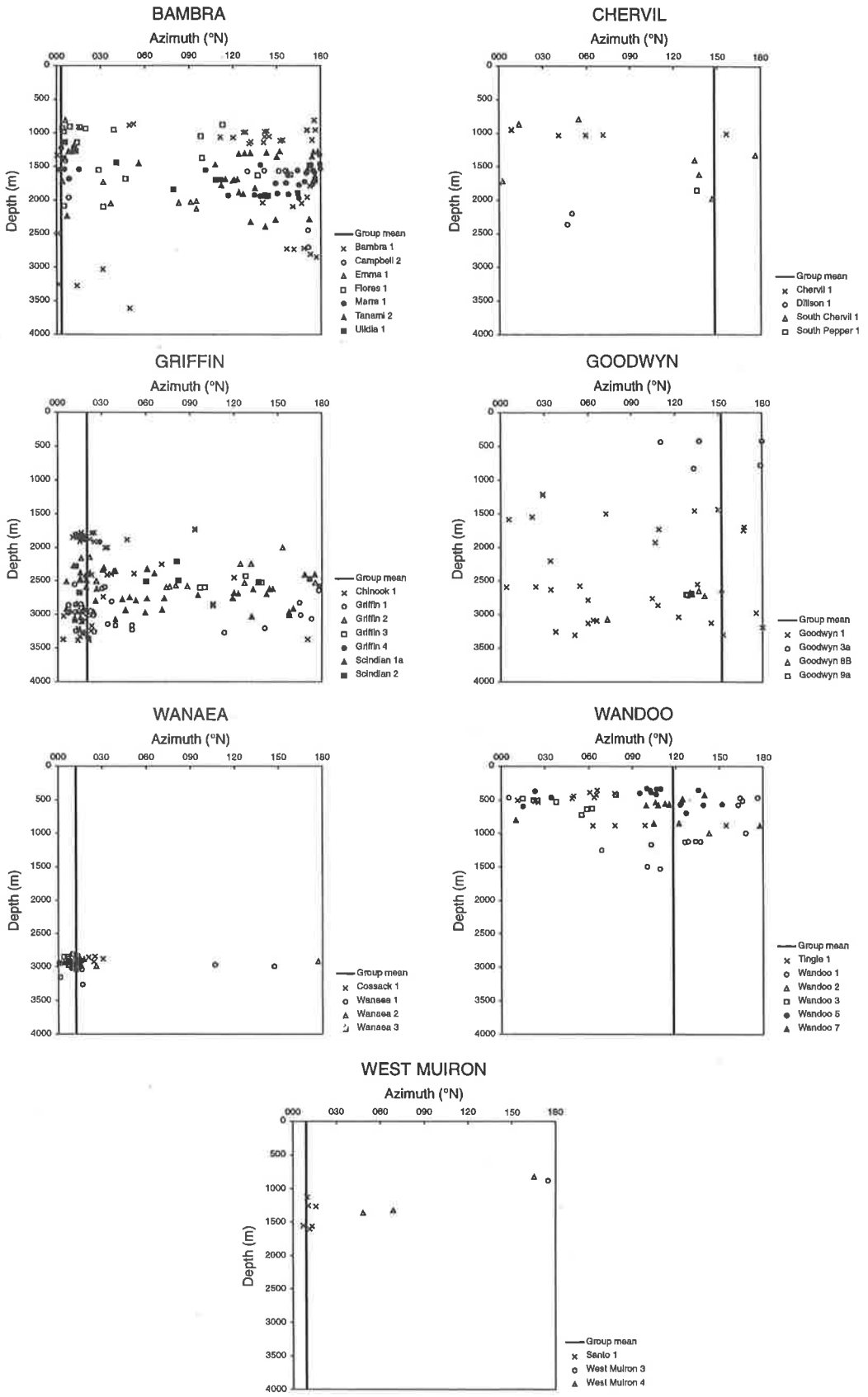

Figure 5.6 Distribution of breakout azimuths with depth for the seven well groups described in the text. The highest quality ranked mean breakout orientation for each well group is also shown.

The Griffin Group consists of 155 breakouts interpreted from seven wells comprising a mean σ_{Hmax} direction oriented 110°N. The group mean is controlled by a large proportion of breakout azimuths oriented approximately 020°N while the remainder show a large degree of scatter. Griffin-2 and Scindian-1a contain accumulations of breakouts oriented between 120-140°N and between 040-080°N. The mean breakout azimuth calculated for Griffin-3 is nearly perpendicular to all other wells and this is reflected on the North West Shelf Stress Map (Figure 5.1).

The Goodwyn Group consists of 45 breakouts interpreted from four wells that have a mean σ_{Hmax} orientation of 062°N. Goodwyn-1 is the exception with a σ_{Hmax} oriented 125°N. The breakout azimuths within Goodwyn-1 show a large degree of scatter and since the total number of breakouts in the Goodwyn Group is dominated by Goodwyn-1 (30/45 breakouts), it controls the mean group σ_{Hmax} orientation. The remaining wells, Goodwyn-3a, Goodwyn-8b and Goodwyn-9a, each have small clusters of consistently oriented breakouts with means at 138°N, 140°N and 129°N, indicating σ_{Hmax} directions of 048°N, 050°N and 039°N respectively.

The Wanaea Group shows an amazing consistency between 42 breakout azimuths from all four wells in the group. With the exception of two breakouts, all infer σ_{Hmax} orientations to be approximately E-W oriented. This consistency is reflected by the excellent quality ratings.

The Wandoo Group consists of 65 breakouts interpreted from six wells comprising a group mean σ_{Hmax} of 028°N. The scatter of the entire group does not appear to favour any particular orientation and again this is recognised by the poor quality rating of the

statistical means. Three wells do have B quality mean σ_{Hmax} directions; Tingle-1 (149°N), Wandoo-3 (160°N) and Wandoo-7 (041°N), none of which are parallel to the group or regional means.

The West Muiron Group consists of 10 breakouts interpreted from three wells that together have an A quality σ_{Hmax} direction of 099°N. This is heavily weighted by the six breakouts interpreted from the Santo-1 well which are consistently aligned at approximately 010°N (σ_{Hmax} = 100°N). Two of the four remaining breakouts are oriented between 040°N and 070°N.

Breakouts azimuths that infer anomalous σ_{Hmax} directions within wells, exist within the basin centre as well as on the flanks. The greater density of anomalous stress indicators on the basin flanks increases the standard deviation of well means and results in low quality ratings. A relationship appears to exist between the more structurally complex basin margins and the anomalous stress directions, however, an explanation for the stress rotation must consider that the stress field also rotates in the basin centre, albeit to a much lesser extent.

The observations made at the basin, well group and well scale pose several important questions pertaining to the orientation of the stress field in the Carnarvon Basin:

- What is the relationship between σ_{Hmax} orientation and the structure of the Carnarvon Basin (i.e. basin centre versus basin flanks)?
- Which orientation is the regional trend in the Carnarvon Basin, the E-W or the NE oriented trend?

- Why is σ_{Hmax} direction in the Bonaparte Basin not affected in the same manner?

These questions will be discussed in the following chapter.

5.3 Contemporary Stress Magnitudes in the North West Shelf of Australia

In the Carnarvon Basin, 36 estimates of stress magnitude (σ_v, σ_{Hmax} and σ_{hmin}) were made, as outlined in Chapter 3, from 24 wells, and 37 estimates were made from 29 wells in the Bonaparte/Browse Basin (Tables 5.4 and 5.5). Not all wells from which stress magnitude data was obtained correspond with wells analysed for stress orientation, however they are distributed within the same areas. The following two sections present the results of all the stress magnitude calculations.

5.3.1 Vertical Stress Magnitudes

Vertical stress magnitudes were calculated as outlined in Section 3.2 for wells where horizontal stress magnitudes were available. Vertical stress magnitudes are consistent within the individual basin areas described in Section 3.2.1 and listed in Table 3.2, enabling the definition of basin-specific σ_v-depth functions (Figure 5.7). A power regression relationship was fitted in each case:

Carnarvon $$\sigma_v = \left(\frac{Depth}{65.881}\right)^{-0.9144} \qquad R^2 = 0.9964 \qquad (5.1)$$

Browse $$\sigma_v = \left(\frac{Depth}{64.227}\right)^{-0.9243} \qquad R^2 = 0.9994 \qquad (5.2)$$

Bonaparte $$\sigma_v = \left(\frac{Depth}{62.759}\right)^{-0.9179} \qquad R^2 = 0.9985 \qquad (5.3)$$

where σ_v is in MPa, depth is in metres and R^2 is the regression coefficient ($R^2 = 0$ implies no correlation and $R^2 = 1$ implies perfect correlation).

Tables 5.4 and 5.5 summarise horizontal to vertical stress ratios. If a vertical stress profile was available for a specific well or for an adjacent well (i.e. same field), then this was used to calculate the stress ratios. The basin-wide relations of Equations 5.1, 5.2 and 5.3 were used where there was no stress profile available for a specific or adjacent well.

WELL NAME	Depth (m)	Leak Off (MPa)	Po (MPa)	σhmin (MPa)	σHmax (MPa)	σv (MPa)	Source of σv	σhmin/σv (MPa)	σHmax/σv (MPa)
Carnarvon Basin									
Bambra 2	812	12.07	8.23	11.51	14.78	17.21	Bambra 2	0.67	0.86
	2427	12.30	24.60	35.04	45.49	51.60	Bambra 2	0.68	0.88
	2459	11.54	24.92	33.31	41.70	52.25	Bambra 2	0.64	0.80
Chinook 1	1721	14.28	17.44	28.85	40.26	36.24	Chinook 1	0.80	1.11
Cygnus 1	1320	12.80	13.38	19.83	26.29	26.53	Carnarvon Eqn	0.75	0.99
East Pepper 1	322	10.50	3.26	3.97	4.67	6.16	Pepper 1	0.64	0.76
	1201	10.70	12.17	15.09	18.00	23.44	Pepper 1	0.64	0.77
Emma 1	565	14.80	5.73	9.82	13.91	11.02	Emma 1	0.89	1.26
	1581	12.93	16.02	24.00	31.97	33.18	Emma 1	0.72	0.96
Flores 1	844	13.40	8.55	13.28	18.00	17.55	Flores 1	0.76	1.03
Griffin 1	1657	13.43	16.79	26.13	35.47	35.44	Griffin 1	0.74	1.00
Griffin 4	1785	13.29	18.09	27.85	37.60	38.17	Griffin 1	0.73	0.99
Griffin 6	1751	13.34	17.75	27.42	37.10	37.45	Griffin 1	0.73	0.99
Harriet 1	898	13.20	9.10	13.92	18.73	18.07	Harriet 1	0.77	1.04
	2000	12.50	20.27	29.35	38.43	41.78	Harriet 1	0.70	0.92
Judy 1	453	11.80	4.59	6.28	7.96	8.24	Carnarvon Eqn	0.76	0.97
	1178	14.40	11.94	19.91	27.89	23.42	Carnarvon Eqn	0.85	1.19
Kanji 1	351	12.52	3.56	5.16	6.76	6.23	Carnarvon Eqn	0.83	1.08
Macedon 1	244	9.18	2.47	2.63	2.79	4.19	Carnarvon Eqn	0.63	0.67
	860	11.10	8.72	11.21	13.70	16.60	Carnarvon Eqn	0.67	0.83
Maitland 1	678	11.01	6.87	8.76	10.66	12.80	Carnarvon Eqn	0.68	0.83
Orion 1	1672	12.52	16.94	24.57	32.19	32.13	Orion 1	0.76	1.00
Pyrenees 1	946	11.93	9.59	13.25	16.92	18.43	Carnarvon Eqn	0.72	0.92
Ramillies 1	1666	14.05	16.88	27.47	38.06	34.22	Carnarvon Eqn	0.80	1.11
Samson 1	700	12.68	7.09	10.42	13.75	14.90	Samson 1	0.70	0.92
	1131	13.94	11.46	18.50	25.54	24.08	Samson 1	0.77	1.06
	2012	11.35	20.39	26.81	33.22	42.81	Samson 1	0.63	0.78
	3249	13.60	32.93	51.89	70.85	73.15	Samson 1	0.71	0.97
Scindian 2	435	10.85	4.41	5.54	6.67	9.30	Scindian 1a	0.60	0.72
Strickland 1	171	11.40	1.73	2.27	2.81	2.83	Carnarvon Eqn	0.80	0.99
	404	15.64	4.09	7.42	10.74	7.27	Carnarvon Eqn	1.02	1.48
Walcott 1	1884	12.43	19.09	27.50	35.91	37.01	Walcott 1	0.74	0.97
	2976	13.27	30.16	46.36	62.55	62.86	Walcott 1	0.74	1.00
West Muiron 3	856	13.52	8.68	13.58	18.49	16.52	Carnarvon Eqn	0.82	1.12
West Muiron 4	805	11.43	8.16	10.80	13.45	15.45	Carnarvon Eqn	0.70	0.87
West Muiron 5	888	12.68	9.00	13.22	17.45	17.20	Carnarvon Eqn	0.77	1.01

Table 5.4 Stress magnitudes calculated for the Carnarvon Basin. Depth is the depth at which a leak-off test was performed, leak-off is the pump pressure at which leak-off occurred, Po is the hydrostatic pore pressure, σ_{hmin} is the minimum horizontal stress magnitude calculated by summing the leak-off pressure and the weight of the mud column, σ_{Hmax} is the maximum horizontal stress magnitude calculated using σ_{hmin} and Po (Equation 3.21) and σ_v is the vertical stress magnitude at the depth of the leak-off test.

WELL NAME	Depth (m)	Leak Off (MPa)	Po (MPa)	σhmin (MPa)	σHmax (MPa)	σv (MPa)	Source of σv	σhmin/σv (MPa)	σHmax/σv (MPa)
Bonaparte and Browse Basins									
Anderdon 1	1802	14.51	18.26	30.69	43.11	44.85	Anderdon 1	0.68	0.96
	2470	14.11	25.03	40.92	56.81	55.33	Anderdon 1	0.74	1.03
Asterias 1	4001	14.16	40.55	66.81	93.07	92.45	Bonaparte Eqn	0.72	1.01
Avocet 1A	514	8.83	5.21	5.33	5.45	10.89	Avocet 1A	0.49	0.50
Barita 1	522	12.10	5.29	7.41	9.54	11.11	Barita 1	0.67	0.86
	1303	12.10	13.21	18.51	23.81	27.80	Barita 1	0.67	0.86
Barnett 2	2227	13.35	22.57	34.91	47.24	48.83	Bonaparte Eqn	0.71	0.97
Berkley 1	806	13.10	8.17	12.40	16.62	16.14	Bonaparte Eqn	0.77	1.03
Brecknock 1	2106	9.93	21.34	24.55	27.76	45.95	Bonaparte Eqn	0.53	0.60
Brewster 1A	3507	14.10	35.54	58.06	80.58	80.08	Bonaparte Eqn	0.73	1.01
	3680	15.69	37.30	67.78	98.26	84.40	Bonaparte Eqn	0.80	1.16
	4220	13.02	42.77	64.49	86.22	97.97	Bonaparte Eqn	0.66	0.88
Buffon 1	3660	13.02	37.09	55.96	74.83	83.90	Bonaparte Eqn	0.67	0.89
Caswell 1	1807	10.77	18.31	22.84	27.36	38.11	Caswell 1	0.60	0.72
Caswell 2	2774	11.60	28.11	37.77	47.43	58.81	Caswell 1	0.64	0.81
Challis 1	1212	14.03	12.28	19.97	27.65	25.62	Challis 1	0.78	1.08
Champagny 1	2133	12.03	21.62	30.13	38.64	46.59	Bonaparte Eqn	0.65	0.83
Darwinia 1A	605	11.75	6.13	8.35	10.56	11.81	Bonaparte Eqn	0.71	0.89
	1335	13.15	13.53	20.61	27.69	27.96	Bonaparte Eqn	0.74	0.99
Delamere 1	937	14.02	9.50	15.42	21.35	19.01	Bonaparte Eqn	0.81	1.12
Eclipse 1	2353	11.43	23.85	31.58	39.32	52.24	Eclipse 1	0.60	0.75
Evans Shoal 1	3001	15.91	30.41	56.05	81.69	67.58	Bonaparte Eqn	0.83	1.21
Fagin 1	2880	14.54	29.19	49.15	69.11	63.00	Fagin 1	0.78	1.10
Hadrian 1	1955	10.59	19.81	24.31	28.81	42.37	Bonaparte Eqn	0.57	0.68
Halcyon 1	601	10.71	6.09	7.55	9.02	11.71	Bonaparte Eqn	0.64	0.77
	954	13.75	9.67	15.39	21.12	19.39	Bonaparte Eqn	0.79	1.09
Iris 1	1805	14.30	18.29	30.30	42.31	39.66	Iris 1	0.76	1.07
Jabiru 1A	2415	14.54	24.47	41.22	57.97	52.87	Jabiru 1a	0.78	1.10
Jacaranda 1	1130	15.70	11.45	20.83	30.20	23.32	Bonaparte Eqn	0.89	1.30
	2590	14.25	26.25	43.33	60.41	57.56	Bonaparte Eqn	0.75	1.05
Kalyptea 1	3458	12.07	35.05	49.00	62.96	74.12	Kalyptea 1	0.66	0.85
Lorikeet 1	1598	13.42	16.19	25.17	34.14	34.01	Bonaparte Eqn	0.74	1.00
Maple 1	1903	11.53	19.29	25.75	32.22	41.14	Bonaparte Eqn	0.63	0.78
Maret 1	1685	9.80	17.08	19.39	21.71	36.04	Bonaparte Eqn	0.54	0.60
Montara 1	1307	11.60	13.25	17.80	22.35	27.32	Bonaparte Eqn	0.65	0.82
Swan 2	442	13.20	4.48	6.85	9.22	9.45	Swan 2	0.72	0.98
	1585	15.20	16.06	28.28	40.50	33.92	Swan 2	0.83	1.19

Table 5.5 Stress magnitudes calculated for the Bonaparte Basin. Depth is the depth at which a leak-off test was performed, leak-off is the pump pressure at which leak-off occurred, Po is the hydrostatic pore pressure, σ_{hmin} is the minimum horizontal stress magnitude calculated by summing the leak-off pressure and the weight of the mud column, σ_{Hmax} is the maximum horizontal stress magnitude calculated using σ_{hmin} and Po (Equation 3.21) and σ_v is the vertical stress magnitude at the depth of the leak-off test.

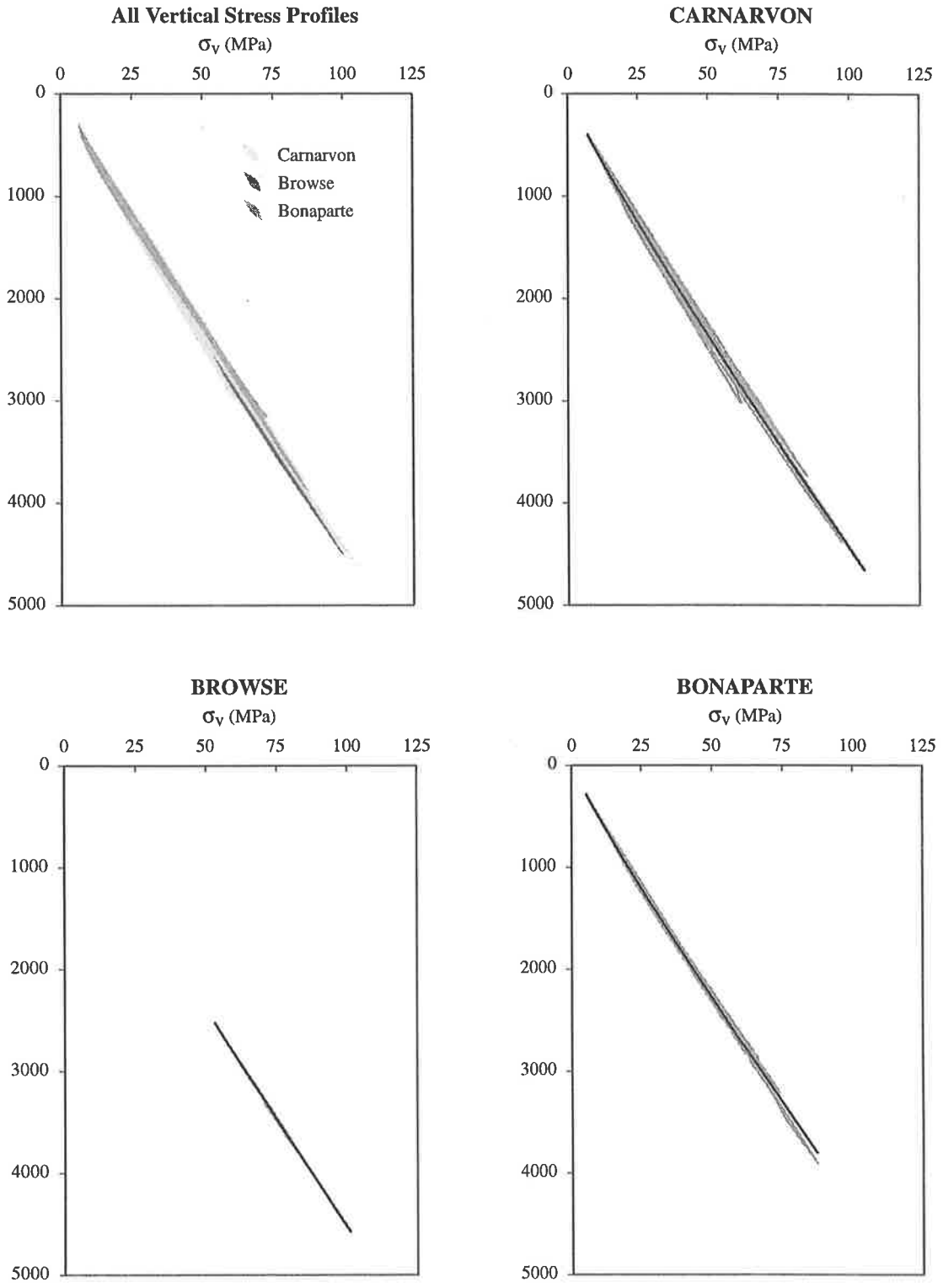

Figure 5.7 Vertical stress magnitude vs. depth from wells (a) in all areas, (b) in the Carnarvon area, (c) in the Browse area and (d) in the Bonaparte area. The σ_v/depth power regression relationships corresponding to Equations 5.1, 5.2 and 5.3 are shown for their respective basins.

5.3.2 Horizontal Stress Magnitudes

As discussed in Section 3.3, the primary method used to calculate horizontal stress magnitudes is based on the assumption that lower bound leak-off pressures are an estimate of fracture opening pressure (Breckels & van Eeckelen, 1982). The fracture opening pressure (Pr) in turn estimates the instantaneous shut-in pressure (ISIP) and hence, σ_{hmin} (Equation 3.20). This assumption is carried over to derive Equation 3.21 in order to calculate σ_{Hmax} from σ_{hmin} and Po. Theoretical constraints derived using the frictional equilibrium relation (Coulomb, 1773) are used to verify the estimates of horizontal stress magnitude using the leak-off method.

Stress Regime in the Carnarvon and Bonaparte Basins

The minimum and maximum horizontal stress magnitudes calculated using the leak-off method (Tables 5.4 and 5.5) are plotted in Figure 5.8. In both the Carnarvon and Bonaparte Basins, σ_{hmin} is consistently less than σ_v. Lower bound σ_{hmin} estimates from leak-off values define σ_{hmin} gradients for the Carnarvon and Bonaparte Basins of 12.6 MPa/km (0.6 psi/ft) and 12.4 MPa/km (0.59 psi/ft) respectively. Maximum horizontal stress magnitudes calculated using Equation 3.21 (Ervine & Bell, 1987), vary considerably, but are generally scattered around σ_v. In summary, the relationship between the stress magnitudes in both basins, can be expressed as:

$$\sigma_{h\,min} < \sigma_{H\,max} \approx \sigma_v \qquad (5.4)$$

This indicates that the stress regime in the Carnarvon and Bonaparte Basins is approximately on the boundary between strike-slip and normal (see Equations 3.2, 3.3, 3.4). Hillis & Williams (1993a) similarly deduced from six extended leak-off tests in the Wanaea and Cossack fields of the Carnarvon Basin that the stress regime was approximately on the boundary between strike-slip and normal.

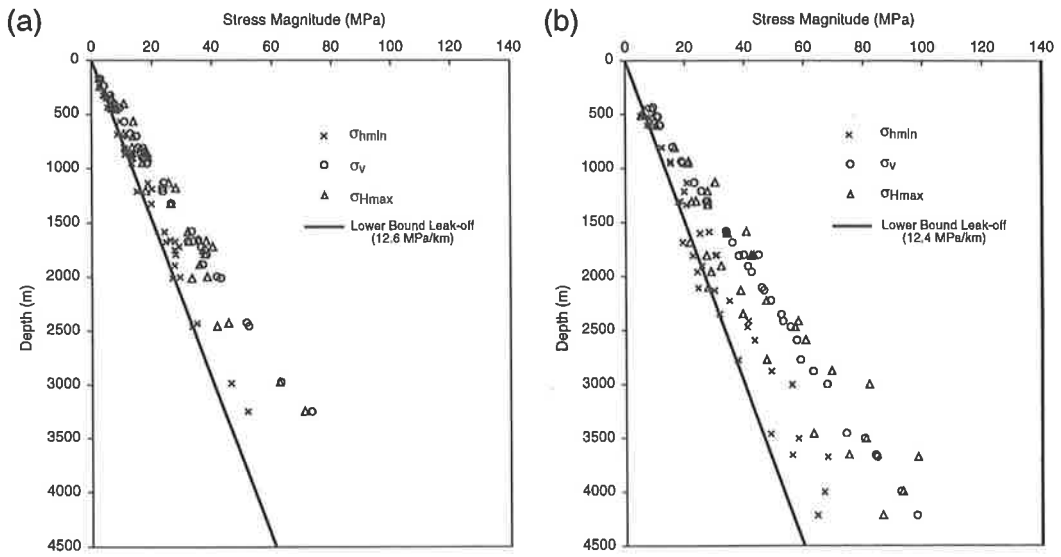

Figure 5.8 Stress magnitudes calculated using the leak-off method, for (a) the Carnarvon Basin (Table 5.4) and (b) the Bonaparte and Browse Basins (Table 5.5).

Constraints on the Stress Regime in the Carnarvon and Bonaparte Basins Using the Frictional Equilibrium Relation

It is possible to place constraints on the ratio of maximum and minimum effective stresses in terms of the strength of the crust, using Mohr-Coulomb failure criteria (Jaeger and Cook, 1979). Coulomb (1773) suggested that the shear stress (τ) leading to shear failure is resisted by the shear strength (S_0) of the material and by a constant (μ), the coefficient of friction, multiplied by the applied normal stress (σ_n), such that:

$$|\tau| = S_0 + \mu\sigma_n \tag{5.5}$$

The normal and shear stresses acting on a plane whose normal makes the angle β with respect to the maximum principal stress (σ_1), are given by:

$$\sigma_n = \frac{1}{2}(\sigma_1 + \sigma_3) + \frac{1}{2}(\sigma_1 - \sigma_3)\cos 2\beta \tag{5.6}$$

$$\tau = \frac{1}{2}(\sigma_1 - \sigma_3)\sin 2\beta \tag{5.7}$$

From these equations it can be shown that, if we assume pre-existing fractures and faults with little or no compressive strength, the frictional limit on the ratio of the

maximum and minimum effective principal stresses, at which faulting will occur, can be defined as a function of the coefficient of friction, such that:

$$\frac{\sigma_1 - P_0}{\sigma_3 - P_0} = \left[\left(\mu^2 + 1 \right)^{\frac{1}{2}} + \mu \right]^2 \qquad (5.8)$$

If the ratio of maximum to minimum effective principal stresses is less than this value, then all faults should be stable and no slip should occur on them. If the ratio is exactly this value, slip should occur only on favorably oriented faults, and all other faults should be stable (Zoback and Healy, 1984). See Jaeger & Cook (1979) for the full derivation of this relationship.

Earthquake activity on the North West Shelf (Gaull & Gregson, 1991), implies that the area is close to frictional equilibrium and suggests that Equation 5.8 can be used to constrain limits on the stress magnitudes in the Carnarvon and Bonaparte Basins for a given stress regime. The stress regime has been shown previously to be on the boundary between strike-slip and normal. If the stress regime is first assumed to be normal in both basins (i.e. $\sigma_{hmin} < \sigma_{Hmax} < \sigma_v$), Equation 5.8 becomes:

$$\frac{\sigma_v - P_0}{\sigma_{hmin} - P_0} \leq \left[\left(\mu^2 + 1 \right)^{\frac{1}{2}} + \mu \right]^2 \qquad (5.9)$$

Using the well constrained values of σ_v and a reasonable range of estimates for μ, an estimate σ_{hmin} can be determined i.e.:

$$\sigma_{hmin} \geq \frac{(\sigma_v - P_0)}{\left[\left(\mu^2 + 1 \right)^{\frac{1}{2}} + \mu \right]} + P_0 \qquad (5.10)$$

There is no available data on the coefficient of friction for sedimentary rocks of the North West Shelf, hence, a range of μ values have been used. Comprehensive laboratory testing of the coefficient of friction of a wide variety of rock types by

Byerlee (1979) indicates that most rocks range between 0.6 and 1.0, and with an average of around 0.7. The stress magnitude calculations using the frictional equation relation have used μ values of 0.6, 0.8 and 1.0.

Minimum horizontal stress gradients were calculated for the Carnarvon and Bonaparte Basins using Equation 5.10 (Figure 5.9). The leak-off derived σ_{hmin} gradient for the Carnarvon Basin plots slightly less than the frictional limit for rocks with a coefficient of friction of $\mu = 0.6$. Similarly, the gradient for the Bonaparte basin plots slightly greater than the frictional limit for rocks with a coefficient of friction of $\mu = 0.8$. Considering that the leak-off derived σ_{hmin} gradients are consistent with effective stress ratios equal to or less than the coefficient of friction function, ($\mu \approx 0.7$ in the Carnarvon and $\mu \approx 0.8$ in the Bonaparte), suggesting that both basins are close to frictional equilibrium and that extensional movement on critically oriented faults is likely.

Considering σ_{Hmax} is approximately equal to σ_v, the frictional equilibrium relation can be expressed in terms of a strike-slip regime. Equation 5.8 becomes:

$$\frac{\sigma_{Hmax} - P_0}{\sigma_{hmin} - P_0} \leq \left[\left(\mu^2 + 1\right)^{\frac{1}{2}} + \mu \right]^2, \qquad (5.11)$$

and it follows that:

$$\sigma_{Hmax} \leq \left(\sigma_{hmin} - P_0\right)\left[\left(\mu^2 + 1\right)^{\frac{1}{2}} + \mu \right]^2 + P_0 \qquad (5.12)$$

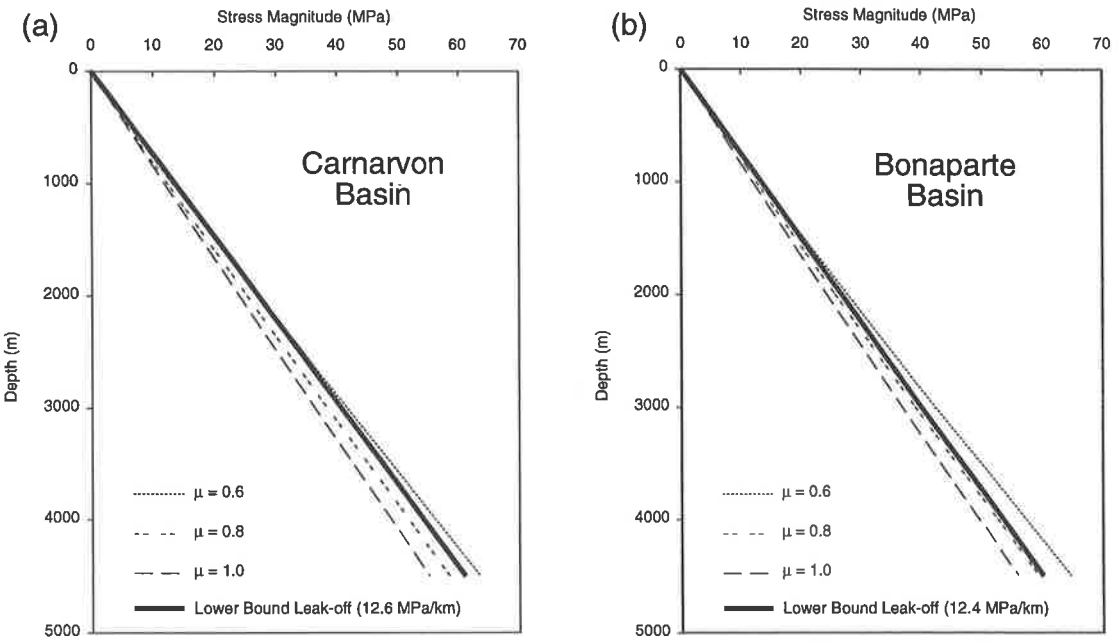

Figure 5.9 A comparison of theoretical σ_{hmin} gradients calculated from Equation 5.10 with approximate σ_{hmin} gradients from leak-off pressures in (a) the Carnarvon Basin and (b) the Bonaparte Basin.

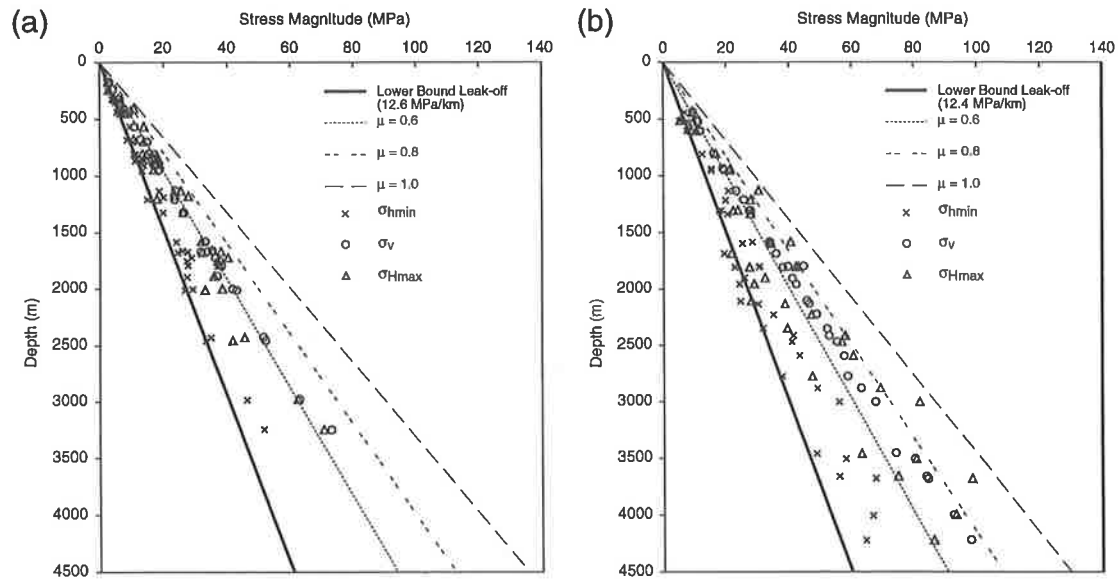

Figure 5.10 Stress magnitudes calculated using the leak-off method, for (a) the Carnarvon Basin (Table 5.4) and (b) the Bonaparte and Browse Basins (Table 5.5). Also shown are three frictional limits for σ_{Hmax} calculated using separate values for the coefficient of friction substituted into Equation 5.12.

The minimum horizontal stress magnitude (σ_{hmin}) can be constrained using σ_v (extensional regime) and μ ranging from 0.6 to 1.0 in Equation 5.10. The results indicate that σ_{Hmax} cannot exceed σ_v without failure occurring. The leak-off values

used in Equation 3.21 to infer σ_{Hmax} magnitudes fall within the range of σ_{Hmax} magnitudes determined using Equation 5.12 (Figure 5.10). Therefore the frictional equilibrium relation suggests the stress regime in the Carnarvon and Bonaparte Basins may be on the boundary between extensional and strike-for average values of μ.

5.3.3 Stress Ratios

Horizontal and vertical stress magnitudes increase with depth. Hence, raw horizontal stress magnitudes cannot be compared with one another because they come from leak-off tests undertaken at a variety of depths. Horizontal stress ratios with respect to σ_v, (i.e $n_h = \sigma_{hmin}/\sigma_v$, and $n_H = \sigma_{Hmax}/\sigma_v$) are independent of depth and reveal changes to the stress regime across a basin. The three types of stress regime, defined in Equations 3.2-3.4, can be represented using stress ratios:

extensional regime (normal fault condition): $n_h < n_H < 1$ (5.13)

strike-slip regime (strike-slip fault condition): $n_h < 1 < n_H$ (5.14)

compressional regime (reverse fault condition): $1 < n_h < n_H$ (5.15)

The horizontal stress ratios calculated from stress magnitudes estimated using leak-off data, are listed in Tables 5.4 and 5.5, and illustrated in Figure 5.1 1. The data from both the Carnarvon and Bonaparte Basins plot within the extensional and strike-slip stress regime domains.

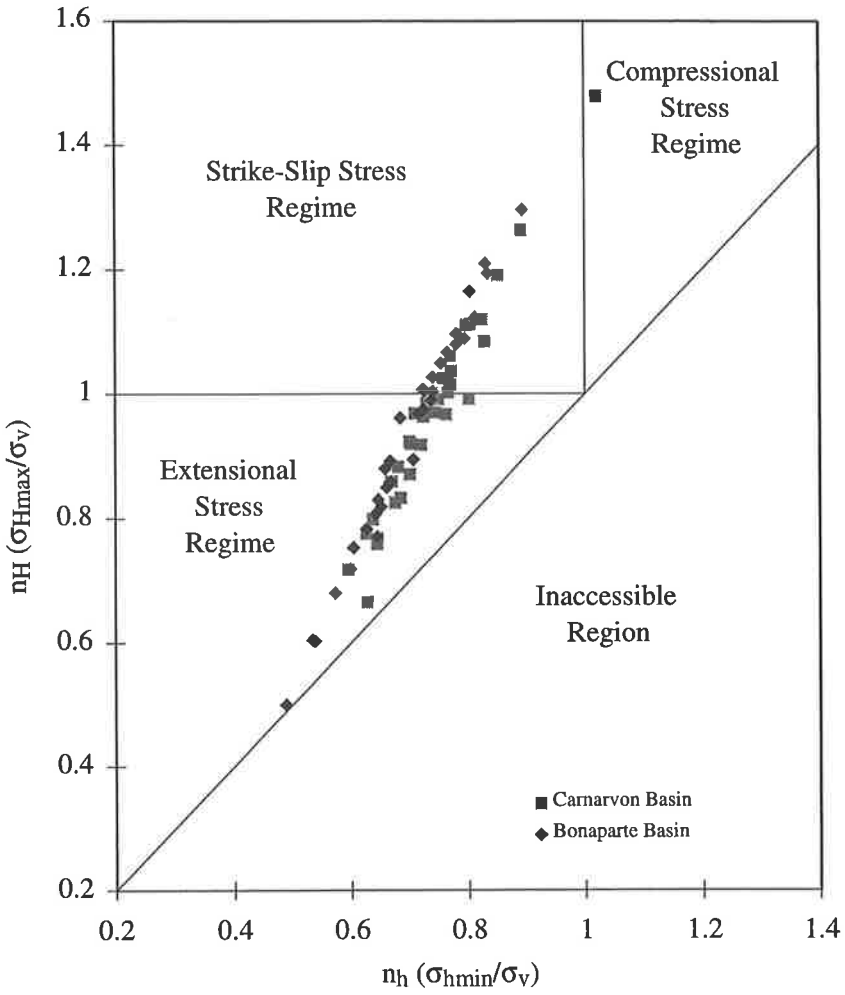

Figure 5.11 Maximum and minimum stress ratios plotted for wells in the Carnarvon and Bonaparte Basins (Tables 5.4 and 5.5). The minimum stress magnitudes are estimated from leak-off tests an the maximum horizontal stress magnitudes are calculated from the σ_{hmin} values using Equation 3.20.

The spatial distribution of stress ratios differs significantly between the Carnarvon and Bonaparte Basins. The Carnarvon Basin shows decreasing n_H values with increasing distance from the coastline across NW-SE trending profiles towards the Indian Ocean Basin (Figure 5.12). In comparison, n_H values from the Bonaparte Basin exhibit a generally increasing trend to the NE along a SW-NE trending profile (Figure 5.13). Hence, in the Carnarvon Basin, the stress regime is strike-slip adjacent to the coastline and becomes extensional towards the Indian Ocean Basin. The stress regime in the SW part of the Bonaparte Basin is extensional and progresses to strike-slip NE

towards the plate margin. The systematic changes is stress magnitude on the North West Shelf will be discussed in the following chapter.

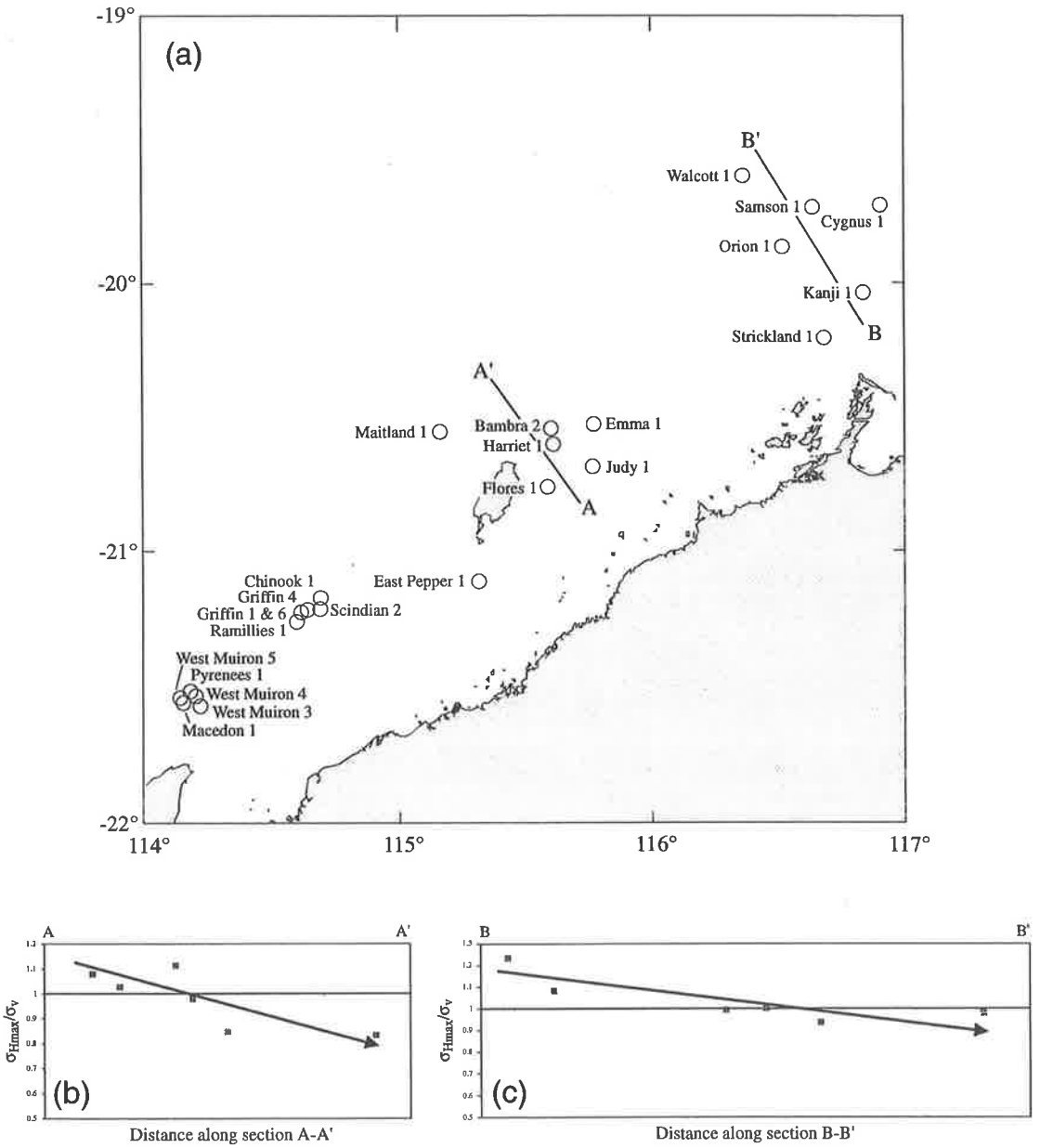

Figure 5.12 (a) the distribution of wells in the Carnarvon Basin from which horizontal stress magnitudes were determined using leak-off tests. (b) and (c) show profiles of n_H values taken from wells adjacent to the lines denoted A-A' and B-B' respectively in Figure 5.11a. The arrows highlight the decreasing trends in the data and the horizontal line at n_H = 1 indicates the transition from an extensional ($n_H < 1$) to a strike-slip ($n_H > 1$) stress regime given that $n_h < 1$.

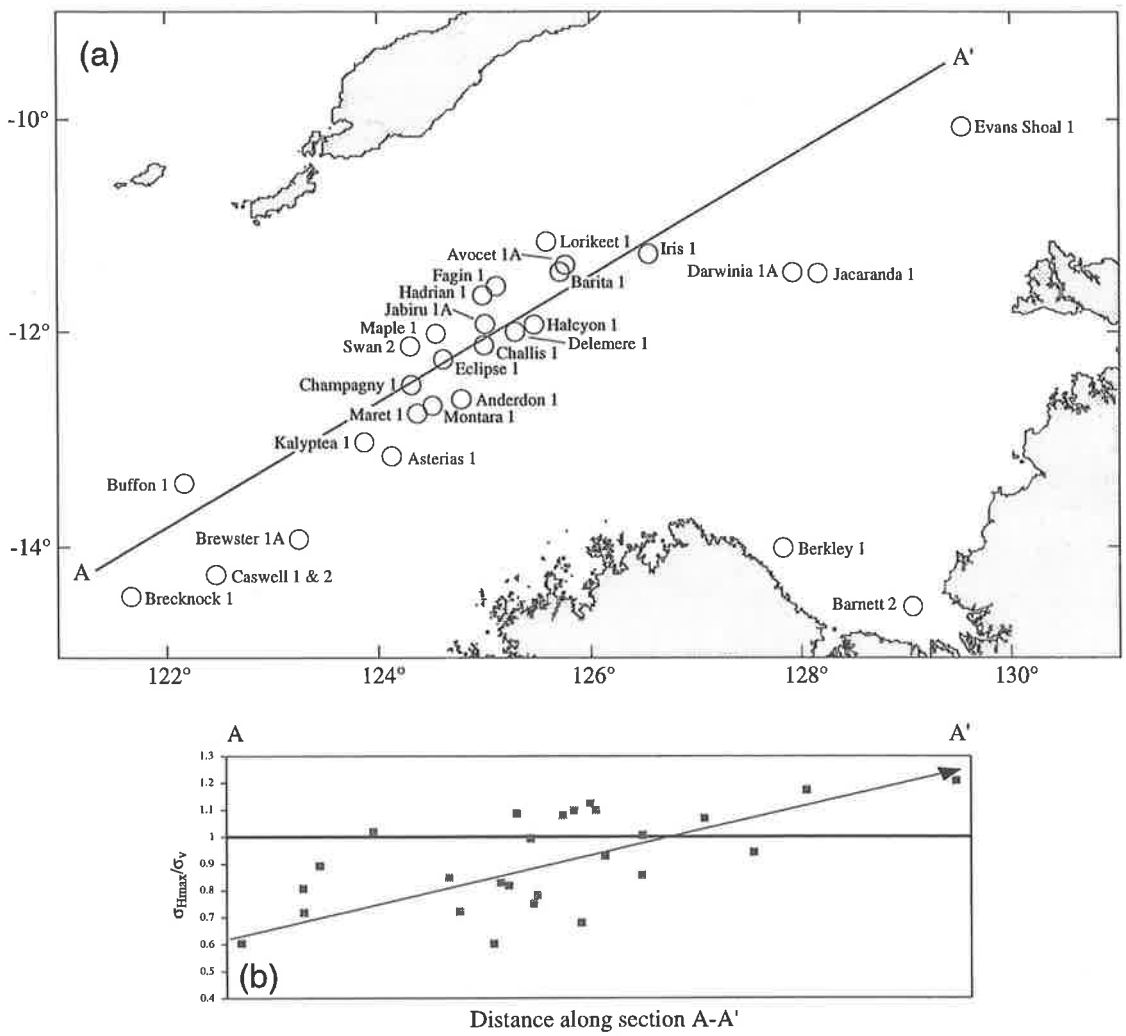

Figure 5.13 (a) the distribution of wells in the Bonaparte Basin from which horizontal stress magnitudes were determined using leak-off tests. (b) shows a profile of n_H values taken from wells adjacent to the line A-A' shown in Figure 5.12a. The arrow highlights the increasing trend in the data and the horizontal line at $n_H = 1$ indicates the transition from an extensional ($n_H < 1$) to a strike-slip ($n_H > 1$) stress regime given that $n_h < 1$.

5.3.4 Stress Anisotropy

Under conditions where the maximum and minimum horizontal stress magnitudes are similar (i.e. isotropic), the orientation of σ_{Hmax} and σ_{hmin} is highly variable, resulting in fluctuating breakout directions. Contemporary stress orientation indicators in the Carnarvon Basin are generally of higher quality than those in the Bonaparte Basin. Stress anisotropy in the two basins was compared to investigate whether the lower quality stress indicators in the Bonaparte Basin may be due to more isotropic conditions compared with the Carnarvon Basin.

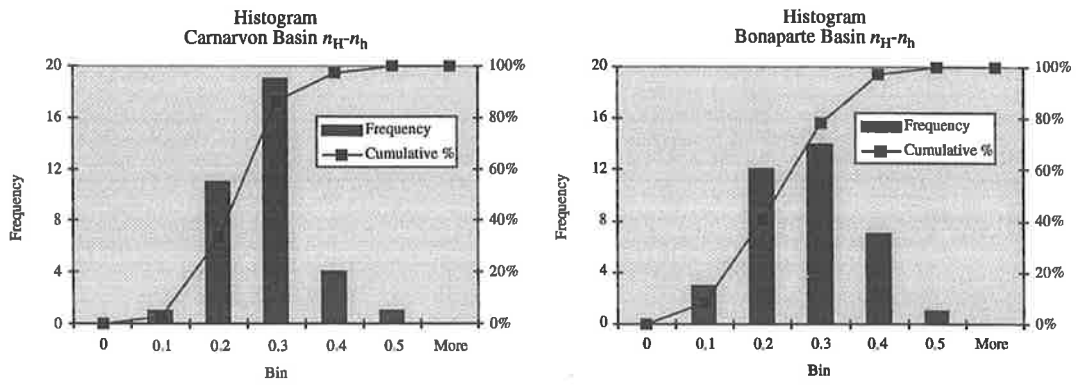

Figure 5.14 Histograms illustrating the difference between the horizontal stress magnitudes normalised by σ_v in (a) the Carnarvon Basin and (b) the Bonaparte Basin. Cumulative frequency is also shown.

Normalised differences between horizontal stress magnitudes (i.e. σ_{Hmax}/σ_v - σ_{hmin}/σ_v), show similar characteristics for both the Carnarvon and Bonaparte Basins (Figure 5.14). Statistical means from each basin are identical ($\bar{x} = 0.23$) although the standard deviation of the Bonaparte data (SD = 0.093) is slightly greater than that of the Carnarvon (SD = 0.079). These results suggest that stress anisotropy is not the cause of the lower quality rated stress orientations in the Bonaparte Basin. This will be discussed further in the following chapter.

Chapter 6

Tectonic Implications of the Contemporary Stress Field

6.1 Introduction

Stresses control tectonic motions of and within the lithosphere. Improved knowledge of the stress field is intimately tied to improving our understanding of the mechanisms that drive plate motion, the dynamics of faulting along both plate boundaries and in intra-plate areas and the overall mechanical, thermal and rheological constraints on active geological processes (Zoback, 1993). The 'first-order' midplate stress fields are believed to be largely the result of forces applied at plate boundaries. 'Second-order' stresses are localised perturbations of the first-order stress field that can be identified once the first-order stress pattern has been defined (Zoback, 1992). The aim of this chapter is to define the first- and second-order stress patterns of the North West Shelf stress field, and constrain the active tectonic processes occurring within the Carnarvon and Bonaparte Basins. Before this can be achieved, the relationship of the stress field to the geomechanical setting must be addressed.

6.2 Geomechanical Setting

The geomechanical nature of the North West Shelf must be considered in order to account correctly for the origin of the contemporary stress regime (Bell, 1993). The potential for detachment surfaces exists in both the Carnarvon and Bonaparte Basins below the depths at which borehole breakouts were identified. They may caused by overpressured horizons within the basin centres associated with areas of hydrocarbon generation (Horstman, 1988), or by the presence of evaporite deposits in the

Bonaparte Basin. However, the presence of an E-W σ_{Hmax} direction within the depositional centres of the Carnarvon Basin implies that there is no dislocation between the upper and lower sequences. By comparison with the findings of Yassir & Bell (1994), if a dislocation did exist, the detached sediments would be extended or stretched downslope to the northwest, resulting in a northeast σ_{Hmax} direction.

It is more difficult to ascertain whether the sedimentary sequence is attached in the Bonaparte Basin. The regional σ_{Hmax} direction is consistently oriented approximately 060°N, parallel to the direction expected if a detachment horizon existed in the subsurface. Evaporitic sediments are not likely to underlie the study area and structural dislocation, if present, will occur at most as a localised feature (Section 2.8).

6.3 Second-Order Stress Patterns in the Carnarvon Basin

Unlike the Bonaparte Basin, there exists a second preferred σ_{Hmax} orientation in the Carnarvon Basin (Section 5.2.3). The mean σ_{Hmax} orientation for the entire basin is oriented approximately E-W (Chapter 5). A closer examination of stress orientation in the basin reveals that the major E-W direction dominates stress indicators from wells in the structureless depocentres of the Barrow and Dampier Sub-basins and that a second, albeit less prominent, NE-SW orientation is more common in wells located on the structurally complex basin margins (Figure 5.5). This section attempts to confirm which of these σ_{Hmax} trends represents the first-order, regional stress direction and discusses the source of the secondary trend.

6.3.1 The Regional Stress Field of the Carnarvon Basin

The rotation of the contemporary stress field within the North West Shelf occurs over a relatively short distance (i.e. 40° over 700 km; Section 5.2.2). Although the mean breakout direction clearly indicates an average σ_{Hmax} direction striking approximately E-W in the Carnarvon Basin, there is a possibility that this orientation is a second-order stress direction and that the first-order trend is oriented NE-SW, as recorded in the Bonaparte Basin.

Broadly speaking, the Carnarvon and Bonaparte Basins are structurally similar. Both consist of a Palaeozoic, NW oriented basin overlain by a NE trending, mostly Mesozoic Basin (Section 2.4). A NE structural trend dominates within both basins as a result of the Mesozoic rifting. The mean orientation of σ_{Hmax} in the Bonaparte Basin is parallel to this structural grain. If the NE σ_{Hmax} trend is the first-order stress direction in the Carnarvon Basin, the same resultant stress pattern would be expected (i.e. consistent NE-SW trending σ_{Hmax}). However, the Carnarvon Basin exhibits a strong E-W σ_{Hmax} direction, oblique to the basin structure.

Detailed analysis of breakout azimuths interpreted from the seven well groups in the Carnarvon Basin reveals that the E-W and NE-SW σ_{Hmax} directions are recorded within wells from nearly all areas of the Carnarvon Basin (Section 5.2.3). Some NW-SE oriented breakouts (i.e. NE/SW inferred σ_{Hmax}) occur in wells within the basin depocentres where the E-W trend dominates (e.g. Bambra-1, Griffin-2 and Marra-1), and some N-S breakouts on the margins (e.g. Goodwyn-3a, South Chervil-1, and Wandoo-1). The E-W σ_{Hmax} orientation dominates the NE-SW orientation within wells located in the centre of the Barrow-Dampier Sub-basin to a far greater extent

than the NE-SW σ_{Hmax} orientation dominates the E-W σ_{Hmax} orientation in wells on the basin margins. Therefore it is suggested that the approximately E-W oriented σ_{Hmax} represents the first-order stress direction and the NE-SW oriented σ_{Hmax} is the result of localised, stress rotation.

6.3.2 Source of the Second-Order Stress Direction in the Carnarvon Basin

Several different mechanisms can cause second order stress directions within a sedimentary basin, such as:

- low stress anisotropy (Zoback et al., 1985);
- elongation of fracture sets intersecting the borehole (Dart & Swolfs, 1992);
- lateral density contrasts (Sonder, 1990; Zoback, 1992);
- sediment loading (Cloetingh & Wortel, 1985; Zoback, 1992);
- contrasting elastic properties (Hudson & Cooling, 1988; Aleksandrowski et al., 1992; Bell et al., 1992a; Dart & Swolfs, 1992; Rawnsley et al., 1992) , and;
- active faulting (Hickman et al., 1985; Paillet & Kim, 1987; Shamir & Zoback, 1992; Barton & Zoback, 1994).

Each possible explanation is discussed below and considered in the context of the 060°N σ_{Hmax} direction associated with wells located on the more structurally complex basin margins. within the Carnarvon Basin. Stress indicators showing the 060°N σ_{Hmax} trend as opposed to the E-W regional trend may be attributed to

Stress Anisotropy

The major influence on breakout orientation within a semi-vertical well drilled through rock which is essentially isotropic in the horizontal plane, is not only the orientation of the incident horizontal stresses, but in the contrast between their magnitudes (Jaeger,

1961; Zoback et al., 1985). In an isotropic stress field, circumferential stresses acting on a borehole are constant, precluding compressional shear failure in any preferred direction. Therefore, consistently oriented breakouts are indicative of stress anisotropy.

Horizontal stress magnitudes measured within the Carnarvon Basin are inferred show considerable anisotropy (Section 5.3.3 and Figure 5.8a) and bulk analysis of all breakout orientations clearly indicates an E-W σ_{Hmax} direction (Figure 5.2). Such a strong signature suggests that there is a significant stress anisotropy, and that low stress anisotropy is unlikely to be responsible for the anomalous NE-SW stress direction.

Fracture Elongation

Elongations of the borehole wall similar to breakout may occur where the wellbore intersects fractures. Indeed breakouts in the Western Canadian Basin were originally interpreted as being due to enlargement of the wellbore along fractures intersected by the wellbore (Babcock, 1978). Fracture elongations of this type could record a similar signature to borehole breakouts on four-arm dipmeter logs. Under these circumstances, the orientation of wellbore failure does not provide a true representation of principal horizontal stress orientations.

A pre-existing fracture trend may exist within the Carnarvon Basin. The greater density of faults on the basin margins implies that fracture intersection and associated elongation of wellbore cross-section is more likely to occur in boreholes drilled on the flanks of the basin than in the depocentre. In order to determine whether such a

fracture set exists and whether it influences interpreted breakout azimuths, borehole image logs (BHTV, FMS, FMI) are needed. Borehole image logs were not generally available for this study and the possibility that elongation of the wellbore associated with fracture intersection may be disrupting the regional σ_{Hmax} signal remains. However, the criteria used in this project to distinguish borehole breakouts from other types of non-circular borehole appear to be robust, and it is unlikely that fracture elongations are being included as false indicators of stress orientation.

Lateral Density Contrasts

Lateral density contrasts can influence the orientation and relative magnitudes of an otherwise uniform lithospheric stress field (Sonder, 1990). The lateral change in density associated with a perturbation in the regional stress field can be defined by measuring two parameters, the angle between the regional σ_{Hmax} direction and the perturbed σ_{Hmax} direction (γ), and the angle between the strike of the density anomaly and the regional σ_{Hmax} direction (θ) (Figure 6.1). A clockwise rotation is defined by a positive value.

In the case of the Carnarvon Basin, potential lateral changes in density occur between the basin depocentres and the basin margins, hence the strike of the density anomaly is assumed to be parallel to the strike of the Barrow-Dampier Sub-basin. The regional σ_{Hmax} direction in the Carnarvon Basin is approximately 100°, the orientation of the perturbed σ_{Hmax} direction is approximately 040° and the orientation of the basin margin is also 040°. Hence, the values of γ and θ are 60° and -60° respectively (Figures 5.5). This implies that the buoyancy forces are extensional and that the source of the stress perturbation is a negative density anomaly (Sonder, 1990). In the context of the

Carnarvon Basin, this infers the flanks of the Barrow-Dampier Sub-basin to be less dense than its depositional centre.

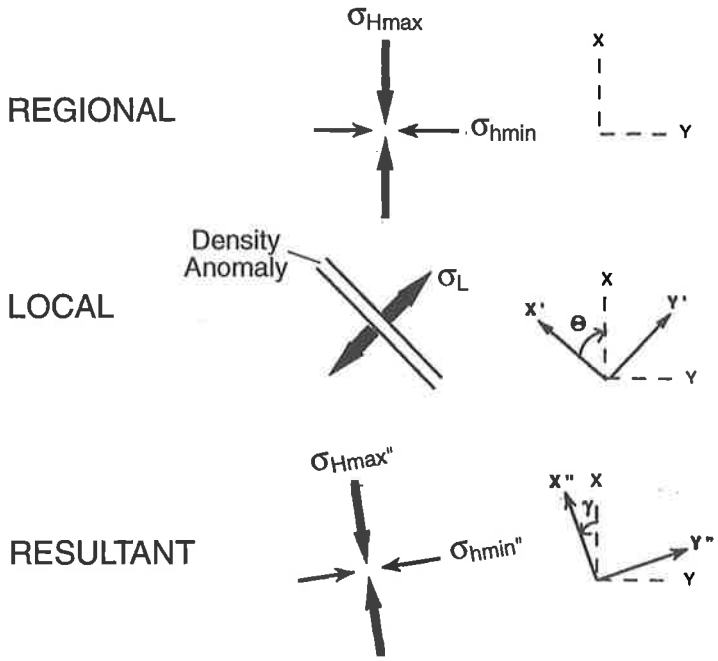

Figure 6.1 Geometry for evaluating stress rotations due to local density contrasts (after Sonder, 1990).

Regional, deep-seismic data show that the basin has an overall 'layer cake' appearance with a generally flat lying sedimentary section (Stagg & Collwell, 1994; Figure 2.11). A pair of flat lying reflectors also exist beneath the basin at approximately 8-11 seconds. These properties infer that substantial change in lithospheric thickness, and hence the presence of a density anomaly is minimal beneath the Carnarvon Basin. It is thus unlikely that a lateral density contrast is responsible for the second-order stress variation in the Carnarvon Basin.

Sediment Loading

Flexural stresses may be created within the lithosphere by adequately loading it with sedimentary sequences (Walcott, 1972; Turcotte et al., 1977; Cloetingh et al., 1982).

Passive margins, such as the North West Shelf of Australia, should be dominated by the sediment-loading effect, and the σ_{Hmax} orientations measured within, should tend to parallel the continental margin (Zoback, 1992; Figure 6.2). Stress indicators in the North West Shelf trend parallel to the continental margin from the onshore Canning Basin to the Bonaparte Basin. The Carnarvon Basin exhibits stress trends both parallel (NE-SW) and oblique (E-W) to the margin. The margin parallel stress indicators within the Carnarvon Basin and the existence of a transition from strike-slip to extensional stress regime, away from the coastline to the NW, suggest that the region may be undergoing flexure. However, the switch from E-W oriented σ_{Hmax} directions to NE from basin depocentre to its flanks is not likely to be explained by sediment loading of the margin which would infer a consistent NE σ_{Hmax} trend across the entire area.

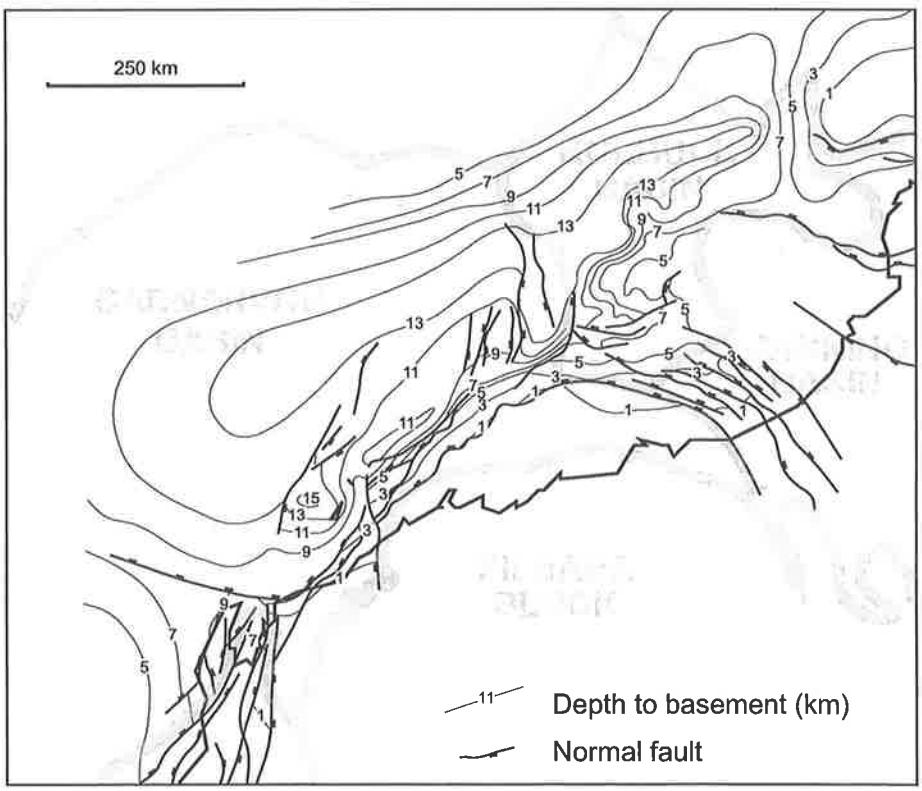

Figure 6.2 Depth to basement and structural elements of the Carnarvon Basin illustrating pattern of sediment distribution (Copp, 1994).

Elastic Properties

The elastic properties of rocks influence their state of stress (Hudson & Cooling, 1988). The presence of a discontinuity within a stress field can cause perturbations of the regional stress field, realigning the σ_{Hmax} direction (Figure 6.3). If the discontinuity is open, effectively having a Young's modulus of zero ($E_D = 0$), σ_{Hmax} is diverted parallel to the discontinuity. If the material in the discontinuity has essentially the same properties as the surrounding rock ($E_D = E$), the principal stresses are unaffected. At the other extreme, if the material in the discontinuity is rigid ($E_D = \infty$), σ_{Hmax} will be diverted perpendicular to the discontinuity (Hudson & Cooling, 1988; Figure 6.3).

Dart & Swolfs (1992) described this phenomenon in the Manetta Basin in south-central Oklahoma and the Bravo Dome area of the central Texas Panhandle. Both areas show a variation in the orientation of σ_{Hmax} trajectories across areas bounded by subparallel faults. They propose that the areas bounded by the faults function as stress discontinuities, possibly re-orienting σ_{Hmax} as a result of fault overlap, fault separation and differences in Young's modulus of the faulted sediments. Similarly, Bell et al. (1992a) recognised that local deflections from the well established regional stresses within the offshore eastern Canada appear to be caused by intersecting or nearby open fractures and non-sealing faults. These features correspond to discontinuities with lower Young's modulus values than the surrounding rock mass and therefore rotate σ_{hmin} perpendicular to their orientation.

The flanks of the Barrow-Dampier Sub-basin are dominated by extensively faulted regions such as the Rankin Platform to the north and the Peedamullah Shelf (including the Flinders Fault System) and the Lambert Shelf to the south (Figure 2.4). These

areas may be acting as large scale discontinuities. The rotation of the stress field parallel to the margins is consistent with their being comprised of material with a low Young's modulus relative to the basin centre (i.e. open fractures and non-sealing faults). The higher concentration of faults at the flanks of the basin margins may be affecting the elastic properties of the rock mass at a range of scales and re-orienting the stress field.

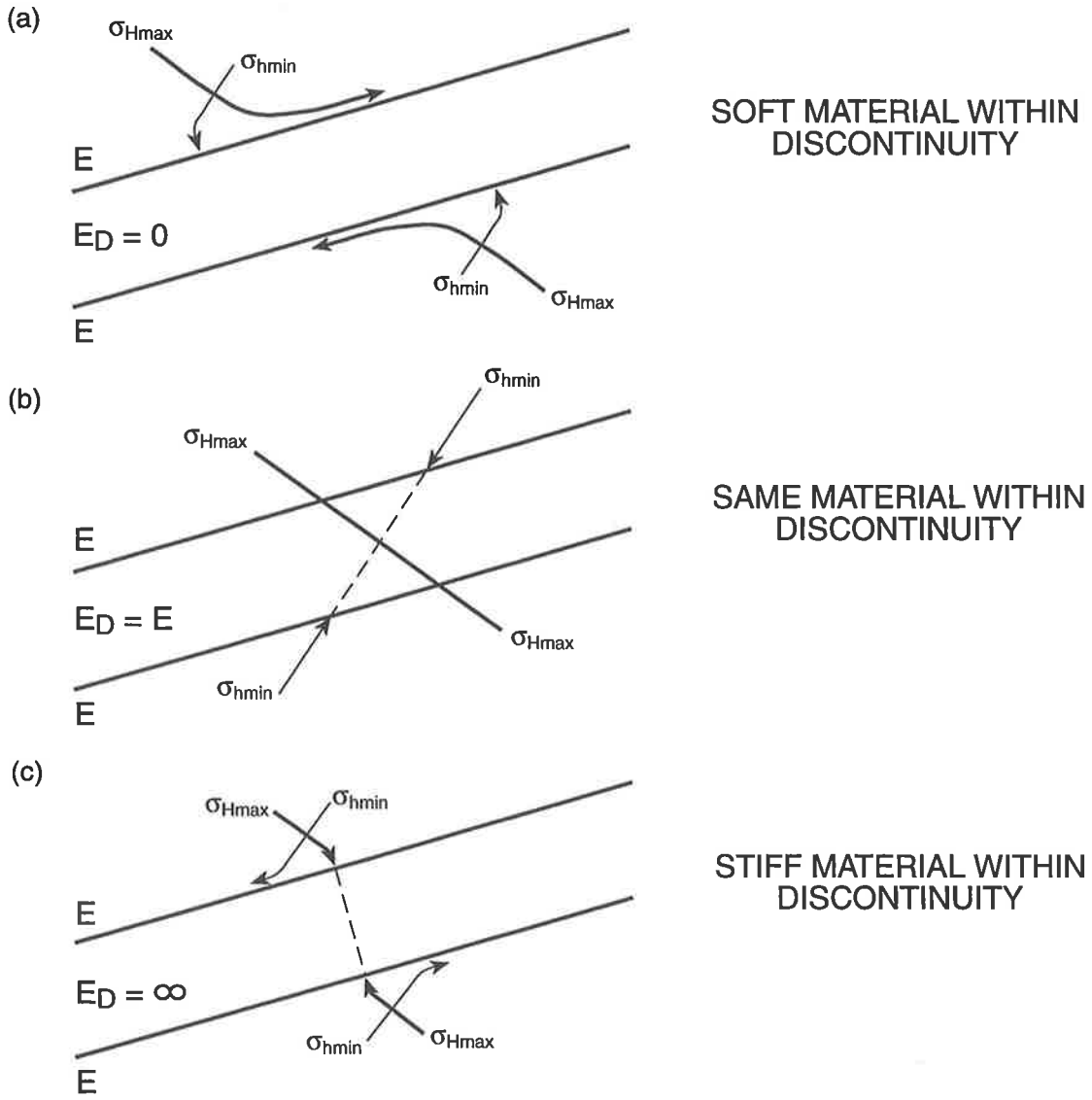

Figure 6.3 Schematic diagram illustrating the influences of Young's modulus (E) of displacement discontinuities (E_D) on maximum and minimum horizontal stress trajectories. Shown are displacement discontinuities of fault-bounded areas with a Young's modulus (a) less than, (b) equal to, and (c) greater than that of the adjacent rock. Modified after Hudson & Cooling (1988) and Dart & Swolfs (1992).

Active Faults

Active faults act as discontinuities and can locally perturb both stress magnitudes and orientations (Hickman et al., 1985; Paillet & Kim, 1987; Shamir & Zoback, 1992; Barton & Zoback, 1994). Active faults intersecting a borehole are expressed by the gradual rotation of breakout orientation and the abrupt termination of the breakout about 1m above the fault zone and are associated with a complete stress drop (Barton & Zoback, 1994). For example, Shamir & Zoback (1992) described a 32° rotation of breakouts interpreted from the Cajon Pass Scientific drillhole adjacent to the San Andreas Fault in southern California. They argue that slip on faults of various sizes are responsible for the fractal-like variability of breakout rotation on a wide range of wavelengths.

Borehole breakout azimuths within wells from the Carnarvon Basin show a rotation of up to 40° from the regional stress direction. The presence of active faults intersecting boreholes interpreted for this study, can neither be confirmed or denied, however, the greatest variability in breakout azimuth within individual wells occurs in the more structurally complex margins of the Barrow-Dampier Sub-basin (i.e. poor quality σ_{Hmax} means). Breakout azimuth rotation is not restricted to wells located on the basin margins. Bambra-1 is an example of a well located in the depositional centre of the Carnarvon Basin that exhibits anomalous stress rotations within.

Thirty-nine breakouts were interpreted from the Bambra-1 well, between 777 m and 3673 m with unweighted, length-weighted and eccentricity-weighted mean σ_{Hmax} azimuths of 073°N, 094°N and 074°N and quality ratings of D, B and D respectively (Figure 6.4). From 750 m to 1300 m the distribution of breakout azimuth is quite

variable. A large cluster of breakouts is oriented between 120°N and 150°N (NE-SW σ_{Hmax}), and several are oriented between 170°N to 180°N (E-W σ_{Hmax}). Below this, there is a gradual rotation in breakout azimuth shown by three relatively long breakouts oriented 175°N to 170°N over an interval of approximately 700m. Immediately below these, breakouts azimuth rotates to 140°N then back between 160°N and 170°N. A north-south oriented breakout extending for nearly 500 m immediately follows and is itself followed by another anti-clockwise rotation of short breakouts at approximately 2700 m. With the exception of one breakout oriented 030°N from 2800 to 3200 m and a short breakout at 050°N, the remaining breakout azimuths below are oriented approximately N-S.

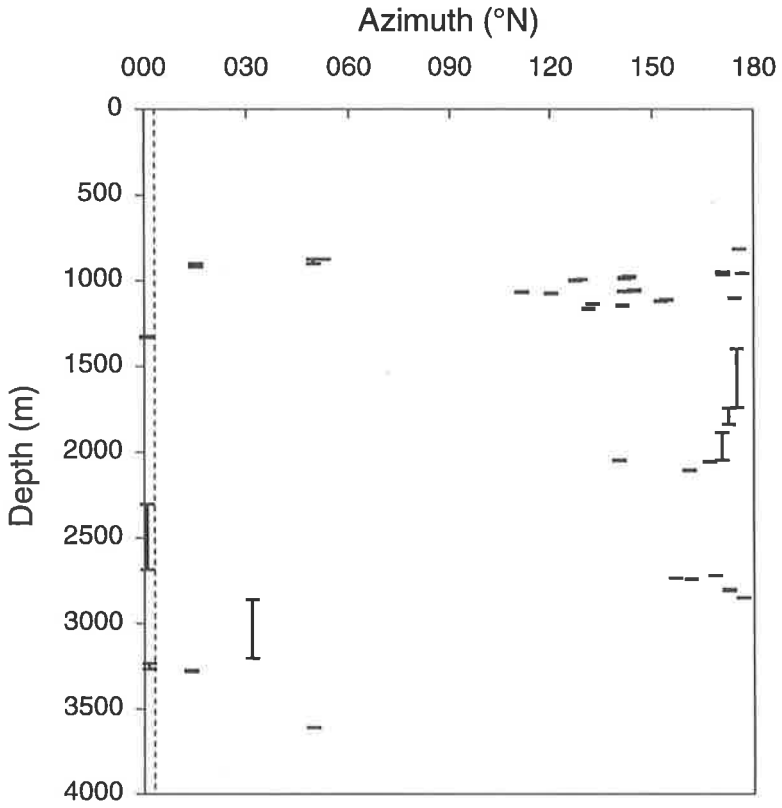

Figure 6.4 Breakout azimuth versus depth for the Bambra-1 well. Depth interval of breakouts are indicated. See text for description. The dotted line indicates the best weighted, mean breakout azimuth for the well.

A possible explanation for the breakout orientations in this well is that the borehole intersects active fault zones at depths of 1300, 2100 and 2700 m, interrupting the regional stress field and locally re-orienting the principal stresses. The variability in breakout orientation is reflected by the poor quality ratings for the unweighted and eccentricity-weighted σ_{Hmax}. However, the long breakouts aligned parallel to the regional stress field are responsible for the B quality rating of the length weighted σ_{Hmax} azimuth.

Summary

The stress rotations most evident at the margins of the Barrow-Dampier Sub-basin within the Carnarvon Basin, are closely linked with the greater density of faults and fractures in these areas. Of the theories discussed above, stress rotation due to contrasting elastic properties, and the intersection of active faults, are the most plausible. Both of these effects are scale independent and relate the rotations to structural features. The greater variation in breakout azimuth within wells on the flanks of the Barrow-Dampier Sub-basin suggests that stress rotations are localised and more likely to be caused by small scale discontinuities between elastic rock properties or by the presence of active faults. Without the use of detailed borehole images (eg BHTV), and detailed structural and stratigraphic data for individual wells, it is not possible to further investigate these hypotheses.

6.4 Fault Activity on the North West Shelf of Australia

The nature of the contemporary stress field can be used to constrain the probable style of present day fault movement. Planes inclined at 45° to the maximum principal stress are subject to the maximum shear stress. However, according to Coulomb-Navier

shear-stress criterion, the angle ψ, between σ_1 and fractures/faults is less than 45° (typically < 30°) such that:

$$\psi = \frac{\pi}{4} - \frac{\alpha}{2} \tag{6.1}$$

where α is the angle of internal friction (Anderson, 1951). Recent tectonism has considerably influenced the structural setting of the North West Shelf and there has been debate regarding the nature of any strike-slip movement, especially in the Timor Sea area (Woods, 1988; Nelson, 1989). The implications of this study for fault activity in the Carnarvon and Bonaparte Basins follows.

6.4.1 Active Faulting in the Carnarvon Basin

The regional σ_{Hmax} direction in the Carnarvon Basin is approximately 100°N to 110°N and the stress regime is in transition between extension and strike-slip. Using the Andersonian classification of stress regimes (Anderson, 1951), the associated preferred orientation of extensional reactivation is along planes oriented parallel to σ_{Hmax} and dipping approximately 30° from the vertical (Section 3.1). Strike-slip reactivation occurs preferentially on vertical planes striking approximately 070°N and 130°N. The mean σ_{Hmax} direction rotates to 060°N on the flanks of the Barrow-Dampier Sub-basin. The associated preferred orientation of extensional reactivation is along planes dipping 30° from the vertical, and striking 060°N. Strike-slip reactivation occurs preferentially on vertical planes oriented approximately 030°N and 090°N.

The Carnarvon Basin is comprised of predominantly NE trending Late Palaeozoic to Mesozoic depocentres and faults. Remnant N-S and NW trending faults of the earlier Palaeozoic rift systems and other E-W faults are also present in the basin (Figure 6.5).

The preferred reactivation style of faults on the margins of the Barrow-Dampier Sub-basin is different to that of faults in the centre of the Sub-basin because of the stress rotation discussed in Section 6.3. In the centre of the Barrow-Dampier Sub-basin, the NE oriented faults would be most susceptible to dextral strike-slip reactivation, the NW faults to sinistral reactivation and the E-W faults to extensional reactivation. The N-S faults, which are suitably oriented for compressional reactivation, are not likely to be reactivated because the stress regime is on the boundary between strike-slip and extension. On the margins of the sub-basins, faults oriented NE are most susceptible to normal reactivation, the E-W faults to sinistral strike-slip reactivation and the N-S faults to dextral strike-slip reactivation. The NW oriented faults, which are suitably oriented for compressional reactivation, are not likely to be reactivated because the stress regime is on the boundary between strike-slip and extension.

These predictions support previous reactivation models for the Carnarvon Basin. Seismic interpretation of the basin (AGSO North West Shelf Study Group, 1994), describes the abundance of high angle faulting, much of which appears to be dominated by strike-slip faulting. Parry & Smith (1988) suggest that significant phases of wrenching occurred in the Late Miocene with right lateral movement taking place mainly along pre-existing normal faults. The implications of the contemporary stress field suggest that this motion is still occurring today as a continuation of the Miocene-Pliocene collision between the Australian Continent and Timor, however, the orientation of strike-slip reactivation is variable between the basin centre and margins.

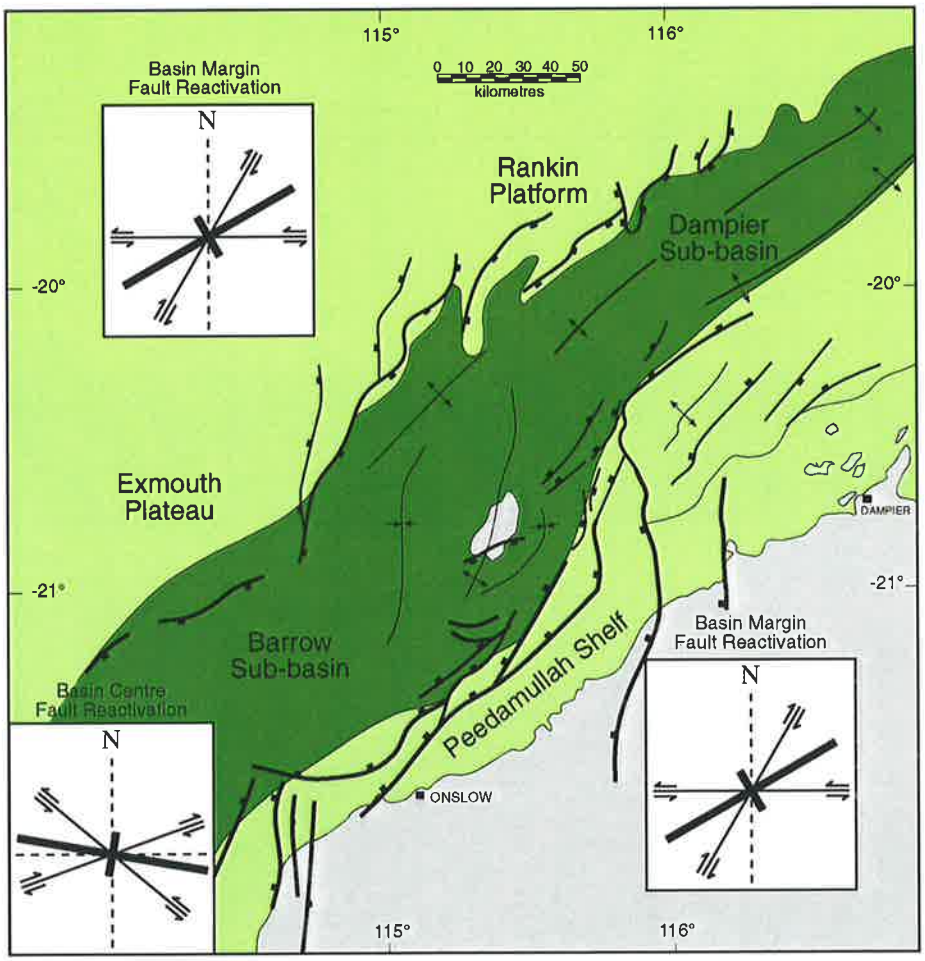

Figure 6.5 Structural elements of the Carnarvon Basin illustrating the orientations of faults susceptible to reactivation. In the basin centre, faults oriented 100°N are most susceptible to extensional reactivation and faults oriented 070°N and 130°N are most susceptible to strike-slip reactivation. On the basin margins, faults oriented 060°N are most susceptible to extensional reactivation and faults oriented 030°N and 090°N are most susceptible to strike-slip reactivation.

6.4.2 Active Faulting in the Bonaparte Basin

The regional σ_{Hmax} direction in the Bonaparte Basin is approximately 055°N to 060°N and the stress regime is in transition between extension and strike-slip. There exist three distinct structural trends in the Bonaparte Basin (Nelson, 1993; O'Brien et al., 1993). Extensional reactivation in the basin is most likely to occur on planes dipping approximately 30° from the vertical, striking parallel to σ_{Hmax}. Strike-slip reactivation occurs preferentially on vertical planes oriented 30° from σ_{Hmax}, i.e. 030°N and 090°N respectively. The Petrel Sub-basin developed along a NW trending fault system. This NW trend was overprinted in the Jurassic by a NE/E-NE trend during creation of the

present day continental margin. E-W trending faults also exist (Figure 6.6). The dominant NE/E-NE structural trend is susceptible to extensional reactivation, the E-W trend is most susceptible to sinistral strike-slip reactivation and the Palaeozoic NW structural trend is susceptible to compressional reactivation, however this is unlikely given that the stress regime is on the boundary between strike-slip and extension (Figure 6.6).

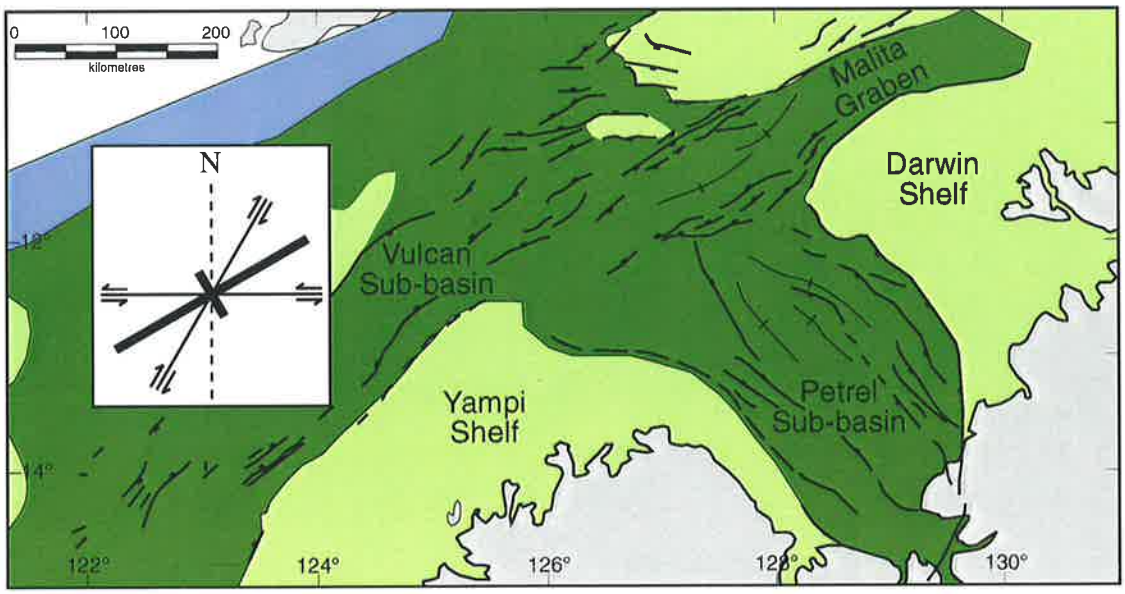

Figure 6.6 Structural elements of the Bonaparte Basin illustrating the orientations of faults susceptible to reactivation. Faults oriented 060°N are most susceptible to extensional reactivation and faults oriented 030°N and 090°N are most susceptible to strike-slip reactivation.

The nature of reactivation in the Bonaparte Basin since the Miocene-Pliocene collision has been extensively debated. Woods (1988) argued that hourglass structures in the Vulcan Sub-basin are a result of rejuvenation of major Jurassic faults by extensional Tertiary tectonism. Nelson (1989) argued that the same structures are a result of strike-slip and dip-slip reactivation along the NE trending fault system. Strike slip motion in the Bonaparte Basin is more likely to occur along E-W oriented faults than the NE trending structural grain which is most susceptible to extensional reactivation. In a regional sense the Woods (1988) extensional model correlates more accurately

with the contemporary stress field than the Nelson (1989) strike-slip model. However, local stress rotations may lead to localised reactivation of the type envisaged by Nelson (1989).

6.5 First-Order Stress Rotation and the Implications for Plate Boundary Forces

As discussed in the introduction, first-order stress patterns are the result of plate boundary forces. The nature of the boundaries of the Indo-Australian Plate has been described in Section 2.3. The complex nature of the NE convergent plate boundary imposes a variety of forces within, and is responsible for major stress rotations which characterise the Indo-Australian Plate (Coblentz et al., 1995). The following discussion presents the results of the NWS stress field analysis in the context of the plate boundary forces acting on the Indo-Australian Plate and compares the observed stress field with theoretical stress models developed by Coblentz et al. (1995).

6.5.1 Observed Stress Field and Plate Boundary Forces

Oceanic lithosphere of the Indo-Australian Plate is being subducted at the Java trench and in New Guinea the Indo-Australian Plate is involved in continent-continent collision with the Pacific Plate. However, the situation in the intervening Banda Arc is more complex, reflecting a transition between these two scenarios. Continental crust is continuous between the Australian Continent and the Banda Arc (Whitford and Jezek, 1982; Chamalaun et al., 1976). The relative aseismicity of the Timor Trough (Cardwell & Isacks, 1978), the slowing of convergent motion in the Trough since the mid Pliocene (Johnston & Bowin, 1981), and the cessation of volcanism 3 Ma in the volcanic arc north of Timor (Abbot & Chamalaun, 1981), all suggest that the arrival of buoyant Australian continental crust has choked the former Banda Arc subduction

system. Global Positioning System measurements suggest that the Banda Arc has been accreted to the Australian continent, and that convergence, now ceased in the Timor Trough, is being taken up on thrusts to the north of the Banda Arc (Genrich et al., 1996).

Given the cessation of convergence between Australia and the Banda Arc, presumably there is no net slab pull force generated in the vicinity of the Timor Trough. McCaffrey et al. (1985) interpreted earthquake fault plane solutions to indicate that the subducted lithosphere is presently detaching from the surface lithosphere north of Timor. However, the σ_{Hmax} orientation in the Bonaparte Basin, which is sub-parallel to the strike of the Banda Arc, suggests that neither is a net push generated by Australia/Banda collision. This is perhaps not surprising, given that the present Timor Trough formed only in the mid Pliocene and a foredeep of 2 km water depth, albeit floored by continental crust, still separates the two areas (DSDP, 1974).

The 050-060°N σ_{Hmax} orientation of much of the northern Australian margin is approximately orthogonal to the trend of the New Guinea orogen. The highlands of the New Guinea orogen, elevated up to 5 km, mark older, and more mature, Oligocene collision than that in the Banda Arc (Pigram and Davies, 1987). Hence, the stress field of the northern Australian margin may be controlled by the New Guinea orogen. The generation of NE-SW oriented stresses in the northern Australian margin by the orthogonally oriented New Guinea orogen is analogous to the NE-SW σ_{Hmax} orientation in the western Canadian Basin due to the orthogonally oriented Rocky Mountain orogen (Bell & Babcock, 1986). The net force orthogonal to the Banda Arc

does not, at least yet, appear to have built up to the level of that imposed by the New Guinea orogen.

6.5.2 The Observed Stress Field and Theoretical Stress Field Models of the Indo-Australian Plate

Elastic finite-element modeling of the stress field of Australian continent has been conducted by Coblentz et al. (1995) to constrain the poorly understood forces acting along the convergent NE boundary of the Indo-Australian Plate. Coblentz et al. (1995) generated four different models of the stress field of the Australian continent, in which a variety of forces were applied at the convergent NE boundary segments (Figures 6.7):

1. entire convergent north-eastern boundary balances topographic forces (principally mid-ocean ridge push) acting on the plate equally along its length, regardless of the nature of the convergent boundary, ie. no additional forces generated at the convergent boundaries, only reaction forces;
2. only the collisional segments of the convergent boundary balance topographic forces (ie. forces balancing the topographic forces focused at segments of continental collision such as New Guinea, but no forces generated at the convergent boundaries);
3. compressive forces generated at the collisional segments incorporated in addition to the topographic forces, with force balance achieved by incorporating the drag force at the base of the lithosphere (no forces generated at subducting boundaries); and
4. topographic, compressive collisional and tensional subduction forces all act on the plate, with force balance achieved by incorporating the drag force at the base of lithosphere.

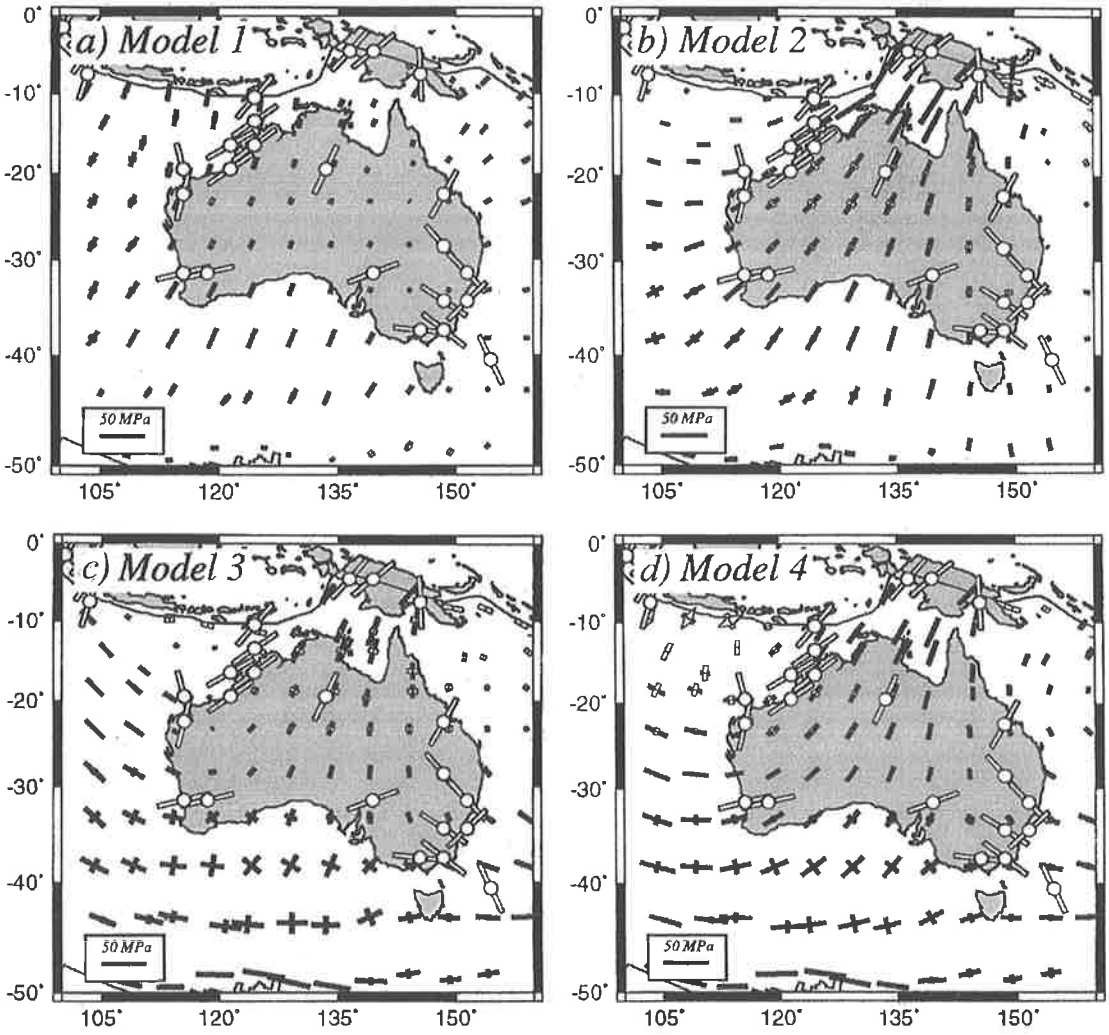

Figure 6.7 Stresses predicted for the Australian Continent by Coblentz et al. (1995) using elastic finite element modeling with different plate boundary forces acting on the Indo-Australian Plate. Solid bars indicate (the direction of maximum) deviatoric compression and open arrows indicate deviatoric tension. Average maximum horizontal stress orientations (σ_{Hmax}) orientations in 3° x 3° bins of data from the World Stress Map (Zoback, 1992) are indicated by open bars centred on open circles. (a) Model 1: topographic forces (principally ridge push) acting on the plate are balanced by fixing the entire north-eastern convergent plate boundary. (b) Model 2: topographic forces are balanced by fixing the collisional segments of the north-eastern convergent boundary, ie. Himalayas, New Guinea and New Zealand. (c) Model 3: Basal drag is used to balance topographic and collisional forces, with other boundaries left free. (d) Model 4: Basal drag is used to balance topographic, collisional and subduction forces acting on the plate. See text for further discussion.

The forces acting in the four models are summarised in Table 6.1 and the force magnitudes applied are given in Table 6.2. The four models were presented in order to determine which fitted best the observed stress field of the Australian continent, and thus assess the relative contribution of the forces applied in the various models. In order to test the models against the observed stress data for the Australian continent,

Coblentz et al. (1995) averaged stress indicators within 3° x 3° bins. Using the previously existing data in the World Stress Map (Zoback, 1992), Coblentz et al. (1995) inferred that the regional σ_{Hmax} orientation in the Carnarvon Basin was approximately N-S (Figure 6.7). The regional σ_{Hmax} orientation in the Carnarvon Basin has now been shown to be E-W.

Model	Ridge Push	Collisional Boundaries	Other Boundaries	Drag Force
1	X	P	P	-
2	X	P	F	-
3	X	X	F	X
4	X	X	X	X

Table 6.1 Description of forces applied by Coblentz et al. (1995) in the four stress field models of the Indo-Australian Plate. Symbols indicate the following: X, applied force; P, pinned boundary, and; F, free boundary. Collisional Boundaries include Himalaya, Papua New Guinea, and New Zealand. Other Boundaries include Sumatra, Java, Banda, Solomon, New Hebrides, and Tonga-Kermadec. See text for discussion.

The models presented by Coblentz et al. (1995) assume the lithosphere to be a constant thickness of 100 km. The predicted horizontal stresses should be interpreted as those stresses which deviate from the lithostatic reference state (Engelder, 1993). Modelled stress orientations and magnitudes are averaged through the entire lithosphere, as opposed to the observed data which come from relatively shallow depths. Thus, although there are differences in the nature of the modelled and observed stresses, it is instructive to compare the predictions of Coblentz et al.'s (1995) 4 models with the observed data. The spurious regional N-S σ_{Hmax} orientation in the Carnarvon Basin fits Coblentz et al.'s (1995) model 1, which predicts a nearly uniform NNE stress orientation across the Australian Continent (Figure 6.7). However, on the basis of other stress indicators from the Australian Continent, Coblentz et al. (1995) argued that model 1 oversimplified the forces acting along the

northeastern plate boundary. This is also supported by the stress field data presented here in that the observed stress rotation along the North West Shelf requires heterogeneous forces acting along the convergent boundary to the north.

Force	Magnitude [x 10^{12}Nm^{-1}]	Total Torque [x 10^{25}Nm]	Latitude [deg]	Longitude [deg]
Collisional Boundaries				
Himalaya	2.0	3.2	0.0 N	17.9 E
Papua New Guinea	2.0	1.9	39.8 S	123.1 W
New Zealand	2.0	2.1	47.2 S	7.9 W
Other Boundaries				
Sumatra	-2.0	1.9	19.0 N	9.6 E
Java	-2.0	2.1	18.7 N	23.7 E
Banda	1.0	1.0	15.7 S	141.8 W
Solomon	-1.0	0.8	39.3 S	102.5 W
New Hebredes	-1.0	0.5	69.7 N	132.1 E
Tonga-Kermadec	1.0	1.3	63.6 S	9.1 E
Non-Boundary Forces				
Ridge Push	—	8.5	30.3 N	34.5 E
Continental Margins	—	2.6	14.7 S	168.3 W
Elevated Continent	—	1.7	18.8 S	169.2 W
Drag (Model 3)	—	4.3	1.8 N	58.3 W
Drag (Model 4)	—	3.8	4.5 N	102.4 W

Table 6.2 Boundary forces and torque contributions for Coblentz et al. (1995) models presented in Figure 6.7. Positive forces are directed towards the interior of the plate. Note: Force magnitude of 1 x 1012 Nm-1 is equivalent to a stress of 10 MPa across a plate of thickness 100km.

Coblentz et al.'s (1995) models 2, 3 and 4 all show reasonable agreement with the observed stress field of the northern Australian margin (Figures 6.7). Discrepancies between the fit of models 2, 3 and 4 to the observed data are less pronounced than the misfit with model 1. The predicted σ_{Hmax} orientations within model 2 fit the observed

stress rotation on the North West Shelf most accurately, although, it predicts σ_{Hmax} to be significantly greater than σ_{hmin} and σ_v (boundary between compressional and strike-slip stress regimes) in the Bonaparte area, instead of the observed transition from normal to strike slip documented in Section 5.3.3. Model 2 also predicts a transition from strike-slip to compression away from the coastline to the northwest in the Carnarvon area, instead of the strike slip to normal transition seen in the observed data (Figure 5.11).

The stresses predicted by model 3 show discrepancies with the observed stress field in the Carnarvon area but compare well in the Bonaparte. The predicted σ_{Hmax} orientation in the Carnarvon Basin is approximately 30° south of the observed 090°N direction. Predicted stress magnitudes in the western part of the Carnarvon indicate a compressional/strike-slip stress regime, and the north and eastern parts are nearly lithostatic. Stresses in the Bonaparte Basin are oriented within 30° of the observed stress orientation and predict a northeast trending transition from an extensional/strike-slip to strike-slip stress regime, much like the observed data.

Model 4 fits the observed stress field in the Carnarvon Basin well, but fails to replicate the stress field observed in the Bonaparte Basin. The σ_{Hmax} orientation in the Carnarvon basin reflects the observed E-W orientation and the deviatoric stress magnitudes predict a northwest transition from strike-slip to extension/strike-slip. Although similarly oriented to model 3, predicted stresses in the Bonaparte Basin indicate compression/strike-slip unlike the transition from extension/strike-slip to strike-slip in model 3.

Models 2, 3 and 4 by Coblentz et al. (1995) are successful in replicating the observed rotation of the stress field along the North West Shelf. This supports the suggestion of Coblentz et al. (1995) that the orientation of the stress field can, to a first-order, be explained in terms of a balance between topographic forces (predominantly comprised of mid ocean ridge push), and resistance to those forces at the collisional segments of the NE boundary of the Indo-Australian Plate (ie. Himalayas, New Guinea and New Zealand). However, none of the models predict the transitions between stress regimes that occur within the two Basins, at once. Models 3 best predicts the observed stress magnitude relationships in the Bonaparte Basin and Model 4 best predicts the stress magnitude relationship in the Carnarvon Basins. A model with boundary conditions set somewhere between the values used for these two models might generate a closer theoretical representation of the observed stress field. The differences between the boundary conditions of these two models can be used to make inferences on the relative contributions of plate boundary forces.

Model 3 employs a resistive force at the collisional Himalayan, Papua New Guinea, and New Zealand segments and no other forces along the NE boundary (Table 6.1). Model 4 includes these forces but also incorporates those acting along the other plate boundary segments (Sumatra, Java, Solomon, New Hebridies and Tonga-Kermadec trenches and the Banda Arc). The tensional forces associated with the Sumatra and Java subduction zones accounts for the predicted transitional stress regimes in the Carnarvon Basin. This is also consistent with the action of tensional forces at subducting plate boundaries, specifically the Sunda Arc, as invoked by Cloetingh and Wortel (1986). The stress transition in the Bonaparte Basin may be replicated by minimising the contribution of collisional forces by the Banda Arc. This agrees with

the previously stated suggestion, based on the observed stress data, that a net push is not yet being generated by the Australia/Banda collision.

The exact magnitude of the forces acting along the northern and eastern boundaries of Indo-Australian Plate remains controversial (Cloetingh & Wortel, 1985). Coblentz et al. (1995) chose forces of the same magnitude but opposite in sense (2.0×10^{12} Nm^{-1}), acting along the collisional boundaries and the subduction zones (Table 6.1). By altering the magnitude of the various boundary segments along the northern margin in the manner suggested it may be possible to better replicate the observed stress field. However, additional finite-element modelling is beyond the scope of this project.

In summary, the critical and confident conclusion that can be made is that the observed stress data clearly indicate that the forces acting along the NE boundary of the Indo-Australian Plate must be heterogeneous. This heterogeneity reflects the complexity of convergent processes along the plate margin.

Chapter 7

Implications of the Contemporary Stress Field for Petroleum Exploration and Production

7.1 Introduction

Knowledge of the contemporary stress field impacts on a number of issues related to hydrocarbon exploration and production; namely:

- wellbore stability (e.g. Bradley, 1979; Addis et al., 1993; Hillis & Williams, 1993a; Tan et al., 1994);
- the orientation of induced, hydraulic fractures and enhanced oil recovery operations (e.g. Bell & Babcock, 1986; Lacy & Smith, 1989; Bell, 1990a), and;
- the orientation of open, natural fractures and fluid flow in reservoirs (e.g. Horn, 1991; Hillis & Williams, 1993b);
- hydraulic seal integrity (e.g. Caillet, 1993; Gaarenstroom et al., 1993; Mildren et al., 1994).

These issues affect hydrocarbon exploration and production on the North West Shelf to varying degrees. This chapter presents some problems encountered in both the Carnarvon and Bonaparte Basins, and discusses how the contemporary stress field can impact on them. Although, for the purposes of discussion, regional stresses are used to address these problems, localised knowledge of the stress field is required to address these issues at the prospect-scale.

7.2 Implications for Borehole Stability

Borehole instability remains a significant problem for many wells drilled on the North West Shelf of Australia (Kingsborough et al., 1991). Vertical and horizontal wells are

both affected by instability. Instability threatens to be the greatest impediment to the realisation of benefits offered by horizontal drilling technology. Borehole instability is most common in shales and can be characterised into two distinct types (Hillis & Williams, 1993a):

- physico-chemical interaction between shales, their formation fluid and the particular mud system, which causes a loss of strength to the shales, and;
- stress related mechanisms, where stresses associated with far-field forces, formation fluid pressure, stress changes arising from the drilling of the borehole, and mechanisms such as the invasion of mud into the formation, combine to exceed the strength of shales.

This section will focus on applying the observed in-situ stress field of the North West Shelf to managing stress induced borehole instability of vertical and deviated wells in the region.

7.2.1 Background Theory of Borehole Stability

Drilling fluids, commonly referred to simply as 'mud', are circulated up and down wells during drilling and are used to control borehole instability. By increasing the density of the circulating fluid, the pressure it exerts on the borehole wall is increased, decreasing the maximum circumferential stress at the borehole wall and inhibiting the formation of breakouts (Equation 3.13). However, if the fluid pressure exceeds the breakdown pressure of the formation (Equation 3.17), a hydraulic fracture will form at the wellbore and fluids will be lost to the formation. The limits placed on fluid pressure by these failure types, defines a range of mud-weights for which the borehole will remain stable which is described by the relationship:

$$3\sigma_{Hmax} - \sigma_{hmin} - S_0 < P_f < 3\sigma_{hmin} - \sigma_{Hmax} - P_p + T_0 \qquad (7.1)$$

where S_0 is the shear strength of the rock. The upper and lower bounds to the safe mud-weight envelope (i.e range within which neither breakouts nor hydraulic fractures develop), are functions of deviation angle and wellbore orientation with respect to the orientation of the in-situ stress field (Hillis & Williams, 1993a). The nature of these relationships is essentially determined by the fault condition, i.e by the relative magnitudes of the vertical and horizontal stresses (Hillis & Williams, 1993a). In general, the greater the stress anisotropy, the higher the lower-bound mud-weight, and the lower the upper-bound mud-weight, minimising the range of mud-weights for borehole stability.

7.2.2 Wellbore Stability on the North West Shelf of Australia

In the Carnarvon and Bonaparte Basins the stress regime is on the boundary between extension and strike-slip (Chapter 5). Given that $\sigma_v \approx \sigma_{Hmax}$, a horizontal well drilled in the σ_{hmin} direction will minimise the stress anisotropy to which the wellbore is subject (Figure 7.1). A well drilled in this orientation will maximise the safe mud-weight envelope and provide the greatest opportunity for wellbore stability. In practice, reservoir geometry/engineering considerations will generally determine drilling direction, however, the above approach allows the propensity of breakout in horizontal wells to be predicted, and suitable well planning, for example of mud weights and casing depths, to be undertaken (Tan et al., 1994).

7.3 Implications for Hydraulic Fracture Orientation

Hydraulic fractures open against the least principal stress, and propagate in a plane parallel to the maximum principal stress direction (Section 3.3.2, Figure 7.2).

Knowledge of the in-situ stresses can be used to predict the orientation of induced hydraulic fractures, and thus to plan various fracturing operations.

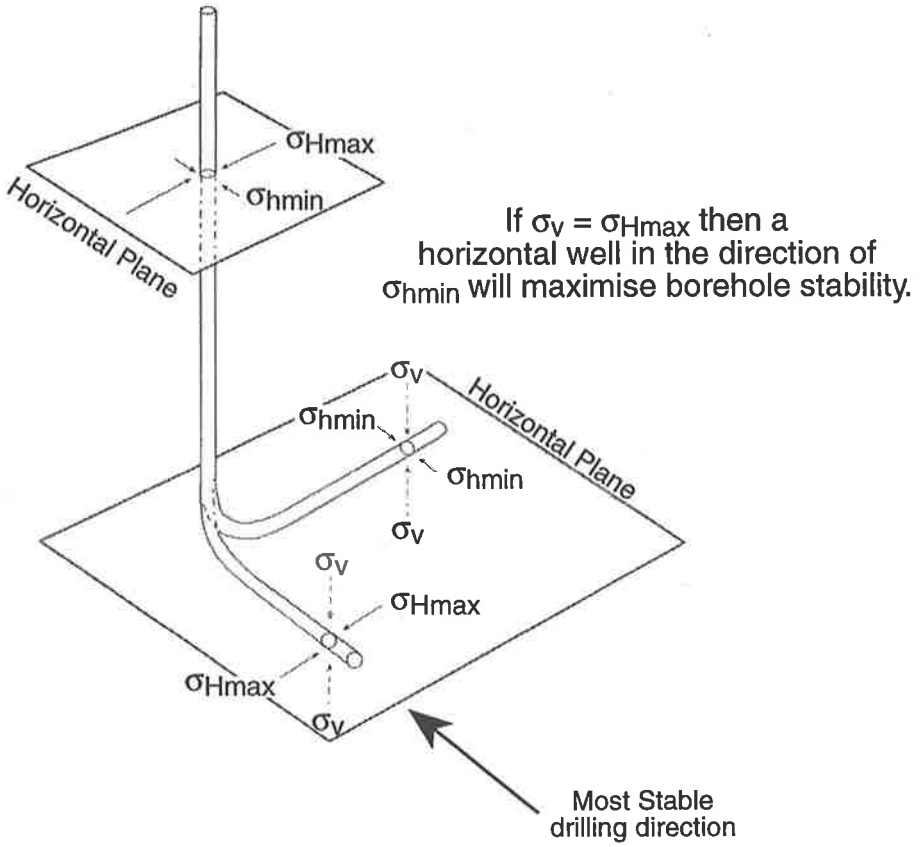

Figure 7.1 Stresses acting on a vertical and horizontally deviated borehole (after Hillis & Williams, 1993a).

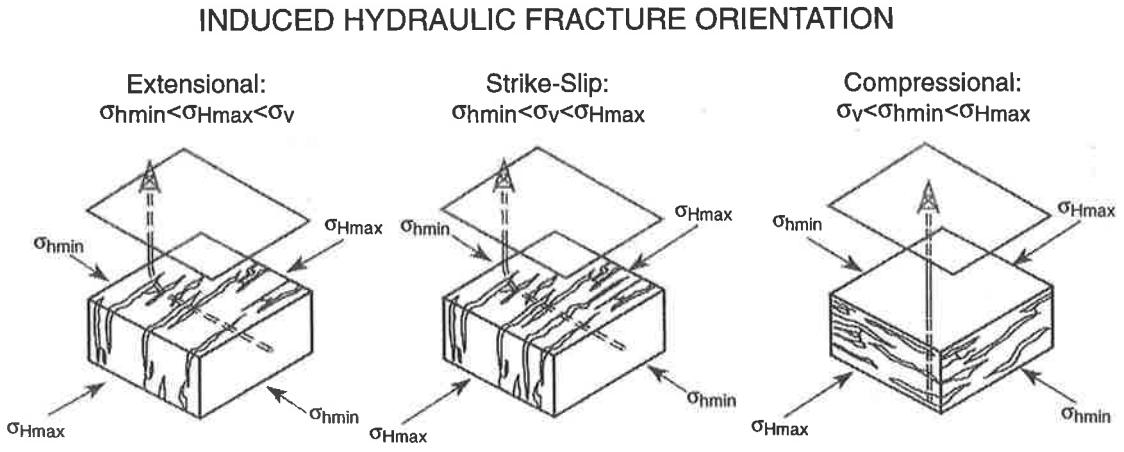

Figure 7.2 The orientation of induced hydraulic fractures (and preferred orientation of open, natural fractures for a given stress regime (after Hillis & Williams, 1993b)

7.3.1 Applications for Hydraulic Fracture Orientation Prediction

Knowledge of hydraulic fracture operation may allow a deviated well to be planned such that it can be stimulated by multiple hydraulic fractures (Bell, 1990a). In the extensional or strike-slip regime hydraulic fractures open orthogonally to σ_{hmin}. If a well is deviated in the σ_{Hmax} direction, an inclined hydraulic fracture will tend to be axial to the well (Figure 7.3a). However, if a well is deviated in the σ_{Hmin} direction, it may be possible to further stimulate production from within the reservoir by multiple hydraulic fractures (Figure 7.3b).

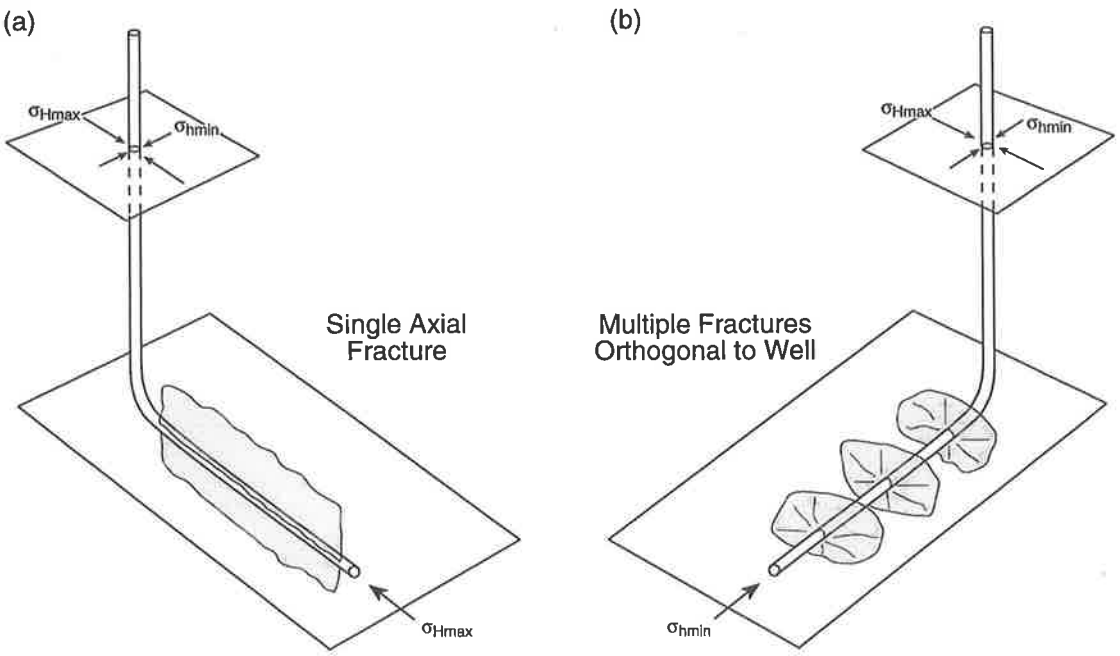

Figure 7.3 Schematic diagram of (a) a single hydraulic fracture, axial to the wellbore deviated in the σ_{Hmax} direction and (b) multiple hydraulic fractures orthogonal to the wellbore drilled in the σ_{hmin} direction.

Although beyond the scope of this thesis to discuss in detail, if planning multiple fractures of a deviated well, consideration should be given to stress concentrations around the wellbore with respect to that in the far field. Stress concentrations around the wellbore may favour axial fractures even where the far field stresses favour

orthogonal fractures. In such a case, fractures may twist from axial to orthogonal as they propagate away from the wellbore. Twisting of the fracture may lead to a loss of fracture conductivity and a loss of any gains associated with multiple hydraulic fractures.

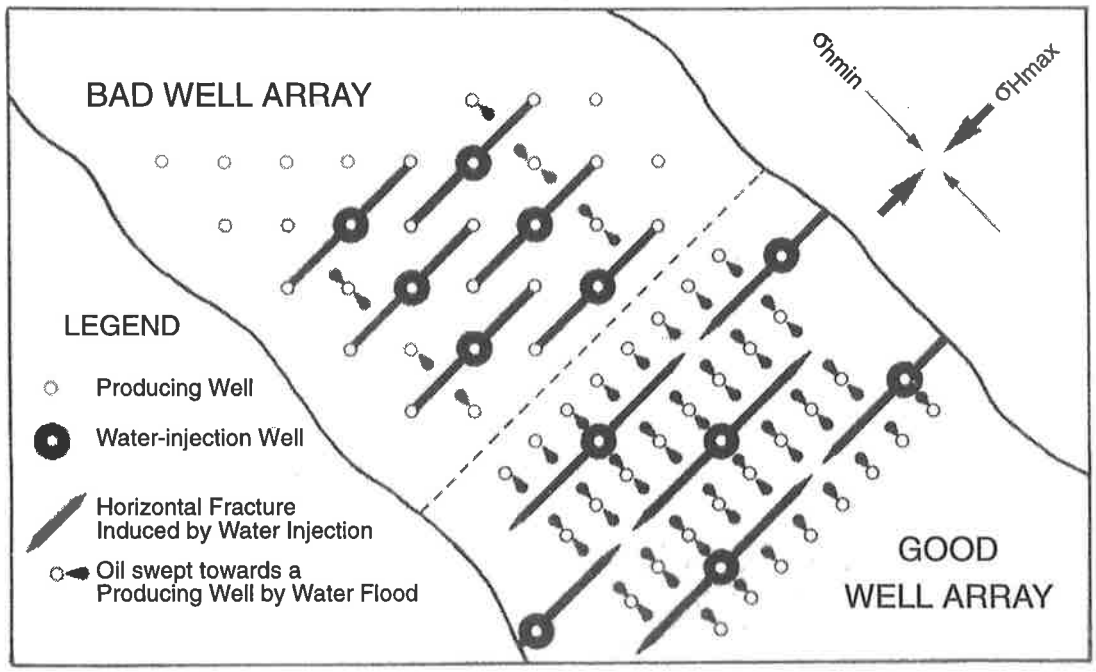

Figure 7.4 Map of well arrays in an oilfield where water flooding promotes hydraulic fracturing (after Bell & Babcock, 1986).

Bell & Babcock (1986) described the application of hydraulic fracture prediction for a situation where an exploration well has missed an isolated target such as a pinnacle reef. Hydraulic fracture can be used to connect the well to the reservoir, avoiding other costly options. Predicted hydraulic fracture propagation directions can be used to design placement of wells for water flooding and production in enhanced oil recovery (EOR) operations (Bell & Babcock, 1986). Previous workers have described reduction of oil recovery by using inappropriate placement of injection and production wells (McLeod, 1977; Hassan, 1982). An idealised well array will prevent direct connectivity of injection water with production wells and distribute the injected water

so that it flushes oil from as much of the reservoir as possible (Bell & Babcock, 1986; Figure 7.4).

7.3.2 Orientation of Hydraulic Fractures on the North West Shelf of Australia

The relationship between the principal stresses in the Carnarvon and Bonaparte Basins indicates that σ_{hmin} is the least principal stress in both areas. Hydraulic fractures will open orthogonally to σ_{hmin} and propagate in a vertical plane defined by σ_{Hmax} and σ_v. Hence, hydraulic fractures will be vertical and oriented approximately 100°N within the depocentres and 060°N on the flanks of the Carnarvon Basin, and 060°N within the Bonaparte Basin.

7.4 Implications for Natural Fracture Orientations

The widespread application of highly deviated and horizontal drilling has led to the exploitation of naturally fractured reservoirs that have an intergranular porosity that would not permit economic recovery of hydrocarbons. Natural fracture orientation is not normally related to the contemporary stress field, however, several studies have shown that in areas where orthogonal sub-vertical fracture sets are present in the surface outcrop, only the fracture set perpendicular to σ_{hmin} is open and controls the reservoir. Such examples include the Austin Chalk in Texas (McNaughton, 1991; Horn, 1991), the Silo Field in Wyoming (Martin & Davis, 1987) and the Conoco Oklahoma test facility (Queen & Rizer, 1990). It appears that in these cases natural fractures are only open and productive when they are orthogonal to σ_{hmin} (Hillis & Williams, 1993a; Figure 7.2). Fractures orthogonal to σ_{Hmax} are often rendered closed and unproductive. On the other hand it should be noted that stiff fractures, such as those in the Ordovician quartzites of the Palm Valley field of central Australia may

tend to be relatively stress insensitive (Berry et al., 1996). Hillis (1997) has discussed the relative role of the in-situ stress field and fracture stiffness in predicting open natural fracture orientations.

The Flamingo Group of the Bonaparte Basin is naturally fractured near the axis of the Sahul Syncline (Lowry, 1995), and is a potential reservoir in the area, though secondary to reservoirs with primary porosity. In order to maximise intersection with, and thus production from natural fractures in this area, wells should be deviated in the 150°N direction. Similarly, for any naturally fractured reservoirs in the Carnarvon Basin, wells should be deviated towards 010°N if they are located within the depositional centre of the basin and 150°N if within the basin margins.

7.5 Implications for Hydraulic Seal Integrity

Seal integrity is a major concern for hydrocarbon explorationists world-wide and in particular, in the Bonaparte Basin on the North West Shelf. Apart from the commercial discoveries of Jabiru, Challis/Cassini and Skua, hydrocarbon exploration results in the Timor Sea have been disappointing. After the drilling of some 150 exploration wells, the estimated total recoverable volume of oil for the region is around 200 million barrels. Recently, however, there have been some more discoveries such as Elang, Kakatua and Undan/Bayu in the Zone of Cooperation (Figure 2.1). The presence of oil fields in the area demonstrates the existence of source, reservoir, seal and migration pathways, and suitable trap formation/migration timings. However, many potential reservoirs appear to have leaked, revealing only residual hydrocarbon columns, which are indicated by inclusions within reservoir cements (Lisk & Eadington, 1994; O'Brien & Woods, 1995). The reactivation of faults associated with

the Mio/Pliocene-Recent collision of the Australian Continent with the Banda Arc (Woods, 1988; Hillis, 1990; Pattillo & Nicholls, 1990; Woods, 1992) may have provided a pathways through which leakages occurred. Since the contemporary stress field of the Timor Sea still reflects the current early stage of the Australia/Banda collision (Hillis, 1991), analysis of the contemporary stress field may reveal which fault trends are more likely to be sealing or non-sealing.

Seals to hydrocarbon reservoirs can be classified as membrane seals or hydraulic seals (Watts, 1987). The dominant trapping mechanism of membrane seals is the capillary properties of the cap rock, where the minimum displacement (or breakthrough) pressure of the cap rock equates to the pressure required for hydrocarbons to enter the largest interconnected pore throat of the seal. A membrane seal will trap a hydrocarbon column until the net buoyancy pressure (related to the difference between the hydrocarbon and water densities) of the hydrocarbons exceeds the capillary breakthrough pressure of the seal. An alternative type of cap rock seal, known as a hydraulic seal, is that where the capillary breakthrough pressure is so high (some tight shales, and various evaporites), that seal failure occurs by natural hydraulic fracturing of the cap rock. Hence, the integrity of hydraulic seals are controlled by the contemporary stress field, and knowledge of the contemporary stress field can be used to help assess hydraulic seal integrity. Unpublished mercury injection capillary tests undertaken on Timor Sea seals suggests that they are effective membrane seals and thus seal failure is believed to be by hydraulic processes and controlled by the contemporary stress field.

The importance of considering the contemporary stress field in predicting hydraulic seal integrity has only recently been realised. Caillet (1993), in a study of the Snorre Field, North Sea, stated that the 'distribution of the stress field linked to structural features and varying with the tectonic context is one of the main parameters controlling the sealing efficiency of faults and caprocks'. Knott (1993), also looking at the North Sea, determined that a correlation existed between fault orientation and its sealing potential. Various authors have shown that pressure and contemporary stress conditions (magnitude) are the key factors governing the fracturing/integrity of reservoir seals (Du Rouchet, 1981; Watts, 1987; Caillet, 1993; Leonard, 1993; Gaarenstroom et al., 1993). This section considers sealing integrity of faults with respect to the principal stresses in the Timor Sea.

7.5.1 Background Theory

Fault-trap integrity is dependent on the orientation and magnitude of the principal stresses and pore pressure, and the orientation of faults/fractures in the seal. The greater the effective normal stress acting on a fault, the greater its probability of sealing (Mildren et al., 1994; Appendix D). The effective normal stress (σ'_n) is defined as the stress that is acting normal (perpendicular) to the fault plane (σ_n) minus the pore pressure (P_0):

$$\sigma'_n = \sigma_n - P_0 \qquad (7.2)$$

In the case of a vertical fault, σ_n will be maximised if σ_{Hmax} is normal to the fault. The greatest sealing potential occurs for a fault perpendicular to σ_{Hmax} (i.e. parallel to σ_{hmin}). For a vertical fault oblique to σ_{Hmax} and σ_{hmin}, their respective components acting on the fault must be combined to determine σ_n according to the relationship:

$$\sigma_n = \frac{(\sigma_{Hmax} + \sigma_{hmin})}{2} + \frac{(\sigma_{Hmax} - \sigma_{hmin})}{2}\cos 2\theta, \qquad (7.3)$$

which gives the normal stress acting across a plane whose normal is inclined at θ to σ_{Hmax} (Hobbs et al., 1976). For a non-vertical fault the component of σ_v acting on the fault must be combined with the σ_{Hmax} and σ_{hmin} components to determine σ_n, and hence σ'_n.

Faults with a low probability of sealing (σ_{Hmax} parallel), may still be shown to have high integrity due to factors such as connectivity, clay smear, age of faulting and fault healing (Knott, 1993; Watts, 1987). Conversely, pore pressure may affect the hydraulic integrity of traps with a high probability of sealing. Natural hydraulic fractures will open parallel to σ_{Hmax} according to the relationship:

$$P_0 \geq \sigma_{h\,min} + T_0 \qquad (7.4)$$

where T_0 is the tensile strength of the rock (Caillet, 1993: du Rouchet, 1981; Figure 7.5). Even if σ_{hmin} is generally greater than P_0 fault-traps may be subject to hydraulic fracturing as a result of natural episodic pressure pulses (Cartwright, 1994).

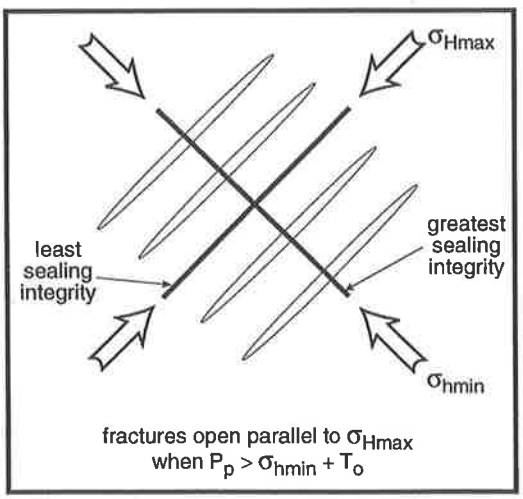

Figure 7.5 Schematic representation of fault sealing-integrity with respect to the orientation of the contemporary stress field.

7.5.2 Generalised Application of Hydraulic Seal Integrity to the Timor Sea

The present orientation of the contemporary stress field in the Timor Sea indicates that, regionally, faults with the highest probability of sealing are oriented NW/NNW. From contemporary stress considerations, the three structural trends observed in the region can be put in order of likelihood of fault sealing: the set least likely to be sealing are the margin-forming NE/ENE oriented elements, followed by those of the E-W trend. The NW trending Palaeozoic component is most likely to provide sealing faults. This work (Mildren et al., 1994, Appendix D) led companies exploring in the Timor Sea to target E-W structures in the Sahul Trough area (Figure 2.4) in preference to the NE-SW structure of the Vulcan Sub-basin (Lowry, pers comm, 1996) and the new fields discovered in the area (e.g. Elang, Kakatua, Undan/Bayu) give support to the contemporary stress field influence on fault-trap integrity. It is important to emphasize that since we are dealing with contemporary stress conditions, the results are only significant with respect to leakage associated with collision-related tectonism and the resulting stress field.

Detailed fault-trap integrity predictions for the Timor Sea can not be made without prospect scale in situ stress data. Indeed this project has spawned a major research project funded by BHP Petroleum and joint venture partners in the Timor Sea into contemporary stresses and seal integrity. The aim of the new project is to collect detailed in situ stress orientation and magnitude data on fields where the seal is intact and on prospects known to have leaked. The detailed in situ stress data will be combined with 3D fault geometries to investigate the link between the risk of both dilational (as discussed above) and shear failure. The aim of the project is to allow

ranking of the likelihood of seal failure (the key exploration variable) in prospects yet to be drilled in the Timor Sea.

Chapter 8

Summary and Conclusions

8.1 Introduction

The primary aim of this thesis was to improve the understanding of the contemporary stress field of the North West Shelf of Australia. Determination of the contemporary stress field has resulted in:

- creation of a North West Shelf Stress Map (Figure 5.1);
- constraints being placed on the forces acting at the plate boundaries adjacent to the North West Shelf;
- the elucidation of stress regimes and the nature of tectonism within the Carnarvon and Bonaparte Basins, and;
- recommendations for various issues related to the exploration for, and development of, hydrocarbon reserves.

A summary of these findings is presented below.

8.2 The Contemporary Stress Field of the North West Shelf

The interpretation of breakouts from dipmeter logs recorded in wells located within the Carnarvon and Bonaparte Basins has provided an additional 88 stress indicators to augment the small number previously published as part of the World Stress Map (Zoback, 1992). The new data in conjunction with the World Stress Map clearly defines the first-order stress orientation along the northern Australian margin. The regional σ_{Hmax} orientation is consistently 050°-060°N from the onshore Canning Basin

eastward to New Guinea, and rotates approximately 40° westward from the onshore Canning Basin to 090°-100°N in the Carnarvon Basin (Figure 5.4).

Stress magnitude calculations based on over 70 leak-off tests performed in 53 wells revealed that in both the Carnarvon and Bonaparte Basins the stress regime is broadly on the boundary between strike-slip and extension. In the Carnarvon Basin the relative magnitudes of the principal stresses suggest that the stress regime changes from strike-slip near the shoreline to extensional with increasing distance northwest towards the Indian Ocean Basin (Figure 5.12). In the Bonaparte Basin the stress regime changes from extension in the southwest to strike-slip northeast towards the plate margin (Figure 5.13).

8.3 Tectonic Implications of the Contemporary Stress Field

8.3.1 Implications for Plate Boundary Forces

The northern Australian margin is characterised by a variety of convergent plate processes occurring along its length. Oceanic lithosphere is subducting beneath the Sunda Arc to the north of the Carnarvon Basin. In the Banda Arc, north of the Bonaparte Basin, the subduction system appears to have choked due to the arrival of buoyant Australian continental crust, as witnessed by the aseismicity of the Timor Trough (Cardwell & Isacks, 1978) and the cessation of volcanism 3 Ma in the volcanic arc north of Timor (Abbot & Chamalaun, 1981). However, σ_{Hmax} orientation in the Bonaparte Basin, which is sub-parallel to the strike of the Banda Arc, suggests that there is no net push yet generated by Australia/Banda collision. The σ_{Hmax} orientation from the Canning Basin to New Guinea is consistent with control by the more mature New Guinea orogenic belt to which it is orthogonal. Comparison of these observations

with finite element models of the intra-plate stress field of the Indo-Australian Plate by Coblentz et al. (1995), indicates that the stress rotation along the northern Australian margin, and indeed the first-order patterns of the Indo-Australian Plate as a whole, can be replicated purely by focusing reaction to the ridge push force along collisional segments of the northeast boundary (i.e. Himalayas, New Guinea and New Zealand). Observed stress orientations do not require an active push from the Banda Arc, nor a slab pull force from the Sunda Arc where oceanic lithosphere is subducting. However, neither are the observed data inconsistent with an active slab pull force acting along the Sunda Arc. The observed stress data do unequivocally show that the forces acting along the northeast boundary of the Indo-Australian Plate must be heterogeneous. This heterogeneity reflects the complexity of convergent processes along the plate margin.

8.3.2 Comparison of Stress Orientations within the Carnarvon and Bonaparte Basins

The large number of stress indicators obtained from the Carnarvon and Bonaparte Basins reveals a significant difference between the stress distribution within the two basins. In the Bonaparte Basin, stress indicators are consistently oriented in the mean σ_{Hmax} direction for the basin. In the Carnarvon Basin, some stress indicators show consistent σ_{Hmax} orientations that deviate from the basin's mean stress orientation (Figure 5.1; Figure 5.2). σ_{Hmax} is consistently oriented E-W within the relatively structureless depocentres of the Barrow-Dampier Sub-basins of the Carnarvon Basin, and oriented NE-SW in the more structurally complex basin margins (Figure 5.5). The stress rotation may be due to the greater density of faults associated with the basin margins and the oblique relationship between the first-order σ_{Hmax} direction and the

dominant structural trend of the basin. The faulted basin margins may be affecting the stress field in two ways;

- due to contrasting elastic properties between rocks forming the basin margins and those comprising the depositional centre (i.e. greater density of open fractures, faults and deformed rock thus a lower Young's modulus on the basin margins), and;
- due to active faults locally perturbing stress magnitude and orientation.

Both of these effects are scale independent and relate the stress rotations to structural features. A greater variation in breakout azimuth is observed within wells located on the basin margins and this suggests that stress rotations which are localised may be caused by small scale discontinuities in elastic properties or the presence of active faults in the vicinity of boreholes. The occurrence of localised stress rotations within the Carnarvon Basin must be considered when making any inferences (eg. related to hydrocarbon exploration and development) using the contemporary stress field. It is considered that the Bonaparte Basin remains unaffected by localised rotations because the first-order σ_{Hmax} direction is parallel to the structural grain.

8.3.3 Tectonism of the Carnarvon and Bonaparte Basins

The nature of the contemporary stress field was used to constrain the probable orientation and style of fault movement in the Carnarvon and Bonaparte Basins. In the depositional centre of the Carnarvon Basin, faults oriented NE would be most susceptible to dextral reactivation, the NW faults to sinistral reactivation and the E-W faults to extensional reactivation. The N-S faults, which are suitably oriented for

compressional reactivation, are not likely to be reactivated because the stress regime is on the boundary between strike-slip and extension.

On the margins of the Barrow-Dampier Sub-basins, faults oriented NE are most susceptible to normal reactivation, the E-W faults to sinistral strike-slip reactivation and the N-S faults to dextral strike-slip reactivation. The NW oriented faults, which are suitably oriented for compressional reactivation, are not likely to be reactivated because the stress regime is on the boundary between strike-slip and extension (Figure 6.4). These predictions suggest that significant phases of wrenching with right lateral movement that occurred in the Late Miocene (Parry & Smith, 1988) are consistent with the contemporary stress field and reflect continuation of the Miocene-Pliocene collision between the Australian Continent and Timor.

In the Bonaparte Basin, the dominant NE/E-NE structural trend is susceptible to extensional reactivation, the E-W trend is most susceptible to sinistral strike-slip reactivation and the Palaeozoic NW structural trend is susceptible to compressional reactivation, however this is unlikely given that the stress regime is on the boundary between strike-slip and extension (Figure 6.5). These predictions have implications for the debate regarding the nature of any strike-slip movement in the Timor Sea area of this basin (Woods, 1988; Nelson, 1989). In a regional sense, the Woods (1988) extension model (Tertiary extensional reactivation of major NE trending Jurassic faults) is more consistent with the contemporary stress field than the Nelson (1989) strike-slip model (strike-slip and dip-slip reactivation of the same NE trending fault system). However, local stress rotations may lead to localised reactivation of the type envisaged by Nelson (1989).

8.4 Implications for Petroleum Exploration and Production

The implications of the contemporary stress field of the North West Shelf for several hydrocarbon related issues are summarised below.

8.4.1 Wellbore Stability

The relative magnitudes of the principal stresses in both the Carnarvon and Bonaparte Basins indicate that $\sigma_v \approx \sigma_{Hmax}$ (boundary between extension and strike-slip). The implications for wellbore stability are such that a horizontal well drilled in the σ_{hmin} will minimise the stress anisotropy to which the wellbore is subject to, thus maximise the safe mud-weight envelope and hence the likelihood of wellbore stability (Figure 7.1). Therefore, with regard to minimisation of wellbore instability due to breakout, wells drilled on the depositional centre of the Carnarvon Basin should be deviated to horizontal towards 000°-010°N, wells drilled on the flanks of the Barrow-Dampier Sub-basin should be deviated to horizontal towards approximately 140°N, and wells drilled in the Bonaparte Basin should be deviated to horizontal towards 145°-150°N.

8.4.2 Orientation of Induced Hydraulic Fractures

Hydraulic fractures propagate in a plane orthogonal to the least principal stress. Given that σ_{hmin} is the least principal stress in the Carnarvon and Bonaparte Basins, hydraulic fractures will open orthogonally to σ_{hmin} and propagate in a vertical plane defined by σ_{Hmax} and σ_v (Figure 7.2). Therefore hydraulic fractures induced within the depositional centre of the Carnarvon Basin will be vertical and striking 090°-100°N. They will be vertical and striking approximately 050°N within the flanks of the Barrow-Dampier Sub-basin, and vertical and striking 055°-060°N in the Bonaparte Basin.

8.4.3 Orientation of Open Natural Fractures

Similarly to induced hydraulic fractures, natural fractures will preferentially be open and productive when aligned parallel to σ_{Hmax}. Therefore, any sub-vertical, natural fractures striking 090°-100°N are likely to be open in the depositional centre of the Carnarvon Basin, sub-vertical, natural fractures striking approximately 050°N are likely to be open within the flanks of the Barrow-Dampier Sub-basin (i.e. possibly affecting the elastic properties of the margin), and sub-vertical, natural fractures striking 055°-060°N are the most likely to be open in the Bonaparte Basin.

8.4.4 Hydraulic Seal Integrity in the Timor Sea

The three structural trends observed in the Bonaparte Basin have been ranked according to their likelihood of dynamic fault sealing. Those faults oriented orthogonal to σ_{Hmax} are likely to have the greatest sealing potential (the NW trending Palaeozoic component). The set least likely to be sealing is the margin-forming NE/ENE oriented elements (parallel to σ_{Hmax}). The E-W trend has an intermediate sealing probability.

8.5 Conclusions

- This project has very successfully constrained stress orientation within the North West Shelf of Australia and discussed the tectonic implications and hydrocarbon applications associated with it.
- Stress magnitudes were not so well constrained and this is certainly an area of possible further work. The author is delighted to note that work associated with this thesis is leading companies in the North West Shelf to undertake extended LOT's (XLOT's) which simulate a hydraulic fracture test and provide much better stress magnitude data.

- The advent of borehole imaging logs such as FMS/FMI has revolutionised analysis of stress orientations. The author has been amazed particularly at the prevalence of drilling-induced hydraulic fractures in these logs. Although becoming open file now, few such logs were available when the author was undertaking stress analyses for this project.

Appendix A

'Vstress': Density Log Integration Program

A.1 Program Description

The program 'Vstress' was written for this project to integrate density log files according to Equation 3.5. The density log input file must be in ascii format, consisting of two columns; depth (in meters) and density (in gcm^{-3}). The program has the facility to incorporate any number of average density values representing depth intervals between the surface (0 meters) and the top most depth of the input file data. The program integrates the input data and outputs the result to a user specified file. This file also consists of two data columns in ascii format; depth (in meters) and vertical stress magnitude (in MPa).

A.2 Flow Diagram

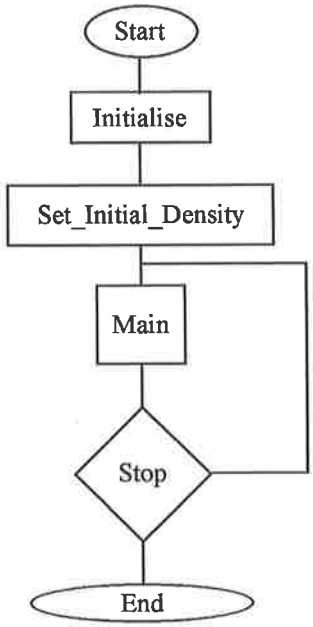

Read input and output filenames
Input average densities from surface to depth at top of density log

Integrate average densities from surface to top of density log interval

Integrate current depth/density values
Write to output file

End of input file?

Figure A.1 Flow diagram for the program 'Vstress'.

A.3 Pascal Code for 'Vstress'

```
program vstress (input, output);

const
   g = 9.81;                          {acceleration due to gravity in ms-2}

var
   z_min : real;                      {top depth in input file which has an accompanying}
                                      {density value}
   z_max : real;                      {bottom depth in input file}
   zo : real := 0.0;                  {initial depth i.e. surface}
   dz : real;                         {change in depth between values}
   depth : real;                      {current value read in from input file}

   d_min : real;                      {first density value in input file which corresponds}
                                      {to z_min}

   density : array[1..10] of real;
   bot_depth : array[0..10] of real;
   top_depth : array[1..10] of real;

   counter : integer;                 {number of average density blocks remaining}

   p : real;                          {running sum of vertical stress in MPa}

   a, f1 : text;                      {file variables}
   input_file : packed array [1..8] of char;   {variables for file names}
   output_file : packed array [1..8] of char;

   i : integer;                       {used in loops}

   den : real;                        {density value used in calculation}
   roh : real;                        {current value read in from input file}
   den_no : integer;                  {number of average densities used from velocity}
                                      {check-shots}

   procedure write_to_file;
   begin
        writeln(f1);
        write(f1, depth:3:3, ' ');
        write(f1, p:3:3);
   end;

   procedure maxmin;                  {sets z_max and z_min by reading input_file}
   begin
        reset(a, input_file);
        while not eof(a) do
        begin
                read(a, z_min, d_min);
                if d_min > 0 then
                begin
                        readln(a);
                        while not eof(a) do
                        begin
                                read(a, z_max);
                                readln(a);
                        end;
```

```
                end
                else readln(a);
        end;
        close(a);
        writeln('d_min := ', d_min);
        writeln('z_min := ', z_min);
        writeln('z_max := ', z_max);
end;

procedure initialise;
begin
        writeln('Name of original data file (8 chars)?');
        readln(input, input_file);
        maxmin;
        writeln('How many average densities used?');
        readln(input, den_no);
        for i := 1 to den_no do
        begin
                writeln('Enter bottom depth of average density interval');
                readln(input, bot_depth[i]);
                writeln('Enter top depth');
                readln(input, top_depth[i]);
                writeln('Enter interval density');
                readln(input, density[i]);
        end;
        writeln('Enter name of output file (8 chars)?');
        readln(input, output_file);
        rewrite(f1, output_file);
        write(f1, 'Depth (m)      Stress (MPa)');
        bot_depth[0] := 0.0;
end;

procedure set_initial_p;
begin
        counter := 0;
        for i := 1 to den_no do
        begin
                writeln('top depth', i, ' := ', top_depth[i]);
                writeln('bot depth', i, ' := ', bot_depth[i]);
                writeln('density', i, ' := ', density[i]);
                if top_depth[1] = 0.0 then
                begin
                        if not(z_min = bot_depth[i-1]) then
                        begin
                                depth := bot_depth[i];
                                dz := depth - top_depth[i];
                                p := p + density[i]*g*dz/1000;
                                counter := counter + 1;
                                write_to_file;
                        end;
                end
                else writeln('ERROR: average density values do not star from surface i.e. = 0');
        end;
end;

procedure main;
begin
        reset(a, input_file);
        repeat
```

```
                read(a, zo);
                readln(a);
        until (zo = bot_depth[counter]) or (zo = z_max);
        while not eof(a) do
        begin
                read(a, depth);
                dz := depth - zo;
                zo := depth;
                if depth  >= top_depth[counter] then
                begin
                        read(a, roh);
                        den := roh;
                end
                else
                begin
                        den := density[counter];
                        if depth = bot_depth[counter] then
                                counter := counter + 1;
                        repeat
                                read(a, zo);
                                readln(a);
                        until (zo = bot_depth[counter]) or (zo = z_max);

                end;
                p := p + den*g*dz/1000;
                write_to_file;
                readln(a);
        end;
    end;

begin
    initialise;
    set_initial_p;
    main;
    close(a);
    close(f1);
end.
```

Appendix B

Borehole Breakouts

B.1 Introduction

This appendix contains a list of all borehole breakouts interpreted from four-arm dipmeter caliper logs of wells in the Carnarvon and Bonaparte Basins. Each breakout has listed it's top and bottom log depth (meters), length (meters), maximum eccentricity of the borehole (inches), mean azimuth (°N) and analysis type (computer or manual selection, 'paper' indicates breakout interpretation from paper logs). In some cases manually selected breakouts overlap computer selected breakouts. Statistical summary of these results (Chapter 5) does not include the overlapped computer selected breakouts in any calculations of mean azimuth.

B.2 Carnarvon Basin

WELL	Top	Bottom	Length	Max ECC	Azimuth	Analysis type
BAMBRA 1	813.21	815.19	1.98	2.03	176	comp
Lat: 20°32'	872.34	875.39	3.05	2.06	053	comp
Long: 115°38'	875.84	901.45	25.60	2.13	050	comp
	901.90	920.65	18.75	2.47	015	comp
	951.13	955.85	4.73	2.36	171	comp
	956.31	958.14	1.83	1.97	176	comp
	961.03	964.39	3.35	1.83	171	comp
	971.25	981.15	9.91	2.33	143	comp
	981.61	989.23	7.62	1.74	142	comp
	989.99	992.73	2.74	1.64	129	comp
	995.78	997.61	1.83	2.02	127	comp
	1053.08	1057.96	4.88	2.55	145	comp
	1058.42	1062.08	3.66	2.66	142	comp
	1064.82	1067.11	2.29	2.70	111	comp
	1071.07	1073.96	2.90	2.13	120	comp
	1103.07	1104.90	1.83	2.09	174	comp
	1107.03	1110.84	3.81	2.41	154	comp
	1117.09	1119.68	2.59	2.31	153	comp
	1135.53	1139.95	4.42	2.66	132	comp
	1143.46	1150.16	6.71	2.45	141	comp
	1162.20	1164.03	1.83	2.03	131	comp

WELL	Top	Bottom	Length	Max ECC	Azimuth	Analysis type
	1326.34	1328.62	2.29	1.67	001	comp
	1330.76	1333.96	3.20	1.89	001	comp
	1397.05	1739.49	342.44	2.58	175	man
	1689.20	1714.20	24.99	2.45	169	comp
	1714.50	1739.49	24.99	2.38	168	comp
	1743.15	1840.23	97.08	2.41	172	man
	1814.78	1818.74	3.96	1.63	170	comp
	1825.60	1828.04	2.44	1.88	177	comp
	1830.02	1834.44	4.42	2.22	163	comp
	1838.10	1840.23	2.13	2.00	174	comp
	1886.10	2048.26	162.15	4.94	171	man
	2015.49	2019.30	3.81	4.94	163	comp
	2021.59	2023.42	1.83	4.06	163	comp
	2025.70	2027.99	2.29	2.43	160	comp
	2034.08	2035.61	1.52	3.25	165	comp
	2037.89	2040.33	2.44	3.84	168	comp
	2041.40	2044.75	3.35	2.82	162	comp
	2045.21	2048.26	3.05	1.96	172	comp
	2048.71	2050.54	1.83	1.09	140	comp
	2054.81	2060.45	5.64	2.47	167	comp
	2104.80	2106.32	1.52	0.44	161	comp
	2303.07	2687.88	384.81	6.03	001	man
	2719.88	2722.02	2.13	0.43	168	comp
	2735.12	2736.95	1.83	2.74	157	comp
	2738.78	2743.20	4.42	1.63	161	comp
	2802.18	2809.80	7.62	2.76	173	comp
	2848.20	2850.03	1.83	2.87	177	comp
	2857.04	3200.86	343.81	4.42	031	man
	3237.13	3267.00	29.87	0.86	001	man
	3272.03	3279.95	7.92	0.70	014	man
	3610.05	3611.73	1.68	0.44	050	comp
CAMPBELL 2	1186.13	1254.86	68.73	4.23	003	man
Lat: 20°25'	1274.06	1557.99	283.92	5.28	006	man
Long: 115°43'	1420.22	1425.40	5.18	2.06	025	comp
	1541.22	1551.13	9.91	4.25	005	comp
	1551.43	1554.48	3.05	3.17	003	comp
	1555.39	1558.14	2.74	3.35	008	comp
	1558.60	1566.82	8.23	1.47	156	comp
	1567.13	1568.81	1.68	0.95	156	comp
	1570.03	1573.38	3.35	0.95	151	comp
	1575.05	1580.85	5.79	1.04	141	comp
	1582.67	1590.75	8.08	1.30	130	comp
	1758.09	2166.98	408.89	3.90	008	man
	2163.93	2166.21	2.29	2.04	010	comp
	2382.01	2538.98	156.97	3.98	171	man
	2639.11	2768.80	129.69	4.48	171	man
	2753.11	2755.39	2.29	4.38	171	comp
	2757.07	2760.73	3.66	3.84	171	comp
	2763.32	2766.52	3.20	3.77	155	comp
	2766.97	2768.80	1.83	1.13	143	comp
CHERVIL 1	953.66	965.93	12.27	2.21	008	comp
Lat: 21°18'	966.58	971.54	4.96	2.70	009	comp
Long: 115°14'	1005.68	1011.29	5.61	0.62	157	comp
	1025.11	1028.84	3.74	1.02	071	comp

WELL	Top	Bottom	Length	Max ECC	Azimuth	Analysis type
	1029.09	1032.34	3.25	1.35	059	comp
	1041.04	1044.94	3.90	0.93	041	man
CHINOOK 1	1728.50	1731.50	3.00	1.18	093	comp
Lat: 21°10'	1739.25	1742.75	3.50	0.73	093	comp
Long: 114°41'	1780.88	1783.00	2.13	2.05	016	comp
	1783.38	1788.13	4.75	3.25	025	comp
	1790.75	1793.13	2.38	3.13	023	comp
	1801.50	1803.13	1.63	2.32	014	comp
	1821.00	1825.75	4.75	2.34	014	comp
	1826.00	1828.75	2.75	3.32	016	comp
	1843.25	1847.00	3.75	2.52	018	comp
	1847.38	1853.13	5.75	3.43	010	comp
	1853.88	1861.63	7.75	3.57	019	comp
	1861.88	1865.50	3.63	3.12	016	comp
	1871.88	1874.63	2.75	3.44	017	comp
	1881.25	1883.13	1.88	2.89	022	comp
	1885.63	1887.88	2.25	2.23	047	comp
	1888.25	1891.38	3.13	3.29	017	comp
	1907.38	1915.00	7.63	3.85	015	comp
	1915.25	1920.00	4.75	2.73	025	comp
	2003.25	2005.88	2.63	2.56	034	comp
	2006.13	2008.75	2.63	2.90	033	comp
	2261.88	2270.75	8.88	0.57	071	comp
	2400.88	2402.75	1.88	0.50	052	comp
	2404.75	2409.88	5.13	4.31	036	comp
	2410.25	2416.25	6.00	7.38	023	comp
	2416.50	2423.50	7.00	6.10	034	comp
	2462.00	2463.75	1.75	0.65	120	comp
	2743.00	2747.00	4.00	3.28	031	comp
	2847.38	2849.13	1.75	0.33	106	comp
	2871.38	2876.75	5.38	0.30	106	comp
	2958.00	2988.00	30.00	4.58	015	man
	3018.00	3033.00	15.00	6.84	004	man
	3080.00	3093.00	13.00	4.13	019	man
	3166.00	3183.00	17.00	3.17	023	man
	3203.00	3228.75	25.75	5.16	014	man
	3224.88	3228.75	3.88	3.27	012	comp
	3244.13	3246.63	2.50	0.47	023	comp
	3257.38	3259.00	1.63	1.90	017	comp
	3285.00	3289.13	4.13	2.72	017	comp
	3324.00	3341.00	17.00	3.49	015	man
	3350.25	3352.75	2.50	1.44	021	comp
	3372.88	3374.88	2.00	1.76	003	comp
	3375.13	3376.88	1.75	0.50	170	comp
	3383.50	3385.13	1.63	2.66	014	comp
	3385.75	3392.13	6.38	2.60	021	comp
COOJONG 1	518.31	520.75	2.44	0.42	039	comp
Lat: 20°01'	526.39	533.55	7.16	1.41	045	comp
Long: 116°33'	541.02	545.90	4.88	2.47	047	man
	556.11	557.94	1.83	1.63	055	man
	568.15	569.37	1.22	1.63	060	man
	572.26	576.99	4.72	1.23	070	comp
	578.21	580.34	2.13	1.13	086	comp
	580.64	585.83	5.18	1.38	078	comp

WELL	Top	Bottom	Length	Max ECC	Azimuth	Analysis type
	586.28	587.28	1.52	1.48	090	comp
	590.55	592.84	2.29	1.39	105	comp
	594.97	599.39	4.42	2.16	093	comp
	605.33	608.69	3.35	2.09	115	comp
	616.31	618.29	1.98	1.88	117	comp
	620.73	622.25	1.52	0.78	160	comp
	626.52	629.87	3.35	0.41	079	man
	675.28	677.57	2.29	0.43	015	comp
	682.75	684.28	1.52	0.72	062	comp
	685.95	690.22	4.27	2.05	054	comp
	697.08	701.95	4.88	3.10	065	man
	708.51	710.18	1.68	1.78	077	comp
	712.78	715.21	2.44	1.70	079	comp
	718.87	720.55	1.68	1.54	091	comp
	735.03	738.99	3.96	1.82	117	man
	754.23	756.36	2.13	1.42	158	comp
	765.66	768.55	2.89	1.82	167	comp
COSSACK 1	2833.87	2886.46	2.59	3.14	009	comp
Lat: 19°34'	2841.04	2852.93	11.89	4.04	025	man
Long: 116°30'	2850.49	2853.23	2.74	3.80	014	comp
	2855.82	2859.94	4.11	2.94	016	comp
	2856.13	2866.95	10.82	4.67	021	man
	2861.62	2863.44	1.83	4.67	021	comp
	2868.47	2873.20	4.72	3.99	012	comp
	2869.08	2888.89	19.81	4.63	031	man
	2873.50	2876.40	2.90	2.74	021	comp
	2876.70	2880.67	3.96	3.41	008	comp
	2925.01	2927.91	2.90	3.26	024	man
	2966.47	2968.75	2.29	0.63	007	comp
DILLSON 1	2206.27	2213.58	7.32	1.02	050	comp
Lat: 21°23'	2368.10	2369.89	1.79	0.67	047	comp
Long: 115°11'						
EMMA 1	727.43	901.73	174.31	4.90	006	man
Lat: 20°32'	978.59	1386.23	407.63	4.60	012	man
Long: 115°47'	981.80	984.54	2.74	1.50	012	comp
	1715.17	1730.72	15.56	2.30	004	man
	1744.45	1748.11	3.66	0.40	032	comp
	2018.49	2034.96	16.47	0.40	095	comp
	2039.08	2050.97	11.89	0.40	091	comp
	2051.89	2053.72	1.83	0.30	083	comp
	2061.50	2067.90	6.40	0.60	037	comp
	2141.56	2146.13	4.57	0.40	095	comp
FLORES 1	867.42	896.24	28.82	1.70	113	comp
Lat: 20°46'	904.48	911.34	6.86	4.30	009	comp
Long: 115°35'	915.00	925.52	10.52	4.30	016	comp
	931.93	934.67	2.74	2.80	004	comp
	938.33	942.45	4.12	1.00	020	comp
	956.18	958.01	1.83	0.40	039	comp
	968.07	985.91	17.84	2.40	005	man
	1047.22	1050.88	3.66	2.30	098	comp
	1100.75	1185.84	85.09	3.20	014	man
	1216.04	1232.96	16.93	1.60	012	man
	1384.40	1388.06	3.66	0.50	099	comp

WELL	Top	Bottom	Length	Max ECC	Azimuth	Analysis type
	1564.65	1566.48	1.83	0.40	029	comp
	1611.77	1636.94	25.16	0.60	159	comp
	1639.68	1649.29	9.61	0.60	137	comp
	1693.67	1698.24	4.57	0.50	047	comp
	1938.43	1944.38	5.95	0.40	142	comp
	1946.21	1948.49	2.29	0.40	144	comp
	1950.32	1953.53	3.20	0.50	143	comp
	2086.66	2088.95	2.29	0.60	005	comp
	2109.08	2112.74	3.66	0.50	032	comp
GOODWYN 1	1205.01	1213.40	8.38	1.49	029	comp
Lat: 19°41'	1221.47	1223.91	2.44	0.85	029	comp
Long: 115°53'	1441.08	1443.06	1.98	0.64	149	comp
	1458.15	1470.65	12.50	1.38	133	comp
	1506.00	1509.97	3.96	0.87	072	comp
	1547.31	1552.03	4.72	0.86	022	comp
	1584.80	1589.82	5.03	1.41	005	comp
	1692.54	1709.31	16.76	1.49	167	comp
	1729.27	1731.25	1.98	0.64	109	comp
	1749.08	1751.52	2.44	0.64	167	comp
	1929.92	1931.59	1.68	0.33	106	comp
	2204.85	2207.28	2.44	1.39	034	comp
	2557.35	2559.17	1.83	1.16	135	comp
	2586.15	2588.89	2.74	2.07	054	comp
	2596.97	2600.02	3.05	0.65	024	comp
	2603.83	2605.35	1.52	0.43	004	comp
	2628.36	2651.83	23.47	3.51	034	comp
	2772.77	2774.44	1.68	0.43	104	comp
	2793.95	2798.98	5.03	1.39	059	comp
	2872.74	7876.25	3.50	0.85	108	comp
	2981.71	2983.54	1.83	0.71	175	comp
	3049.22	3051.05	1.83	0.52	122	comp
	3097.99	3100.12	2.13	2.75	063	comp
	3101.65	3104.24	2.59	0.61	066	comp
	3132.73	3135.17	2.44	0.33	144	comp
	3139.59	3134.57	1.98	0.41	059	comp
	3187.90	3189.43	1.52	0.75	180	comp
	3264.41	3265.93	1.52	0.40	037	comp
	3299.46	3301.59	2.13	0.44	153	comp
	3314.09	3315.77	1.68	1.31	050	comp
GOODWYN 3A	420.32	422.33	2.01	1.90	180	comp
Lat: 19°44'	424.92	426.75	1.83	1.20	137	comp
Long: 115°52'	444.64	446.32	1.68	0.50	110	comp
	780.59	782.39	1.80	3.40	179	comp
	823.45	835.52	12.07	3.90	133	man
	829.48	832.50	3.02	3.30	128	comp
GOODWYN 8B	2629.07	2648.01	18.94	1.10	152	comp
Lat: 19°38'	2650.01	2667.45	17.44	0.70	136	comp
Long: 115°54'	2682.90	2688.88	5.98	0.60	130	comp
	2707.33	2712.31	4.98	0.50	131	comp
	2732.75	2738.23	5.48	0.30	140	comp
	3083.43	3085.43	2.00	0.40	073	comp

WELL	Top	Bottom	Length	Max ECC	Azimuth	Analysis type
GOODWYN 9A	2694.28	2700.68	6.40	1.16	131	comp
Lat: 19°36'	2705.41	2707.23	1.83	0.70	130	comp
Long: 115°58'	2710.89	2716.68	5.79	1.35	127	comp
	2719.88	2723.69	3.81	0.66	128	comp
GRIFFIN 1	2544.00	2567.00	23.00	7.54	011	man
Lat: 21°14'	2584.13	2606.75	22.63	4.24	032	comp
Long: 114°37'	2607.25	2617.50	10.25	4.63	030	comp
	2645.75	2647.38	1.63	0.33	178	comp
	2818.63	2820.63	2.00	0.34	037	comp
	2833.50	2838.38	4.88	0.44	164	comp
	2850.25	2852.50	2.25	1.26	016	comp
	2855.13	2857.88	2.75	1.17	012	comp
	2862.38	2869.25	6.88	6.42	007	comp
	2880.00	2934.00	54.00	5.86	016	man
	2939.00	2961.00	22.00	9.94	022	man
	2965.50	2969.00	3.50	1.59	012	man
	2966.75	2968.75	2.00	1.59	012	comp
	2975.00	2983.00	8.00	1.36	007	man
	2993.00	2996.00	3.00	2.39	019	man
	3011.13	3012.75	1.63	4.45	021	comp
	3013.38	3017.25	3.88	3.06	024	comp
	3017.63	3020.63	3.00	0.92	165	comp
	3073.13	3075.63	2.50	0.75	173	comp
	3154.00	3155.00	1.00	1.79	034	man
	3169.00	3170.75	1.75	0.45	051	comp
	3172.50	3174.25	1.75	0.60	039	comp
	3215.00	3216.75	1.75	0.45	141	comp
	3236.63	3238.38	1.75	0.33	051	comp
	3238.75	3243.13	4.38	1.44	014	comp
	3243.50	3249.50	6.00	3.99	012	comp
	3257.38	3262.13	4.75	2.28	025	comp
	3277.38	3279.13	1.75	0.42	113	comp
	3286.00	3290.00	4.00	5.08	018	man
	3348.88	3350.75	1.88	1.30	021	comp
GRIFFIN 2	2009.88	2018.50	8.63	1.37	153	comp
Lat: 21°13'	2147.00	2150.00	3.00	2.29	022	man
Long: 114°37'	2165.00	2167.00	2.00	2.87	016	man
	2250.38	2254.75	4.38	1.45	132	comp
	2259.00	2261.25	2.25	0.75	124	comp
	2277.00	2280.25	3.25	1.89	011	comp
	2302.00	2326.00	24.00	6.62	032	man
	2344.00	2346.00	2.00	1.85	031	man
	2367.63	2373.00	5.38	1.12	038	comp
	2378.38	2381.25	2.88	1.15	022	comp
	2415.00	2430.00	15.00	9.67	019	man
	2472.00	2474.00	2.00	3.38	015	man
	2489.00	2499.00	10.00	2.91	015	man
	2507.75	2511.38	3.63	0.74	026	comp
	2513.13	2519.13	6.00	0.64	006	comp
	2528.63	2533.75	5.13	1.67	175	comp
	2536.75	2542.88	6.13	0.81	137	comp
	2543.25	2547.38	4.13	0.80	127	comp
	2578.63	2584.38	5.75	1.11	080	comp
	2588.75	2594.00	5.25	1.12	088	comp

WELL	Top	Bottom	Length	Max ECC	Azimuth	Analysis type
	2596.13	2603.88	7.75	1.26	076	comp
	2604.25	2613.00	8.75	1.23	074	comp
GRIFFIN 3	2425.00	2456.63	31.63	1.10	128	comp
Lat: 21°14'						
Long: 114°37'						
	2531.63	2533.25	1.63	1.60	137	comp
	2535.13	2539.38	4.25	1.58	139	comp
	2603.88	2608.13	4.25	1.30	100	comp
	2608.63	2615.75	7.13	1.10	097	comp
GRIFFIN 4	1834.00	1866.00	32.00	2.48	014	man
Lat: 21°13'	1894.00	1942.00	48.00	2.17	029	man
Long: 114°38'						
KANJI 1	357.07	382.98	25.91	2.72	019	man
Lat: 20°02'	404.17	415.75	11.58	2.80	004	comp
Long: 116°50'	582.32	584.15	1.83	2.22	037	comp
	624.08	628.50	4.42	1.64	032	comp
	630.48	633.37	2.90	1.06	043	comp
	643.28	645.41	2.13	1.23	040	comp
	686.11	687.63	1.52	1.36	026	comp
	753.47	754.99	1.52	0.61	113	comp
	811.99	814.73	2.74	1.48	153	comp
	819.91	821.74	1.83	1.17	151	comp
	822.50	824.94	2.44	1.38	149	comp
	880.11	887.27	7.16	1.01	112	comp
	889.71	895.05	5.33	1.34	092	comp
	895.50	897.18	1.68	1.03	053	comp
	900.68	902.67	1.98	0.77	093	comp
	936.19	938.63	2.44	0.76	115	comp
	944.42	947.32	2.90	0.81	120	comp
	949.45	950.98	1.52	0.92	111	comp
	955.40	957.38	1.98	0.46	114	comp
	957.99	961.34	3.35	0.88	084	comp
	961.64	963.32	1.68	0.59	069	comp
	983.13	987.86	4.72	1.13	178	man
	993.65	995.17	1.52	0.75	006	comp
	998.68	1002.03	3.35	0.84	171	comp
	1007.06	1010.56	3.51	0.69	173	comp
	1021.54	1023.37	1.83	0.73	117	comp
	1104.90	1106.73	1.83	0.58	131	comp
	1142.24	1144.07	1.83	0.66	104	comp
	1164.95	1166.62	1.68	0.52	103	comp
	1182.62	1184.91	2.29	0.37	094	man
	1187.35	1190.70	3.35	0.92	076	comp
	1194.36	1197.71	3.35	0.79	072	comp
	1207.62	1209.90	2.29	0.50	097	man
MAITLAND 1	812.98	814.54	1.56	1.01	072	comp
Lat: 20°30'	1259.55	1261.19	1.64	2.72	013	comp
Long: 115°10'	1264.20	1266.03	1.83	4.71	004	comp
	1295.02	1298.98	3.96	2.75	013	man
	1346.61	1348.90	2.29	3.20	011	comp
	1356.55	1358.38	1.83	0.41	038	comp
	1413.02	1417.97	4.95	2.40	015	man
	1426.01	1442.96	16.95	4.66	013	man

WELL	Top	Bottom	Length	Max ECC	Azimuth	Analysis type
	1454.89	1457.56	2.67	2.42	014	comp
	1475.01	1482.97	7.96	5.93	012	man
	1486.02	1492.00	5.98	7.99	018	man
MARRA 1	1302.26	1343.41	41.15	5.03	179	man
Lat: 20°36'	1460.91	1466.55	5.64	1.39	179	comp
Long: 115°38'	1467.16	1484.68	17.53	2.52	173	comp
	1488.03	1492.15	4.11	0.96	139	comp
	1530.25	1534.97	4.72	1.88	180	comp
	1539.39	1542.29	2.90	2.42	005	comp
	1543.51	1548.54	5.03	1.00	001	comp
	1552.50	1555.24	2.74	1.06	015	comp
	1555.70	1557.83	2.13	0.90	175	comp
	1558.29	1560.12	1.83	0.36	164	comp
	1565.61	1568.50	2.90	0.49	101	comp
	1588.31	1593.04	4.72	1.74	176	comp
	1594.71	1598.83	4.11	1.59	170	comp
	1631.90	1634.34	2.44	0.78	158	comp
	1668.02	1670.15	2.13	0.74	176	comp
	1683.11	1684.63	1.52	0.45	008	comp
	1714.50	1719.38	4.88	0.81	176	comp
	1722.73	1731.26	8.53	1.15	169	comp
	1744.37	1746.20	1.83	0.47	156	comp
	1748.79	1751.69	2.90	0.40	149	comp
	1767.23	1771.19	3.96	0.69	174	comp
	1772.11	1774.24	2.13	0.41	165	comp
	1908.81	1915.67	6.86	0.49	150	comp
	1917.50	1932.28	14.78	0.84	158	comp
	1934.87	1937.00	2.13	0.51	135	comp
	1940.05	1944.17	4.11	0.58	117	comp
	1952.24	1955.44	3.20	0.92	138	comp
	1979.22	1981.05	1.83	0.47	165	comp
MONTEBELLO 1	1710.13	1712.93	2.80	1.39	056	comp
Lat: 20°05'	1741.62	1745.11	3.49	0.82	079	comp
Long: 116°17'	1748.16	1750.19	2.03	1.12	066	comp
	1801.36	1804.12	2.76	0.69	063	comp
	1827.00	1837.85	10.85	1.26	152	comp
	1839.64	1845.53	5.89	0.83	131	comp
	1845.94	1847.44	1.50	0.94	132	comp
	1864.43	1870.08	5.65	1.00	120	comp
	1870.20	1874.91	4.71	2.32	099	comp
	1877.15	1884.87	7.72	1.47	086	comp
	1893.69	1896.86	3.17	0.71	064	comp
	1911.77	1914.29	2.52	1.35	033	comp
	1923.40	1925.39	1.99	0.81	054	comp
	1929.74	1931.40	1.67	0.47	034	comp
	1955.02	1956.56	1.54	0.82	005	comp
	1962.86	1966.52	3.66	1.09	172	comp
	1970.99	1972.78	1.79	0.99	165	comp
	1972.94	1980.66	7.72	0.73	155	comp
	1998.01	2011.99	13.98	1.12	150	man
	2018.01	2032.96	14.96	1.05	153	man
	2073.40	2079.41	6.02	0.76	015	comp
	2083.36	2086.04	2.68	0.52	051	comp
	2086.93	2091.93	5.00	0.73	071	comp

WELL	Top	Bottom	Length	Max ECC	Azimuth	Analysis type
	2106.77	2108.88	2.11	0.47	060	comp
	2283.01	2285.70	2.68	0.67	107	comp
	2323.13	2326.50	3.37	1.24	046	comp
	2334.22	2335.76	1.54	1.01	059	comp
	2339.87	2342.96	3.09	0.88	074	comp
	2397.70	2400.02	2.32	1.00	104	comp
	2443.26	2445.45	2.19	0.44	084	comp
	2446.63	2452.81	6.18	1.14	096	comp
	2463.46	2469.27	5.81	0.92	103	comp
	2492.15	2497.96	5.81	0.67	142	comp
	2509.62	2511.65	2.03	0.47	090	comp
	2520.59	2522.50	1.91	0.40	111	comp
	2531.97	2537.54	5.57	0.92	124	comp
SANTO 1	1102.61	1163.88	61.27	4.83	010	man
Lat: 21°33'	1253.03	1267.36	14.33	3.65	010	man
Long: 114°19'	1272.08	1276.96	4.88	4.63	016	man
	1556.00	1560.88	4.88	2.36	007	man
	1563.01	1567.89	4.88	1.91	013	man
	1594.10	1623.37	29.26	3.46	011	man
SCINDIAN 1A	2326.00	2343.88	17.88	0.88	061	comp
Lat: 21°11'	2359.13	2366.25	7.13	1.13	039	comp
Long: 114°42'	2371.00	2397.00	26.00	7.60	016	man
	2397.50	2401.00	3.50	0.54	066	comp
	2403.25	2405.50	2.25	0.55	020	comp
	2407.75	2409.63	1.88	0.43	175	comp
	2410.00	2414.38	4.38	0.40	168	comp
	2479.63	2482.88	3.25	4.13	015	comp
	2484.25	2487.00	2.75	5.03	019	comp
	2487.25	2509.38	22.13	5.76	020	comp
	2579.88	2619.13	39.25	7.11	019	comp
	2620.88	2624.25	3.38	0.70	027	comp
	2630.88	2632.75	1.88	0.40	144	comp
	2634.00	2635.63	1.63	0.36	146	comp
	2636.13	2637.88	1.75	0.30	144	comp
	2638.38	2640.13	1.75	0.35	133	comp
	2687.13	2694.88	7.75	0.46	120	comp
	2700.63	2703.25	2.63	0.46	123	comp
	2708.00	2709.75	1.75	0.99	142	comp
	2725.88	2727.50	1.63	0.34	096	comp
	2755.50	2757.63	2.13	0.45	049	comp
	2766.25	2769.25	3.00	0.35	119	comp
	2771.88	2773.63	1.75	0.34	072	comp
	2774.25	2776.25	2.00	0.39	061	comp
	2785.00	2787.63	2.63	0.43	044	comp
	2804.00	2806.88	2.88	0.50	053	comp
	2808.25	2812.50	4.25	2.03	026	comp
	2816.00	2880.00	64.00	7.13	013	man
	2860.63	2866.50	5.88	7.09	021	comp
	2867.75	2872.13	4.38	7.13	013	comp
	2873.75	2880.25	6.50	3.89	018	comp
	2903.00	2915.00	12.00	2.28	018	man
	2922.75	2924.38	1.63	0.49	006	comp
	2926.63	2928.25	1.63	0.60	160	comp
	2941.38	2945.25	3.88	0.49	071	comp

WELL	Top	Bottom	Length	Max ECC	Azimuth	Analysis type
	2946.88	2948.63	1.75	0.58	046	comp
	2949.00	2955.13	6.13	0.34	008	comp
	2955.75	2958.13	2.38	0.40	013	comp
	2960.38	2963.13	2.75	0.47	016	comp
	2965.13	2970.13	5.00	2.44	025	comp
	2977.00	2978.63	1.63	0.38	157	comp
	2982.13	2986.38	4.25	0.54	060	comp
	3020.63	3022.25	1.63	0.45	157	comp
	3038.00	3039.63	1.63	0.57	132	comp
	3048.00	3053.00	5.00	3.97	015	man
	3056.00	3058.00	2.00	2.73	011	man
	3080.25	3087.88	7.63	1.23	039	comp
	3089.13	3091.13	2.00	1.83	012	comp
	3107.00	3109.88	2.88	0.76	016	comp
SCINDIAN 2	1796.00	1840.00	44.00	2.09	012	man
Lat: 21°13'	2217.00	2229.00	12.00	0.52	081	comp
Long: 114°41'	2284.00	2286.00	2.00	0.44	012	comp
	2469.00	2471.00	5.00	2.10	171	comp
	2504.00	2507.00	3.00	0.69	082	comp
	2516.00	2525.00	9.00	0.95	060	comp
	2583.00	2587.00	4.00	0.57	178	comp
	2675.00	2687.00	12.00	2.87	015	man
SOUTH CHERVIL 1	804.02	809.96	5.93	0.78	054	man
Lat: 21°20'	880.02	883.92	3.90	2.90	014	man
Long: 115°12'	1322.01	1346.97	24.96	2.88	176	man
	1405.01	1420.94	15.93	2.36	134	man
	1561.06	1699.97	138.91	5.53	138	man
	1725.00	1739.96	14.96	2.05	002	man
	1956.00	1994.93	38.93	3.61	147	man
SOUTH PEPPER 1	1857.01	1865.95	8.94	0.79	136	man
Lat: 21°07'						
Long: 115°16'						
TANAMI 2	1276.81	1278.33	1.52	1.60	008	comp
Lat: 20°41'	1278.79	1280.31	1.52	1.00	010	comp
Long: 115°36'	1280.77	1283.36	2.59	2.10	178	comp
	1284.73	1287.78	3.05	2.70	175	comp
	1288.69	1293.88	5.18	4.10	152	comp
	1297.08	1314.91	17.83	5.00	143	man
	1314.91	1317.04	2.13	4.40	138	comp
	1317.35	1318.87	1.52	4.20	132	comp
	1319.33	1321.00	1.68	4.30	128	comp
	1321.31	1322.83	1.52	4.40	124	comp
	1339.14	1367.94	28.80	5.40	174	man
	1340.36	1342.80	2.44	4.20	001	comp
	1344.78	1346.91	2.13	4.00	180	comp
	1347.22	1352.55	5.33	4.80	180	comp
	1364.74	1366.88	2.13	4.60	003	comp
	1367.64	1369.16	1.52	4.40	177	comp
	1369.62	1372.36	2.74	4.90	150	comp
	1462.13	1469.90	7.77	3.10	056	man
	1485.14	1489.86	4.72	2.40	108	man
	1485.44	1491.23	5.79	2.40	108	comp
	1520.04	1563.93	43.89	2.70	171	man

WELL	Top	Bottom	Length	Max ECC	Azimuth	Analysis type
	1557.38	1559.66	2.29	1.60	169	comp
	1559.97	1562.56	2.59	2.10	178	comp
	1563.93	1568.81	4.88	2.20	176	comp
	1569.26	1579.32	10.06	1.10	157	comp
	1697.43	1704.59	7.16	1.30	115	comp
	1705.36	1708.40	3.05	0.80	123	comp
	1713.74	1716.02	2.29	0.70	121	comp
	1724.25	1727.61	3.35	0.90	120	comp
	1730.05	1745.89	15.85	2.80	174	man
	1769.06	1818.89	49.84	2.10	112	man
	1833.07	1840.99	7.92	2.50	135	man
	1891.13	1899.97	8.84	4.90	124	man
	1911.10	1940.97	29.87	4.80	127	man
	2232.05	2242.87	10.82	3.30	007	man
	2293.01	2301.85	8.84	2.30	172	man
	2295.14	2298.65	3.50	2.30	172	comp
	2298.95	2300.78	1.83	1.20	175	comp
	2302.31	2304.59	2.29	1.00	149	comp
	2333.09	2346.96	13.87	0.70	132	man
	2403.04	2419.35	16.31	0.80	142	man
TINGLE 1	339.09	388.93	49.83	2.63	066	man
Lat: 20°10'	392.13	399.90	7.77	2.00	061	man
Long: 116°28'	409.04	416.97	7.92	1.63	078	man
	430.07	434.95	4.88	1.48	065	man
	447.90	456.74	8.84	1.43	049	comp
	464.67	473.66	8.99	1.09	063	comp
	482.96	484.63	1.68	0.97	048	comp
	511.76	519.68	7.92	1.72	011	comp
	522.28	532.64	10.36	1.88	023	comp
	541.02	542.85	1.83	0.69	025	man
	882.70	884.38	1.68	0.44	155	comp
	889.10	891.08	1.98	0.34	098	comp
	892.91	894.44	1.52	0.37	078	comp
	895.20	896.72	1.52	0.69	062	comp
TRAFALGAR 1	2147.42	2155.38	7.97	0.46	141	comp
Lat: 19°10'	2225.77	2251.62	25.85	1.15	082	comp
Long: 117°19'						
TREALLA 1A	1329.71	1331.74	2.03	0.50	082	comp
Lat: 22°17'	1363.04	1366.98	3.94	0.51	143	man
Long: 114°04'	1375.02	1378.97	3.94	0.49	134	man
	1383.64	1385.79	2.15	0.80	129	comp
	1394.33	1395.99	1.67	0.50	101	comp
	1398.84	1400.47	1.63	0.53	102	comp
	1456.02	1458.42	2.40	0.73	006	comp
	1459.23	1462.68	3.45	2.62	006	comp
	1468.78	1471.50	2.72	3.24	010	comp
ULIDIA 1	1108.10	1167.99	59.89	4.32	006	man
Lat: 20°31'	1235.05	1299.97	64.92	2.99	013	man
Long: 115°43'	1266.14	1267.97	1.83	1.67	042	comp
	1297.69	1314.45	16.76	2.70	014	comp
	1356.06	1398.88	42.82	2.06	005	man
	1452.22	1454.81	2.59	0.38	041	comp
	1480.57	1488.49	7.92	0.39	173	comp

WELL	Top	Bottom	Length	Max ECC	Azimuth	Analysis type
	1704.75	1710.08	5.33	0.60	112	comp
	1710.69	1712.21	1.52	0.41	108	comp
	1833.07	1871.93	38.86	0.97	079	man
	1903.32	1907.74	4.42	0.98	164	comp
WANAEA 1	2805.08	2821.99	16.92	7.55	010	man
Lat: 19°35'	2835.10	2844.85	9.75	5.70	013	man
Long: 116°26'	2856.13	2866.95	10.82	8.27	012	man
	2876.09	2882.95	6.86	7.10	007	man
	2888.13	2894.99	6.86	4.42	014	man
	2902.00	2904.90	2.90	2.27	015	man
	2902.15	2904.59	2.44	2.27	015	comp
	2911.75	2913.74	1.98	0.47	016	comp
	2932.79	2934.62	1.83	4.01	015	comp
	2933.09	2934.92	1.83	4.01	015	man
	2937.05	2938.88	1.83	6.31	001	man
	2941.78	2944.83	3.05	7.26	012	comp
	2942.08	2948.94	6.86	7.26	012	man
	2952.14	2954.88	2.74	7.05	012	man
	2965.40	2966.92	1.52	0.45	107	comp
	2983.08	2984.91	1.83	6.61	015	man
	2992.68	2996.18	3.50	0.99	147	comp
	3004.11	3007.92	3.81	2.82	015	man
	3012.03	3014.93	2.90	2.15	010	man
	3012.34	3015.69	3.35	2.15	010	comp
	3022.09	3030.93	8.84	3.46	009	man
	3041.14	3042.97	1.83	3.13	016	man
	3047.09	3051.96	4.88	4.67	012	man
	3057.60	3251.00	193.40	5.95	001	man
	3201.47	3205.73	4.27	4.54	029	comp
	3230.12	3232.25	2.13	5.95	001	comp
	3241.09	3245.21	4.11	5.22	005	comp
	3245.51	3251.00	5.49	3.53	013	comp
	3265.02	3268.07	3.05	4.99	016	comp
WANAEA 2	2885.08	2888.13	3.05	3.03	012	comp
Lat: 19°37'	2890.27	2893.31	3.05	3.67	018	comp
Long: 116°25'	2908.55	2912.06	3.51	1.13	008	comp
	2934.92	2936.75	1.83	0.83	004	comp
	2939.64	2941.93	2.29	1.21	006	comp
	2942.69	2947.72	5.03	3.82	001	comp
	2948.03	2951.38	3.35	4.22	012	comp
	2967.38	2969.51	2.13	1.22	010	comp
	2981.10	2986.89	5.79	3.82	016	man
	2918.46	2923.34	4.88	1.13	177	comp
	2981.55	2985.21	3.66	3.82	016	comp
	2991.00	2992.98	1.98	1.38	026	man
WANAEA 3	2812.39	2818.18	5.79	4.06	010	comp
Lat: 19°34'	2812.39	2823.97	11.58	4.06	010	man
Long: 116°26'	2818.49	2822.45	3.96	2.62	012	comp
	2848.36	2849.88	1.52	0.87	008	comp
	2848.51	2850.95	2.44	1.28	006	man
	2854.15	2854.91	0.76	1.22	004	man
	2919.07	2921.36	2.29	0.73	005	comp
	2922.12	2923.95	1.83	0.73	009	man

WELL	Top	Bottom	Length	Max ECC	Azimuth	Analysis type
WANDOO 1	466.19	470.58	4.39	0.80	177	comp
Lat: 20°08'	472.04	474.24	2.19	0.60	005	comp
Long: 116°25'	475.46	485.45	10.00	1.38	164	comp
	495.21	543.97	48.77	3.53	166	man
	579.09	586.89	7.80	2.80	163	man
	985.11	1016.36	31.24	0.95	168	man
	1123.49	1127.46	3.96	0.48	133	comp
	1127.91	1130.96	3.05	0.58	128	comp
	1131.57	1134.92	3.35	0.68	137	comp
	1135.23	1136.75	1.52	0.42	126	comp
	1164.03	1184.91	20.88	0.25	103	man
	1248.16	1250.44	2.29	0.40	069	comp
	1498.09	1509.37	11.28	0.54	100	man
	1521.10	1555.85	34.75	0.37	109	man
WANDOO 2	1005.08	1012.85	7.77	0.24	143	man
Lat: 20°07'						
Long: 116°26'						
WANDOO 3	401.12	459.94	58.83	1.63	079	man
Lat: 20°08'	489.05	493.93	4.88	0.67	015	man
Long: 116°26'	510.08	513.89	3.81	0.58	022	man
	517.09	519.99	2.90	0.38	025	man
	537.06	539.95	2.90	0.87	038	man
	636.88	640.39	3.51	0.30	062	comp
	640.84	646.94	6.10	0.28	058	comp
	730.91	733.04	2.13	0.54	055	comp
WANDOO 5	339.24	341.53	2.29	1.25	100	comp
Lat: 20°09'	345.34	347.47	2.13	1.73	110	comp
Long: 116°26'	348.39	352.65	4.27	1.34	107	comp
	360.12	362.41	2.29	1.27	136	comp
	363.93	365.79	1.83	0.87	102	comp
	374.14	379.93	5.79	0.53	023	man
	391.52	395.63	4.11	1.14	103	comp
	407.37	410.26	2.90	0.68	095	comp
	424.13	426.26	2.13	0.85	106	comp
	472.59	474.12	1.52	0.59	034	comp
	573.79	576.38	2.59	0.51	152	comp
	579.73	582.32	2.59	1.05	123	comp
	586.13	587.81	1.68	0.49	139	comp
	600.15	601.98	1.83	0.83	015	comp
	704.55	707.14	2.59	0.63	127	comp
WANDOO 7	395.02	481.89	86.87	3.39	140	man
Lat: 20°07'	490.12	509.93	19.81	2.10	124	man
Long: 116°26'	524.10	527.00	2.90	0.88	123	man
	531.11	542.85	11.74	1.37	124	man
	545.14	556.87	11.74	1.67	106	man
	559.77	577.14	17.37	2.67	112	comp
	577.90	579.73	1.83	1.95	115	comp
	586.28	589.18	2.90	0.65	108	comp
	590.40	591.92	1.52	1.15	099	comp
	810.62	812.44	1.83	0.53	010	comp
	855.73	857.25	1.52	0.41	122	comp
	859.84	863.19	3.35	0.66	105	comp
	884.07	890.93	6.86	0.51	178	man

WELL	Top	Bottom	Length	Max ECC	Azimuth	Analysis type
WEST BARROW 1A	2540.98	2544.06	3.09	0.47	123	comp
Lat: 20°53'	2603.81	2606.41	2.60	0.38	148	comp
Long: 114°55'	2617.05	2625.99	8.94	4.52	004	man
	2639.57	2641.28	1.71	0.28	168	comp
	2658.02	2680.94	22.92	4.66	177	man
	2698.42	2700.20	1.79	0.55	009	comp
	2738.16	2741.66	3.50	0.65	002	comp
	2771.65	2773.36	1.71	1.11	015	comp
	2779.21	2781.73	2.52	2.55	006	comp
	2787.17	2788.72	1.54	0.55	155	comp
	2816.03	2817.98	1.95	3.01	005	comp
	2829.03	2844.96	15.93	3.76	178	man
	2857.07	2984.93	127.85	6.73	004	man
	2945.59	2963.88	18.29	5.54	016	comp
	2965.75	2971.43	5.69	5.78	010	comp
	2980.05	2985.33	5.28	4.04	011	comp
	2988.42	2992.00	3.58	1.38	040	comp
	2994.03	3043.94	49.91	3.71	009	man
	3003.70	3044.83	41.13	3.71	009	comp
	3047.84	3050.28	2.44	4.06	005	comp
	3050.52	3053.53	3.01	2.56	004	comp
	3054.58	3057.51	2.93	3.37	175	comp
	3062.96	3064.74	1.79	2.92	178	comp
	3077.99	3079.94	1.95	2.21	002	comp
	3086.85	3088.97	2.11	1.66	002	comp
	3094.57	3096.20	1.63	1.30	005	comp
	3108.31	3116.19	7.88	1.38	179	comp
	3116.76	3119.53	2.76	1.30	179	comp
	3119.85	3126.35	6.50	1.02	002	comp
	3120.01	3151.96	21.95	1.02	008	man
	3127.09	3130.99	3.90	0.66	006	comp
	3153.10	3156.35	3.25	1.75	005	comp
	3165.53	3167.32	1.79	0.47	179	comp
	3167.56	3169.11	1.54	0.55	163	comp
	3194.39	3196.50	2.11	1.76	008	comp
	3201.29	3203.08	1.79	0.93	005	comp
	3206.17	3208.69	2.52	0.66	169	comp
	3209.67	3211.70	2.03	0.46	042	comp
WEST MUIRON 3	886.00	888.00	2.00	2.01	175	comp
Lat: 21°34'						
Long: 114°13'						
WEST MUIRON 4	823.00	833.00	10.00	1.31	165	comp
Lat: 21°32'	1330.00	1332.00	2.00	0.38	069	comp
Long: 114°12'	1367.00	1369.00	2.00	0.40	048	comp

B.3 Bonaparte Basin

WELL	Top	Bottom	Length	Max ECC	Azimuth	Analysis Type
ANDERDON 1	2485.00	2495.00	10.00	0.90	85.00	man/paper
Lat: 12°38'	2507.00	2512.00	5.00	0.30	19.00	man/paper
Long: 124°47'	2532.00	2537.00	5.00	0.60	112.00	man/paper
	2557.00	2569.00	12.00	0.90	136.00	man/paper
	2583.00	2600.00	17.00	1.20	128.00	man/paper
	2680.00	2686.00	6.00	0.30	161.00	man/paper
	2696.00	2704.00	8.00	0.50	161.00	man/paper
ARUNTA 1	1789.41	1793.92	4.51	0.37	31.09	comp
Lat: 11°58'	1794.04	1796.77	2.72	0.38	2.81	comp
Long: 124°57'	1824.12	1832.65	8.54	0.48	73.76	comp
	1897.27	1905.27	8.01	0.57	109.58	comp
	1905.76	1914.09	8.33	0.51	112.26	comp
	1915.80	1917.87	2.07	0.80	107.82	comp
	1926.16	1930.63	4.47	0.59	106.57	comp
	2084.17	2101.69	17.51	0.59	44.63	comp
	2114.25	2118.63	4.39	0.78	11.01	comp
	2121.72	2126.03	4.31	0.71	176.49	comp
	2298.87	2300.38	1.50	0.55	97.78	comp
AVOCET 2	1230.17	1232.04	1.87	1.03	20.13	comp
Lat: 11°22'	1291.78	1294.14	2.36	1.70	132.25	comp
Long: 125°46'	1299.67	1302.68	3.01	2.22	116.25	comp
	1307.63	1309.42	1.79	1.95	120.75	comp
	1325.68	1327.22	1.54	0.65	148.88	comp
	1331.53	1335.11	3.58	1.07	166.25	comp
	1339.33	1344.62	5.28	2.09	159.00	comp
	1346.48	1352.17	5.69	1.77	145.88	comp
	1352.34	1354.86	2.52	1.93	150.13	comp
	1425.16	1429.47	4.31	3.97	138.63	comp
	1439.06	1442.80	3.74	2.90	137.13	comp
	1444.83	1447.11	2.28	2.49	124.38	comp
	1447.35	1450.52	3.17	1.95	115.63	comp
	1472.71	1474.71	2.11	1.16	88.25	comp
	1488.81	1491.33	2.52	1.25	65.38	comp
	1497.58	1500.10	2.52	1.66	46.50	comp
	1514.41	1518.96	4.55	1.21	56.13	comp
	1520.83	1522.54	1.71	0.85	29.98	comp
	1587.48	1592.03	4.55	1.29	158.25	comp
	1614.14	1618.29	4.15	2.73	126.50	comp
	1623.41	1625.11	1.71	2.01	138.00	comp
	1674.12	1675.75	1.63	0.77	120.75	comp
	1684.61	1687.78	3.17	0.67	106.25	comp
	1692.01	1695.18	3.17	0.85	89.00	comp
	1816.12	1818.23	2.11	0.69	100.56	comp
BELUGA 1	2506.71	2521.00	14.29	3.28	91.07	man
Lat: 11°00'	2624.10	2628.56	4.46	2.82	97.23	man
Long: 129°33'	2632.10	2634.96	2.86	3.45	88.72	man
	2988.03	2989.29	1.26	2.69	80.47	man
	3028.15	3034.55	6.40	0.64	116.20	comp
	3102.56	3104.16	1.60	0.41	35.61	comp

WELL	Top	Bottom	Length	Max ECC	Azimuth	Analysis Type
CASSINI 2	1310.00	1447.00	137.00	3.77	148.65	man
Lat: 12°08'	1407.00	1427.00	20.00	2.04	158.84	comp
Long: 124°56'	1432.00	1435.00	3.00	1.88	156.65	comp
	1440.00	1448.00	8.00	0.72	158.44	comp
	1450.00	1456.00	6.00	0.79	146.08	comp
	1627.00	1629.00	2.00	0.43	6.07	comp
	1651.00	1656.00	5.00	4.54	144.94	man
	1823.00	1833.00	10.00	0.73	109.63	man
	2171.00	2175.00	4.00	0.75	131.29	comp
CHALLIS 1	1195.00	1206.00	11.00	8.14	131.12	man
Lat: 12°07'	1342.00	1357.00	15.00	1.56	10.56	comp
Long: 125°00'	1360.00	1367.00	7.00	1.43	162.32	comp
	1373.00	1376.00	3.00	2.14	134.00	comp
	1379.00	1381.00	2.00	3.34	136.80	comp
	1383.00	1386.00	3.00	0.54	33.40	comp
	1470.00	1472.00	2.00	0.30	8.60	comp
	1498.00	1500.00	2.00	0.30	169.00	comp
CHALLIS 3	1230.00	1233.00	3.00	0.30	154.00	comp
Lat: 12°07'						
Long: 125°01'						
	1314.00	1332.00	18.00	2.99	152.36	man
	1338.00	1344.00	6.00	0.40	61.20	comp
	1347.00	1349.00	2.00	0.50	57.57	comp
	1375.00	1378.00	3.00	3.76	150.56	comp
	1394.00	1398.00	4.00	3.17	145.38	man
CHALLIS 5	1149.00	1161.00	12.00	1.70	159.96	comp
Lat: 12°07'	1164.00	1182.00	18.00	1.71	172.38	comp
Long: 125°00'	1184.00	1187.00	3.00	0.46	174.88	comp
	1267.00	1275.00	8.00	0.60	145.00	comp
	1280.00	1282.00	2.00	0.57	151.68	comp
	1289.00	1291.00	2.00	0.44	143.64	comp
	1309.00	1311.00	2.00	0.40	156.72	comp
	1324.00	1326.00	2.00	0.30	37.10	comp
	1345.00	1347.00	2.00	0.44	161.40	comp
	1396.00	1405.00	9.00	2.49	142.16	man
	1462.00	1464.00	2.00	0.40	144.50	comp
	1475.00	1477.00	2.00	0.38	63.92	comp
CHALLIS 8	1152.00	1193.00	41.00	2.90	164.89	man
Lat: 12°07'	1242.00	1257.00	15.00	5.19	145.52	man
Long: 125°00'	1322.00	1349.00	27.00	2.58	160.18	comp
	1354.00	1359.00	5.00	2.43	138.93	comp
	1523.00	1531.00	8.00	1.68	161.48	man
CHALLIS 10	1627.02	1647.99	20.97	4.41	134.99	man
Lat: 12°08'	1682.01	1695.46	13.45	1.06	132.13	man
Long: 125°01'						
CHALLIS 11	1094.00	1099.00	5.00	0.28	126.87	comp
Lat: 12°07'	1108.00	1110.00	2.00	2.22	44.77	comp
Long: 125°03'	1140.00	1145.00	5.00	2.89	177.52	comp
	1212.00	1214.00	2.00	6.68	160.43	comp
	1296.00	1318.00	22.00	5.23	151.73	man
	1349.00	1480.00	131.00	6.00	136.51	man

WELL	Top	Bottom	Length	Max ECC	Azimuth	Analysis Type
	1603.00	1609.00	6.00	2.02	117.48	comp
	1687.00	1694.00	7.00	0.38	145.33	comp
CHALLIS 12	1165.00	1173.00	8.00	1.84	150.64	man
Lat: 12°07'	1213.00	1215.00	2.00	0.78	140.56	comp
Long: 125°00'	1223.00	1228.00	5.00	0.86	144.04	comp
	1236.00	1238.00	2.00	0.91	135.13	comp
	1249.00	1256.00	7.00	8.70	145.81	man
	1289.00	1293.00	4.00	0.49	166.60	comp
	1303.00	1314.00	11.00	1.42	5.27	comp
	1316.00	1320.00	4.00	1.29	13.31	comp
	1320.00	1346.00	26.00	6.58	143.61	man
	1362.00	1376.00	14.00	7.30	147.26	man
	1508.00	1517.00	9.00	0.55	112.90	man
CLEIA 1	2892.25	2893.77	1.52	0.99	173.00	comp
Lat: 10°55'	2895.75	2897.28	1.52	0.87	160.30	comp
Long: 125°06'	2898.80	2900.48	1.68	1.12	165.38	comp
	2902.46	2904.90	2.44	0.92	160.63	comp
	2905.20	2907.18	1.98	0.93	159.17	comp
	2908.25	2912.52	4.27	1.76	149.73	comp
	2930.96	2957.17	26.21	3.39	124.08	comp
	2959.30	2966.62	7.31	3.00	114.08	comp
	2966.92	2970.73	3.81	1.76	108.30	comp
	2977.59	2991.00	13.41	1.49	98.60	comp
	2991.31	2992.83	1.52	0.74	71.16	comp
	2993.14	2994.66	1.52	0.75	71.96	comp
	3005.33	3040.69	35.36	1.50	47.66	comp
	3044.04	3045.56	1.52	0.28	111.51	comp
	3044.95	3046.63	1.68	0.37	113.98	comp
	3065.07	3067.51	2.44	0.66	141.33	comp
	3067.66	3077.87	10.21	0.67	122.65	comp
	3068.27	3077.57	9.30	0.66	121.39	comp
	3088.69	3090.37	1.68	3.78	166.24	comp
	3100.12	3108.96	8.84	1.24	28.30	man
	3101.19	3103.47	2.29	0.64	38.71	comp
	3101.95	3105.46	3.51	0.65	40.43	comp
	3105.00	3109.42	4.42	1.24	28.30	comp
	3105.76	3109.11	3.35	0.62	33.09	comp
	3113.53	3115.06	1.52	0.85	33.65	comp
	3116.73	3122.37	5.64	1.00	33.01	comp
	3117.04	3127.40	10.36	1.00	33.01	man
	3122.68	3127.55	4.88	0.91	37.33	comp
	3151.94	3167.94	16.00	1.41	157.02	comp
	3168.40	3172.97	4.57	0.77	20.57	comp
	3295.80	3300.98	5.18	0.69	92.38	comp
	3301.44	3314.70	13.26	0.68	87.87	comp
	3315.16	3331.62	16.46	0.68	71.67	comp
	3332.23	3345.79	13.56	0.51	18.65	comp
	3375.20	3434.64	59.44	1.08	141.21	comp
	3511.14	3532.94	21.79	0.50	136.45	man
	3589.63	3592.07	2.44	0.50	11.09	comp
	3608.22	3611.58	3.35	0.29	5.65	comp
	3613.25	3617.82	4.57	0.38	178.60	comp

WELL	Top	Bottom	Length	Max ECC	Azimuth	Analysis Type
	3618.28	3620.26	1.98	0.39	159.66	comp
	3688.08	3693.45	5.37	0.65	169.49	comp
	3693.57	3695.21	1.64	0.65	165.79	comp
	3705.57	3709.38	3.81	1.02	139.37	comp
	3730.03	3733.99	3.96	1.99	142.26	man
	3766.76	3768.66	1.91	0.74	100.89	comp
	3777.01	3778.99	1.98	0.90	154.83	man
CONWAY 1	2010.04	2014.04	4.00	2.13	121.21	comp
Lat: 12°46'	2014.20	2019.00	4.80	1.59	128.81	comp
Long: 124°40'	2019.45	2028.44	8.99	1.13	117.67	comp
	2029.40	2040.52	11.13	1.44	99.94	comp
	2040.64	2050.16	9.52	1.05	89.53	comp
	2051.72	2054.54	2.82	0.86	82.02	comp
	2078.01	2137.98	59.97	1.28	77.73	man
DILLON SHOALS 1	2654.00	2658.30	4.30	1.10	155.00	man/paper
Lat: 11°08'	3350.00	3433.00	83.00	2.30	142.00	man/paper
Long: 125°16'	3435.00	3450.00	15.00	0.80	131.00	man/paper
	3453.00	3469.20	16.20	0.70	132.00	man/paper
	3519.00	3521.00	2.00	0.50	93.00	man/paper
	3746.00	3748.20	2.20	0.60	3.00	man/paper
	3827.00	3831.70	4.70	0.50	176.00	man/paper
	3845.00	3848.40	3.40	0.50	137.00	man/paper
	3862.50	3874.30	11.80	0.60	119.00	man/paper
	3906.80	3913.60	6.80	0.60	142.00	man/paper
	3918.00	3921.20	3.20	0.40	122.00	man/paper
	3926.40	3929.20	2.80	0.60	129.00	man/paper
DISCORBIS 1	3392.47	3397.99	5.53	0.35	154.75	comp
Lat: 12°53'	3404.86	3407.66	2.80	0.35	136.43	comp
Long: 123°49'	3407.79	3410.79	3.01	0.36	116.18	comp
	3413.52	3415.14	1.63	0.24	45.46	comp
	3416.56	3418.07	1.50	0.24	172.35	comp
	3420.06	3421.56	1.50	0.28	59.58	comp
	3422.25	3424.08	1.83	0.38	8.77	comp
	3425.46	3428.19	2.72	0.57	133.83	comp
	3432.37	3433.88	1.50	0.29	177.05	comp
	3436.76	3438.43	1.67	0.25	78.72	comp
	3444.85	3447.25	2.40	0.41	67.48	comp
	3447.37	3449.93	2.56	0.32	48.83	comp
	3450.50	3453.14	2.64	0.43	4.52	comp
	3455.17	3457.77	2.60	0.31	123.47	comp
	3457.90	3460.54	2.64	0.43	108.95	comp
	3461.47	3464.24	2.76	0.43	66.37	comp
	3464.36	3467.61	3.25	0.46	44.78	comp
	3467.73	3470.82	3.09	0.34	169.91	comp
	3470.94	3473.54	2.60	0.45	166.90	comp
	3473.66	3476.63	2.97	0.31	136.57	comp
	3483.95	3485.73	1.79	0.35	33.01	comp
	3485.86	3489.72	3.86	0.45	5.93	comp
	3489.84	3493.05	3.21	0.45	0.89	comp
	3493.17	3496.26	3.09	0.43	150.10	comp
	3496.38	3499.51	3.13	0.42	90.80	comp
	3499.63	3502.19	2.56	0.44	79.98	comp

WELL	Top	Bottom	Length	Max ECC	Azimuth	Analysis Type
	3502.32	3505.04	2.72	0.45	35.44	comp
	3505.16	3508.29	3.13	0.55	6.73	comp
	3508.41	3510.12	1.71	0.64	174.33	comp
	3510.24	3512.19	1.95	0.46	148.14	comp
	3512.31	3514.87	2.56	0.34	110.35	comp
	3515.32	3517.80	2.48	0.39	72.27	comp
	3517.92	3520.16	2.24	0.45	34.16	comp
	3520.28	3522.07	1.79	0.46	17.06	comp
	3522.19	3524.18	1.99	0.41	164.79	comp
	3527.55	3530.44	2.89	0.37	114.15	comp
	3531.86	3534.42	2.56	0.29	58.83	comp
	3542.55	3545.47	2.93	0.28	3.72	comp
	3545.60	3547.55	1.95	0.25	130.62	comp
	3547.67	3549.99	2.32	0.25	100.19	comp
	3554.05	3557.06	3.01	0.41	38.89	comp
	3557.18	3561.00	3.82	0.93	177.15	comp
	3562.38	3564.17	1.79	1.20	162.86	comp
	3582.58	3584.94	2.36	0.58	126.34	comp
DRAKE 1	1411.02	1439.96	28.94	4.32	114.94	man
Lat: 11°17'	1454.83	1456.54	1.71	1.84	156.06	comp
Long: 125°50'	1467.02	1506.93	39.91	1.88	140.34	man
	1551.64	1553.59	1.95	1.63	51.72	comp
	1612.03	1629.99	17.96	0.98	111.42	man
	1681.03	1686.97	5.93	3.72	151.00	man
	1740.04	1773.94	33.89	2.60	155.25	man
	1784.02	1848.96	64.94	2.46	175.50	man
	2249.99	2251.78	1.79	0.41	96.19	comp
	2335.66	2353.87	18.21	0.59	135.25	comp
	2354.44	2357.28	2.84	0.50	131.00	comp
ECLIPSE 2	2074.00	2131.60	57.60	1.50	36.00	man/paper
Lat: 12°14'	2132.30	2145.40	13.10	0.60	51.00	man/paper
Long: 124°38'	2154.80	2176.70	21.90	0.90	81.00	man/paper
	2176.70	2179.30	2.60	1.60	161.00	man/paper
	2192.60	2208.00	15.40	1.90	53.00	man/paper
	2211.00	2213.60	2.60	1.90	35.00	man/paper
	2216.00	2260.00	44.00	2.20	167.00	man/paper
	2273.90	2295.00	21.10	0.70	64.00	man/paper
	2335.00	2375.00	40.00	5.60	155.00	man/paper
	2462.20	2495.00	32.80	7.10	155.00	man/paper
	2503.40	2508.20	4.80	5.70	129.00	man/paper
	2513.50	2524.00	10.50	3.30	161.00	man/paper
	2530.10	2550.00	19.90	2.80	164.00	man/paper
	2553.30	2616.60	63.30	2.70	165.00	man/paper
	2765.70	2784.70	19.00	1.10	146.00	man/paper
FAGIN 1	2215.16	2220.85	5.69	1.60	130.54	comp
Lat: 11°34'	2220.98	2229.35	8.37	1.66	105.86	comp
Long: 125°08'	2243.73	2261.41	17.68	2.92	135.79	comp
	2261.54	2265.72	4.19	3.00	130.04	comp
	2265.92	2275.23	9.31	3.27	121.47	comp
	2308.96	2314.04	5.08	0.69	51.50	comp
	2324.36	2335.42	11.05	2.08	106.22	comp
	2383.98	2387.60	3.62	0.36	165.41	comp

WELL	Top	Bottom	Length	Max ECC	Azimuth	Analysis Type
	2403.98	2413.00	9.02	1.67	156.24	comp
	2421.66	2452.14	30.48	3.14	148.86	comp
	2452.30	2469.86	17.56	3.06	152.08	comp
	2475.42	2501.56	26.13	1.51	117.61	comp
	2516.31	2518.46	2.15	1.28	8.57	comp
	2572.51	2583.61	11.09	1.36	137.65	comp
	2611.81	2619.13	7.31	1.03	135.92	comp
	2670.78	2678.62	7.84	0.71	152.38	comp
	2702.15	2708.78	6.62	0.66	7.33	comp
	2728.85	2730.89	2.03	0.69	168.42	comp
	2742.43	2746.53	4.10	0.57	162.22	comp
GARGANEY 1st1	1211.72	1213.67	1.95	0.52	172.75	comp
Lat: 11°22'	1217.25	1219.53	2.28	1.08	68.25	comp
Long: 125°55'	1224.73	1228.06	3.33	0.53	161.25	comp
	1233.59	1235.21	1.63	0.62	129.50	comp
	1237.08	1238.79	1.71	0.53	96.38	comp
	1242.93	1244.80	1.87	0.53	74.81	comp
	1247.08	1249.84	2.76	0.54	28.64	comp
	1260.98	1264.31	3.33	0.53	119.25	comp
	1265.37	1267.89	2.52	0.71	97.75	comp
	1268.29	1270.33	2.03	0.45	84.75	comp
	1345.92	1347.46	1.54	1.28	150.75	comp
	1357.05	1360.47	3.41	0.87	129.25	comp
	1360.71	1366.40	5.69	0.70	99.25	comp
	1366.64	1369.57	2.93	0.62	69.00	comp
	1411.02	1445.97	34.95	3.64	179.88	man
	1581.30	1583.42	2.11	1.69	119.25	comp
	1584.15	1588.54	4.39	1.19	125.25	comp
	1692.01	1710.94	18.94	2.41	170.25	man
	1837.01	2002.98	165.97	5.68	140.88	man
	2030.46	2032.65	2.19	1.77	97.75	comp
	2099.06	2102.55	3.50	2.14	82.00	comp
	2103.69	2107.10	3.41	2.23	77.63	comp
	2127.42	2130.11	2.68	0.87	69.00	comp
	2131.24	2132.95	1.71	0.78	12.88	comp
	2145.96	2147.91	1.95	0.63	166.75	comp
	2178.47	2185.54	7.07	0.63	24.38	comp
	2218.86	2220.57	1.71	0.51	36.50	comp
	2229.67	2231.62	1.95	0.63	87.75	comp
	2236.18	2239.51	3.33	0.45	32.75	comp
	2245.44	2247.64	2.20	0.45	152.50	comp
	2253.00	2254.55	1.54	0.54	76.25	comp
	2269.83	2271.78	1.95	0.54	138.00	comp
	2272.02	2274.54	2.52	0.54	86.00	comp
	2277.30	2280.39	3.09	0.45	78.75	comp
	2312.58	2314.45	1.87	0.53	175.38	comp
	2330.14	2331.92	1.79	0.37	97.75	comp
	2349.64	2351.35	1.71	0.42	108.38	comp
	2353.63	2355.90	2.28	0.34	91.25	comp
	2356.96	2359.15	2.20	0.43	92.50	comp
	2395.24	2399.63	4.39	0.69	171.88	comp
	2399.79	2401.42	1.63	0.34	163.06	comp

WELL	Top	Bottom	Length	Max ECC	Azimuth	Analysis Type
	2403.21	2404.75	1.54	0.43	131.63	comp
GREBE 1	2293.30	2353.70	60.40	1.00	110.00	man/paper
Lat: 12°16'						
Long: 124°09'						
HARBINGER 1	1955.86	1964.44	8.57	2.06	25.92	man
Lat: 12°19'	2009.81	2012.33	2.52	0.34	100.17	comp
Long: 126°55'	2036.33	2038.96	2.63	0.47	172.22	comp
	2041.36	2043.30	1.94	0.30	162.48	comp
	2049.13	2050.73	1.60	0.32	7.46	comp
	2064.11	2073.48	9.37	0.28	9.79	comp
	2074.16	2076.91	2.74	0.27	2.69	comp
	2077.25	2078.97	1.72	0.29	162.85	comp
	2084.22	2086.28	2.06	0.29	139.32	comp
	2101.71	2103.77	2.06	0.54	135.58	comp
	2129.71	2131.09	1.37	0.31	81.49	man
	2143.20	2146.40	3.20	0.24	15.88	man
	2175.21	2179.89	4.69	0.34	101.79	man
IRIS 1	3503.15	3506.24	3.09	12.99	28.80	comp
Lat: 11°17'	3516.64	3518.24	1.60	12.12	129.57	man
Long: 126°33'	3548.07	3549.22	1.14	11.45	131.80	man
	3550.02	3550.36	0.34	12.04	45.29	man
	3571.96	3574.48	2.52	11.54	64.91	man
	3611.62	3613.80	2.17	11.61	29.20	comp
JABIRU 1A	1251.00	1263.00	12.00	2.63	137.00	comp
Lat: 11°56'	1370.00	1375.00	5.00	0.59	70.00	comp
Long: 125°00'	1377.00	1381.00	4.00	0.37	68.00	comp
	1431.00	1454.00	23.00	3.33	149.00	man
	1490.00	1524.00	34.00	3.00	155.96	comp
	1527.00	1530.00	3.00	0.50	142.18	comp
	1542.00	1583.00	41.00	3.28	155.22	man
	1660.00	1663.00	3.00	0.30	171.00	comp
	1667.00	1670.00	3.00	0.30	150.76	comp
	1750.00	1755.00	5.00	1.20	65.18	comp
	1825.00	1828.00	3.00	1.17	64.52	comp
	1873.00	1875.00	2.00	0.50	81.63	comp
	2118.00	2121.00	3.00	1.96	157.16	comp
	2174.00	2178.00	4.00	0.80	52.67	comp
	2269.00	2272.00	3.00	1.25	141.39	comp
	2400.00	2406.00	6.00	1.80	137.18	man
	2420.00	2450.00	30.00	2.30	151.33	man
	2522.00	2528.00	6.00	1.19	138.47	man
	2534.00	2544.00	10.00	1.74	133.37	man
	2548.00	2561.00	13.00	1.78	146.60	man
	2672.00	2677.00	5.00	0.68	145.00	man
	2749.00	2759.00	10.00	1.84	146.88	man
	2897.00	2940.00	43.00	4.30	144.67	man
JABIRU 6	1425.00	1609.00	184.00	5.19	104.69	man
Lat: 11°56'	1594.00	1605.00	11.00	3.63	121.00	comp
Long: 125°01'						

WELL	Top	Bottom	Length	Max ECC	Azimuth	Analysis Type
JABIRU 7	1365.00	1374.00	9.00	2.22	90.55	comp
Lat: 11°55'	1392.00	1395.00	3.00	0.75	139.38	comp
Long: 125°01'	1477.00	1481.00	4.00	0.94	139.36	comp
	1522.00	1526.00	4.00	0.35	133.00	comp
	1528.00	1530.00	2.00	0.52	142.60	comp
	1567.00	1582.00	15.00	0.56	142.64	man
	1586.00	1593.00	7.00	0.75	142.52	man
JABIRU 9st	1361.00	1414.00	53.00	6.36	150.21	man
Lat: 11°57'	1578.00	1608.00	30.00	1.17	153.82	man
Long: 124°59'	1620.00	1622.00	2.00	0.47	170.73	comp
	1640.00	1645.00	5.00	1.71	136.53	comp
	1651.00	1664.00	13.00	2.35	129.40	man
	1653.00	1655.00	2.00	2.34	133.74	comp
	1658.00	1660.00	2.00	2.35	129.40	comp
KALYPTEA 1	2019.95	2032.26	12.31	1.29	4.61	comp
Lat: 13°02'	2033.84	2046.52	12.68	0.89	174.12	comp
Long: 123°52'	2046.65	2048.39	1.75	0.40	1.27	comp
	2067.05	2071.52	4.47	0.47	101.63	comp
	2071.60	2074.53	2.93	0.50	100.36	comp
	2075.99	2081.15	5.16	0.49	104.63	comp
	2090.46	2092.28	1.83	0.39	134.66	comp
	2095.78	2101.71	5.93	0.64	146.05	comp
	2102.93	2104.52	1.59	0.38	148.28	comp
	2107.24	2109.76	2.52	0.47	143.40	comp
	2148.08	2150.81	2.72	0.66	83.80	comp
	2174.38	2176.25	1.87	0.62	57.43	comp
	2183.48	2195.39	11.91	1.49	37.93	comp
	2278.50	2283.01	4.51	0.43	146.84	comp
	2316.41	2320.93	4.51	0.59	128.22	comp
	2361.40	2371.52	10.12	1.23	94.15	comp
	2373.35	2375.30	1.95	1.37	89.63	comp
	2376.48	2388.55	12.07	1.79	82.43	comp
	2388.83	2401.60	12.76	1.66	79.59	comp
	2490.92	2494.95	4.02	0.71	96.64	comp
	2495.88	2497.47	1.59	0.42	99.68	comp
	2501.29	2502.99	1.71	0.50	98.98	comp
	2603.01	2650.96	47.95	8.48	158.90	man
	2671.69	2692.33	20.65	4.12	161.91	comp
	2696.40	2706.27	9.88	2.56	172.42	comp
	2768.01	2813.97	45.96	4.81	157.64	man
	2854.00	2855.87	1.87	4.09	145.20	comp
	2865.26	2866.96	1.71	1.20	101.09	comp
	2868.83	2873.55	4.72	1.67	105.08	comp
	2877.49	2880.82	3.33	1.56	103.42	comp
	2881.03	2883.51	2.48	0.87	116.29	comp
	2886.31	2889.72	3.41	0.87	95.90	comp
	2901.02	2902.52	1.50	0.58	127.76	comp
	2924.10	2926.01	1.91	1.05	178.81	comp
	2926.49	2928.98	2.52	1.53	0.29	comp
	2940.60	2943.04	2.44	0.91	3.72	comp
	2943.94	2945.44	1.50	0.67	124.14	comp
	2960.11	2962.27	2.15	1.54	144.59	comp

WELL	Top	Bottom	Length	Max ECC	Azimuth	Analysis Type
	2967.02	2968.69	1.67	1.09	140.58	comp
	2972.59	2974.46	1.87	0.66	120.67	comp
	2976.53	2980.59	4.06	1.92	106.08	comp
	3020.01	3026.96	6.95	7.56	162.14	man
	3062.44	3067.36	4.92	1.19	130.07	comp
	3084.67	3090.73	6.05	1.07	118.77	comp
	3109.26	3113.65	4.39	2.08	120.36	comp
	3115.48	3125.56	10.08	1.29	123.12	comp
	3126.17	3129.78	3.62	1.23	107.82	comp
	3129.99	3131.94	1.95	1.33	115.44	comp
	3132.67	3134.42	1.75	0.88	118.87	comp
	3135.43	3138.60	3.17	1.32	86.27	comp
	3138.81	3141.81	3.01	0.96	80.18	comp
	3145.47	3147.95	2.48	0.63	84.20	comp
	3163.72	3165.42	1.71	1.18	137.06	comp
	3181.80	3183.88	2.07	1.71	144.59	comp
	3186.96	3188.47	1.50	0.82	18.90	comp
	3194.81	3196.80	1.99	1.32	159.57	comp
	3249.02	3273.00	23.98	6.98	152.27	man
	3309.53	3311.48	1.95	0.85	60.46	comp
	3321.60	3323.92	2.32	0.90	117.20	comp
	3344.77	3346.31	1.54	0.52	153.65	comp
	3346.39	3349.28	2.89	1.24	153.65	comp
	3353.22	3356.68	3.45	0.51	14.93	comp
	3357.61	3359.81	2.19	0.55	178.20	comp
	3392.48	3394.35	1.87	0.37	43.61	comp
	3398.29	3400.16	1.87	0.46	24.03	comp
	3406.91	3409.96	3.05	0.44	22.09	comp
	3410.16	3412.23	2.07	0.50	21.96	comp
	3418.57	3420.93	2.36	0.37	155.67	comp
MAPLE 1	2837.04	2843.99	6.95	1.96	148.46	man
Lat: 12°01'	2846.10	2848.25	2.15	0.62	156.65	comp
Long: 124°32'	2872.84	2875.69	2.84	0.92	39.34	comp
	2890.03	2898.97	8.94	0.96	35.17	man
	2916.33	2924.74	8.41	1.02	132.44	comp
	2924.86	2936.65	11.78	0.84	105.82	comp
	2997.57	2999.35	1.79	0.35	152.26	comp
	3058.77	3061.09	2.32	0.60	123.48	comp
	3206.01	3219.99	13.98	2.58	150.68	man
	3260.02	3290.99	30.97	1.90	83.46	man
	3313.34	3317.57	4.23	0.51	101.70	comp
	3317.73	3319.31	1.58	0.49	100.28	comp
	3319.44	3324.88	5.44	1.43	84.00	comp
	3325.65	3331.34	5.69	1.08	97.49	comp
	3332.24	3335.24	3.01	1.35	91.69	comp
	3335.33	3337.32	1.99	1.20	91.73	comp
	3337.52	3342.40	4.88	0.97	86.17	comp
	3342.52	3346.70	4.19	0.61	69.24	comp
	3349.26	3351.13	1.87	0.49	0.86	comp
	3351.91	3367.88	15.97	1.16	161.99	comp
	3368.00	3390.60	22.60	0.83	133.62	comp
	3460.46	3462.93	2.48	0.39	169.36	comp

WELL	Top	Bottom	Length	Max ECC	Azimuth	Analysis Type
	3679.46	3681.09	1.63	1.22	155.46	comp
	3684.02	3703.48	19.47	4.00	164.62	man
	3726.04	3757.98	31.94	2.44	149.97	man
MONTARA 1	2650.00	2673.98	23.98	1.65	177.04	man
Lat: 12°41'	2778.30	2782.45	4.15	0.95	137.66	comp
Long: 124°32'	2782.90	2785.54	2.64	0.64	146.93	comp
	2784.24	2789.76	2.52	0.50	166.16	comp
	2791.47	2801.18	9.71	1.20	168.11	comp
	2804.52	2808.05	3.53	0.69	173.47	comp
	2834.67	2836.46	1.79	0.30	60.39	comp
	2896.08	2897.58	1.50	0.26	169.00	comp
	2902.21	2911.16	8.94	0.39	120.52	comp
	2911.28	2933.67	22.39	0.59	98.48	comp
	2933.79	2942.94	9.14	0.55	84.14	comp
	2943.30	2946.07	2.76	0.60	63.05	comp
	2946.19	2948.67	2.48	0.47	43.63	comp
	3083.18	3086.44	3.25	0.56	8.68	comp
	3087.49	3089.12	1.63	0.63	148.29	comp
	3110.58	3121.63	11.05	0.34	46.52	comp
	3152.72	3159.34	6.62	0.43	8.85	comp
	3160.16	3172.23	12.07	0.36	29.70	comp
NOME 1	1321.00	1342.30	21.30	0.50	63.00	man/paper
Lat: 11°39'	1348.00	1350.50	2.50	0.60	150.00	man/paper
Long: 125°13'						
	1551.00	1554.70	3.70	0.40	132.00	man/paper
	1556.30	1558.20	1.90	1.00	131.00	man/paper
	1563.00	1567.00	4.00	0.90	147.00	man/paper
	1580.00	1582.70	2.70	0.50	140.00	man/paper
	1596.20	1599.90	3.70	0.70	180.00	man/paper
	1614.90	1625.30	10.40	1.70	138.00	man/paper
PUFFIN 1	2123.80	2139.70	15.80	1.50	151.00	man/paper
Lat: 12°11'	2247.00	2249.40	2.40	1.20	149.00	man/paper
Long: 124°12'	2261.60	2273.80	12.20	1.40	84.00	man/paper
	2363.40	2365.20	1.80	0.80	106.00	man/paper
	2851.10	2856.00	4.90	0.60	149.00	man/paper
RAINBOW 1	1704.00	1747.00	43.00	5.10	140.00	man/paper
Lat: 11°56'	1758.00	1778.00	20.00	2.20	131.00	man/paper
Long: 124°20'	1875.50	1881.00	5.50	0.80	56.00	man/paper
	1931.00	2017.00	86.00	4.00	150.00	man/paper
	2033.50	2044.30	10.80	1.00	96.00	man/paper
	2047.00	2056.00	9.00	0.80	139.00	man/paper
	2097.40	2120.00	22.60	2.60	20.00	man/paper
	2154.00	2158.00	4.00	0.80	96.00	man/paper
	2165.00	2168.10	3.10	0.60	109.00	man/paper
	2175.00	2180.40	5.40	1.00	117.00	man/paper
	2222.00	2226.00	4.00	1.20	161.00	man/paper
	2240.00	2252.00	12.00	1.60	137.00	man/paper
	2252.50	2287.80	35.30	5.30	159.00	man/paper
	2293.00	2295.00	2.00	2.40	123.00	man/paper
	2301.20	2325.00	23.80	3.00	151.00	man/paper
	2334.00	2342.00	8.00	3.30	151.00	man/paper

WELL	Top	Bottom	Length	Max ECC	Azimuth	Analysis Type
	2418.00	2428.00	10.00	0.70	171.00	man/paper
	2558.70	2560.50	1.80	4.50	159.00	man/paper
RAINIER 1	1228.91	1230.70	1.79	0.65	147.76	comp
Lat: 12°04'	1231.19	1233.95	2.76	1.00	159.63	comp
Long: 125°01'	1234.44	1238.83	4.39	1.05	17.49	comp
	1245.49	1254.60	9.10	0.49	8.89	comp
	1255.09	1256.87	1.79	0.54	178.46	comp
	1291.01	1393.91	102.90	5.34	159.88	man
	1345.31	1348.23	2.93	5.27	160.51	comp
	1348.56	1351.00	2.44	4.94	163.95	comp
	1351.81	1359.45	7.64	4.93	162.60	comp
	1359.77	1362.86	3.09	5.00	171.16	comp
	1363.35	1370.34	6.99	4.77	166.98	comp
	1370.83	1375.71	4.88	3.90	172.19	comp
	1376.52	1382.37	5.85	3.76	174.78	comp
	1382.86	1393.59	10.73	2.49	14.15	comp
	1398.79	1402.53	3.74	1.22	40.56	comp
	1402.85	1404.97	2.11	0.78	43.48	comp
	1464.95	1517.46	52.51	1.23	127.56	comp
	1595.16	1653.85	58.68	3.79	9.35	man
	1627.51	1630.27	2.76	2.43	11.94	comp
	1630.76	1645.23	14.47	2.85	19.10	comp
	1645.72	1652.54	6.83	2.00	21.50	comp
	1799.17	1814.13	14.96	0.29	72.37	comp
	1822.09	1830.55	8.45	0.30	82.41	comp
	1978.80	1989.37	10.57	0.29	118.26	comp
	2069.35	2072.44	3.09	0.32	135.48	comp
	2120.88	2122.51	1.63	0.69	109.73	comp
	2122.99	2124.78	1.79	0.63	106.67	comp
	2186.07	2204.92	18.86	4.94	159.49	man
	2299.86	2301.81	1.95	1.13	47.43	comp
ROWAN 1st	2563.08	2574.71	11.62	0.93	6.27	comp
Lat: 12°29'	2576.01	2577.63	1.63	2.77	65.02	comp
Long: 124°23'	2580.27	2582.06	1.79	1.08	154.96	comp
	2587.22	2589.87	2.64	1.09	149.54	comp
	2607.71	2609.90	2.19	0.65	148.71	comp
	2625.99	2639.24	13.25	0.63	170.13	comp
	2654.40	2656.31	1.91	0.40	40.39	comp
	2686.47	2691.55	5.08	3.22	161.18	comp
	2746.78	2768.15	21.38	0.98	177.49	comp
	2788.96	2795.50	6.54	0.63	177.94	comp
	2797.98	2803.02	5.04	0.82	162.46	comp
	2807.33	2810.13	2.80	0.55	145.21	comp
	2889.26	2893.49	4.23	0.46	131.85	comp
	2893.61	2916.61	23.00	0.72	123.25	comp
	2926.20	2933.44	7.23	0.66	149.46	comp
	2933.56	2956.97	23.41	0.87	132.00	comp
	2957.09	2963.35	6.26	0.63	129.91	comp
	2969.73	2974.77	5.04	0.56	143.03	comp
	2972.53	2974.85	2.32	0.85	148.96	comp
	2977.21	2982.33	5.12	0.81	147.34	comp
	2984.56	2990.49	5.93	0.64	155.79	comp

WELL	Top	Bottom	Length	Max ECC	Azimuth	Analysis Type
	3072.47	3074.05	1.58	0.32	13.88	comp
	3074.62	3076.29	1.67	0.37	4.46	comp
	3076.53	3083.44	6.91	0.77	166.76	comp
	3085.80	3091.97	6.18	0.76	153.69	comp
	3110.50	3112.09	1.59	0.37	148.90	comp
	3149.48	3152.65	3.17	0.50	175.99	comp
	3152.77	3155.13	2.36	0.53	159.06	comp
	3199.06	3202.60	3.54	1.97	142.41	comp
	3303.30	3306.02	2.72	0.57	9.20	comp
SHALIMAR 1	2474.52	2488.24	13.72	0.80	123.01	man
Lat: 11°58'	2504.54	2519.32	14.78	0.86	151.33	man
Long: 125°12'	2535.63	2557.42	21.79	0.91	136.76	man
	2586.38	2588.51	5.18	0.34	33.92	man
	2592.63	2594.15	1.52	0.36	72.85	comp
	2597.05	2598.73	1.68	0.32	69.17	comp
	2619.76	2621.89	2.13	0.52	6.36	comp
	2640.64	2649.78	9.14	1.01	179.83	man
	2668.52	2673.40	4.88	0.35	44.30	comp
	2673.86	2675.38	1.52	0.33	17.28	comp
	2681.78	2683.61	1.83	0.35	62.35	comp
	2714.09	2718.51	4.42	0.40	34.89	comp
SKUA 2	2056.00	2080.00	24.00	0.60	170.00	man/paper
Lat: 12°30'	2085.00	2090.00	5.00	1.40	23.00	man/paper
Long: 124°24'	2098.00	2118.00	20.00	1.40	40.00	man/paper
	2225.00	2278.00	53.00	2.10	86.00	man/paper
	2287.00	2306.00	19.00	1.50	141.00	man/paper
	2313.00	2323.00	10.00	0.90	6.00	man/paper
	2346.00	2352.00	6.00	1.00	105.00	man/paper
	2353.40	2356.20	2.80	0.20	124.00	man/paper
	2356.50	2366.00	9.50	0.80	125.00	man/paper
	2375.60	2377.40	1.80	0.40	111.00	man/paper
SKUA 4	2320.00	2320.00	2.00	0.39	110.35	comp
Lat: 12°29'	2327.00	2331.00	4.00	4.79	162.86	man
Long: 124°26'						
SKUA 5	2324.00	2340.00	16.00	2.39	124.07	man
Lat: 12°28'	2395.00	2400.00	5.00	0.55	156.34	man
Long: 124°26'						
SKUA 6	1441.00	1497.00	56.00	0.93	25.18	comp
Lat: 12°29'	1532.00	1536.00	4.00	0.35	140.59	comp
Long: 124°26'	1538.00	1540.00	2.00	0.34	133.82	comp
	1543.00	1546.00	3.00	0.31	119.73	comp
SKUA 9st	1962.00	1964.00	2.00	0.72	114.00	comp
Lat: 12°30'	2182.00	2197.00	15.00	0.90	72.12	man
Long: 124°25'	2219.00	2232.00	13.00	0.80	86.82	comp
SWAN 2	3300.00	3337.80	37.80	2.70	84.00	man/paper
Lat: 12°07'	3346.00	3348.80	2.80	0.90	116.00	man/paper
Long: 124°18'	3600.00	3662.00	62.00	2.50	163.00	man/paper
	3692.00	3747.20	55.20	2.90	141.00	man/paper
	3750.00	3753.00	3.00	1.90	141.00	man/paper
	3770.00	3870.00	100.00	3.20	13.00	man/paper

WELL	Top	Bottom	Length	Max ECC	Azimuth	Analysis Type
	3871.80	3878.20	6.40	1.30	109.00	man/paper
	3940.50	3981.00	40.50	2.00	86.00	man/paper
	3989.00	3997.00	8.00	1.30	7.00	man/paper
SWIFT 1	2000.00	2003.00	2.40	0.50	142.00	man/paper
Lat: 12°32'	2461.70	2464.40	2.70	0.70	79.00	man/paper
Long: 124°27'						
TALTARNI 1	2511.67	2523.62	11.95	0.78	24.66	comp
Lat: 12°37'	2583.49	2585.19	1.71	0.30	82.05	comp
Long: 124°35'	2589.13	2591.00	1.87	0.47	84.73	comp
	2596.21	2597.71	1.50	0.27	76.77	comp
	2598.68	2604.13	5.45	0.40	80.24	comp
	2635.75	2637.94	2.19	0.36	0.20	comp
	2758.07	2759.74	1.67	0.38	173.18	comp
	2793.31	2806.52	13.21	0.51	134.14	comp
	2811.23	2814.97	3.74	0.30	146.87	comp
	2838.09	2842.48	4.39	0.32	46.19	comp
	2959.58	2963.68	4.10	0.31	45.60	comp
	2975.22	2979.33	4.10	0.33	11.85	comp
	3046.26	3050.20	3.94	0.84	73.92	comp
	3227.51	3253.00	25.48	3.39	98.53	man
	3278.03	3288.96	10.93	1.40	127.45	man
VULCAN 1B	1834.90	1966.00	131.00	2.20	169.00	man/paper
Lat: 12°09'	1996.40	2164.10	167.60	2.30	41.00	man/paper
Long: 124°20'	2178.70	2272.60	93.90	3.00	74.00	man/paper
	2286.00	2291.80	5.80	0.70	54.00	man/paper
	2297.30	2304.00	6.70	2.70	142.00	man/paper
	2308.60	2346.40	37.80	1.40	43.00	man/paper
	2349.40	2426.50	77.10	2.10	63.00	man/paper
	2441.40	2458.50	17.10	0.60	74.00	man/paper
	2511.60	2645.70	134.10	2.50	167.00	man/paper
WOODBINE 1	2050.80	2210.00	159.20	3.80	155.00	man/paper
Lat: 12°23'	2397.00	2428.00	31.00	1.80	9.00	man/paper
Long: 124°05'	2435.70	2439.00	3.30	0.80	102.00	man/paper
	2640.40	2642.00	1.60	1.20	31.00	man/paper
	2755.50	2825.00	69.50	4.60	154.00	man/paper

Appendix C

Rose Diagrams

C.1 Description

This appendix contains unweighted rose diagrams of borehole breakout orientations from each well analysed in this study. Each rose diagram is comprised of 15° petals and scaled relative to the size of the largest petal. N is the number of breakouts in each sample.

C.2 Carnarvon Basin

Bambra 1

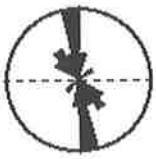

N = 39

Campbell 2

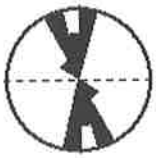

N = 10

Chervil 1

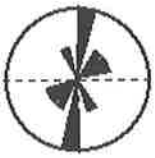

N = 6

Chinook 1

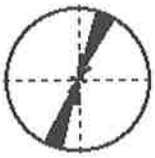

N = 43

Coojong 1

N = 25

Cossack 1

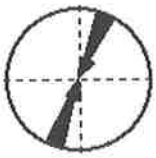

N = 5

Dillson 1

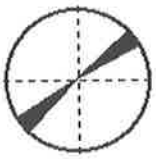

N = 2

Emma 1

N = 9

Flores 1

N = 20

Goodwyn 1

N = 30

Goodwyn 3a

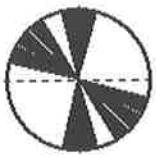

N = 5

Goodwyn 8b

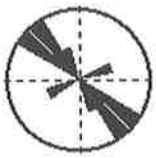

N = 6

Goodwyn 9a

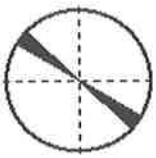

N = 4

Griffin 1

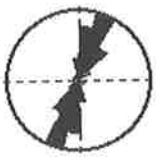

N = 29

Griffin 2

N = 22

Griffin 3

N = 5

Griffin 4

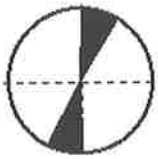

N = 2

Kanji 1

N = 33

Maitland 1

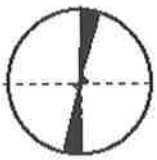

N = 11

Marra 1

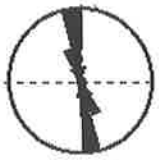

N = 28

Montebello 1

N = 36

Santo 1

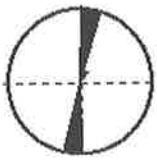

N = 6

Scindian 1a

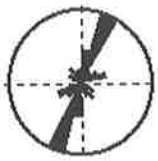

N = 46

Scindian 2

N = 8

South Chervil 1

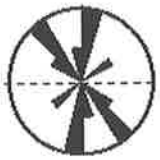

N = 7

South Pepper 1

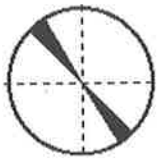

N = 1

Tanami 2

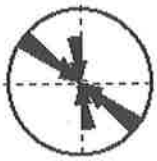

N = 29

Tingle 1

N = 14

Trafalgar 1

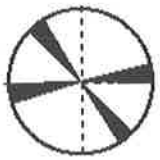

N = 2

Trealla 1a

N = 9

Ulidia 1

N = 9

Wanaea 1

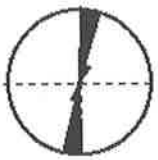

N = 21

Wanaea 2

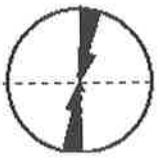

N = 11

Wanaea 3

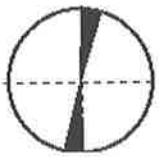

N = 5

Wandoo 1

N = 14

Wandoo 2

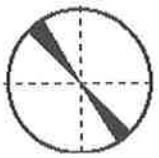

N = 1

Wandoo 3

N = 8

Wandoo 5

N = 15

Wandoo 7

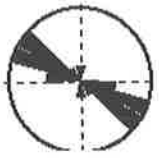

N = 13

West Barrow 1a

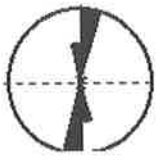

N = 32

West Muiron 3

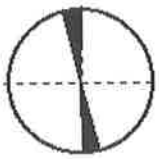

N = 1

West Muiron 4

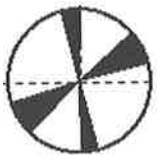

N = 3

C.3 Bonaparte Basin

Anderdon 1

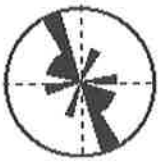

N = 7

Arunta 1

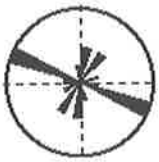

N = 11

Avocet 2

N = 25

Beluga 1

N = 6

Cassini 2

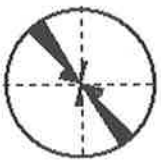

N = 6

Challis 1

N = 8

Challis 3

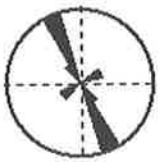

N = 6

Challis 5

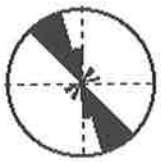

N = 12

Challis 8

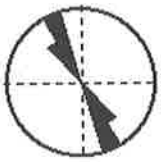

N = 5

Challis 10

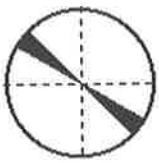

N = 2

Challis 11

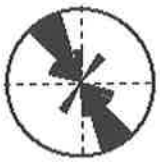

N = 8

Challis 12

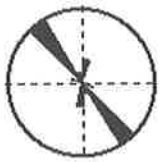

N = 11

Cleia 1

N = 40

Conway 1

N = 7

Dillon Shoals 1

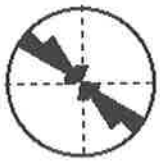

N = 12

Discorbis 1

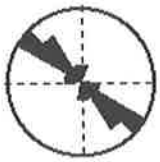

N = 44

Drake 1

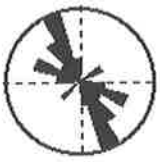

N = 11

Eclipse 2

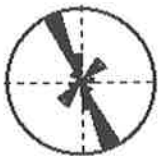

N = 15

Fagin 1

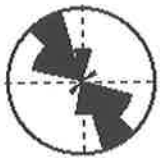

N = 19

Garganey 1st

N = 42

Grebe 1

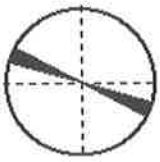

N = 1

Harbinger 1

N = 13

Iris 1

N = 6

Jabiru 1a

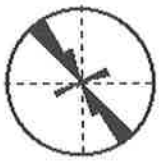

N = 23

Jabiru 6

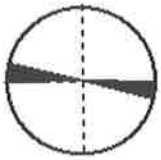

N = 1

Jabiru 7

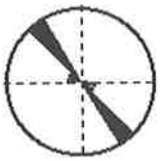

N = 7

Jabiru 9st

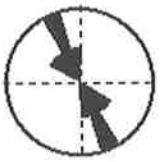

N = 5

Kalyptea 1

N = 68

Maple 1

N = 25

Montara 1

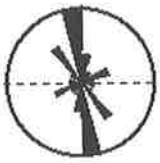

N = 18

Nome 1

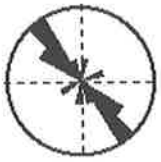

N = 8

Puffin 1

N = 5

Rainbow 1

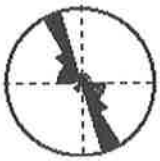

N = 18

Rainier 1

N = 18

Rowan 1st

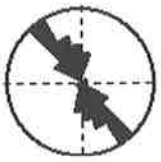

N = 30

Shalimar 1

N = 12

Skua 2

N = 10

Skua 4

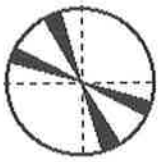

N = 2

Skua 5

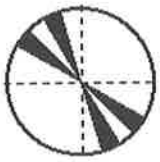

N = 2

Skua 6

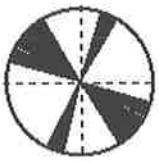

N = 4

Skua 9st

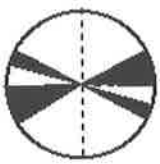

N = 3

Swan 2

N = 9

Swift 1

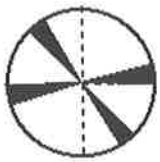

N = 2

Taltarni 1

N = 15

Vulcan 1b

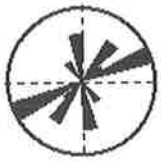

N = 9

Woodbine 1

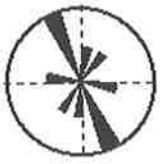

N = 5

Appendix D

Published Papers

D.1 Description

This appendix contains reprints of reviewed and published material, produced as a consequence of research for this thesis.

D.2 Timor Sea Fault-trap Integrity

Mildren, S.D., Hillis, R.R., Fett, T., and Robinson, P.H., 1995- Contemporary Stresses in the Timor Sea: implications for fault-trap integrity. In: Purcell, P.G., and R.R. (eds), The Sedimentary Basins of Western Australia, Proceedings of PESA symposium, Perth, 1994, 291-300.

D.3 Australian North West Shelf Stress Orientation

Hillis, R.H., Mildren, S.D., Pigram, C.J., and Willoughby, D.R., Rotation of horizontal stresses in the Australian North West Continental Shelf due to the collision of the Indo-Australian and Eurasian Plates, *Tectonics*, 16 (2), 323-335.

Mildren, S.D., Hillis, R.R., Fett, T., and Robinson, P.H., (1994) Contemporary stresses in the Timor Sea: implications for fault trap integrity.
In: Purcell, P.G., and Purcell, R.R., (eds.), *The Sedimentary Basins of Western Australia: Proceedings of the Petroleum Exploration Society of Australia Symposium, pp. 291-300.*

Hillis, R.R., Mildren, S.D., Pigram, C.J., and Willoughby, D.R., (1997) Rotation of horizontal stresses in the Australian North West continental shelf due to the collision of the Indo-Australian and Eurasian Plates.
Tectonics, v. 16 (2), pp. 323-335.

Bibliography

Abbott, M., & Chamalaun, F., Geochronology of some Banda Arc volcanics, in *The Geology and Tectonics of Eastern Indonesia*, edited by A. Barber, & S. Wiryosujuno, *Spec. Publ.*, 2, pp. 253-268, Geological Research Development Centre, Bandung, Indonesia, 1981.

Addis, T., Boulter, D., Roca-Ramsia, L., Plumb, D., & Last, N., The quest for borehole stability in the Cuisiana Field, Colombia, *Oilfield Review*, April/July, pp. 33-43, 1993.

Aleksandrowski, P., Inderhaug, O.H., & Knapstad, B., Tectonics structures and wellbore breakout orientation, in *Rock Mechanics, Proceedings of the 33rd U.S. Symposium*, edited by J.R. Tillerson & W.R. Wawersik, pp. 29-37, A.A. Balkema, Rotterdam, Netherlands, 1992.

Allen, G.A., Pearce, L.G.G., & Gardner, W.E., A regional interpretation of the Browse Basin, *The APEA Journal*, 18(1), pp. 23-33, 1978.

Anderson, E.M., The dynamics of faulting and dyke formation, (2nd edition), Oliver and Boyd, London, pp. 206, 1951.

Audley-Charles, M.G., Rates of Neogene and Quaternary tectonic movements in the Southern Banda Arc based on micropalaeontology, *Journal of the Geological Society of London*, 143, pp. 161-175, 1986.

Australian Geological Survey Organisation (AGSO) North West Shelf Study Group, Deep reflections on the North West Shelf: changing perceptions of basin formation, in *The Sedimentary Basins of Western Australia, Proceedings of Petroleum Exploration Society, Australian Symposium,* edited by P.G. Purcell & R.R. Purcell, pp. 63-76, Petroleum Exploration Society, Perth, Australia, 1994.

Babcock, E.A., Measurement of subsurface fractures from dipmeter logs, *Bulletin of the American Association of Petroleum Geologists*, 62, pp. 1111-1126, 1978.

Baillie, P.W, Geological development and petroleum resources, *PESA News*, June/July, pp. 30-31, 1995.

Baillie, P.W., Powell, C.McA., Li, Z.X., & Ryall, A.M., The tectonic framework of Western Australia's Neoproterozoic to Recent sedimentary basins, in *The Sedimentary Basins of Western Australia, Proceedings of Petroleum Exploration Society, Australian Symposium,* edited by P.G. Purcell & R.R. Purcell, pp. 45-62, Petroleum Exploration Society, Perth, Australia, 1994.

Balch, A.H., & Lee, M.W., Vertical seismic profiling: techniques, applications, and case histories, Boston, International Human Resources Development Corporation, p. 488, 1984.

Baldasso, F., Palaeotectonic reconstruction and evolution of pertroleum systems at the Copernicus Basin Margin, northeastern Browse Basin, *Honours Thesis*, University of Adelaide, unpublished, 1993.

Barber, P., Sequence stratigraphy and petrolrum potential of Upper Jurassic-Lower Cretaceous Depositional Systems in the Dampier Sub-basin, North West Shelf, Australia, in *The Sedimentary Basins of Western Australia, Proceedings of Petroleum Exploration Society, Australian Symposium,* edited by P.G. Purcell & R.R. Purcell, pp. 525-542, Petroleum Exploration Society, Perth, Australia, 1994.

Barton, C.A. & Zoback, M.D., Stress perturbations associated with active faults penetrated by boreholes: possible evidence for near-complete stress drop and a technique for stress magnitude measurement, *Journal of Geophysical Research*, 99, No. B5, pp. 9373-9390, 1994.

Baumann, H., Regional stress field and rifting in western Europe, *Tectonophysics*, 73, pp. 105-111, 1981.

Baumann, H., & Becker, A., Lokale variation regionaler spannungsfelder an zwei beispielen aus SW-Deutschland un der Schweiz, *Proceedings of the International Symposium on Rock Stress Measurements*, Stockholm, September 1-3, pp. 45-53, 1986.

Becker, A., Blenkinsop, T.G., & Hancock, P.L., Comparison and tectonic interpretation of in situ stress measurements by flatjack and doorstopper techniques in Gloucestershire, England, *Annales Tectonicae*, 4, (1), pp. 3-18, 1990.

Bell, J.S., Investigating stress regimes in sedimentary basins using information from oil industry wireline logs and drilling records, in *Geological Applications of Wireline Logs*, edited by A. Hurst & M.A. Lovell, *Geological Society Special Publication*, 48, pp. 305-325, 1990a.

Bell, J.S., The stress regime of the Scotian Shelf offshore eastern Canada to 6 kilometers depth and implications for rock mechanics and hydrocarbon migration, in *Rock at Great Depth*, edited by V. Maury & D. Fourmaintraux, pp. 1243- 1265 A.A. Balkema, Rotterdam, Netherlands, 1990b.

Bell, J.S., The Global Sedimentary Basin Stress Project of the International Lithosphere Program, Poster, p. 71, *55th Meeting of European Association of Exploration Geophysicists*, Stavanger, Norway, June 7-11, 1993.

Bell, J.S., & Babcock, E.A., The stress regime of the Western Canadian Basin and implications for hydrocarbon production, *Bulletin of Canadian Petroleum Geology*, 34(3), pp. 364-378, 1986.

Bell, J.S., Caillet, G., & Adams, J., Attempts to detect open fractures and non-sealing faults with dipmeter logs, in *Geological Applications of Wireline Logs II*, edited by A. Hurst, C.M. Griffiths, & P.F. Worthington, *Geological Society Special Publication*, 65, pp. 211-220, 1992a.

Bell, J.S., Caillet, G., & Le Marrec, A., The present-day stress regime of the southwestern part of the Aquaitaine Basin, France, as indicated by oil-well data, *Journal of Structural Geology*, 14, pp. 1019-1032, 1992b.

Berry, M.D., Stearns, D.W., & Friedman, M., The development of a fractured reservoir model for the Palm Valley gasfield, in *The APEA Journal*, 36(1), pp. 82-103, 1996.

Bradley, W.B., Failure of inclined boreholes, *Journal of Energy Resources Technology*, 101, pp. 232-39, 1979.

Bradshaw, M.T., Yeates, A.N. Beynon, R.M., Brakel, A.T., Langford, R.P., Totterdell, J.M., & Yeung, M., Palaeogeographic evolution of the North West Shelf region, in *The North West Shelf Australia, Proceedings of Petroleum Exploration Society, Australian Symposium*, edited by P.G. Purcell and R.R. Purcell, pp. 29-54, Petroleum Exploration Society, Perth, Australia, 1988.

Breckels, I.M., & Van Eekelen, H.A.M., Relationship between horizontal stress and depth in sedimentary basins, *Journal of Petroleum Technology*, September, pp. 2191-2199, 1982.

Bredehoeft, J.D., Wolff, R.G., Keys, W.S., & Shuter, E., Hydraulic fracturing to determine the regional in situ stress field, Piceance Basin, Colorado, *Geological Society of America Bulletin*, 87, pp. 250-258, 1976.

Brown, S.A., Boserio, I.M., Jackson, K.S., & Spence, K.W., The geological evolution of the Canning Basin, implications for petroleum exploration, in *The Canning Basin, W.A., Proceedings of Petroleum Exploration Society, Australian Symposium*, edited by P.G. Purcell, pp. 85-96, Petroleum Exploration Society, Perth, Australia, 1984.

Burke, K., & Dewey, J.F., Plume-generated triple junctions: key indicators in applying plate tectonics to old rocks, *Journal of Geology*, 81, pp. 406-433, 1973.

Byerlee, J.D., Friction of rock, *Pure and Applied Geophysics*, 116, pp. 615-626, 1979.

Caillet, G., The caprock of the Snorre Field, Norway: a possible leakage by hydraulic fracturing, *Marine and Petroleum Geology*, 10, pp. 42-50, 1993.

Caputo, M.V., & Crowell, J.C., Migration of glacial centers across Gondwana during Paleozoic Era, *Geological Society of America Bulletin*, 96, pp. 1020-1036, 1985.

Cardwell, R.K., & Isacks, B.L., Geometry of the subducted lithosphere beneath the Banda Sea in eastern Indonesia from seismicity and fault plane solutions, *Journal of Geophysical Research*, 83, 2825-2838, 1978.

Cartwright, J.A., Episodic basin-wide fluid expulsion from geopressured shale sequences in the North Sea basin, *Geology*, 22, pp. 447-450, May, 1994.

Castillo, D.A., & O'Niell, B., Constraints on the state of stress in old oceanic crust of the Indo-Australian plate, northwest of Australia, in *Proceedings of ODP, Scientific Results 123*, edited by Ludden, J.N., Gradstein, F.M., et. al., College Station, Texas, pp. 503-513, 1992.

Chamalaun, F., Lockwood, K., & White, A., The Bouguer gravity field of east Timor, *Tectonophysics*, 30, pp. 241-259, 1976.

Chen, Z., LI, Z.X., Powell, C.McA., & Balme, B.E., Paleomagnetism of the Brewer Conglomerate in central Australia, and fast movement of Gondwanaland during the Late Devonian, *Geophysical Journal International*, 115, pp. 564-574, 1993.

Chen, Z., LI, Z.X., Powell, C.McA., & Balme, B.E., An Early Carboniferous paleomagnetic pole for Gondwanaland: new results from the Mount Eclipse Sandstone in the Ngalia Basin, central Australia, *Journal of Geophysical Research*, 99, pp. 2909-2924, 1994.

Cloetingh, S., Stein, C., Reemst, P., Gradstein, F., Williamson, P., Exon, N., & von Rad, U., The relationship between continental margin stratigraphy, deformation, and intraplate stresses for the Indo-Australian region, Ocean Drilling Project Proceedings Leg 123, volume B, 1990.

Cloetingh, S., Wortel, R., & Vlaar, N.J., State of stress at passive margins and initiation of subduction zones, *Nature*, 297, pp. 139-142, 1982.

Cloetingh, S., & Wortel, R., Regional stress field in the Indian plate, *Geophysical Research Letters*, 12, pp. 77-80, 1985.

Cloetingh, S., & Wortel, R., Stress in the Indo-Australian plate, *Tectonophysics*, 132, pp. 49-67, 1986.

Coblentz, D.D., Sandiford, M., Richardson, R.M., Zhou, S., & Hillis, R., The origins of the intraplate stress field in continental Australia, *Earth and Planetary Science Letters*, 133, pp. 299-309, 1995.

Cockbain, A.E., The North West Shelf, *The APEA Journal*, 29(1), pp. 529-545, 1989.

Colwell, J.B., & Stagg, H.M.J., Structure of the offshore Canning Basin: first impressions from a new regional deep-seismic data set, in *The Sedimentary Basins of Western Australia, Proceedings of Petroleum Exploration Society, Australian Symposium*, edited by P.G. Purcell & R.R. Purcell, pp. 757-767, Petroleum Exploration Society, Perth, Australia, 1994.

Copp, I.A., Depth to base Phanerozoic map of Western Australia: explanatory notes, with contributions from Iasky, R.P., Hocking, R.M., Mory, A.J. & Luck, G.R., Geological Survey of Western Australia, Record 9, p. 11, 1994.

Corbett, K., Friedman, M., & Spang, J., Fracture development and mechanical stratigraphy of the Austin Chalk, Texas, *American Association of Petroleum Geologists Bulletin*, 71, pp. 17-28, 1987.

Cornet, F.H., & Valette, B., In situ stress determination from hydraulic injection test data, *Journal of Geophysical Research*, 89(B13), pp. 11527-11537, 1984.

Coulomb, C.A., Sur une application des regles de maximus et minimus a quelques problemes de statique relatifs a l'architecture, Acad. Roy. des Sci., Memoirs de Math. Et de Physique par divers savans, 7, pp. 343-382, 1773.

Dart, R.L., & Swolfs, H.S., Subparallel faults and horizontal stress orientations: an evaluation of in-situ stresses inferred from elliptical wellbore enlargements, in *Structural and tectonic modelling and its application to petroleum geology*, edited by R.M. Larsen, H. Brekke, B.T. Larsen and E. Talleraas, NPF Special Publication 1, pp. 519-529, Elseveir, Amsterdam, 1992.

Dart, R.L., & Zoback, M.L., Wellbore breakout stress analysis within the central and eastern continental United States, *Log Analyst*, 30(1), pp. 12-25, 1989.

Deep Sea Drilling Project Leg 27 Shipboard Scientific Party, Site 261, *Initial Report Deep Sea Drilling Project*, 27, pp. 129-192, 1974.

Denham, D., & Windsor, C.R., The crustal stress pattern in the Australian continent, *Exploration Geophysics*, 22, pp. 101-105, 1991.

Du Rouchet, J.H., Stress Fields, A Key to Oil Migration, *The American Association of Petroleum Geologists Bulletin*, 65, (1), pp. 74-85, 1981.

Elliott, L.G., Post-Carboniferous tectonic evolution of eastern Australia, *The APEA Journal*, 33, pp. 215-236, 1993.

Enever, J.R., Ten years experience with hydraulic fracture stress measurements in Australia, *Proceedings 2nd International Workshop on Hydraulic Fracturing Stress Measurements,* Geological Engineering Program, University of Winconsin-Madison, pp. 1-92, 1988.

Enever, J.R., Yassir, N., Willoughby, D.R., & Addis, M.A., Recent experience with extended leak-off tests for in-situ stress measurements in Australia, *The APEA Journal*, 36, pp. 528-535, 1996.

Engelder, T., Stress Regimes in the Lithosphere, Princeton, New Jersey, Princeton University Press, 1993.

Ervine, W.B., & Bell, J.S., Subsurface in situ stress magnitudes from oil-well drilling records: an example from the Venture area, offshore eastern Canada, *Canadian Journal of Earth Sciences*, 24, pp. 1748-1759, 1987.

Forrest, J.T., & Horstman, E.L., The Northwest Shelf of Australia-geologic review of a potential major petroleum province of the future, in *Future petroleum provinces of the world, proceedings of the Wallace C. Pratt Memorial Conference*, edited by M.T. Halbouty, Phoenix, 1984, *American Association of Petroleum Geologists Memoir*, 40, pp. 457-485, 1986.

Froidevaux, C., Paquin, C., & Souriau, M., Tectonic stresses in France: in situ measurements with a Flat Jack, *Journal of Geophysical Research*, 85, pp. 6342-6345, 1980.

Gaarenstroom, L., Tromp, R.A.J., de Jong, M.C., & Brandenburg, A.M., Overpressure in the Central North Sea: implications for trap integrity and drilling safety, in *Petroleum Geology of Northwest Europe: Proceedings of the 4th Conference*, edited by J.R. Parker, The Geological Society, London, pp. 1305- 1313, 1993.

Gaull, B.A., & Gregson, P.J., A new local magnitude scale for Western Australian earthquakes, *Australian Journal of Earth Sciences*, 38, pp. 251-260, 1991.

Genrich, J.F., Bock, Y., McCaffrey, R., Calais, E., Stevens, C.W., & Subarya, C., Accretion of the southern Banda arc to the Australian plate margin determined by global positioning system measurements, *Tectonics*, 15, pp. 288-295, 1996.

Gough, D.I., Bell, J.S., Stress orientations from borehole wall fractures with examples from Colorado, east Texas, and northern Canada, *Canadian Journal of Earth Sciences*, 19, pp. 1358-1370, 1982.

Guenot, A., & Santarelli, F.J., Borehole stability: a new challenge for an old problem, in Key Questions in Rock Mechanics, edited by Cundall et al., A.A. Balkema, Rotterdam, Nederlands, pp. 453-460, 1988.

Gunn, P.J., Hydrocarbon discoveries in the Bonaparte Basin, in *The North West Shelf Australia, Proceedings of Petroleum Exploration Society, Australian Symposium*, P.G. Purcell & R.R. Purcell, pp. 419-424, Petroleum Exploration Society, Perth, Australia, 1988.

Haimson, B., & Fairhurst, C., Initiation and extension of hydraulic fractures in rocks, *Society of Petroleum Engineers Journal*, 7, pp. 310-318, 1967.

Haimson, B., & Herrick, C.G., Borehole breakouts- a new tool for estimating in situ stress?, *Proceedings of the International Symposium on Rock Stress Measurements, Stockholm, 1-3 September*, pp. 271-280, 1986.

Haq, B.U., Hardenbol, J., & Vail, P.R., Chronology of fluctuating sea levels since the Triassic, *Science*, 235, pp. 1156-1167, 1987.

Hassan, D., A method for predicting hydraulic fracture azimuth and the implication thereof to improve hydrocarbon recovery, *Paper 82-33-19, 33rd Annual Technical Meeting of the Petroleum Society of the Canadian Institute of Mining and Metallurgy*, Calgary, June6-9, 1982.

Hickman, S.H., Healy, J.H., & Zoback, M.D., In situ stress, natural fracture distribution, and borehole elongation in the Auburn Geothermal Well, Auburn, New York, *Journal of Geophysical Research*, 90(B7), pp. 4597-5512, 1985.

Hillis, R.R., Does the in situ stress field control the orientation of open natural fractures in sub-surface reservoirs?, *Exploration Geophysics*, 28, pp. 80-87, 1987.

Hillis, R.R., Post-Permian subsidence and tectonics, Vulcan Sub-basin, North West Shelf, Australia, *Pacific Rim Congress 90, Gold Coast, May 1990*, 2, pp. 203-211, 1990.

Hillis, R.R., Australia-Banda Arc collision and in-situ stress in the Vulcan Sub-basin (Timor Sea) as revealed by borehole breakout data, *Exploration Geophysics*, 22, pp. 189-194, 1991.

Hillis, R.R., Mildren, S.D., Pigram, C.J., & Willoughby, D.R., Rotation of horizontal stresses in the Australian North West Continental Shelf due to the collision of the Indo-Australian and Eurasian Plates, *Tectonics*, 16 (2), pp. 323-335, 1997.

Hillis, R.R., Monte, S.A., Tan, C.P., & Willoughby, D.R., The contemporary stress field of the Otway Basin, South Australia: implications for hydrocarbon exploration and production, *The APEA Journal*, 35, pp. 494-506, 1995.

Hillis, R.R., & Williams, A.F., Borehole breakouts and stress analysis in the Timor Sea, in *Geological Applications of Wireline Logs II*, edited by A. Hurst, C.M. Griffiths, & P.F. Worthington, *Geological Society Special Publication*, 65, pp. 157-168, 1992.

Hillis, R.R., & Williams, A.F., The stress field of the North West Shelf and wellbore stability, *The APEA Journal*, 33, pp. 373-385, 1993a.

Hillis, R.R., & Williams, A.F., The contemporary stress field of the Barrow-Dampier sub-basin and its implications for horizontal drilling, *Exploration Geophysics*, 24, 567-576, 1993b.

Hobbs, B.E., Means, W.D., & Williams, P.F., An outline of structural geology, John Wiley and Sons, Singapore, p. 571, 1976.

Hocking, R.M., Regional geology of the northern Carnarvon Basin, in *The North West Shelf Australia, Proceedings of Petroleum Exploration Society, Australian Symposium*, P.G. Purcell & R.R. Purcell, pp. 97-113, Petroleum Exploration Society, Perth, Australia, 1988.

Hocking, R.M., Mory, A.J., & Williams, I.R., An atlas of Neoproterozoic and Phanerozoic basins of Western Australia, in *The Sedimentary Basins of Western Australia, Proceedings of Petroleum Exploration Society, Australian Symposium*, edited by P.G. Purcell & R.R. Purcell, pp. 21-43, Petroleum Exploration Society, Perth, Australia, 1994.

Horn, M.K., Play concepts for horizontal drilling, in *Geological aspects of horizontal drilling*, edited by R.D. Fritz, M.K. Horn & S.D. Joshi, American Association of Petroleum Geologists Continuing Education Course Note Series 33, pp. 189-323, 1991.

Horstman, E.L., Source maturity, overpressure and production, North West Shelf, Australia, in *The North West Shelf Australia, Proceedings of Petroleum Exploration Society, Australian Symposium*, P.G. Purcell & R.R. Purcell, pp. 529-537, Petroleum Exploration Society, Perth, Australia, 1988.

Horstman, E.L., & Purcell, P.G., The offshore Canning Basin- a review, in *The North West Shelf Australia, Proceedings of Petroleum Exploration Society, Australian Symposium*, P.G. Purcell & R.R. Purcell, pp. 253-257, Petroleum Exploration Society, Perth, Australia, 1988.

Howell, E.A., The Harriet Oil Field, in *The North West Shelf Australia, Proceedings of Petroleum Exploration Society, Australian Symposium*, edited by P.G. Purcell and R.R. Purcell, pp. 391-401, Petroleum Exploration Society, Perth, Australia, 1988.

Hubbert, M.K., & Willis, D.G., Mechanics of hydraulic fracturing, *Transactions of AIME,* 210, pp. 153-168, 1957.

Hudson, J.A., & Cooling, C.M., In situ rock stresses and their measurement in the U.K.- Part I. The current state of knowledge, International Journal of Rock Mechanics, Mineral Science & Geomechanics Abstracts, 25, No. 6, pp. 363-370, 1988.

Jackobson, R.S., Shor, Jr., G.G., Kieckhefer, R.M., & Purdy, G.M., Seismic refraction and reflection studies in the Timor-Aru Trough system and Australian continental shelf, *American Association Petroleum Geology Memoir*, 29, pp. 209-222, 1978.

Jaeger, J.C., Elasticity, fracture and flow, Methuen, p. 212, 1961.

Jaeger, J.C., & Cook, N., Fundamentals of rock mechanics, Methuen and Co. Ltd, London, 1969.

Johnston, C.R., & Bowin, C.O., Crustal reactions resulting from the mid Pliocene-Recent continental-island arc collision in the Timor region, *Bureau of Mineral Resources, Journal of Australian Geology and Geophysics*, 6, pp. 223-243, 1981.

Jones, H.A., Marine geology of the northwest Australian continental shelf, *Bureau of Mineral Resources, Australia,* Bulletin 136, 1973.

Kennard, J.M., Jackson, M.J., Romine, K.K., Shaw, R.D., & Southgate, P.N., - Depositional sequences and associated petroleum systems of the Canning Basin, W.A, in *The Sedimentary Basins of Western Australia, Proceedings of Petroleum Exploration Society, Australian Symposium*, edited by P.G. Purcell & R.R. Purcell, pp. 657-676, Petroleum Exploration Society, Perth, Australia, 1994.

Kingsborough, R.H., Williams, A.F., & Hillis, R.R., Borehole instability on the North West Shelf of Australia, *Proceedings of the Society of Petroleum Engineers Asia-Pacific Conference, Perth, WA, November 1991*, pp. 653-662, 1991.

Kirsch, G., Die theorie der elastizitat und die Dedurfnisse der fertigkeirslehre, VDI Z. 42, pp. 797, 1898.

Knott, S.D., Fault seal analysis in the North Sea, *The American Association of Petroleum Geologists Bulletin*, 77, (5), pp. 778-792, 1993.

Lacey, L.L., & Smith, M.B., Fracture azimuth and geometry determination, in *Recent advances in hydraulic fracturing*, edited by J.L. Gidley, S.A. Holditch, D.E. Nierode, & R.W. Veatch Jr., Society of Petroleum Engineers Monograph Series 12, pp. 341-356, 1989.

Lavering, I.H., & Ozimic, S., Bonaparte Basin petroleum accumulations, in *The North West Shelf Australia, Proceedings of Petroleum Exploration Society, Australian Symposium*, P.G. Purcell & R.R. Purcell, pp. 331-337, Petroleum Exploration Society, Perth, Australia, 1988.

Lee, R.J., & Gunn, P.J., Bonaparte Basin, in *Petroleum in Australia, The First Century*, Australian Petroleum Exploration Association publication, pp. 252-269, 1988.

Lipski, P., Structural framework and depositional history of the Bedout and Rowley Sub-basins, in *The Sedimentary Basins of Western Australia, Proceedings of Petroleum Exploration Society, Australian Symposium*, edited by P.G. Purcell & R.R. Purcell, pp. 769-777, Petroleum Exploration Society, Perth, Australia, 1994.

Lisk, M., & Eadington, P., Oil migration in the Cartier Trough, Vulcan Sub-basin, in *The Sedimentary Basins of Western Australia, Proceedings of Petroleum Exploration Society, Australian Symposium*, edited by P.G. Purcell & R.R. Purcell, pp. 301-312, Petroleum Exploration Society, Perth, Australia, 1994.

Leonard, R.C., Distribution of sub-surface pressure in the Norwegian Central Graben and applications for exploration, *Petroleum Geology of Northwest Europe: Proceedings of the 4th Conference*, The Geological Society, London, 1993.

Lowry, D.C., Fighting fractured flamingo: lessons from rambler-1, Timor Sea, The APEA Journal, 35, pp. 655-665, 1995.

Ludwig, W.E., Nafe, J.E., & Drake, C.L., Seismic refraction, in The Sea, edited by A.E. Maxwell, 4, pp. 53-84, Wiley-Interscience, New York, 1970.

McCaffrey, R., Molnar, P., & Roecker, S.W., Microearthquake seismicity and fault plane solutions related to arc-continent collision in the eastern Sunda Arc, Indonesia, *Journal of Geophysical Research*, 90, pp. 4511-4528, 1985.

McGarr, A., & Gay, N.C., State of stress in the Earth's crust, *Ann. Rev. Earth Planet. Sci.*, 6, pp. 405-436, 1978.

McLeod, J.G.F., Successful injection pattern alteration, Pembina J Lease, Alberta, *paper presented at the 28th Annual Meeting of Petroleum Society of Canadian Institute Mining*, Edmonton, 1977.

McNaughton, D.A., Horizontal drilling vs. hydraulic fracturing, American Association of Petroleum Geologists Explorer 12, January, p. 139, 1991.

Mardia, K.V., Statistics of directional data, Academic, London, New York, 1972.

Martin, M.A., & Davis, T.L., Shear-wave birefringence: a new tool for evaluating fractured reservoirs, *The leading edge*, 6, October, pp. 22-28, 1987.

Maung, T.U., Cadman, S., & West, B., A review of the petroleum potential of the Browse Basin, in *The Sedimentary Basins of Western Australia, Proceedings of Petroleum Exploration Society, Australian Symposium*, edited by P.G. Purcell & R.R. Purcell, pp. 336-346, Petroleum Exploration Society, Perth, Australia, 1994.

Mildren, S.D., Hillis, R.R., Fett, T., & Robinson, P.H., Contemporary Stresses in the Timor Sea: implications for fault-trap integrity, in *The Sedimentary Basins of Western Australia, Proceedings of Petroleum Exploration Society, Australian Symposium*, edited by P.G. Purcell & R.R. Purcell, pp. 291-300, Petroleum Exploration Society, Perth, Australia, 1994.

Minster, J.B., & Jordan, T.H., Present-day plate motion, *Journal of Geophysical Research*, 83, pp. 5331-5334, 1978.

Mory, A.J., Regional geology of the offshore Bonaparte Basin, in *The North West Shelf Australia, Proceedings of Petroleum Exploration Society, Australian Symposium*, P.G. Purcell & R.R. Purcell, pp. 287-309, Petroleum Exploration Society, Perth, Australia, 1988.

Nelson, A.W., Jaribu field - Horst, sub-horst or inverted graben?, *The APEA Journal*, 29, pp. 176-194, 1989.

Nelson, A.W., Wrench and inversion structures in the Timor Sea region, *Petroleum Exploration Society of Australia Journal*, July, pp. 3-30, 1993.

North, F.K., Petroleum Geology, Allen & Unwin, Boston, p. 607, 1985.

O'Brien, G.W., Etheridge, M.A., Willcox, J.B., Morse, M., Symonds, P., Norman, C., & Needham, D.J., The structural architecture of the Timor Sea, north-western Australia: Implications for basin development and hydrocarbon exploration, *The APEA Journal*, 33, (1), pp. 258-278, 1993.

O'Brien, G.W., & Woods, E.P., Hydrocarbon-related diagenetic zones (HRDZs) in the Vulcan Sub-basin, Timor Sea: recognition and exploration implications, *The APEA Journal*, 35, pp. 220-252, 1995.

Paillet, F.L., & Kim, K., The character and distribution of borehole breakouts and their relationship to borehole breakouts in deep Columbia River basalts, *Journal of Geophysical Research Letters*, 92, B7, pp. 6223-6234, 1987.

Parry, J.C., & Smith, D.N., The Barrow and Exmouth Sub-basins, in *The North West Shelf Australia, Proceedings of Petroleum Exploration Society, Australian Symposium*, P.G. Purcell & R.R. Purcell, pp. 129-145, Petroleum Exploration Society, Perth, Australia, 1988.

Passmore, V.L., Browse Basin region explanatory notes and stratigraphic columns, *Bureau of Mineral resources, Record 1980/42*, unpublished, 1980.

Patillo, J., & Nicholls, P.J., A tectono-stratigraphic framework for the Vulcan Graben, Timor Sea region, *The APEA Journal*, 30, pp. 27-51, 1990.

Peska, P., & Zobak, M.D., Compressive and tensile failure of inclines well bores and determination of in situ stress and rock strength, *Journal of Geophysical Research*, 100(B7), pp. 12791-12811, 1995.

Pigram, C.J., & Davies, H.L., Terranes and the accretion history of the New Guinea orogen, *BMR Journal of Australian Geology and Geophysics*, 10, pp. 193-211, 1987.

Pigram, C.J., & Symonds, P.A., A review of the timing of the major tectonic events in the New Guinea Orogen, *Journal of Southeast Asian Earth Sciences*, 6(3/4), pp. 397-318, 1991.

Pilkington, P.E., Fracture gradient estimates in Tertiary basins, *Pet. Eng. Intl.*, May, pp. 138-148, 1978.

Playford, P.E., Devonian reef prospects in the Canning Basin: implications of the Blina oil discovery, *The APEA Journal*, 22(1), pp. 258-271, 1980.

Playford, P.E., Cope, R.N., Cockbain, A.E., Low, G.H., & Lowry, D.C., Phanerozoic, in *Geology of Western Australia: Geological Survey of Western Australia*, Memoir 2, pp. 223-435, 1975.

Plumb, R.A., Fracture patterns associated with incipient wellbore breakouts, in *Rock at Great Depth*, edited by V. Maury & D. Fourmaintraux, A.A. Balkema, Rotterdam, 2, pp. 761-768, 1989.

Plumb, R.A., & Hickman, S.H., Stress induced borehole elongation: a comparison between the four-arm dipmeter and the borehole televiewer in the Auburn geothermal well, *Journal of Geophysical Research*, 90, pp. 5513-5321, 1985.

Powell, C.McA., & Veevers, J.J., Namurian uplift I Australia and South America triggered the main Gondwanan glaciation, *Nature*, 326, pp. 177-179, 1987.

Purcell, P.G., & Purcell R.R., The North West Shelf, Australia- an introduction, in *The North West Shelf Australia, Proceedings of Petroleum Exploration Society, Australian Symposium*, P.G. Purcell & R.R. Purcell, pp. 3-15, Petroleum Exploration Society, Perth, Australia, 1988.

Purcell, P.G., & Purcell R.R., The sedimentary basins of Western Australia: an introduction, in *The Sedimentary Basins of Western Australia, Proceedings of Petroleum Exploration Society, Australian Symposium*, edited by P.G. Purcell & R.R. Purcell, pp. 3-18, Petroleum Exploration Society, Perth, Australia, 1994.

Queen, J.H., & Rizer, W.D., An integrated study of seismic anisotropy and the natural fracture system at the Conoco borehole test facility, Kay County, Oklahoma, *Journal of Geophysical Research*, 95, pp. 11255-11273, 1990.

Rawnsley, K.D., Rives, T., Petit, J.P., Hencher, S.R., & Lumsden, A.C., Joint development in perturbed stress fields near faults, *Journal of Structural Geology*, 14, No. 8/9, pp. 939-951, 1992.

Sengor, A.M.C., Tectonics in the Tethysides: orogenic collage development in a collisional setting, *Annual Reviews of Earth and Planetary Science*, 15, pp. 213-244, 1987.

Serra, O., Fundamentals of well-log interpretation, translated from French by P. Westaway & H. Abbott, *Development in Petroleum Science*, Amsterdam, Elsevier, 1984.

Shamir, G., & Zoback, M.D., Stress orientation profile to 3.5 km depth near the San Andreas Fault at Cajon Pass, California, *Journal of Geophysical Research*, 97, B4, pp. 5059-5080, 1992.

Sonder, L.J., Effects of density contrasts on the orientation of stresses in the lithosphere: Relation to principal stress directions in the Transverse ranges, California, *Tectonics*, 9, pp. 761-771, 1990.

Stagg, H.M.J., & Colwell, J.B., The structural foundations of the northern Carnarvon Basin, in *The Sedimentary Basins of Western Australia, Proceedings of Petroleum Exploration Society, Australian Symposium*, edited by P.G. Purcell & R.R. Purcell, pp. 349-364, Petroleum Exploration Society, Perth, Australia, 1994.

Tan, C.P., Willoughby, D.R., Hillis, R.R., Zhou, S., Muhlhaus, H.B., & Aoki, T., Wellbore instability in the North West Shelf of Australia, *The APEA Journal*, 34, pp. 3-18, 1994.

Taylor, L.W.H., 1994 exploration review: Australia and Timor gap zone of co-operation, *The APEA Journal*, part 2, pp. 84-89, 1995.

Teichert, C., Australia and Gondwanaland, *Geologische Rundschau*, Sonderdruck, 47(2), pp. 562-590, 1958.

Teufel, L.W., Influence of lithology and geologic sructure on in situ stress: examples of stress heterogeneity in reservoirs, in *Reservoir Characterization II*, edited by L.W. Lake, H.B. Carroll Jr. & T.C. Wesson, pp. 565-578, Academic, San Diego, California, 1991.

Turcotte, D.L., Ahern, J.L., & Bird, J.M., The state of stress at continental margins, *Tectonophysics*, 42, pp. 1-28, 1977.

Vail, P.R., Mitchum, R.M. & Thompson, S., Seismic stratigraphy and global changes of sea level, part 4: global cycles of relative changes of sea level, *American Association of Petroleum Geologists Memoir*, 26, pp. 83-97, 1977.

Veevers, J.J., Early Phanerozoic events on and alongside the Australasian-Antarctic platform, *Geological Society of Australia Journal*, 23, pp. 183-206, 1976.

Veevers, J.J., Morphotectonics of Australia's northwestern margin- a review, in *The North West Shelf Australia, Proceedings of Petroleum Exploration Society, Australian Symposium*, P.G. Purcell & R.R. Purcell, pp. 19-27, Petroleum Exploration Society, Perth, Australia, 1988.

Veevers, J.J., & Powell, C.McA., Late Proterozoic glacial episodes in Gondwanaland reflected in transgressive-regressive depositional sequences in Euramerica, *Geological Society of America Bulletin*, 98, pp. 475-487, 1987.

Veevers, J.J., Powell, C.McA., & Roots, S.R., Review of seafloor spreading around Australia. I. Synthesis of the patterns of spreading, *Australian Journal of Earth Sciences*, 38, pp. 373-389, 1991.

Walcott, R.I., Gravity flexure and the growth of sedimentary basins at a continent edge, *Geological Society of America Bulletin*, 83, pp. 1845-1848, 1972.

Watts, N.L., Theoretical aspects of cap-rock and fault seals for single and two phase hydrocarbon columns, *Marine and Petroleum Geology*, 4, pp. 274-307, 1987.

Whitford, D.J., & Jezek, P.A., Isotopic constraints on the role of subducted sialic material in Indonesian island-arc magmatism, *Geological Society of America Bulletin*, 93, pp. 504-513, 1982.

Woodland, D.C., Borehole instability in the Western Canadian Overthrust Belt, SPE Paper 17508, *Rocky Mountain Regional Meeting, Society of Petroleum Engineers of AIME*, Casper, Wyoming, May 11-13, 1988.

Woods, E.P., Extensional structures of the Jabiru Terrace, Vulcan Sub-basin, in *The North West Shelf Australia, Proceedings of Petroleum Exploration Society, Australian Symposium*, P.G. Purcell & R.R. Purcell, pp. 311-330, Petroleum Exploration Society, Perth, Australia, 1988.

Woods, E.P., Vulcan Sub-Basin fault styles - implications for hydrocarbon migration and entrapment, *The APEA Journal*, 32, (1), pp. 138-158, 1992.

Woodside Offshore Petroleum, A review of the petroleum geology and hydrocarbon potential of the Barrow-Dampier Sub-basin and environs, in *Petroleum in Australia, The First Century*, Australian Petroleum Exploration Association publication, pp. 213-231, 1988

Yassir, N.A., & Bell, J.S., Relationships between pore pressure, stresses, and present-day geodynamics in the Scotian Shelf, offshore eastern Canada, *AAPG Bulletin*, 78(12), pp. 1863-1880, 1994.

Yeates, A.N., Bradshaw, M.T., Dickins, J.M., Brackel, A.T., Exon, N.F., Langford, R.P., Mulholland, S.M., Totterdell, J.M., & Yeung, M., The Westralian Superasin: an Australian link with Tethys, in *Proceedings, Second Shallow Tethys Conference*, edited by K.G. McKenzie, Wagga Wagga, NSW, Australia, pp. 199-213, A.A. Balkema, Rotterdam, Boston, 1987.

Zoback, M.D., State of stress and crustal deformation along weak transform faults, *Philos. Trans. R. Soc. London, Ser. A*, 337, pp. 111-126, 1991.

Zoback, M.D., In situ stress measurements and geologic processes, *A short course in modern in situ stress measurement methods, The 34th U.S. Symposium on Rock Mechanics*, June 27-30, pp. 1-23, 1993.

Zoback, M.D., & Healy, J., Friction, faulting and in situ stress, *Annales Geophysicae*, 2, No. 6, pp. 689-698, 1984.

Zoback, M.D., Mastin, L., Barton, C., In-situ stress measurements in deep boreholes using hydraulic fracturing, wellbore breakouts, and stonely wave polarization, in *Proceedings of the International Symposium on Rock Stress Measurements*, Stockholm, September 1-3, pp. 289-299, 1986.

Zoback, M.D., Moos, D., Mastin, L., & Anderson, R.N., Wellbore breakouts and in situ stress, Journal of Geophysical Research, 90, pp. 5523-5530, 1985.

Zoback, M.D., & Zoback, M.L., Tectonic stress field of North America and relative plate motions, chapter 19, in *Neotectonics of North America*, edited by D.B. Slemmons, E.R. Engdahl, M.D. Zoback & D.D. Blackwell, *Geology Society of America*, Decade Map Volume 1, pp. 339-366, 1991.

Zoback, M.L., First and second-order patterns of stress in the lithosphere: the world stress map project, *Journal of Geophysical Research*, 97(B8), pp. 11703-11728, 1992.

Zoback, M.L., Zoback, M.D., Adams, J., Assumpcao, M., Bell, S., Bergman, E.A., Blumling, P., Brereton, N.R., Denham, D., Ding, J., Fuchs, K., Gay, N., Gregersen, S., Gupta, H.K., Gvishiani, A., Jacob, K., Klein, R., Knoll, P., Magee, M., Mercier, J.L., Muller, B.C., Paquin, C., Rajendran, K., Stephansson, O., Suarez, G., Suter, M., Udias, A., Xu., Z.H., & Zhizhin, M., Global patterns of tectonic stress, *Nature*, 341, pp. 291-298, 1989.